

REPORT DOCUMENTATION PAGE

Form Approved OMB NO. 0704-0188

The public reporting burden for this collection of information is estimated to average 1 hour per response, including the time for reviewing instructions, searching existing data sources, gathering and maintaining the data needed, and completing and reviewing the collection of information. Send comments regarding this burden estimate or any other aspect of this collection of information, including suggestions for reducing this burden, to Washington Headquarters Services, Directorate for Information Operations and Reports, 1215 Jefferson Davis Highway, Suite 1204, Arlington VA, 22202-4302. Respondents should be aware that notwithstanding any other provision of law, no person shall be subject to any penalty for failing to comply with a collection of information if it does not display a currently valid OMB control number.

PLEASE DO NOT RETURN YOUR FORM TO THE ABOVE ADDRESS.

1. REPORT DATE (DD-MM-YYYY) 03-08-2010	2. REPORT TYPE Final Report	3. DATES COVERED (From - To) 15-Jun-2006 - 14-Jun-2010		
4. TITLE AND SUBTITLE Understanding and Quantifying the Reactivity of Energetic NanoParticles and NanoComposites		5a. CONTRACT NUMBER W911NF-06-1-0215		
		5b. GRANT NUMBER		
		5c. PROGRAM ELEMENT NUMBER 611102		
6. AUTHORS Michael R. Zachariah		5d. PROJECT NUMBER		
		5e. TASK NUMBER		
		5f. WORK UNIT NUMBER		
7. PERFORMING ORGANIZATION NAMES AND ADDRESSES University of Maryland - College Park Office of Research Administration & Advancement University of Maryland, College Park College Park, MD 20742 -5141		8. PERFORMING ORGANIZATION REPORT NUMBER		
9. SPONSORING/MONITORING AGENCY NAME(S) AND ADDRESS(ES) U.S. Army Research Office P.O. Box 12211 Research Triangle Park, NC 27709-2211		10. SPONSOR/MONITOR'S ACRONYM(S) ARO		
		11. SPONSOR/MONITOR'S REPORT NUMBER(S) 49022-EG.11		
12. DISTRIBUTION AVAILABILITY STATEMENT Approved for Public Release; Distribution Unlimited				
13. SUPPLEMENTARY NOTES The views, opinions and/or findings contained in this report are those of the author(s) and should not be construed as an official Department of the Army position, policy or decision, unless so designated by other documentation.				
14. ABSTRACT The focus of this work is to understand quantitatively, the nature of the reactivity of nanoparticles and nanocomposites for energetic materials application. Our approach takes two thrusts.				
1. Single Particle Kinetics 2. Ensemble Fuel/Oxide Nanocomposite Kinetics.				
15. SUBJECT TERMS Energetic Materials				
16. SECURITY CLASSIFICATION OF: a. REPORT UU		17. LIMITATION OF ABSTRACT UU	15. NUMBER OF PAGES	19a. NAME OF RESPONSIBLE PERSON Michael Zachariah
				19b. TELEPHONE NUMBER 301-405-4311

Report Title

Understanding and Quantifying the Reactivity of Energetic NanoParticles and NanoComposites

ABSTRACT

The focus of this work is to understand quantitatively, the nature of the reactivity of nanoparticles and nanocomposites for energetic materials application. Our approach takes two thrusts.

1. Single Particle Kinetics
2. Ensemble Fuel/Oxide Nanocomposite Kinetics.

Our goal was to:

- A. Explore the size resolved reactivity of nanoparticles, comprised of composites or core-shell nanostructures.
- B. Explain the behavior using phenomenological modeling and compare with bulk materials.
- C. Explore solid-solid ensemble kinetics of unique nanocomposites of fuel/oxidizers.

List of papers submitted or published that acknowledge ARO support during this reporting period. List the papers, including journal references, in the following categories:

(a) Papers published in peer-reviewed journals (N/A for none)

L. Zhou, K. Park, H. Milchberg, and M.R. Zachariah

"Understanding the Interaction of an Intense Laser Pulse with Nanoparticles: Application to Quantification of Single Particle Mass Spectrometry" Aerosol Science and Technology 41 818-827 (2007)

L Zhou, A. Rai, N. Piekiel, X. Ma, and M.R. Zachariah

"Ion-Mobility Spectrometry of Nickel Nanoparticle Oxidation Kinetics: Application to Energetic Materials" Journal of Physical Chemistry C. 112, 16209 (2008)

K.Sullivan, G. Young, and M.R. Zachariah " Enhanced Reactivity of Nano-B/Al/CuO MIC's"

Combustion and Flame 156, 302 (2009)

G. Young, K. Sulivan , M.R. Zachariah, K.Yu "Combustion Characteristics of Boron Nanoparticles" Combustion and Flame 156, 322 (2009)

B. Henz, T. Hawa, and M.R. Zachariah "Molecular Dynamics Simulation of the Kinetic Reaction between Ni and Al Nanoparticles" Journal of Applied Physics 105, 124310 (2009)

L. Zhou, N. Piekiel, S. Chowdhury, D. Lee and M. R. Zachariah

"Transient ion ejection during nanocomposite thermite reactions" Journal of Applied Physics 106, 083306 (2009)

L Zhou, N. Piekiel, S. Chowdhury, and M.R. Zachariah

"T-Jump/Time-of-Flight Mass Spectrometry for Time Resolved Analysis of Energetic Materials" Rapid Communications in Mass Spectrometry 23, 194 (2009)

S. Chowdhury, K. Sullivan, N. Piekiel, L. Zhou and M. R. Zachariah

"Diffusive vs. Explosive Reaction at the Nanoscale" J. Phys. Chem. C 114, 9191 (2010)

K. Sullivan and M.R. Zachariah Simultaneous Pressure and Optical Measurements of Nanoaluminum Thermites: Investigating the Reaction Mechanism Journal of Propulsion and Power, 26, 467 (2010)

B. Henz, T. Hawa, and M.R. Zachariah "On the Role of Built-in Electric Fields on the Ignition of Oxide Coated NanoAluminum: Ion mobility versus Fickian Diffusion."Journal of Applied Physics, 107, 024901 (2010)

Number of Papers published in peer-reviewed journals: 10.00

(b) Papers published in non-peer-reviewed journals or in conference proceedings (N/A for none)

Number of Papers published in non peer-reviewed journals:

2.00

(c) Presentations

Number of Presentations: 20.00

Non Peer-Reviewed Conference Proceeding publications (other than abstracts):

Number of Non Peer-Reviewed Conference Proceeding publications (other than abstracts):

0

Peer-Reviewed Conference Proceeding publications (other than abstracts):

A. Rai, K. Park, D. Lee and M.R. Zachariah

"Size Resolved Measurements and Theory of Aluminum Nanoparticle Oxidation"Advancements in Energetic Materials and Chemical Propulsion, Begell House, Inc. 2007

Number of Peer-Reviewed Conference Proceeding publications (other than abstracts):

1

(d) Manuscripts

L. Zhou, N. Piekiel, S. Chowdhury, M.R. Zachariah,

"Time Resolved Mass Spectrometry of the Exothermic Reaction between Nanoaluminum and Metal Oxides: The Role of Oxygen Release"

J. Physical Chemistry C. in press

Number of Manuscripts: 1.00

Patents Submitted

Patents Awarded

Graduate Students

<u>NAME</u>	<u>PERCENT_SUPPORTED</u>
Zhou Lei	1.00
Henz	0.00
Kyle Sullivan	1.00
FTE Equivalent:	2.00
Total Number:	3

Names of Post Doctorates

<u>NAME</u>	<u>PERCENT_SUPPORTED</u>
FTE Equivalent:	
Total Number:	

Names of Faculty Supported

<u>NAME</u>	<u>PERCENT SUPPORTED</u>	National Academy Member
Michael R. Zachariah	0.10	No
FTE Equivalent:	0.10	
Total Number:	1	

Names of Under Graduate students supported

<u>NAME</u>	<u>PERCENT SUPPORTED</u>
FTE Equivalent:	
Total Number:	

Student Metrics

This section only applies to graduating undergraduates supported by this agreement in this reporting period

The number of undergraduates funded by this agreement who graduated during this period: 0.00

The number of undergraduates funded by this agreement who graduated during this period with a degree in science, mathematics, engineering, or technology fields:..... 0.00

The number of undergraduates funded by your agreement who graduated during this period and will continue to pursue a graduate or Ph.D. degree in science, mathematics, engineering, or technology fields:..... 0.00

Number of graduating undergraduates who achieved a 3.5 GPA to 4.0 (4.0 max scale):..... 0.00

Number of graduating undergraduates funded by a DoD funded Center of Excellence grant for Education, Research and Engineering:..... 0.00

The number of undergraduates funded by your agreement who graduated during this period and intend to work for the Department of Defense 0.00

The number of undergraduates funded by your agreement who graduated during this period and will receive scholarships or fellowships for further studies in science, mathematics, engineering or technology fields:..... 0.00

Names of Personnel receiving masters degrees

NAME

Total Number:

Names of personnel receiving PHDs

NAME

Lei Zhou

Total Number:

1

Names of other research staff

NAME

PERCENT SUPPORTED

FTE Equivalent:

Total Number:

Sub Contractors (DD882)

Inventions (DD882)

Final Report August 30, 2010
Grant # W911NF0610215

**Understanding and Quantifying the Reactivity of Energetic
NanoParticles and NanoComposites**

From

**Michael R. Zachariah
Department of Mechanical Engineering
and Department of Chemistry and Biochemistry
University of Maryland, College Park**

mrz@umd.edu

www.enme.umd.edu/~mrz

INTRODUCTION

The focus of this work is to understand quantitatively, the nature of the reactivity of nanoparticles and nanocomposites for energetic materials application. Our approach takes two thrusts.

1. *Single Particle Kinetics*
2. *Ensemble Fuel/Oxide Nanocomposite Kinetics.*

Our goal was to:

- A. Explore the size resolved reactivity of nanoparticles, comprised of composites or core-shell nanostructures.
- B. Explain the behavior using phenomenological modeling and compare with bulk materials.
- C. Explore solid-solid ensemble kinetics of unique nanocomposites of fuel/oxidizers.

First we have determined that the extraction of the intrinsic reactivity of nanoparticles requires an experimental protocol that probes reactivity in the absence of other corrupting influences such as particle-particle mass transfer, heat and mass transfer to the particle, etc. We employ a unique experimental capability to measure quantitatively the composition of individual nanoparticles and monitor the change in the particle as it is reacted. We will describe the uses of Tandem Differential Mobility Analysis (TDMA) and Aerosol Mass Analysis (DMA-APM) to study intrinsic single particle size resolved reactivity.

A second thrust will focus on ensemble kinetics and in particular MIC formulations. Our first talk is to create a new type of measurement protocol to study this class of reactions. As part of this work we will also develop new approaches to study thermite type reactions. Most import of these is a new type of mass spectrometry (MS-T-Jump) being developed in our laboratory, which will enable the study of fast solid-state reactions. One of the unique features of this work will be the ability to create samples which have an extremely narrow particle size distribution through on-the-fly gas-phase electrophoretic separation of particles.

The combination of new architectures, with the new MS-T-Jump characterization will afford the opportunity to explore new types of structures that may point the direction on how best to assemble fuel/and oxidizers at the nanoscale to optimize energy release. The new diagnostic approach presents an opportunity to develop a tool to study from a microscopic point of view, reactions between solids. In the latter case the new tool should be of utility to a wide variety of problems in energetic materials well beyond those of thermite chemistry.

This report complies several bodies of work that collective comprise this project:

A. Rai, K. Park, D. Lee and M.R. Zachariah

“Size Resolved Measurements and Theory of Aluminum Nanoparticle Oxidation”

Advancements in Energetic Materials and Chemical Propulsion, Begell House, Inc. 2007

L. Zhou, K. Park, H. Milchberg, and M.R. Zachariah

“Understanding the Interaction of an Intense Laser Pulse with Nanoparticles: Application to Quantification of Single Particle Mass Spectrometry”

Aerosol Science and Technology 41 818-827 (2007)

L Zhou, A. Rai, N. Piekiel, X. Ma, and M.R. Zachariah

“Ion-Mobility Spectrometry of Nickel Nanoparticle Oxidation Kinetics: Application to Energetic Materials”

Journal of Physical Chemistry C. 112, 16209 (2008)

K.Sullivan, G. Young, and M.R. Zachariah

“Enhanced Reactivity of Nano-B/Al/CuO MIC’s”

Combustion and Flame 156, 302 (2009)

G. Young, K. Sullivan , M.R. Zachariah, K.Yu

“Combustion Characteristics of Boron Nanoparticles”

Combustion and Flame 156, 322 (2009)

B. Henz, T. Hawa, and M.R. Zachariah

“Molecular Dynamics Simulation of the Kinetic Reaction between Ni and Al Nanoparticles”

Journal of Applied Physics 105, 124310 (2009)

L. Zhou, N. Piekiel, S. Chowdhury, D. Lee and M. R. Zachariah

“Transient ion ejection during nanocomposite thermite reactions”

Journal of Applied Physics 106, 083306 (2009)

L Zhou, N. Piekiel, S. Chowdhury, and M.R. Zachariah

“T-Jump/Time-of-Flight Mass Spectrometry for Time Resolved Analysis of Energetic Materials”

Rapid Communications in Mass Spectrometry 23, 194 (2009)

S. Chowdhury, K. Sullivan, N. Piekiel, L. Zhou and M. R. Zachariah

“Diffusive vs. Explosive Reaction at the Nanoscale”

J. Phys. Chem. C 114, 9191 (2010)

K. Sullivan and M.R. Zachariah

“Simultaneous Pressure and Optical Measurements of Nanoaluminum Thermites: Investigating the Reaction Mechanism”

Journal of Propulsion and Power, 26, 467 (2010)

B. Henz, T. Hawa, and M.R. Zachariah

“On the Role of Built-in Electric Fields on the Ignition of Oxide Coated NanoAluminum: Ion mobility versus Fickian Diffusion.”

Journal of Applied Physics, 107, 024901 (2010)

L. Zhou, N. Piekiel, S. Chowdhury, M.R. Zachariah,

"Time Resolved Mass Spectrometry of the Exothermic Reaction between Nanoaluminum and Metal Oxides: The Role of Oxygen Release"

J. Physical Chemistry C. in press

Understanding the interaction of an intense laser pulse with nanoparticles: Application to the quantification of single particle mass spectrometry

ABSTRACT

Understanding the characteristic behavior of ions produced from the interaction of a high energy laser pulse with nanoparticles is essential for the quantitative determination of composition and size of nanoparticles from single particle mass spectrometry. Here we employed a one-dimensional hydrodynamic model, where the laser field is coupled to the non-equilibrium time-dependent plasma hydrodynamics of the heated clusters, or droplets. We focus on regimes of laser width from 0.01 ns to 10 ns (532 nm wave length, 100mJ/pluse) and particle size (20 - 400 nm in diameter) most relevant to commonly used single particle mass spectrometers, and determine the properties of ions generated during the interaction with a strong laser pulse. We compare the simulation results with experiments conducted on aluminum nanoparticles.

The laser-particle interaction is separated into a “soft heating” regime followed by a hydrodynamic expansion. Simulation results showed that the ablation/ionization is effectively complete well before the laser ever reaches its peak intensity. As the pulse width decreased for a given pulse energy (i.e., laser intensity increased), the kinetic energy of ions and ion charge states increased, suggesting that too short a pulse laser (i.e., high laser intensity) would not be desirable for the single particle mass spectrometry because the higher energetic

ions lead to lower detection efficiency in the single particle mass spectrometry. Results also show that for particle sizes in the range of 100 nm ~ 400 nm, that as particle size increased, the kinetic energy of ions produced from the particle increased with a power law relationship. We found that the size-dependent energetic ion formation is consistent with a power-law relationship between particle size and ion peak area experimentally determined by single particle mass spectrometry. Lastly our simulations indicated that ions on the surface of the particle are of higher energy and therefore have lower detection efficiency. This implies that surface species that have absorbtivities on par with the bulk particle may not be detected with the same efficiency.

Introduction

Many advances in single-particle mass spectrometry for quantitative characterization of size and composition of particles have been made in the last decade(Salt, Noble et al. 1996; Suess and Prather 1999; Christopher A. Noble 2000; Jayne, Leard et al. 2000; Murray 2000; Reents and Ge 2000; Kane, Oktem et al. 2001; Mahadevan, Lee et al. 2002). Typically for these experiments a pulsed laser is used as the ionization source, from which time-of-flight mass-spectrometry can be used to deduce composition. The common practice is to use some other method such as light scattering to deduce the size of the particle just prior to ionization , thereby obtaining a measure of both size and composition(Salt, Noble et al. 1996). While the technique has proven itself to be highly reliable, it suffers from the limitations inherent to all light scattering, namely the high power dependence on particle size, which has generally limited the technique to particles greater than ~200 nm. More generically a light scattering, or other particle selection approach however, (e.g. mobility selection, size selective aerodynamic focusing, etc) does not take advantage of the inherent capability of the mass spectrometer, to not only provide composition information, but total mass as has been attempted by our group and the work of Reents(Reents and Ge 2000; Lee, Park et al. 2005).

Recently, we and others, with the use of a highly focused pulse laser, determined both total particle mass (i.e., size) and composition quantitatively using only the ion signal from a laser ionization time-of-flight mass spectrometer(Reents and Ge 2000; Mahadevan, Lee et al. 2002; Lee, Park et al.

2005; Park, Lee et al. 2005). The quantification of composition and size of nanoparticles can be achieved with reasonable accuracy when two primary conditions are met. One is near complete atomization/ionization of the particle constituents (i.e., all neutral atoms are converted to ions with few molecular species), and two, ions produced from the particle should be detected independent of composition and size, or with a known relationship(Lee, Park et al. 2005). Typically a strong laser peak fluence ($\sim 10^{11}$ W/cm²) that is several orders of magnitude higher than the theoretical energy to atomize and singly ionize all atoms in the particle has been employed. On the other hand, the detection efficiency of ions in the single particle mass spectrometry is highly sensitive to their properties (e.g., kinetic energy) and the laser parameters (e.g. pulse width). The strong laser pulses might produce highly energetic ions so that their transmission efficiency to the detector in the aerosol mass spectrometry (usually through the time-of-flight tube) would be degraded(Lee, Park et al. 2005). This suggests if size-dependent or composition-dependent energetic ions are formed, and their relationships are not understood, it will degrade our ability to quantify the composition and size of particles.

The objective of this paper are to understand in greater detail the interaction of a laser pulse with a nanoparticle so as to determine the characteristic properties of ions produced from the particle. In the present study, we employed a modified 1-D hydrodynamic model based on prior work of Milchberg et al.(Milchberg, McNaught et al. 2001) to simulate the temporal evolution of ionization state, and energy as a function of particle size of aluminum that was

heated and ionized by a nanosecond 532nm Nd:YAG laser. The effects of the laser pulse width (i.e. laser intensity) on the ion properties produced after laser-particle interaction were also examined. The simulation results are compared to measurements obtained with a well characterized single particle mass spectrometer (SPMS)(Mahadevan, Lee et al. 2002; Lee, Park et al. 2005).

Model description

Several models to describe the interaction of clusters with a laser pulse have been developed(Ditmire, Donnelly et al. 1996; Lezius, Dobosz et al. 1998; Milchberg, McNaught et al. 2001). In the coulomb explosion model, laser-heated electrons can escape the cluster early in the laser-cluster interaction, leading to a charge buildup in the cluster. This charge buildup will lead electrostatic forces to be dominant in the cluster expansion, resulting in a so called coulomb explosion. On the other hand, in the hydrodynamic model, the plasma dynamics are driven in response to hydrodynamic forces rather than electrostatic forces. Milchberg et al. showed that the hydrodynamic forces dominate electrostatic forces for clusters larger than 5 nm, and a laser peak intensity of $>10^{14}$ W/cm². However, for typical single particle mass spectrometry operation the situation is typically more complicated. For a peak intensity $\sim 10^{11}$ W/cm², and particles of 20 - 400 nm, a purely hydrodynamic model is only valid after sufficient laser heating has taken place to overcome the cohesive energy of the solid. Essentially we can think of the laser interaction process as taking place in two steps. First a rapid

laser heating, with evaporation of neutrals from the particle surface followed by a second step of resonant absorption and hydrodynamic plasma expansion.

In a previous work(Rai 2006), we developed a phenomenological model to study the mass and energy transfer processes for the combustion of aluminum nanoparticles. In this study, a similar model was employed to account for the laser-particle heating, and particle evaporative cooling, and integrated into a one-dimensional hydrodynamic model to derive ion properties resulting from a laser-particle interaction(Milchberg, McNaught et al. 2001). While our calculations are focused on Aluminum, because of our experimental measurements and because modeling a mono-atomic particle are considerably easier, the results on the features of laser-particle interactions are expected to be qualitatively generic, and should lead to a greater mechanistic understanding, and as a guide for future experimental developments.

1. “Soft” Particle Heating

During the early stages of the laser pulse, the laser intensity is relatively low, such that the amount of energy absorbed is below the cohesive energy, so that the particle experiences a “soft” heating and results in neutrals being evaporated. The particle temperature and radius are determined by a coupling of laser heating and evaporative cooling. The effect of vaporization was examined by solving the energy balance in the free molecule regime(Milchberg, McNaught et

al. 2001; Rai 2006). The energy absorbed from the laser, q_{abs} , is balanced with the energy used to evaporate aluminum from the particle, q_{evap} and the energy used to heat the particle, as follows.

$$q_{abs} = q_{evap} + \frac{d}{dt} (m_p c_p T_p) \quad (1)$$

$$q_{abs} = \frac{1}{2} \omega \text{Im}(\gamma) |E|^2 \quad (2)$$

$$q_{evap} = L_{vap,Al} \times w_{Al} \times 4\pi r^2 \quad (3)$$

Here m_p is the mass of aluminum particle, c_p is the specific heat of aluminum, r is the radius of particle, and T_p is the temperature of particle. q_{abs} can be calculated using laser angular frequency ω , the imaginary part of particle polarizability $\text{Im}(\gamma)$ and the electric field generated by the laser E, $L_{vap,Al}$ is latent heat of vaporization for aluminum, w_{Al} is the free molecular evaporation flux of aluminum atoms, and is given by

$$w_{Al} = \frac{P_d}{\sqrt{2\pi R T M}} \quad (4)$$

R is the gas constant, and P_d is the equilibrium vapor pressure of aluminum as determined by the Kelvin equation:

$$P_d = P_0 \times \exp\left(\frac{4\sigma v_1}{T(ev)d \times 1.6 \times 10^{-19}}\right) \quad (5)$$

Here P_0 is the vapor pressure over a flat surface at temperature T , σ is the surface tension of aluminum, v_1 is the monomer volume and d is the diameter of the drop. Vapor pressure P_0 and surface tension σ can be calculated by equation (5) and (6).

$$P_0 = \exp\left(13.07 - \frac{3}{T(ev)}\right) \times 1.01 \times 10^6 \text{ Dyne/cm}^2 \quad (6)$$

And

$$\sigma = 948 - 0.245 \times 10^4 T(ev) \text{ Dyne/cm} \quad (7)$$

The use of equation 7 is only valid to approximate 0.5ev, at which point the surface tension becomes negative implying that the particle is mechanically unstable. In such a case, the free molecular evaporation rate w_{Al} is obtained from the effective equilibrium condensation rate and detailed balancing(Friedlander 2000)

$$w_{Al} = \frac{P_0}{\sqrt{2\pi IRTM}} \quad (8)$$

The energy balance is solved to obtain a temporal profile of particle size and temperature, and the results are used as input parameters for the hydrodynamic model.

2. Hydrodynamic Model

The hydrodynamic simulation is based on a one-fluid two temperature (i.e., electron and ion temperature) model, which includes thermal conduction, and a collision-radiative model for the ionization dynamics, the complete details for which are presented elsewhere(Milchberg, McNaught et al. 2001). Briefly, the laser's electric field (= $E(r)$, 1-D solid angle averaged electric field) is used to heat, and ionize the particle, and to advance the non-equilibrium time-dependent plasma hydrodynamics of the heated particle. The electric near field is described by, $\nabla \cdot (\epsilon E) = 0$, where $\epsilon(r)$ is the dielectric function, and is coupled to a 1-D radial

Lagrangian hydrocode. A near field approximation is appropriate for the case when the product, $ka \ll 1$, where $k (= 2\pi/\lambda)$ is the laser wave number, and a is the particle radius. For example, for a 20 nm diameter particle, excited with a visible laser, $ka \sim 0.1$. The dielectric response ($\epsilon(r)$) of the laser-heated plasma is taken to be a Drude form, which is appropriate for strongly heated near-solid-density plasmas with little electronic band structure(Parra, Alexeev et al. 2003). The 1-D radial Lagrangian hydrocode model is outlined below including the mass (9), momentum (10), and energy (11) equations.

$$\frac{\partial \rho}{\partial t} + \nabla \cdot (\rho \vec{v}) = 0 \quad (9)$$

$$\frac{\partial \rho \vec{v}}{\partial t} + \nabla \cdot (\rho \vec{v} \vec{v} + P) = 0 \quad (10)$$

$$\frac{\partial(\rho e + \frac{1}{2} \rho v^2)}{\partial t} + \nabla \cdot ((\rho e + \frac{1}{2} \rho v^2) \vec{v} + P \vec{v} + \vec{q}) = S_{laser} \pm S_{\text{ionization/recombination}} \quad (11)$$

where ρ is the mass density, v is the fluid velocity, P is the pressure, taken to be isotropic, e is the internal energy per unit mass of the fluid, q is the heat flux, S_{laser} is the energy deposition rate by the laser per unit volume, and $S_{\text{ionization/recombination}}$ is the energy stored in the ionization state of the plasma, and the plasma internal energy. The rate equation for the ion species, which includes collisional ionization, recombination, and field ionization, are as follows:

$$\frac{dN_j}{dt} = S_{j-1}N_{j-1}N_e - (S_j + \alpha_j)N_jN_e + (\alpha_{j+1})N_{j+1}N_e + w_{j-1}(|E|)N_{j-1} - w_j(|E|)N_j \quad (12)$$

where N_j is the number density of ion at the ionization state j , S_j is the collisional ionization rate, α_j is the recombination rate, N_e is the electron density, E is the laser electric field, and w_j is the field ionization coefficient(Ammosov, Delone et al. 1986). At each time step, the electric near field is solved using the density and temperature profiles of neutrals, ions, and electrons of the previous time step. The resulting electric field ionizes, and heats the plasma, temporally evolving the density and temperature profiles. Field and collisional ionization, recombination, and thermal conduction either gradient based or flux limited are taken into account in the calculation as shown in the above equations. The ideal gas equation of state is used to relate the plasma temperature and pressure.

Single Particle Mass Spectrometer

In order to experimentally determine the relationship between particle size and the amount of ions detected with the single particle mass spectrometer (SPMS), we first need to generate aerosols and transport them to the SPMS. For generation of aerosols, we dispersed commercial aluminum nanopowders (Aveka Inc.) in methanol, and silver nitrate and sodium chloride in deionized water, and suspended them in the air using a Collison atomizer. These particles were passed through several aerosol diffusion driers to remove the solvent. The aerosol was then passed through a differential mobility analyzer (DMA)(Knutson

and Whitby 1975) to select particles of known size for direct delivery to the inlet of the SPMS. Detailed descriptions on the SPMS can be found in our previous paper(Mahadevan, Lee et al. 2002; Park, Lee et al. 2005). Briefly, the SPMS consists of an aerodynamic lens inlet, three stage differential vacuum systems, a free firing pulsed laser for particle ionization, a liner time-of-flight mass spectrometer, and a 500 MHz digital oscilloscope and PC for data acquisition. The aerodynamic lens system produces a narrow collimated particle beam and transports particles of 30 – 300 nm into the high vacuum system with a high transmission efficiency. The free firing pulsed laser (a frequency-doubled Nd:YAG laser operated at 10 Hz, 532 nm wavelength), through a spherical plano-convex lens, is tightly focused at the extraction field of the mass spectrometer and intersects the particle beam with a laser beam diameter of ~0.1 mm and a laser pulse duration of ~5 ns. We have found that a pulse energy of ~100 mJ/pulse, corresponding to a peak laser power density at the focal point of approximately $\sim 10^{11}$ W/cm², provided sufficiently high level of ion currents to provide quantitative composition measurement. When the laser hits a particle successfully, positive ions formed from the particle are accelerated along ~1 m time-of-flight tube and detected by microchannel plates (MCP).

Results and discussion

In our present (experimental) study, aluminum nanoparticles are irradiated with a 532 nm, 5 ns FWHM 100 mJ Gaussian pulse (Nd:Yag laser) with a peak

laser intensity of $\sim 1.55 \times 10^{11}$ W/cm². As mentioned above, the particle first undergoes a soft heating process to overcome the cohesive energy of aluminum and then transitions to a hydrodynamic plasma expansion. The temporal and spatial profiles (1-D) for density, temperature, and velocity of electrons and ions from the laser-particle interaction can be obtained by a complete simulation of both models.

Figure 1 shows results for the temporal variation in temperature and particle mass, for the early stage of particle heating for aluminum of 200nm diameter. The laser peak is at $t = 0$ and the interaction between laser and particle is observed from $t = -9$ ns. As discussed above, the cohesive energy of aluminum will delay the hydrodynamic expansion of the particle in the early stage of the laser-particle interaction, until the temperature reaches the cohesive energy threshold (~ 3 eV). After the particle temperature reaches the cohesive energy threshold, electrons and ions energies are high enough such that the particle rapidly transitions into a dense plasma and expands in response to hydrodynamic forces, where the high-density collisional processes are dominant in particle ionization and heating. During hydrodynamic expansion, the particle is rapidly heated to a very high temperature ($> 10^5$ K) and then cools rapidly due to expansion cooling as shown in figure 1. It is also interesting to note that the temperature increases so rapidly that particle heating is much faster than the ability to evaporate mass, as evidenced by the near constant mass of the particle.

The normalized electron density and electric field for a 100 nm diameter particle during the hydrodynamic expansion are presented in figure 2 (a) and (b). The initial electron density of aluminum is $6.026 \times 10^{22}/\text{cm}^3$. In figure 2 (a) the electron density (N_e) is normalized by the critical plasma density ($N_{cr} = m_e \omega^2 / 4\pi e^2 = 3.95 \times 10^{21}/\text{cm}^3$) where m_e is the electron mass, ω is the laser frequency, and e is electron charge. Results are presented from the point in time when the temperature reaches the cohesive energy threshold, at -5.644 ns. The critical plasma density defines the point below which the plasma becomes transparent to the laser beam, and no further energy deposition takes place. Figure 2 (a) indicates that the electron density profile is non-uniform during the expansion, and that there is a critical density surface (i.e., $N_e \sim N_{cr}$) where resonant laser light absorption occurs, and is maintained from -5.644 ns to -5.634 ns, about ~ 10 ps. Figure 2 (b) presents the vacuum level normalized electric field during the hydrodynamic expansion as a function of radial location and time. Near the region of the critical density surface (radial location) the corresponding electric field is significantly enhanced with respect to its vacuum value as shown in figure 2 (b). This time (~ 10 ps) can be defined as the critical density lifetime (τ_{cr}), which is the time for a laser heated cluster to expand to a local electron density, which is below the critical density (i.e., $N_e < N_{cr}$). At times greater than the critical density lifetime (τ_{cr}), laser light absorption will decrease significantly.

The results from figure 2 (a) and (b) indicates that the laser-particle interaction occurs over a period of ~ 3 ns (from -9 ns to -5.6 ns) for the Gaussian 5ns FWHM laser pulse, and that most of the time is spent to overcome the

cohesive energy threshold. On the other hand, if we look at the absolute energy deposited to the particle during the interaction (figure 3), it is clear that although the hydrodynamic plasma expansion occurs over a very short time ($\sim 10\text{ps}$), the energy deposition rate is much faster ($\sim 10^{12} \text{ ev/sec}$) than in the “soft heating” regime (18eV in 3 ns). Figure 3 also shows that the energy deposition is completed after the critical density life time, which is consistent with the discussion above.

Thus, in our nanosecond laser pulse, the energy absorption of the particle only takes place during the leading edge of the pulse, and after τ_{cr} , the coupling is no better than in a gas. In other words, the ablation/ionization is over well before a nanosecond laser ever reaches its peak intensity. This observation is qualitatively consistent with previous results for the interaction of the laser pulse (peak intensity $>10^{14} \text{ W/cm}^2$) with argon clusters(Parra, Alexeev et al. 2003).

As mentioned early, the SPMS can be used to estimate particle size using the predetermined relationship between the ion signal (i.e., the amount of ions detected in the measured mass spectrum) and particle size. However, the formation of energetic ions will affect the transport efficiency through the SPMS time-of-flight tube and therefore sensitivity. In our previous study(Lee, Park et al. 2005), we defined the detection efficiency (DE) as

$$\text{DE} = \frac{\text{number of ions detected by SPMS}}{\text{total number of ions}}$$

the ion trajectories in the TOF tube were simulated using SIMION, and the detection efficiency was calculated as a function of initial ion kinetic energy. The

result shown in figure 4 demonstrates that the detection efficiency for ions in the SPMS depends strongly on the ion-kinetic energy;

$$DE (\%) \text{ (detection efficiency)} \sim E_k^{-0.99},$$

i.e. as the kinetic energy of ions increase, the detection efficiency decreases.

Clearly, the initial kinetic energy of ions plays an important role in the application of SPMS : ions with high kinetic energy are harder to collimate with the extraction fields and as a consequence, both the detection sensitivity, and the ability of quantitatively characterize single nanoparticle are degraded. Thus we are especially interested in the kinetic energy of constituent ions produced from the laser pulse. The remainder of this paper explores the influence of the laser pulse intensity on the kinetic energy of ions produced from the laser-particle interaction, as well as the particle size dependent energetic ion formation.

The kinetic energy of ions was computed using the velocity profiles obtained from the simulation results. Figure 5 (a) shows the kinetic energy ($= 1/2mv^2$) profiles as a function of radial distance at various times, for an aluminum particle of initial diameter of 100 nm. Evidently the ions at the surface of the expanding plasma cloud have the highest kinetic energy. From the practical point of view a bias to higher kinetic energy for the surface atoms will lead to lower detection efficiency as shown in Fig. 4 and therefore a bias against surface species. We have also plotted the number weighted average kinetic energy (i.e., $E_{k_mean} = \sum E_k(r) * N_i(r) / \sum N_i$) where r is the radius and N is the ion number, and its maximum value are plotted against time in figure 5 (b). Note that the

kinetic energy increases rapidly initially, but reaches an asymptotic value after ~ 5.634 ns. This occurs because most of laser energy is absorbed onto the particle during the leading edge of the pulse till we achieve τ_{cr} (~10 ps).

The hydrodynamic simulation results suggested that most of the laser energy is not deposited into the particle because of the poor coupling between laser pulse and the plasma. Obviously, for the single particle mass spectrometer, a hot plasma is preferable to ensure complete ionization, which can be achieved by employing a higher laser intensity or absorption efficiency. However, a hotter plasma should produce more energetic ions, which will result in greater ion loss during the transport in the TOF. In other words, too intense a photon flux or too much absorption may decrease the overall ability to quantify SPMS data, by possible species biases in the detection efficiency of ions, while too weak a laser cannot ensure complete conversion of constituent atoms to ions. Ideally one would like to understand where the optimum lies.

Based on the above discussion, we conducted simulations to investigate ion formation from a 100nm aluminum nanoparticle after their interaction with laser light of varying pulse widths (10 ps ~ 10 ns). The motivations are based on our previous discussion that indicated that the critical plasma density is achieved well before a nanosecond laser reaches its peak intensity. Furthermore all experimental work on particle mass spectrometry to date, at least to our knowledge has employed nanosecond lasers. To explore the role of pulse width we used the following conditions for our simulation; 10 ps ($7.75 \times 10^{13} \text{ W/cm}^2$), 100 ps ($7.75 \times 10^{12} \text{ W/cm}^2$), 0.5 ns ($1.55 \times 10^{12} \text{ W/cm}^2$), 5 ns ($1.55 \times 10^{11} \text{ W/cm}^2$), 10

ns ($=7.75 \times 10^{10}$ W/cm²), Figure 6 plots the number weighted average kinetic energy and average ionization state of ions for different laser intensity. The results show a monotonic increase in both the mean kinetic energy and average charge of ions as the pulse width is decreased. The results indicate that going to a shorter laser pulse creates a much more aggressive laser interaction. If we consider the nano-second laser sources as our base case condition, it is quite clear that a longer pulse laser would be the wrong direction to go to ensure the complete ionization approach. The next question is if pico-second lasers which are readily available offer some advantages. The results suggested that for a pico-second laser, the mean kinetic energy and average ionization state of ions could be very high, such that complete ionization criterion can be guaranteed, however, the higher kinetic energy of ions will result in a low detection efficiency given standard ion optics employed in TOF systems. On the other hand the pico-second laser has the highest likelihood that poor absorbers of surface coated material that might preferentially be blown-off without being ionized may be detected with a shorter pulse laser providing a more aggressive ionization(Zhou, Rai et al. 2006).

The above result invites the question, would a lower pulse energy for pico-second lasers have some advantages for SPMS application. Further simulations for 100 ps and 10 ps pulses were carried out with laser pulse energy of 50 mJ and 10 mJ. As one would expect, the simulations give lower mean ion kinetic energy and average charge of ions with the decrease of laser pulse energy, but

in general is seen to be a an insensitive parameter, likely because the absorption time is shorter than the pulse duration in any case. Thus once a threshold energy is achieved the resulting ionization process becomes relatively insensitive to pulse energy. For example, as the laser pulse energy decreases from 100 mJ to 10 mJ, the resulting ions mean kinetic energy decreases by a factor of 1.3 (from 517 eV to 395 eV), and 1.04 (from 20762 eV to 19826 eV) for 100 ps and 10 ps lasers, respectively.

The present results suggest that a nano-second laser may in fact provide the optimal laser source, for the present design of time-of-flight optics. However experiments on pico-second laser are warranted. In the latter case, other configurations, such as a high pressure ionization region where the kinetic energy of ions can be absorbed may offer interesting avenues for exploiting pico-second lasers.

To further illustrate the effect of laser pulse width on the laser-particle interaction, the normalized Gaussian laser pulses are plotted in figure 7 (a). For each laser pulse, we also define the temporal regions that correspond to the “soft heating” and hydrodynamic expansion, and the fraction of laser energy absorbed as a function of pulse width plotted in figure 7 (b). Note that in figure 7 (a), we should compare the relative fraction of “soft heating” and hydrodynamic expansion time in each pulse rather than the absolute interaction time. We can see that the hydrodynamic interaction regime become significantly longer as the laser pulse width is decreased. Considering that the energy absorption during this part of the interaction is much more aggressive, the result shown in figure

7(a), implies that there is more energy deposited onto the particle for a shorter laser pulse, which is manifested as an increase in ion energy and ionization state. This conclusion is confirmed by the calculation of energy absorption efficiency shown in figure 7 (b), which indicates a monotonic increase in absorption efficiency as the pulse width is decreased.

Next we turn our attention to the effect of particle size on the kinetic energy of ions produced. In our previous work, we hypothesized that the non-linear relationship between the ion signal and particle size observed in our experiment is due to the formation of size-dependent energetic ions(Lee, Park et al. 2005). In this work, simulations of laser interactions with particles in size range of 20 ~ 400 nm were carried out and the resulting ions energy were examined to understand their size dependence.

The number weighted average kinetic energy for particles in the 20-400nm range are shown in figure 8. We found that as size increases, the average kinetic energy of ions increases, and for particle size ~100 nm and larger, the kinetic energy follows a power law relationship in particle diameter ($E_k \sim D_p^{1.43}$). One possible explanation for the size-dependent kinetic energy formation is that with increasing particle size, the critical density lifetime increases (i.e., it takes longer for the average density of the larger particle to drop below the critical density), and therefore the particle absorbs energy for a longer period of time. Increased absorption time results in greater heating, leading to a higher initial kinetic energy and charge state for larger particles.

We are now in a position to compare the simulation results with our experiment. In our previous study(Lee, Park et al. 2005), we simulated the detection efficiency (DE) of ions traveling through the time-of-flight tube in the single particle mass spectrometry, and showed that the DE depends on their initial kinetic energy (E_k), providing the relationship $DE\text{ }(\%) \sim E_k^{-0.99}$. This indicates that DE decreases with higher kinetic energy ions. In that study, we hypothesized that the non-linear relationship between ion peak area, and particle size was caused by the more energetic ion formation from larger particles. Our current simulation results ($E_k \sim D_p^{1.42}$) qualitatively showed that this should be true.

By employing the relationship ($E_k \sim D_p^{1.43}$) from the current simulation results, and the $DE\text{ }(\%) \sim E_k^{-0.99}$ from the previous ion trajectory simulation, we obtain $DE\text{ }(\%) \sim D_p^{-1.42}$. Since the DE is related to the integrated peak area in a single particle mass spectrum by the equation of

$$Peak\ Area = C \times DE \times total\ number\ of\ ions$$

where C is the proportionality constant between detector signal (peak area) and the number of detected ions. Thus, we can obtained the relationship between the integrated peak area and particle size, giving $peak\ area \sim D_p^{1.58}$, or $peak\ area^{1/3} \sim D_p^{0.53}$, and the proportionality constant C can also be determined by fitting the above relation to the experimental data of aluminum. Now we compare the above relationship ($peak\ area^{1/3} \sim D_p^{0.53}$) with experimental measurements with the single particle mass spectrometer for aluminum particles. The comparisons shown in figure 9 clearly indicates that the simulation correctly captures the basic

trends observed in the experiment. The power dependence from the theoretical calculations for aluminum particles is 0.53, while the experimental values are 0.58. The experimental results for a variety of materials are also shown in figure 9. The power dependence between peak area^{1/3} and particle size is 0.45, 0.30, for sodium chloride and silver nitrate, respectively. Based on the data presented in figure 9 it is quite reasonable to assume the proportionality constant C between signal and number of ions detected is material independent, so that with the value obtained for aluminum, we can estimate the KE of other materials. Our estimate yields a value for mean KE of about 5.13 eV and 19.3 eV for ions generated from a 100 nm sodium chloride and silver nitrate particle, respectively. Compared to the with mean KE of 29 eV for 100 nm aluminum, our experimental results suggest that even though particles of different materials would have different KE's, the MS signal are remarkably similar. This should be expected because the experimental result is mass based, (peak area corresponding to mass of particle) which is $\sim D_p^3$. So the peak area obtained from experiment is less sensitive to D_p , and hence not as sensitive to KE. In fact, this is one of the potential advantages of using SPMS to determine particle size: with a pre-determined power dependence, we can quantitatively determine particle size within a reasonable accuracy regardless of particle composition.

It is also interesting to note that for smaller particles, there is a discrepancy between the average kinetic energy and the power law relationship, $E_k \sim D_p^{1.43}$, obtained above, the kinetic energy for particles in small size range have a relative higher value. The high kinetic energy suggests a relatively more

aggressive energy absorption and particle ionization for a smaller particle. This result is consistent with a recent experiment observation by Wang et al(Wang, Zordan et al. 2006). who developed a nanoaerosol mass spectrometer (NAMS) using the complete ionization technique. Quantitative chemical characterization for particle with diameter \sim 10 nm was achieved with a quadrupole ion guide and quadrupole ion trap system. In their work, multiple charged ions peaks (+4) were frequently observed in the spectra, which imply highly ionization states were achieved for particle sizes $<$ \sim 10 nm.

Conclusions

The objective of this paper was to understand pulsed laser interactions with small particles as it applies to the implementation and quantification of single particle mass spectrometry. In this study we applied a one-dimensional hydrodynamic model to determine the characteristic behavior of ions produced from aluminum nanoparticles as a result of interaction with a strong laser pulse. During the early stages of interaction, the particle experiences a “soft heating” regime to overcome the cohesive energy of solid. Subsequently, the laser-particle interaction transitions to a resonant absorption and hydrodynamic plasma expansion. The effect of laser parameters such as pulse width, energy, and particle size were investigated in this work.

Our simulation results showed that the ablation/ionization process is finished well before the laser ever reaches its peak intensity. We found that shorter laser pulses lead to greater energy absorption and produce a more

intense plasma, which will result in higher ionization state and higher ion kinetic energy. However the higher kinetic energy of the shorter pulse lasers will likely lead to a significantly degraded detection efficiency for ions in traditional TOF ion optics. The simulations suggested that nano-second lasers may in-fact provide an optimized solution for SPMS application.

We also found particle size-dependent energetic ions are formed from the laser-particle interaction, and the kinetic energy of ions is proportional to the particle size with a power law relationship ($E_k \sim D_p^{1.42}$). This result is show to be consistent with our experimental observation, and suggest that particle size-dependent energetic ions led to the power-law relationship between peak area and particle size observed in a single particle mass spectrometer.

References

Ammosov, M. V., N. B. Delone, et al. (1986). "Tunnel Ionization of Complex Atoms and Atomic Ions in a Varying Electromagnetic-Field." Zhurnal Eksperimentalnoi I Teoreticheskoi Fiziki **91**(6): 2008-2013.

Christopher A. Noble, K. A. P. (2000). "Real-time single particle mass spectrometry: A historical review of a quarter century of the chemical analysis of aerosols." Mass Spectrometry Reviews **19**(4): 248-274.

Ditmire, T., T. Donnelly, et al. (1996). "Interaction of intense laser pulses with atomic clusters." Physical Review A: Atomic, Molecular, and Optical Physics **53**(5): 3379-3402.

Friedlander, S. F. (2000). "Smoke, Dust, and Haze." Smoke, Dust, and Haze, Oxford University Press, Inc.

Jayne, J. T., D. C. Leard, et al. (2000). "Development of an aerosol mass spectrometer for size and composition analysis of submicron particles." Aerosol Science and Technology **33**(1-2): 49-70.

Kane, D. B., B. Oktem, et al. (2001). "Nanoparticle detection by aerosol mass spectrometry." Aerosol Science and Technology **34**(6): 520-527.

Knutson, E. O. and K. T. Whitby (1975). "Aerosol classification by electric mobility: apparatus, theory, and applications." Journal of Aerosol Science **6**(6): 443-451.

Lee, D., K. Park, et al. (2005). "Determination of the size distribution of polydisperse nanoparticles with single-particle mass spectrometry: The role of ion kinetic energy." Aerosol Science and Technology **39**(2): 162-169.

Lezius, M., S. Dobosz, et al. (1998). "Explosion Dynamics of Rare Gas Clusters in Strong Laser Fields." Physical Review Letters **80**(2): 261.

Mahadevan, R., D. Lee, et al. (2002). "Measurement of Condensed-Phase Reaction Kinetics in the Aerosol Phase Using Single Particle Mass Spectrometry." J. Phys. Chem. A **106**(46): 11083-11092.

Milchberg, H. M., S. J. McNaught, et al. (2001). "Plasma hydrodynamics of the intense laser-cluster interaction." Physical Review E: Statistical, Nonlinear, and Soft Matter Physics **64**(5-2): 056402/1-056402/7.

Murray, V. J. (2000). "Sampling and analysis of individual particles by aerosol mass spectrometry." Journal of Mass Spectrometry **35**(5): 585-595.

Park, K., D. Lee, et al. (2005). "Size-Resolved Kinetic Measurements of Aluminum Nanoparticle Oxidation with Single Particle Mass Spectrometry." J. Phys. Chem. B **109**(15): 7290-7299.

Parra, E., I. Alexeev, et al. (2003). "Hydrodynamic time scales for intense laser-heated clusters." Journal of the Optical Society of America B: Optical Physics **20**(1): 118-124.

Rai, A., Park, K., Zhou, L. and M.R. Zachariah (2006). "Understanding the Mechanism of Aluminum Nanoparticle Oxidation." Combustion Theory and Modeling **In Press**.

Reents, W. D. and Z. Ge (2000). "Simultaneous elemental composition and size distributions of submicron particles in real time using laser atomization/ionization mass spectrometry." Aerosol Science and Technology **33**(1-2): 122-134.

Salt, K., C. A. Noble, et al. (1996). "Aerodynamic Particle Sizing versus Light Scattering Intensity Measurement as Methods for Real-Time Particle Sizing Coupled with Time-of-Flight Mass Spectrometry." Anal. Chem. **68**(1): 230-234.

Suess, D. T. and K. A. Prather (1999). "Mass Spectrometry of Aerosols." Chem. Rev. **99**(10): 3007-3036.

Wang, S., C. A. Zordan, et al. (2006). "Chemical Characterization of Individual, Airborne Sub-10-nm Particles and Molecules." Anal. Chem. **78**(6): 1750-1754.

Zhou, L., A. Rai, et al. (2006). "Component and morphology biases on quantifying the composition of nanoparticles using single-particle mass spectrometry." International Journal of Mass Spectrometry **258**(1-3): 104-112.

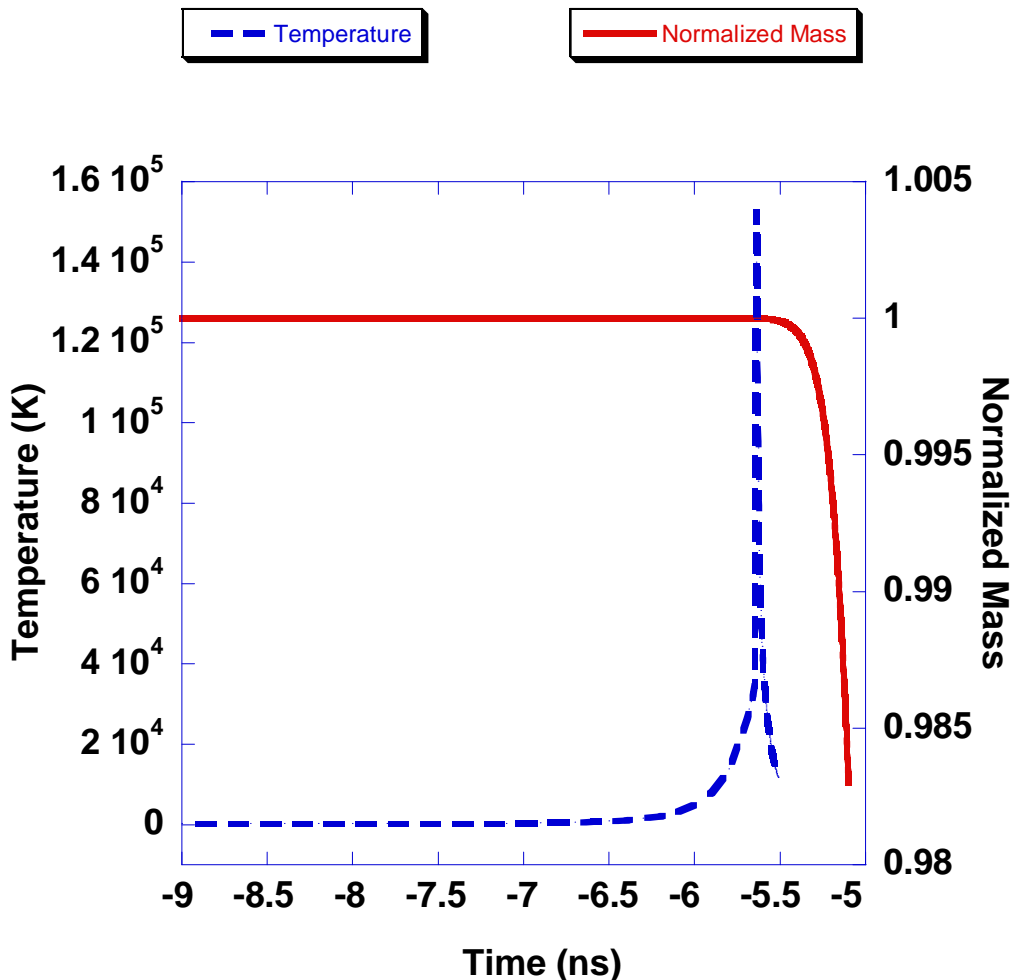


Figure 1 Soft laser heating of 100 nm Aluminum as a function to time. Time=0 corresponds to the peak in the 532 nm, 5 ns FWHM 100 mJ Gaussian laser pulse.

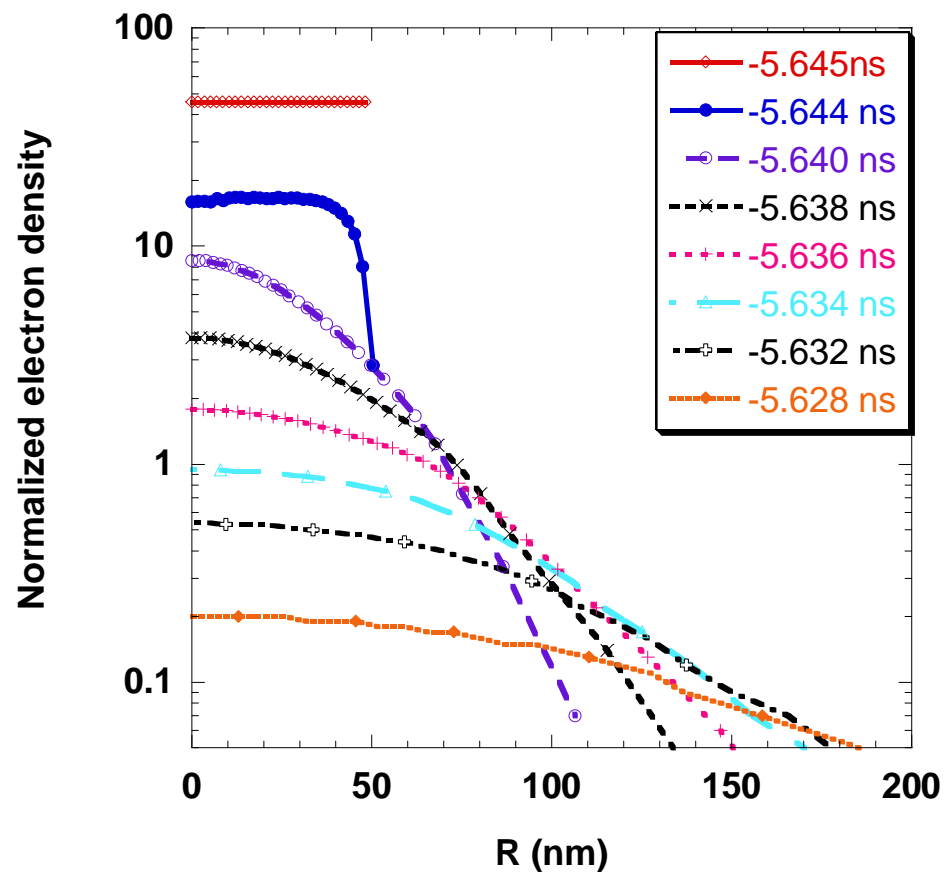


Figure 2(a)

Figure 2 (a) Temporal variation of normalized electron density with radius

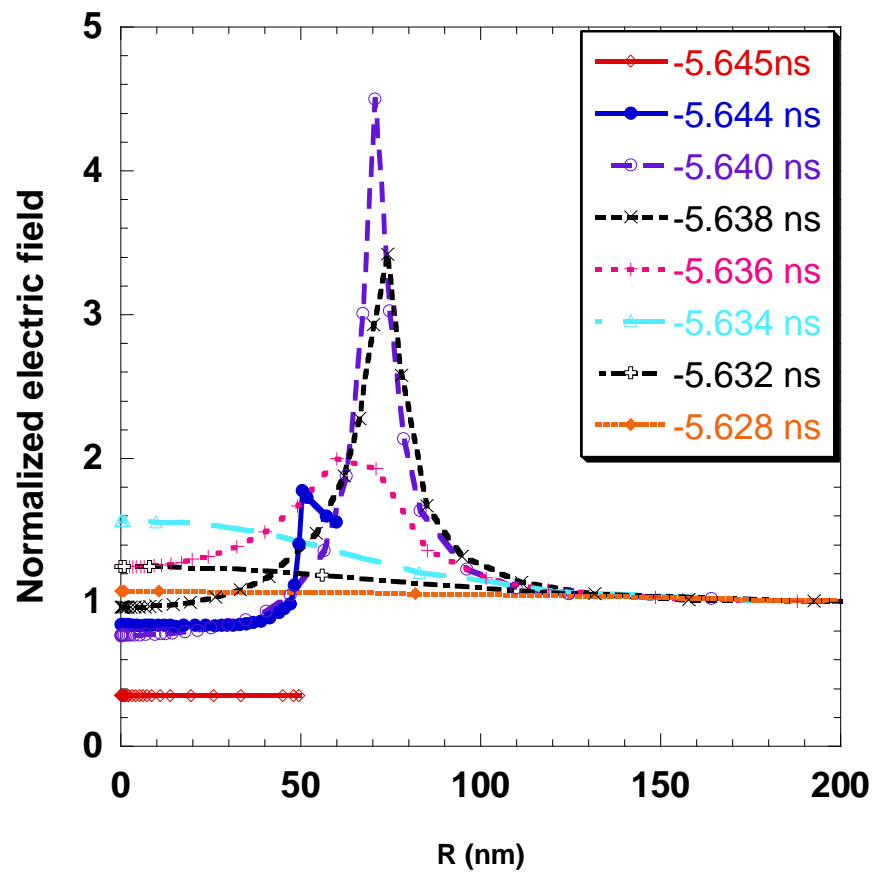


Figure 2(b)

Figure 2 (b) Temporal variation of normalized electric field with radius

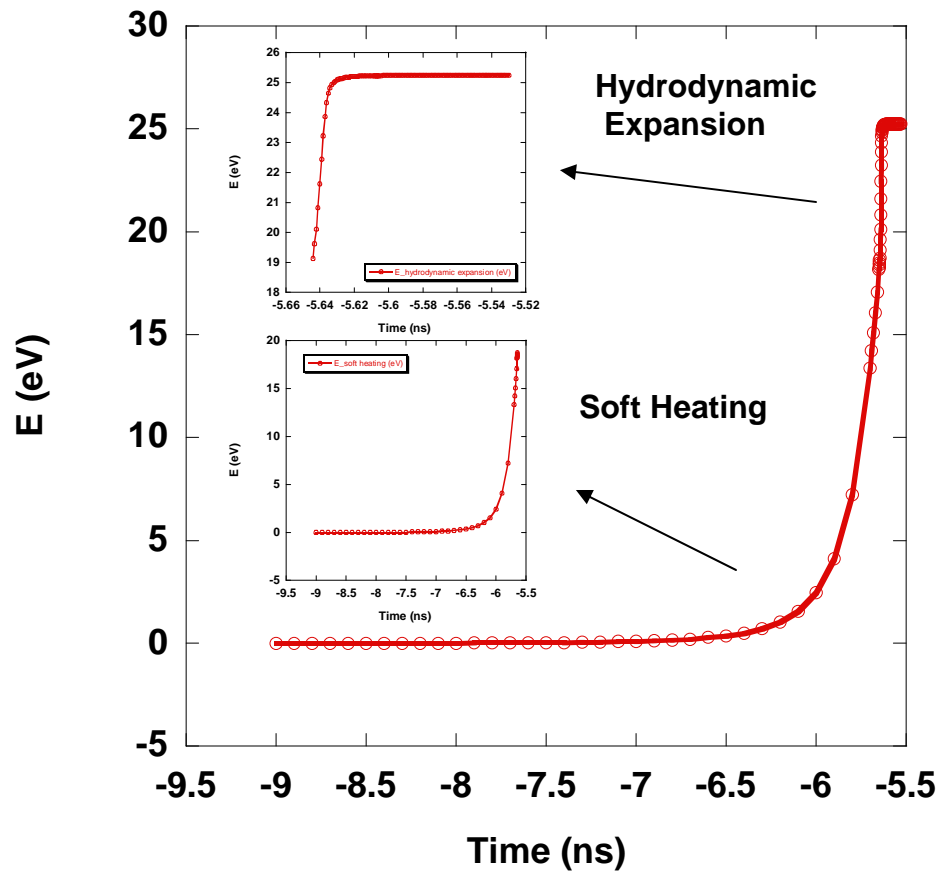


Figure 3 The absolute energy deposition on the particle during the interaction

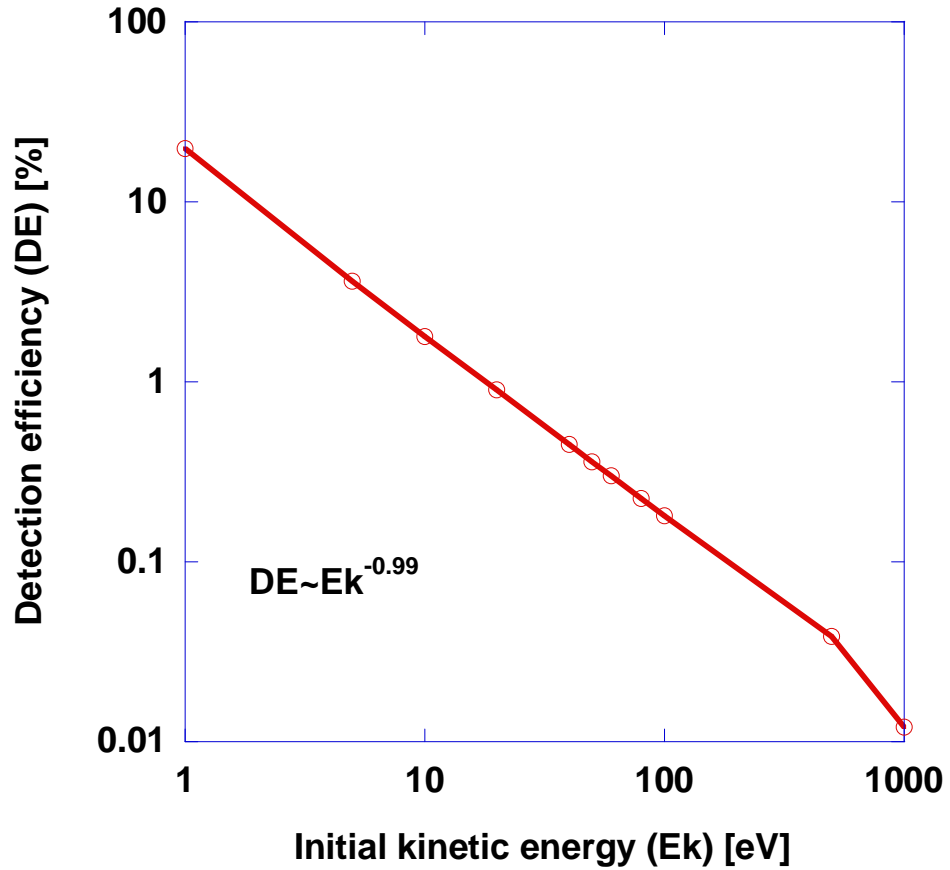


Figure 4 Effect of initial kinetic energy on detection efficiency of the SPMS.

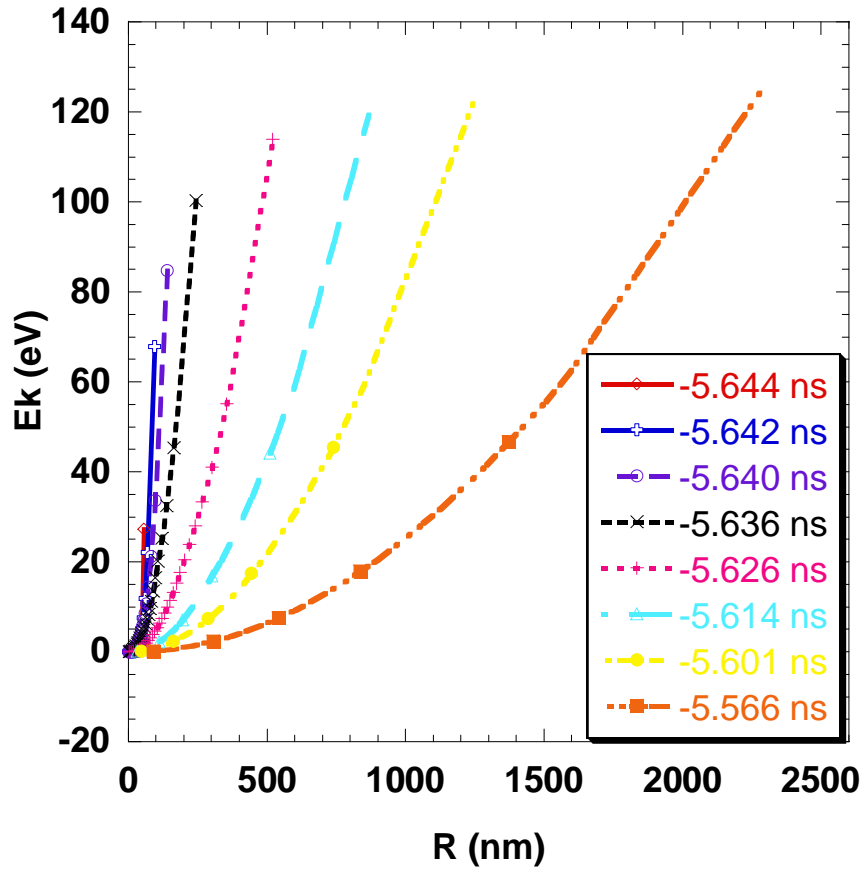


Figure 5 (a) Kinetic energy profile as a function of radial distance at various times for an aluminum particle of initial diameter of 100 nm

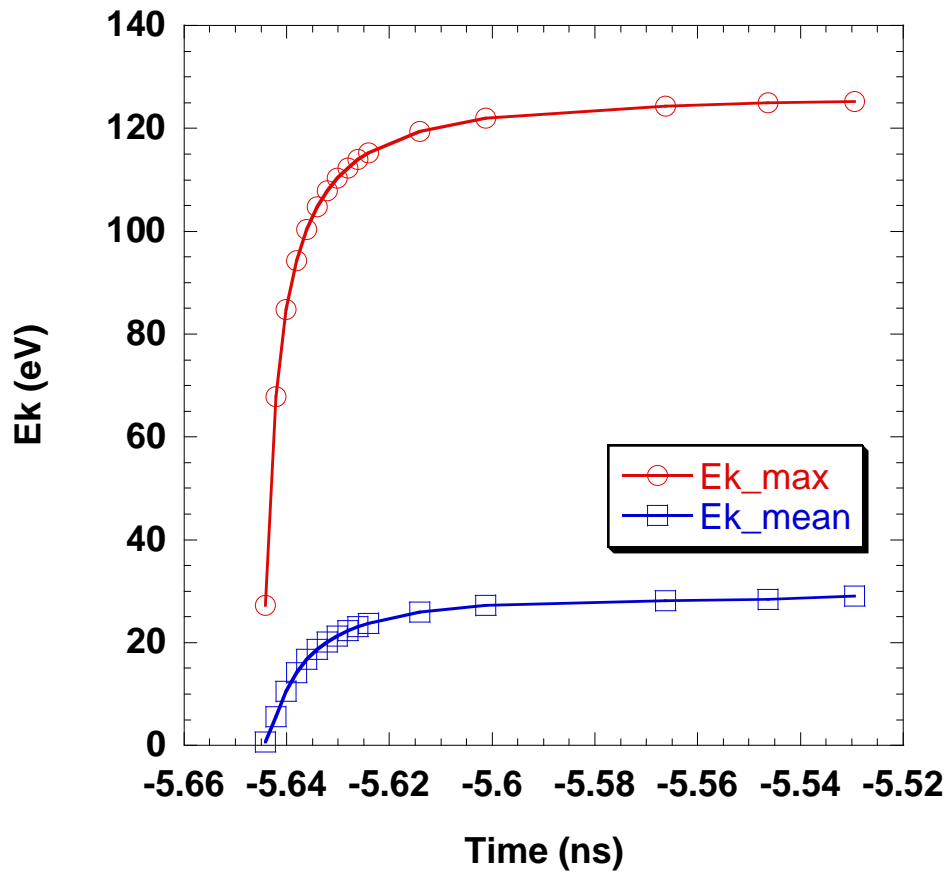


Figure 5 (b)

Figure 5 (b) Temporal variation of the average and maximum kinetic energy for an aluminum particle of initial diameter of 100 nm

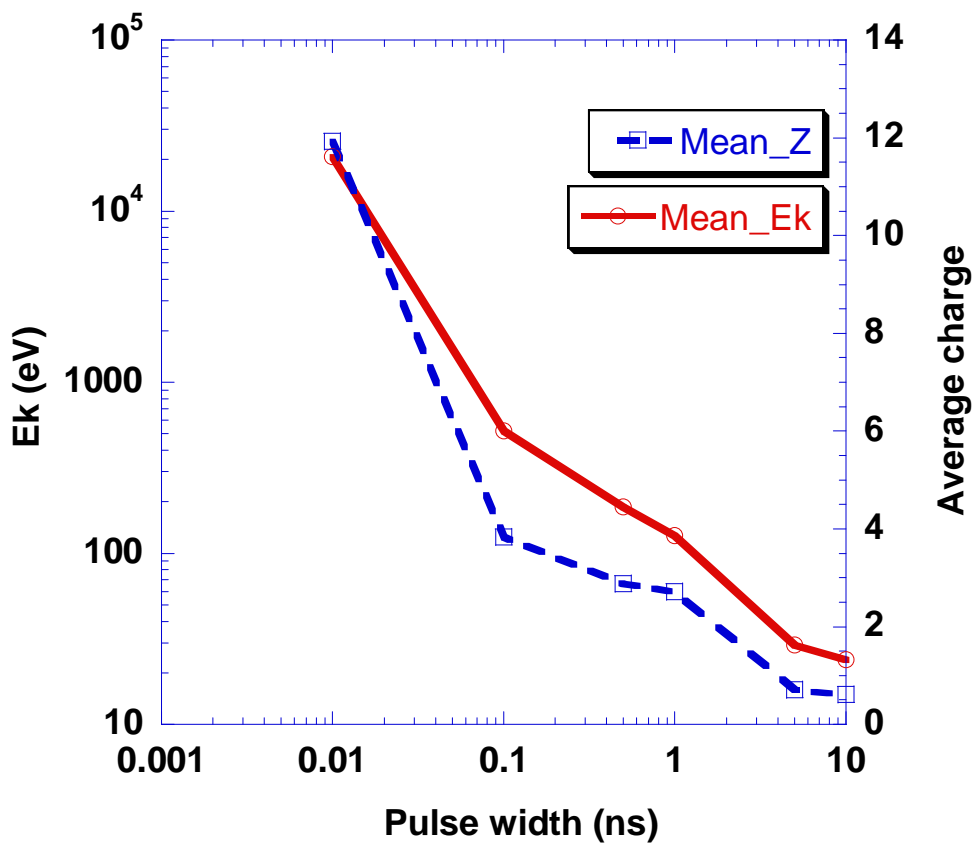


Figure 6 Effect of laser pulse width on average kinetic energy and average ionization state for an aluminum particle of initial diameter of 100 nm.

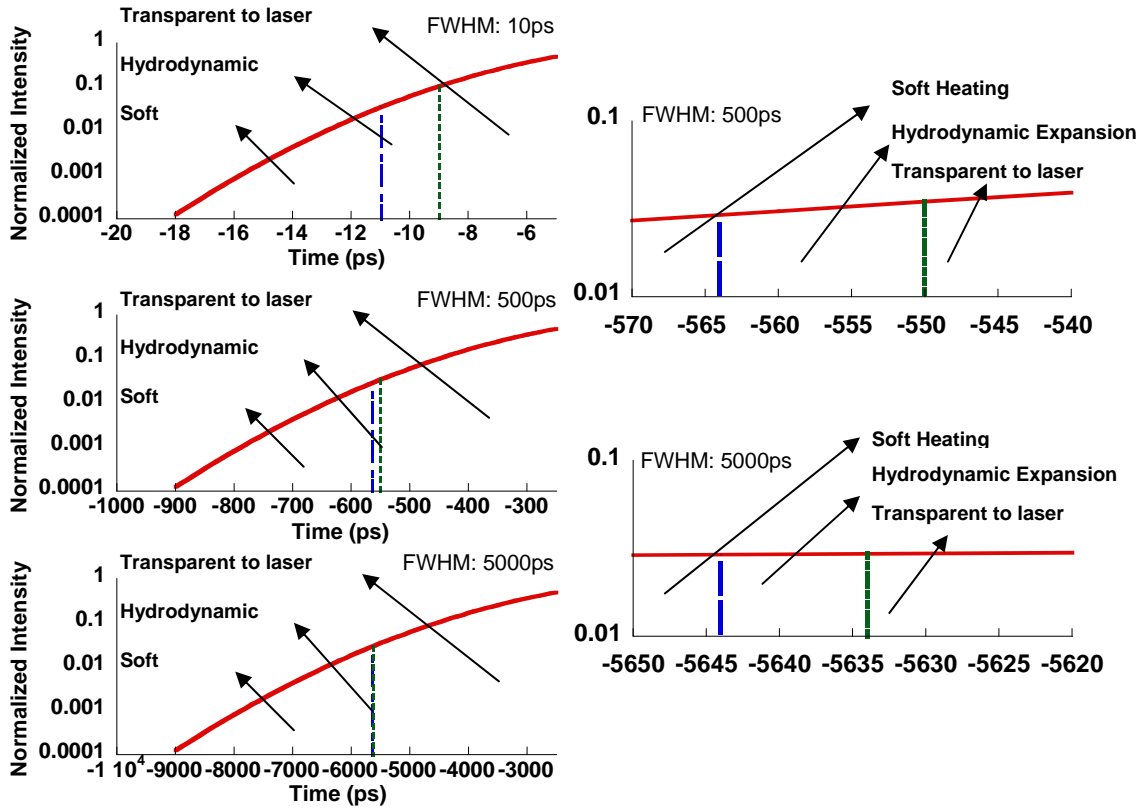


Figure 7 (a). Left: Gaussian laser pulses of various width overlaid with the “soft-heating” and hydrodynamic expansion regions for an aluminum particle of initial diameter of 100 nm. Right: Detailed view of “soft-heating” and hydrodynamic expansion regions for FWHM 5000ps and FWHM 500ps laser pulses

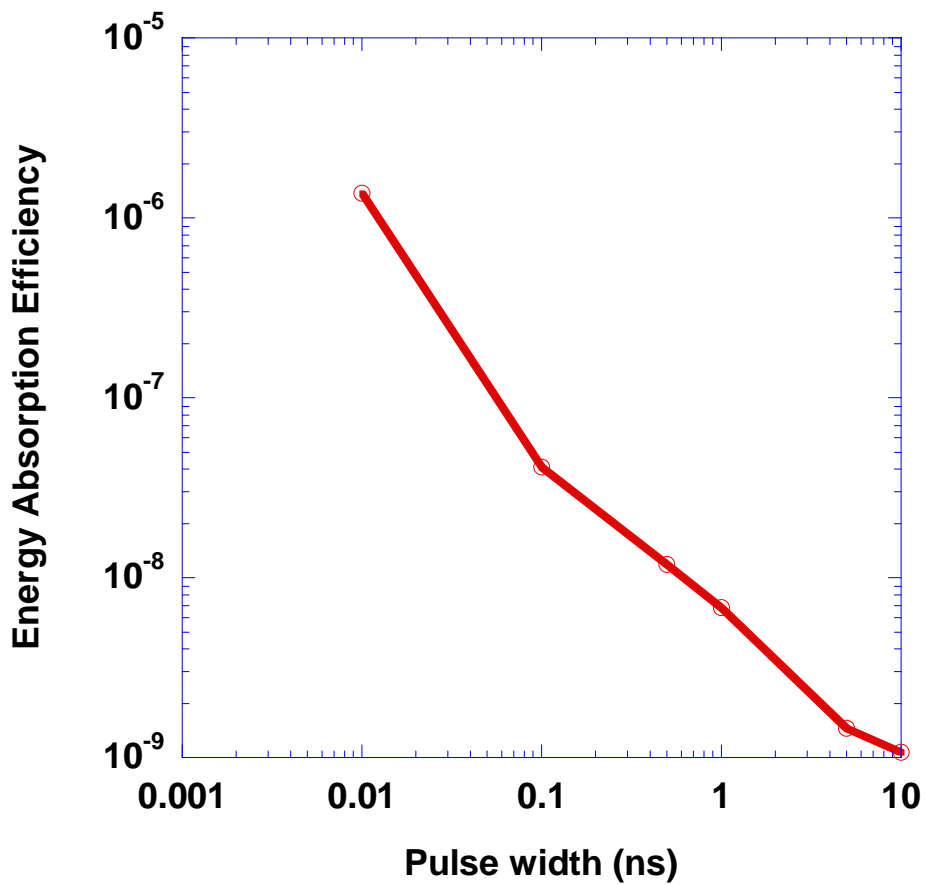


Figure 7 (b) Fraction of the laser energy absorbed for a 100nm aluminum particle as a function of pulse width

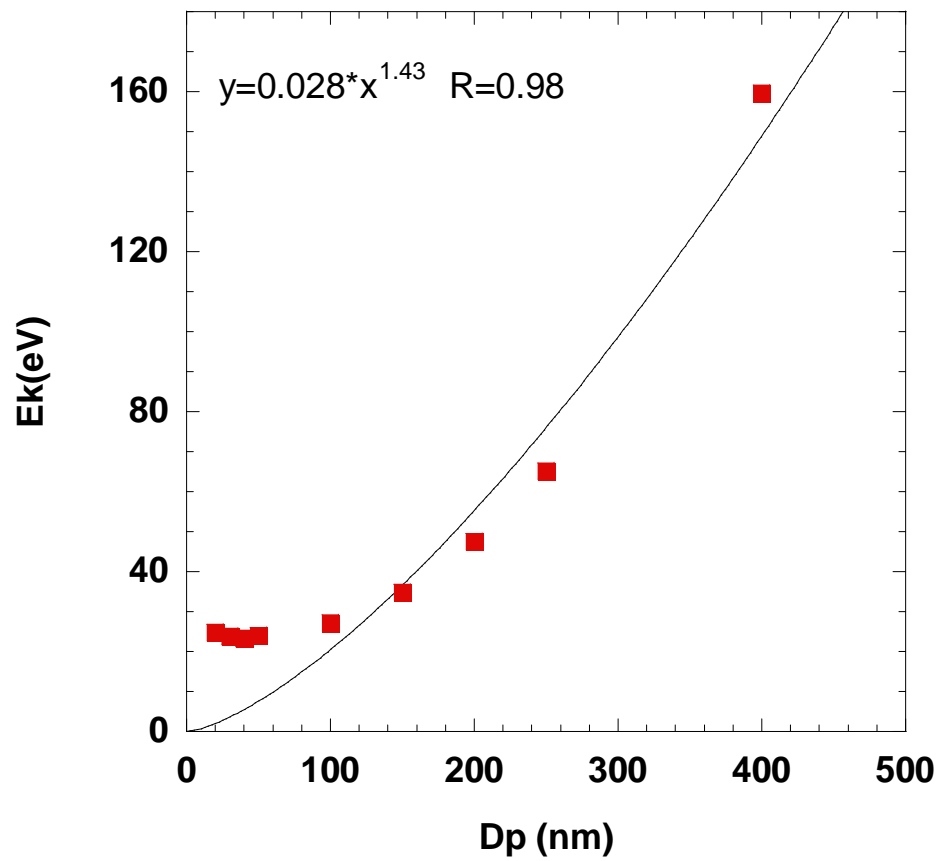


Figure 8. Mean kinetic energy of ions as a function of particle diameter

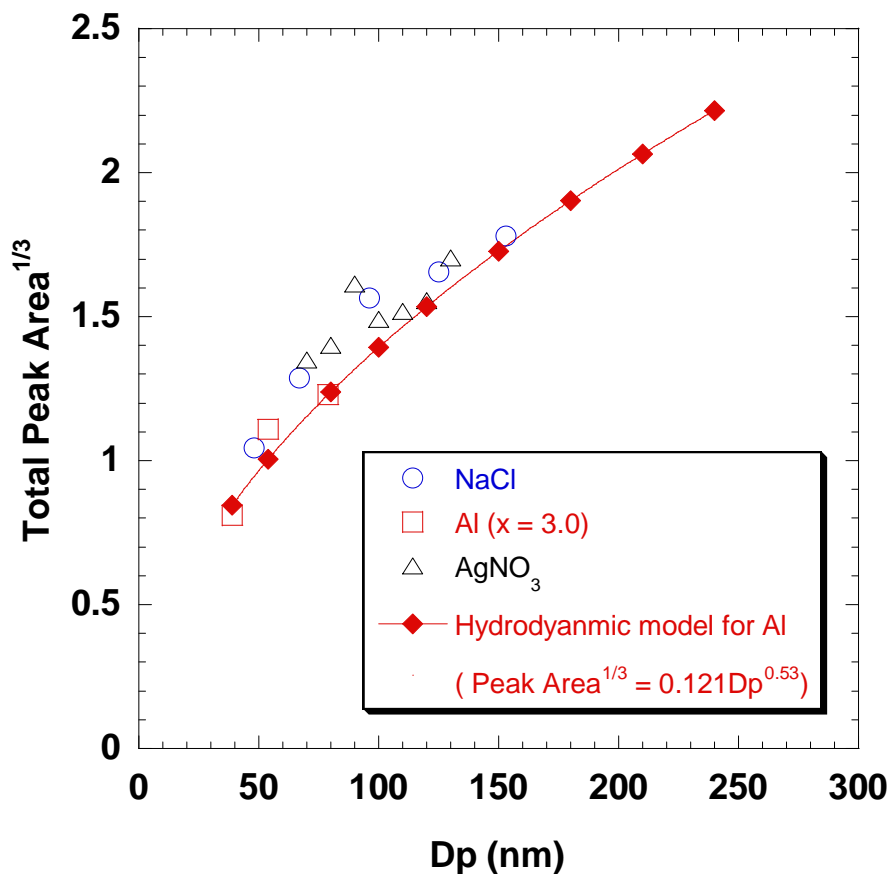


Figure 9 Comparison of the relationship between ion peak area and particle size from simulation results, and experimentally determined by the single particle mass spectrometer.

Ion-Mobility Spectrometry of Nickel Nanoparticle Oxidation Kinetics: Application to Energetic Materials.

Abstract

Nano-scaled nickel particles have attracted interest for its potential use as a fuel in energetic materials. In this work, we combined two ion-mobility spectrometry approaches; tandem differential mobility analysis (TDMA) and tandem differential mobility – particle mass analysis (DMA-APM) to study the size resolved reactivity of nickel nanoparticles. Nickel nanoparticles were generated in-situ using gas-phase thermal pyrolysis of nickel carbonyl. Four particle sizes (40, 62, 81 and 96 nm, mobility size) were then selected by using a differential mobility analyzer. These particles were sequentially oxidized in a flow reactor at various temperatures (25-1100 °C). The size and mass change of the size selected and reacted particles were then measured by a second DMA, or an APM. We found that both particle size and mass were increased as the temperature increased. However, at higher temperature (600-1100°C), a different mass and size change behavior was observed which could attribute to a phase transition between NiO and Ni₂O₃. A shrinking core model employed to extract the size- resolved kinetic parameters shows that the activation energy for oxidation decreased with decreasing particle size. The burning time power dependence on particle size was found to be less than 2 and nickel particles were found to be kinetically more active than aluminum.

Introduction

Recent advancement on field of so called “nanoenergetic” materials are focused on either enhancing or tuning reactivity. On one level this issues reduces to a length-scale argument, whereby smaller fuel/oxidizer combinations result in smaller diffusion lengths and therefore higher reactivity. On another level, this discussion leads to choices of different thermite formulation. Although there have been considerable successes in enhancing the energy release rate of thermite systems, the goal of tuning the reactivity is still a subject for further research. In one of our previous works, we reported a method to control the energy release rate of energetic nanoparticles by creation of a core shell nanostructure on the oxidizer particle¹. Similarly, the reactivity of nanoenergetic material can also be controlled by modifying the structure of the aluminum fuel². More recently we have seen that mixtures of nanoaluminum and nanoboron outperform either material on their own³. Those results suggest both material choices (e.g. Ni, Ti, etc.) and nanoarchitecture as means to tune the energy release profiles of materials beyond aluminum. The application of those materials would take the form of composite materials e.g. Al/Ni alloy, or metal particles with a different morphology such as aluminum core with nickel coating. While considerable opportunity exists for improvements, in actuality very little attention has been paid to the kinetics of reactivity of small metal particles beyond nanoaluminum. While the oxidation of nickel in form of bulk sample or thin films has been studied for over a century⁴⁻²⁷, there are only a few studies on the oxidation of nickel nanoparticles^{5,28-32}. Carter developed a solid state kinetic model based on a diffusion controlled mechanism, for oxidation of ~100 micron particles using a microbalance²². Fromhold obtained the same oxidation rate law using a coupled current

approach with the assumption of zero space charge⁶. Karmhag and Niklasson explored the oxidation kinetics of micron size nickel particles using thermogravimetric measurements, and obtained a lower activation energy than bulk nickel^{31,32}. As particle size decreases into the nano-scale, the mass transfer limitations should be reduced and we should expect to see an enhancement in reactivity. Our previous work on the oxidation of nanoaluminum particles show that both the overall rate constant and activation energy are size dependent^{33,34}. Karmhag et al. studied the oxidation of nano sized nickel particles at low temperatures (135°C-235°C) using thermogravimetric measurements, and suggested that nonlinear diffusion resulting from space and local charging occurs in this case, and results in a higher rate constant and lower activation energy²⁹. The same group also probed the size dependent oxidation kinetics, and found that the rate constant roughly goes as the square of the inverse of particle diameter³⁰. They further proposed a phenomenological model to consider the nonlinear effect in oxidation of nano scaled particles²⁸.

All the above studies were carried out using conventional dynamic thermal techniques such as thermogravimetry. It is well known that those methods are greatly influenced by heat and mass transfer effects such that the results are biased by experimental artifacts^{34,35}. In this work we employ aerosol based techniques to study the oxidation kinetics of Ni nanoparticles. Our previous results on the study the solid-gas phase reaction kinetics show that the reaction rate obtained using aerosol based techniques, are much higher than conventional methods, which may represent the intrinsic reactivity of nanoparticles^{34,35}.

The basic idea of the experimental approach is to prepare Ni particles of characterized size/shape (i.e. Monodisperse), and monitor changes during oxidation in free-flight (i.e. no substrate). This study consists of two experiments, both of which rely on ion-mobility separation. A Tandem Differential Mobility Analyzer (DMA) system^{12,36,37} is used to measure the size change after oxidation, while the mass change is tracked by a DMA-APM (Aerosol Particle Mass Analyzer) system^{33,38-40}. The mass and size changes of nanoparticles are studied from room temperature to 1100 C. The average density obtained from mass and size measurements show the nickel nanoparticle oxidation process can be correlated to the formation of both NiO and Ni₂O₃ ($4\text{Ni}+3\text{O}_2 \rightarrow 2\text{Ni}_2\text{O}_3$, $2\text{Ni}+\text{O}_2 \rightarrow 2\text{NiO}$) and a phase change region where both the oxidation of nickel and decomposition of Ni₂O₃ to NiO ($2\text{Ni}_2\text{O}_3 \rightarrow 4\text{NiO}+\text{O}_2$) occur simultaneously. The reaction rates were then extracted from the experiment data as a function of particle size.

Experimental Approach

The experiment system consists of three components. Preparation of monodisperse nickel particles, second, exposure of size selected nickel particles into a controlled oxidation region, and third, measurement of the size and mass change resulting from reaction. A complete schematic of the experimental setup with temperature and flow rate control is shown in Figure 1.

A. In-situ Generation of Nickel Nanoparticles

In this work, high purity nickel nanoparticles was prepared in an oxygen free environment using gas-phase thermal pyrolysis of nickel carbonyl^{41,42}. Because of the high toxicity of nickel carbonyl, it was generated in-situ by flowing of a small amount of carbon monoxide (99.5%) through a nickel powder bed (3 um, 99.7% Sigma Aldrich), which was placed immediately upstream of an isothermal tube reactor to thermally decompose Ni(CO)₄ so as to form nickel particles as shown in Fig 1. Before each experiment, the nickel bed was heated to ~350°C with a hydrogen flow (99.5%) for about 4 hours to clean the surface of the nickel powder. After the hydrogen pre-treatment, activated nickel powder is reacted with CO at ~50°C to generate Ni(CO)₄. The generated Ni(CO)₄ was mixed with a flow of Ar (industrial grade) and passed to the cracking reactor held at ~400°C, to create nickel particles (Ni(CO)₄->Ni + 4CO). Since the resulting particles are agglomerated and our experimental protocol requires individual primary particles, the generated nickel particles were size selected by the first DMA (to be described below), and subsequently heated to 1100°C to form spherical particles, so as to prepare monodisperse particles for the oxidation step.

B. Differential Mobility Analyzer (DMA) and Aerosol Particle Mass Analyzer (APM)

The primary analytical tools employed in the experiments were a tandem differential mobility analyzer system (TDMA)^{12,36,37,43,44} and DMA-APM (aerosol particle mass analyzer) systems^{33,38-40}. In these experiments, particles were first charged with a

Boltzmann charge distribution by exposing the aerosol to a Po-210 radiation source, before the first DMA. The average charge state of sample particles under Boltzmann distribution is roughly neutral, with most of particles uncharged and equal amount of particles carry +/- 1 charge and +/-2 charges, etc. For example, in the case of 50 nm particles, 60.2% particles will be neutral, 19.3% carry +/-1 charge, 0.6% carry +/- 2 charges, and higher charge state would be even less⁴⁵. Considering the small percentage in the multiple charged states, we ignore multiple charged particles and assume the charged particles are all singly charged. Both the DMA and APM are configured to classify positively charge particles for these experiments.

The TDMA system set up was similar to our previous work^{36,37,43,44}. The DMA consists of an annular region between two concentric cylinders, with the center cylinder held at high voltage and the outer one at ground. Charged particles of the right polarity feel an attractive force toward the center electrode and move radically inward at an electrophoretic velocity determined by the particle charge, and the particle size dependent drag force. At fixed voltage all particles exiting the instrument have equivalent mobility size (equivalent projected surface area), or alternatively by scanning the voltage a size distribution measurement can be obtained. When charged particles flow within the annular region the electric force on the particle is balanced by the drag force, and at a fixed voltage all particle exiting the instrument have (to the resolution of the instrument) equivalent mobility sizes. By scanning the voltage a range of particle sizes can be extracted and counted to yield a size distribution. In our system, DMA-1 is held at a fixed

voltage, and thus is used as a band pass-filter to create the monodisperse particle source, by selecting particles with the same electrical mobility size. In the size range of consideration here, the DMA functions as a source of mono-area particles⁴⁶. However, since DMA-1 selected particles are aggregates, a sintering furnace was placed after DMA-1 to form individual spherical particles for the oxidation step. A second DMA was operated in voltage-step mode with a condensation particle counter (CPC) as a particle size distribution measurement tool to track the size change after the oxidation process. A second Po-210 neutralizer was placed between the oxidation furnace, and DMA-2 to recharge the particles. This was necessary as the high temperature treatment (sintering or high oxidation temperatures) some of the particles lost their charge. In summary the TDMA experiment tracks changes in physical size as a result of oxidation.

In a parallel experiment the change in particle mass after oxidation was measured by an aerosol particle mass analyzer (APM) coupled with a CPC. The APM is a relatively new technique that can determine the particle mass distribution based on particle mass to charge ratio⁴⁰. The APM consists of two concentric cylindrical electrodes that rotate together at a controlled speed. An electrical field is created by applying high voltage on the inner electrode while the outer one is held at ground. Charged particles flowing within the concentric cylinders experience opposing centrifugal and electrostatic forces and as a result particles exiting the instrument at fixed voltage and rotation speed all have the same nominal mass. By scanning either the voltage or the rotation speed, the particle mass distribution (independent of particle shape) can be determined. Our previous

experiments have used the DMA-APM technique to measure the inherent density of nanoparticles, as well as to study the mechanism of aluminum oxidation^{33,38}.

Based on operating conditions for the DMA and APM we estimate uncertainties as follows. For the DMA operating conditions the uncertainty is based on the theoretical transfer function which will give an uncertainty in the peak particle size of +/- 4 %. We then use Gaussian fit to determine the peak size which would have a precision uncertainty of no more than 1%. A similar result can be obtained for the APM however the uncertainties are not due to the transfer function but uncertainties in the step voltage which has a resolution of only +/-0.5V, which gives an uncertainty in mass of ~4%. Using the root-sum-square (RSS) method, we can estimated the uncertainty of density calculation ~5% . This is consistent with prior work (unpublished) using combined DMA/APM on reference aerosols (NaCl and DOP) which gave an experimentally determined uncertainly in density of 4%.

C. Nickel Nanoparticles Characterization, Sampling and Oxidation

In this study, nickel nanoparticles with mobility sizes of 70, 135, 200 and 240 nm were selected using the first DMA. To successfully measure the size and mass change resulting from oxidation using Tandem DMA and DMA-APM system, the particle number concentration in the selected size range must be tuned. This is accomplished by varying the concentration of Ni(CO)₄ in the various dilution steps used. The Ar carrier gas flow varied from 2 LPM (Liter Per Minute) to 10 LPM, and the dilution Ar flow varied from

0.2 LPM to 0.45 LPM. Figure 2 shows an example size distribution taken before the sintering furnace. The system in this case was tuned to create a peak mobility size of about 120 nm, with sufficient particles for further measurement at the size range from 70 to 240 nm.

Size selected nickel particles coming from DMA-1 were subsequently sintered at 1100°C to form monodisperse spherical particles, whose size and mass can be measured by DMA-2 and APM, under condition of no-oxidation. The size of particles shrink to a mobility size of 40, 62, 81, and 96 nm after sintering, and are thus the initial particle size before oxidation. The sintered particles were then mixed with dry air with 1:1 ratio, and enter a well characterized tube reactor for oxidation at a controlled temperature (25~1100°C). The oxidation rector consisted of a quartz reactor tube of 1 cm i.d. and 120 cm long with a heated length of 36 cm. The axial temperature profiles along the quartz tube were measured at each selective temperature using a thermocouple, and are shown in figure 3. For the nominal operating condition of 1 LPM through the oxidation furnace, the residence time estimated from the measured temperature profiles, give ~1.3 seconds for room temperature to ~0.3 second at 1100°C. A more detailed discussion for the measurement of temperature profile in the tube furnace and calculation of the resident time can be found in our previous work^{36,44}.

Finally the reacted particles are directed to the second DMA, or the APM, for the size and mass measurement. Transmission Electron Microscopy (TEM) was also used to examine the structure of nickel nanoparticles before and after sintering to evaluate the sintering process. An electrostatic precipitator was used after the reaction furnace to collect particles on Formvar coated 200 mesh copper TEM grids. TEM characterization was

performed with a Zeiss EM10 TEM (accelerating voltage: 80 kV and magnification: 100x-200000x)

Results and Discussion

A. Size and Mass Measurements of Nickel Nanoparticle Oxidation

The morphology of nickel nanoparticles as they exit the generator are shown in Figure 4 (a) and indicate the particles are highly aggregated with primary particles sizes less than 5 nm. At the high oxidation temperatures, oxidation and sintering (which decreases surface area) would occur simultaneously for such small primary particle size, and make the measurements and subsequent data analysis too ambiguous. For this reason we choose to sinter the aggregates to spheres. TEM images of the polydisperse particles sampled after the sintering furnace is shown in Figure 4 (b) and confirms that the aggregates were successfully sintered to form spheres. Note that the TEM sample was prepared by sintering polydisperse particles without DMA-1 selection, although the sintering process would result in perfectly spherical particles without any aggregate structure⁴⁷, the high number concentration of generated particles leads to re-aggregation. This re-aggregation can be prevented by first size selecting particles with DMA-1. Mobility sizes of 70, 135, 200 and 240 nm aggregate particles were selected, their size and mass after sintering were subsequently measured using DMA-2 and APM and the results are show in figure 5. The particle sizes shrink to 40, 62, 81, and 96 nm after sintering and the measured mass (APM) and size (DMA) show a relationship of mass $\sim D_p^{3.006}$, implying that individual spherical nickel particles were obtained for the subsequent oxidation step.

We now turn to the size selected measurements. Mobility size selected Ni particles of 40, 62, 81 and 96 nm (after sintering) were mixed with air and oxidized, following which the size or mass of the reacted particles is measured by a second DMA or APM.

Figure 6 (a), (b), (c) and (d) show normalized particle size distributions measured by DMA-2 at selected furnace temperatures for initial mobility size of 40, 62, 81 and 96 nm, respectively. The size distributions obtained for each furnace temperature were fit to a Gaussian distribution to determine the peak size. As mentioned above, the initial unreacted particle size is determined from DMA 2 at 25°C. Furthermore measurements of particle oxidation at 200°C show no size change, indicating that reaction if there is any is below our detection limit, which we estimate from prior work to be ~0.3 nm in diameter.

The TDMA experimental results in Figure 6 show that the particle size first increases as we increase the furnace temperature, and reach a size maximum at 600°C (for particles with initial size 40 nm), 700°C (for particles with initial size 62 nm and 81 nm) and 800°C (for particles with initial size 96 nm). Further increases in the reaction temperature, result in decreases in particle size as the peak size decreased from a maximum of 51.3 nm to 49 nm, 81.4 nm to 77.5 nm, 106.9 nm to 102.5 nm and 124.8 nm to 121.8 nm, for particles with initial size 40, 62, 81 and 96 nm, respectively. The detailed particle peak size data are shown in Table 1, and the size change ΔD_p as function of furnace temperature is shown in figure 7.

The TDMA experiment indicates that the oxidation starts at ~300°C as evidenced by an increase in particle size. This size increase results because nickel oxidation forms a lower density oxide than the zero valent metal. However, the size increase is not continuous in temperature and in the higher temperature regions (above 600°C), a significant size decrease is observed for all particle sizes. There are several possible reasons that can contribute to the shrinkage of particles at high temperatures. First, some particles are not perfectly spherical, and some may be slightly aggregated, so that one may argue that what was seeing at these temperatures is really sintering or rearrangement of particle morphology. However, as we have discussed above, this is an unlikely explanation considering the fractal dimension of the particles is ~3 based on the experimental result shown in figure 5. As a result, any size change after particles pass through the oxidation furnace can be attributed solely to oxidation, e.g. not from the rearrangement of particle morphology.

The most likely explanation for our experimental observation (and consistent with APM results to be presented later) would be the formation of an intermediate phase of the oxide, Ni_2O_3 , at low temperatures, and further decomposition of Ni_2O_3 to NiO at higher temperatures. This is consistent with the fact that Ni_2O_3 is the thermodynamically favorable phase at low temperature, and decomposes into NiO and oxygen at temperatures above 600°C.

The reacted particle size can be estimated by assuming spherical particles of Ni completely convert to Ni_2O_3 or NiO . Our experimental values fall within this calculated

size range. For example, for an initial 40 nm and 96 nm Ni particle, the particle size should increase to 55.6 nm and 132.6 nm for complete conversion to Ni_2O_3 , and then decrease to 48.3 nm and 115.2 nm upon forming NiO , while our experimental value for an initial 40 nm particle increases to 51.3 nm at 600°C, and then shrinks to 49 nm at 1000°C. For an initial size of 96 nm particle the size is 124.8 nm at 800°C and 121.8 nm at 1100°C. Also these results show that the smaller the initial particles size, the closer we achieve to full conversion, while larger particles require a higher temperature to achieve full conversion.

To further investigate the oxidation of nickel nanoparticles and evaluate the phase behavior observed in the TDMA experiments, we substitute the APM for the second DMA in order to track particle mass changes due to oxidation. As discussed previously, the APM classifies particles by mass through a balance of electrostatic and the centrifugal forces⁴⁰. For each particle mobility size, the APM was operated at fixed rotation speed, and as such the applied voltage can be directly related to particle mass. Figure 8 (a), (b) (c) and (d) show the results of the APM measured mass distribution at selected furnace temperatures for initial mobility size of 40, 62, 81 and 96 nm, respectively. Figure 9 shows the mass change ΔM as function of furnace temperature. Because the APM has a broader transfer function compare to the DMA, especially at the low end of the APM range, a plot of the experimental data for each temperature would overlap, and would be difficult to read. For this reason, we only show the experimental results at furnace temperatures of 25°C and 700°C. The particle peak mass distribution data at each furnace temperature were fit to a Gaussian function to obtain the peak mass

and are shown in table 2. It is clear from figure 8 and table 2 that there is a mass increase, with increasing furnace temperature, which reaches a maximum at above 600°C. On the other hand, from figure 9, we can see in the hypothesized phase change region, the measured value for the mass fluctuates within the experimental uncertainty for initial 40, 62, and 81 nm particles, and increases slowly with increased temperature for the initial 96 nm particle. As we discussed above, the theoretical particle size should grow to 55.6 nm and 136.6 nm for an initial 40 nm and 96 nm nickel particle, if we assume complete conversion, while the DMA measured value is 51.3 nm and 124.8 nm. This suggests that the nickel particle could act as a multi-component oxide during the oxidation process.

Presumably the particle would have a nickel core with an outer oxide layer which contains both NiO and Ni₂O₃. Both the oxidation of the nickel core and decomposition of the outer Ni₂O₃ layer could occur simultaneously and result in a roughly constant particle mass as observed for small particles, and slow mass gain for large particles.

Our previous work showed that the APM when combined with TEM image analysis can accurately determine particle density³⁸. More recently, the DMA-APM technique was used as an online measurement tool to obtain the particle density in understanding aluminum oxidation³³. In this work, the average density profiles of reacted particles are calculated using the TDMA and APM measured particle size and mass, and shown in figure 10. We find that as the furnace temperature increases, the average density of the reacted particles decreased monotonically to 4.7-5.0 g/cm³, consistent with the density of Ni₂O₃ (4.84 g/cm³)^{48,49}. At higher temperatures the particle density increases to 5.5-

5.7 g/cm³ and at the highest temperature investigated is roughly at a density half way between NiO (6.67 g/cm³) and Ni₂O₃ (4.84 g/cm³). The oxidation to form Ni₂O₃ should be dominant in the low temperature region while the process of formation of the two types of oxides, and the phase transition are coupled at higher temperatures.

B. Size-resolved Oxidation Kinetics of Nickel Nanoparticles

Metal oxidation theories and the transport properties of the oxides have been studied for several decades. It is believed that the diffusion of ionic vacancies and electron holes is the dominant transport process for nickel oxidation⁷. Thus, the well known diffusion controlled shrinking core model^{50,51} can be employed to extract the reaction rate constant. The theories proposed by Wagner for thick film growth are based on conditions of charge-neutrality, and diffusion of ions and electrons being the rate-limiting step, lead to a parabolic rate law for a planar geometry²⁷. Carter later applied the same assumptions to the shrinking core model for a spherical geometry, and derived an oxidation rate law for metal particle oxidation²². However, Wagner's theory is restricted to thick films in which the characteristic length is given by the Debye –Hückel length, which is probably on the orders of hundreds of nanometers^{7,8,11}. Given the particle sizes we are studying, many of the assumptions of the theory would likely be invalid. For example, the charge-neutrality condition of Wagner's theory would no longer hold due to the space charge effects. Cabrera and Mott's, on the other hand, describe the thin film growth²⁶ assuming thermal electron emission and tunneling of electrons, to be easier than ionic diffusion, so that an electric field is developed across the thin film to assist the transport of the ions. The

electric field caused by the surface-charge could be on the order of $\sim 10^7$ V/cm such that a nonlinear behavior has to be considered. The rate law for thin films was derived and a characteristic length L_{crit} was suggested, below which the field is so strong that the drift velocity of ions is not proportional to the field but has an exponential dependence, and this nonlinear effect should be consider when $L(t) < L_{crit}$. The upper limit for Cabrera and Mott's theory is ~ 10 nm for nickel, and L_{crit} is as small as 2 nm. No analytical result has been developed for the spherical geometry.

Fromhold and co-workers had given a more general theoretical model for metal oxidation^{8,11,15,17,20}. However, the equations can only be solved numerically. In our case, the particle sizes falls in the range between the Wagner's theory and Cabrera and Mott's theory. Nickel nanoparticle oxidation is most likely in a low-field region where surface-charge and space-charge should be considered. Fromhold and Cook had evaluated the space-charge and surface-charge modification on the oxidation kinetics with a coupled current approach based on the idea that the diffusion currents are in the steady state in the presence of surface/space charge, the growth kinetics was obtained by summing the ionic and electronic diffusion currents of all the species¹⁵. The results can only be solved numerically and no results are available for spherical particle oxidation.

More recently Fromhold has developed a model focused on the oxidation rate of spherical metal particles in the low space charge limit using the coupled current approach for oxide thicknesses below 100 nm⁶. Only surface charge and linear diffusion were considered in their study, and a same rate law similar to Carter's work was obtained. This

suggested to us that the diffusion controlled shrinking core model could be applied to our study as a relatively straightforward way to process our experimental results.

Following Carter's analysis at steady state, the diffusion flux through the oxide shell can be related to the reaction rate of reactant, by

$$\frac{dN_{O_2}}{dt} = -4\pi DeCo_2 \frac{r_1 r_2}{r_2 - r_1} \quad (1)$$

In equation (1) r_1, r_2 are the radius of the nickel core, and the reacted particle radius. Co_2 is the oxygen molar concentration in gas and N_{O_2} is the moles of oxygen in oxide layer.

De is the diffusion coefficient for ion diffusion in the oxide layer:

$$De = A_m \exp(-\frac{E_a}{RT}) \quad (2)$$

Here A_m is the pre-exponential factor, E_a is reaction activation energy, and R is the gas constant. Equation (1) immediately leads to the mass change rate for the reacted nickel nanoparticle, as

$$\frac{dM}{dt} = 4\pi M_{O_2} DeCo_2 \frac{r_1 r_2}{r_2 - r_1} \quad (3)$$

where M_{O_2} is the molecular weight of oxygen. Knowing the furnace temperature profiles from figure 3, the particle mass change, Δm can be obtained by integrating equation (3) as the particle travel down the oxidation furnace. However, as we discussed above, the nickel nanoparticle oxidation should be a composite between formation of NiO and Ni_2O_3 , and the phase transition. Therefore the relative concentration of NiO and Ni_2O_3 within the oxide layer is temperature dependent. As a result, the instantaneous mass

changing rate $\frac{dM}{dt}$ can not be determined with our current experimental approach.

Considering the exponential temperature dependence of the rate constant and the fact that most of the reaction would occur at the center of the furnace at the peak temperature, we approximate the instantaneous mass changing rate $\frac{dM}{dt}$ in equation (3) with the average mass changing rate to get

$$\ln \frac{\Delta M}{\tau} = -E_a / RT + \ln(4\pi M_{O_2} C_{O_2} A_m \frac{r_1 r_2}{r_2 - r_1}) \quad (4)$$

Here the peak temperature determined from figure 3 is used, and by using the mass change measured from the APM, the average mass change rate can be calculate for each furnace temperature. The size-resolved activation energy can be obtained from an Arrehenius plot as shown in figure 11. Considering that only very small mass changes were observed at 300°C, we do not use results from that temperature to process the data. Two different regions can be distinguished from the Arrehenius plot, as the oxidation process transitions to a phase change region at ~600-700°C. The kinetic parameters for both regions can be determined using linear fit. The curve fit parameter as well as the size-resolved activation energies obtained are summarized in table 3 and the results for the low temperature region are also shown in figure 11. The calculated activation energies in the low temperature region decrease from 54 KJ/mol to 35 KJ/mol as the particle mobility size decreases from 96 nm to 40 nm. The activation energies are significantly lower in the phase transition region, and further investigation is needed to understand this phase behavior. The activation energy obtained here (~0.4 eV) are considerably smaller than the value of 1.5 eV reported by Karmhag et. al. for micro size Ni particles oxidation and 1.34 eV for nano size Ni particles oxidation^{29,32}, and also smaller than 1.78 eV for grain boundary diffusion limited thin film oxidation reported by

Atkinson⁷. This difference between conventional methods and our approach has been consistently observed in previous work^{34,35}. Moreover, the activation energy obtained here are much closer to the value of 0.6~0.9 eV for electron transport in single crystal nickel oxide⁵², and consistent with the reported activation energy of 0.3 eV for single crystal Ni oxidation in the early film-thickening stage⁵³. It is well known that there are significant drawbacks of the conventional methods associated with the influence of experimental artifacts⁵⁴. In those methods, usually milligrams of bulk sample are needed, while the sample mass of our aerosol based techniques is ~ 1 fg. For a highly exothermic reaction such as metal oxidation process, the large exotherm in a bulk sample will corrupt the observed onsite temperature, and the rapid reaction will lead to heat and mass transfer effect for bulk sample. As a consequence, the kinetic parameters extracted from the conventional methods are obscured. The TDMA and DMA-APM techniques employed here allow a direct measure of mass and volume change of individual particles thus enables us to explore the intrinsic reactivity of nanoparticles with minimizing the sampling error introduced by mass and heat transfer.

The effective diffusion coefficient is determined by calculating the unreacted nickel core radius r_1 . Although the oxide layer contains both NiO and Ni₂O₃, and their relative concentration can not be determined, the oxygen concentration is roughly uniform for NiO and Ni₂O₃. Calculation shows that the relative oxygen density in NiO is 1.42 g/cm³ and in Ni₂O₃ are 1.40 g/cm³. The uniform oxygen density enables us to estimate the nickel core radius using the mass change of particle measured by the APM. Therefore the effective diffusion coefficient can be calculated from equation (3). Since the shrinking-

core model used here can only count for the oxidation process, the phase transition in high temperature region will corrupt the calculation of the effective diffusion coefficient. As the consequence, the calculation is only valid in the low temperature region and the results are shown in figure 12. Due to the well known kinetic compensation effect, although the activation energy is considerably smaller than the value measured by the conventional offline methods , the measured diffusion coefficient are within the range of reported values⁷. Since aluminum has been well studied and has been used extensively as a primary thermite based material, the effective diffusion coefficients for aluminum oxidation obtained from our previous work³⁴ is also plotted in the figure for comparison. Surprisingly to see that that nickel is actually more active than aluminum although it should be pointed out that the aluminum measurements were made with a totally different experimental approach. However despite the apparent faster kinetics of Ni, the higher enthalpy of aluminum oxide (-1675.7 kJ/mol vs. -489.5 kJ/mol for Ni_2O_3 or -239.7 kJ/mol)^{48,55} implies aluminum is still a more promising energetic material than nickel. Nevertheless, Ni might find applications as an ignition source for example, or in tuning the reaction profile in mixed metal nanocomposites.

Particle burn time for different initial particle size at different temperatures was also calculated using the burn rate and the total mass change measured from the APM. These results are plotted on a log scale in figure 13, and show for all temperatures a diameter dependence well less than 2 ($\sim D_p^{1.4}$). For large size particles (micron size), the diffusion controlled reaction would lead to a $\sim D_p^2$ dependence⁵¹, and a $\sim D_p^{1.8}$ dependent is reported experimentally⁵⁶. For nano size particles, however, a much weaker size

dependent has frequently been observed⁵⁶⁻⁵⁸. A melt dispersion mechanism for very fast reaction of nano thermites were recently proposed to explain this observation⁵⁷. Fast heating creates huge thermal stresses between the metal core and oxidation shell and results in the spallation of the shell and complete explosion of the core, the oxidation of dispersed metal clusters, is much faster than diffusion and is independent of particle size. However, this mechanism is valid for particles with a melting core, and a solid shell, and is expected only for very fast heating rate ($\sim 10^7$ °C/s) as compared with our $\sim 10^3\text{-}10^4$ °C/s heating rates. A phenomenological model was developed for aluminum oxidation in our previous work³³ which indicated that due to the internal pressure gradient in the particle, a $\sim D_p^{1.6}$ dependent was found. More generally, for the oxidation of metal, Formhold^{8,15} shows that a space charge layer in the growing oxide could have significant effects on the oxidation process for particles in the range of 10 nm \sim 100 nm, which can either retard or enhance the diffusion flux through the oxidation shell depending on ionic or electronic species as rate limiting^{8,15}. Our results for particle burn time suggested that a model that includes both the pressure gradient and space charge effect would be worthy of investigation.

Conclusions

We applied online aerosol ion-mobility based methods to study oxidation and reactivity of nickel nanoparticles. The nickel nanoparticles were generated in-situ during the oxidation experiments using gas-phase thermal pyrolysis of nickel carbonyl. Particles of

well controlled sizes and structure were generated and subsequently size selected using a DMA. The mass and size changes of reacted particles were measured using an APM and a second DMA. The experimental data can be divided into an oxidation region and a phase transit region. Based on the diffusion-controlled rate equation in the shrinking core model, we found that the activation energy of oxidation decreased from 54 KJ/mol to 35 KJ/mol as the particle size decrease from 96 nm to 40 nm at low temperatures. The absolute burning time and the effective diffusion coefficient were also determined.

References

- (1) Prakash, A.; McCormick, A. V.; Zachariah, M. R. *Nano Letters* **2005**, *5*, 1357.
- (2) Park, K. R. A. a. Z. M. R. *J. NanoParticle Research* **2005**, *in press*.
- (3) K. Sullivan; Young, G.; Zachariah, M. R. *submitted to Combustion and Flame*. **2007**.
- (4) Mrowec, S.; Grzesik, Z. *Journal of Physics and Chemistry of Solids* **2004**, *65*, 1651.
- (5) Rellinghaus, B.; Stappert, S.; Wassermann, E. F.; Sauer, H.; Spliethoff, B. *European Physical Journal D* **2001**, *16*, 249.
- (6) Fromhold, J. A. T. *Journal of Physics and Chemistry of Solids* **1988**, *49*, 1159.
- (7) Atkinson, A. *Reviews of Modern Physics* **1985**, *57*, 437.
- (8) A. T. Fromhold, Jr. *Theory of Metal Oxidation Volume 2*; North-Holland Publishing Company, 1980; Vol. 2.
- (9) Sales, B. C.; Maple, M. B.; Vernon, F. L. *Physical Review B* **1978**, *18*, 486.
- (10) Sales, B. C.; Maple, M. B. *Physical Review Letters* **1977**, *39*, 1636.
- (11) A. T. Fromhold, Jr. *Theory of Metal Oxidation Volume 1*; North-Holland Publishing Company, 1976; Vol. 1.
- (12) Knutson, E. O.; Whitby, K. T. *Journal of Aerosol Science* **1975**, *6*, 443.
- (13) Graham, M. J.; Cohen, M. *Journal of The Electrochemical Society* **1972**, *119*, 879.
- (14) Caplan, D.; Graham, M. J.; Cohen, M. *Journal of The Electrochemical Society* **1972**, *119*, 1205.
- (15) Fromhold, A. T.; Cook, E. L. *Physical Review* **1968**, *175*, 877.
- (16) Pizzini, S.; Morlotti, R. *Journal of The Electrochemical Society* **1967**, *114*, 1179.
- (17) Fromhold, A. T.; Cook, E. L. *Physical Review* **1967**, *163*, 650.
- (18) A. T. Fromhold, Jr.; Earl, L. C. *Journal of Applied Physics* **1967**, *38*, 1546.
- (19) Kazuo, F.; J. Bruce Wagner, Jr. *Journal of The Electrochemical Society* **1965**, *112*, 384.
- (20) A. T. Fromhold, Jr. *The Journal of Chemical Physics* **1964**, *41*, 509.
- (21) W. L. Phillips, Jr. *Journal of The Electrochemical Society* **1963**, *110*, 1014.
- (22) Carter, R. E. *Journal of Chemical Physics* **1961**, *34*, 2010.
- (23) Gulbransen, E. A.; Andrew, K. F. *Journal of the Electrochemical Society* **1957**, *104*, 451.
- (24) Gulbransen, E. A.; Andrew, K. F. *Journal of the Electrochemical Society* **1954**, *101*, 128.
- (25) Dravnieks, A. *Journal of the American Chemical Society* **1950**, *72*, 3761.
- (26) Cabrera, N.; Mott, N. F. *Reports on Progress in Physics* **1948**, *12*, 163.
- (27) Wagner, C. Z. *Phys. Chem. Abt. B* **1933**, *21*.
- (28) Niklasson, G. A.; Karmhag, R. *Surface Science* **2003**, *532*, 324.
- (29) Karmhag, R.; Niklasson, G. A.; Nygren, M. *Journal of Applied Physics* **2001**, *89*, 3012.

- (30) Karmhag, R.; Tesfamichael, T.; Wackelgard, E.; Niklasson, G. A.; Nygren, M. *Solar Energy* **2000**, *68*, 329.
- (31) Karmhag, R.; Niklasson, G. A.; Nygren, M. *Journal of Materials Research* **1999**, *14*, 3051.
- (32) Karmhag, R.; Niklasson, G. A.; Nygren, M. *Journal of Applied Physics* **1999**, *85*, 1186.
- (33) Rai, A.; Park, K.; Zhou, L.; Zachariah, M. R. *Combustion Theory and Modelling* **2006**, *10*, 843
- (34) Park, K.; Lee, D.; Rai, A.; Mukherjee, D.; Zachariah, M. R. *J. Phys. Chem. B* **2005**, *109*, 7290.
- (35) Mahadevan, R.; Lee, D.; Sakurai, H.; Zachariah, M. R. *J. Phys. Chem. A* **2002**, *106*, 11083.
- (36) Higgins, K. J.; Jung, H. J.; Kittelson, D. B.; Roberts, J. T.; Zachariah, M. R. *Journal of Physical Chemistry A* **2002**, *106*, 96.
- (37) Kim, S. H.; Fletcher, R. A.; Zachariah, M. R. *Environmental Science & Technology* **2005**, *39*, 4021.
- (38) Park, K.; Kittelson, D. B.; Zachariah, M. R.; McMurry, P. H. *Journal of Nanoparticle Research* **2004**, *6*, 267.
- (39) McMurry, P. H.; Wang, X.; Park, K.; Ehara, K. *Aerosol Science and Technology* **2002**, *36*, 227
- (40) Ehara, K.; Hagwood, C.; Coakley, K. J. *Journal of Aerosol Science* **1996**, *27*, 217.
- (41) Sahoo, Y.; He, Y.; Swihart, M. T.; Wang, S.; Luo, H.; Furlani, E. P.; Prasad, P. N. *Journal of Applied Physics* **2005**, *98*, 054308/1.
- (42) He, Y. Q.; Li, X. G.; Swihart, M. T. *Chemistry of Materials* **2005**, *17*, 1017.
- (43) Kim, S. H.; Zachariah, M. R. *Journal of Physical Chemistry B* **2006**, *110*, 4555.
- (44) Higgins, K. J.; Jung, H. J.; Kittelson, D. B.; Roberts, J. T.; Zachariah, M. R. *Environmental Science & Technology* **2003**, *37*, 1949.
- (45) Hinds, W. C. *Aerosol Technology: Properties, Behavior, and Measurement of airborne particles*, 2 ed.; John Wiley & Sons, Inc.: New York, NY, 1999.
- (46) Jung, H.; Kittelson, D. B.; Zachariah, M. R. *Combustion and Flame* **2005**, *142*, 276.
- (47) Tsyganov, S.; Kastner, J.; Rellinghaus, B.; Kauffeldt, T.; Westerhoff, F.; Wolf, D. *Physical Review B* **2007**, *75*.
- (48) *ICT Database of thermochemical values*; Fraunhofer Institut für Chemische Technologie: Pfinztal, Germany, 2001.
- (49) Antonsen, D. H.; Meshri, D. T. *Kirk-Othmer Encyclopedia of Chemical Technology (5th Edition)* **2006**, *17*, 106.
- (50) Smith, J. M. *Chemical Engineering Kinetics*, 3rd ed.; McGraw-Hill, Inc, 1981.
- (51) Levenspiel, O. *Chemical Reaction Engineering*, 3rd ed.; John Wiley & Sons, 1999.
- (52) Aiken, J. G.; Jordan, A. G. *Journal of Physics and Chemistry of Solids* **1968**, *29*, 2153.

- (53) Mitchell, D. F.; Graham, M. J. *Surface Science* **1982**, *114*, 546.
- (54) Ortega, A. *International Journal of Chemical Kinetics* **2001**, *33*, 343.
- (55) *CRC Handbook of Chemistry and Physics*; Hampden Data Services Ltd., 2002.
- (56) Huang, Y.; Risha, G. A.; Yang, V.; Yetter, R. A. *Proceedings of the Combustion Institute* **2007**, *31*, 2001.
- (57) Valery, I. L.; Blaine, W. A.; Steven, F. S.; Michelle, P. *Applied Physics Letters* **2006**, *89*, 071909.
- (58) Young, G.; Sullivan, K.; Zachariah, M. R. “Investigation of Boron Nanoparticle Combustion”; 46th AIAA Aerospace Sciences Meeting and Exhibit AIAA-2008-0942, 2007, Reno, Nevada.

TABLE 1: Change in particle size as a function of oxidation temperature
 Furnace
 Setting

(°C)	40	62	81	96
25	40.0	62.0	81.0	96.6
200	40.0	62.0	81.0	96.6
300	40.2	62.5	81.3	96.9
400	41.5	63.6	81.8	97.5
500	45.9	67.0	87.1	101.2
600	51.3	77.9	95.8	110.2
700	51.2	81.4	106.9	122.7
800	50.9	81.2	106.9	124.8
900	50.1	80.7	106.5	124.7
1000	49.0	78.7	104.8	123.8
1100	50.3	77.5	102.5	121.8

TABLE 2: Change in particle mass as a function of oxidation temperature.

Furnace Setting (°C)	40	62	81	96
25	2.48	9.19	21.43	36.81
300	2.50	9.40	21.44	37.25
400	2.65	9.73	21.93	37.40
500	2.82	10.29	23.10	38.30
600	3.03	11.42	25.12	41.15
700	3.08	11.89	27.12	44.85
800	3.11	12.03	27.21	46.34
900	3.10	11.98	27.39	47.28
1000	3.10	11.94	27.15	47.88
1100	3.11	12.23	28.16	48.40

TABLE 3: Summary for Arrehenius parameters for nickel nanoparticle oxidation.

Particle Mobility Size (nm)	Temperature range (°C)	Curve fit parameters ($Y = aX + b$)		Activation energy (KJ/mol)	Effective Diffusion Coefficients ($10^{-9}\text{cm}^2/\text{s}$)
		<i>a</i>	<i>b</i>		
40	400~600	4216.7	-38.8	35.0 ± 0.8	0.56~4.64
62	400~600	4844.9	-36.7	40.3 ± 2.6	1.02~17.0
81	400~700	6119.4	-34.8	50.8 ± 3.0	0.27~33.7
96	400~700	6566.2	-34.1	54.6 ± 2.9	0.18~35.4
40	700~1100	1267.7	-42.2	10.5 ± 0.5	NA
62	700~1100	1336.9	-40.6	11.1 ± 1.5	NA
81	800~1100	1479.8	-39.7	12.3 ± 2.2	NA
96	800~1100	2085.3	-38.7	17.3 ± 0.4	NA

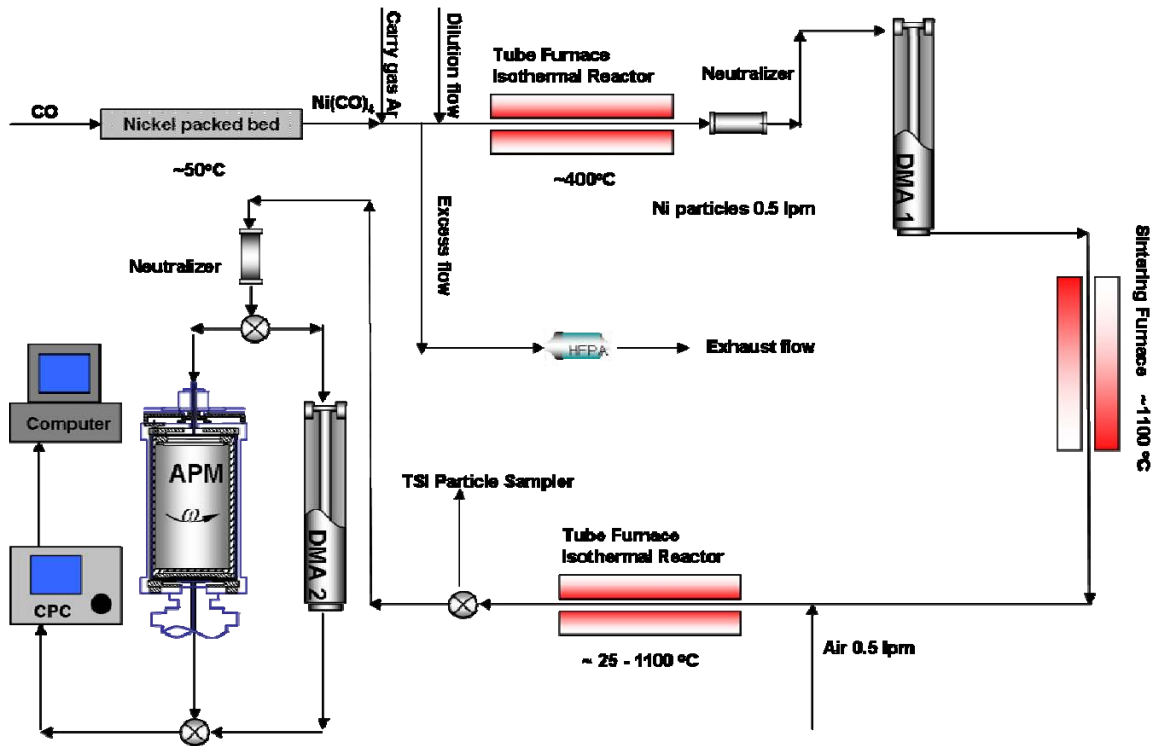


Figure 1: Schematic of Ni generation, size selection, sintering, oxidation and subsequent size and mass measurement.

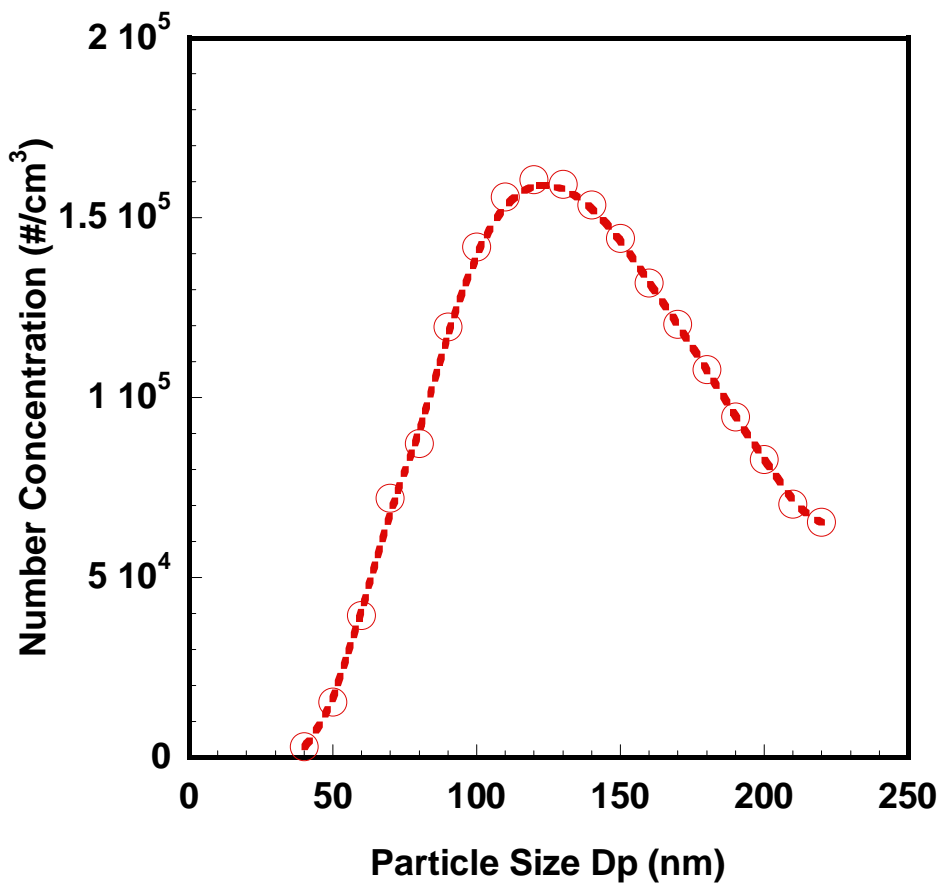


Figure 2: Single DMA scan of the overall nickel particle size distribution sampled before sintering. (The circles are the data points and the dash line is the smooth fit to the data).

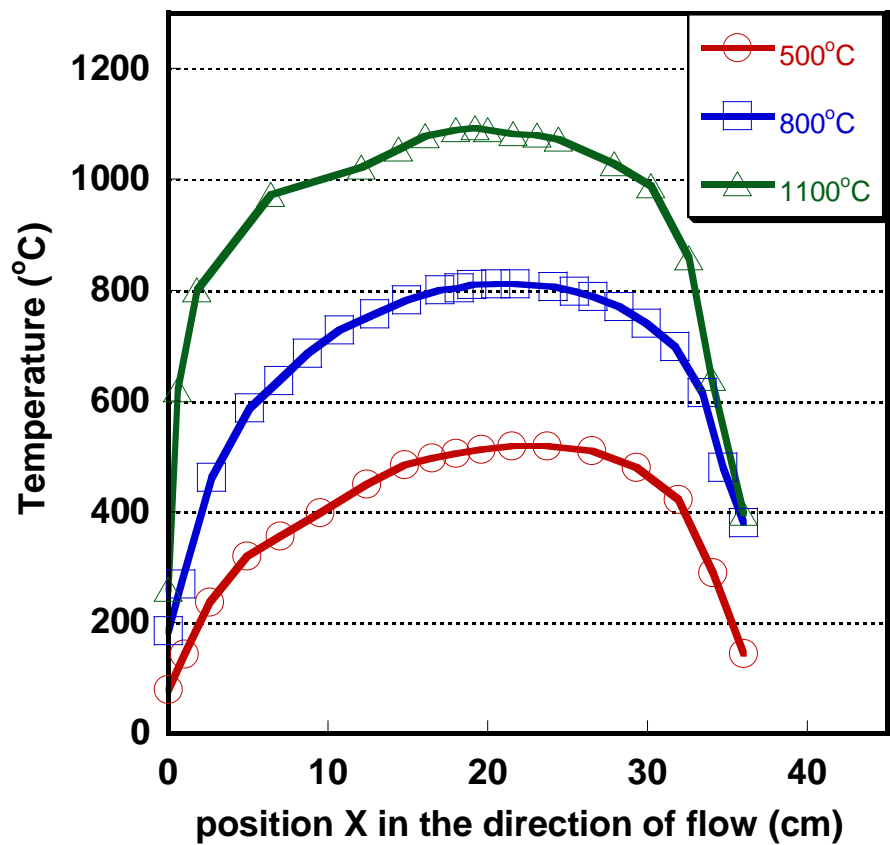
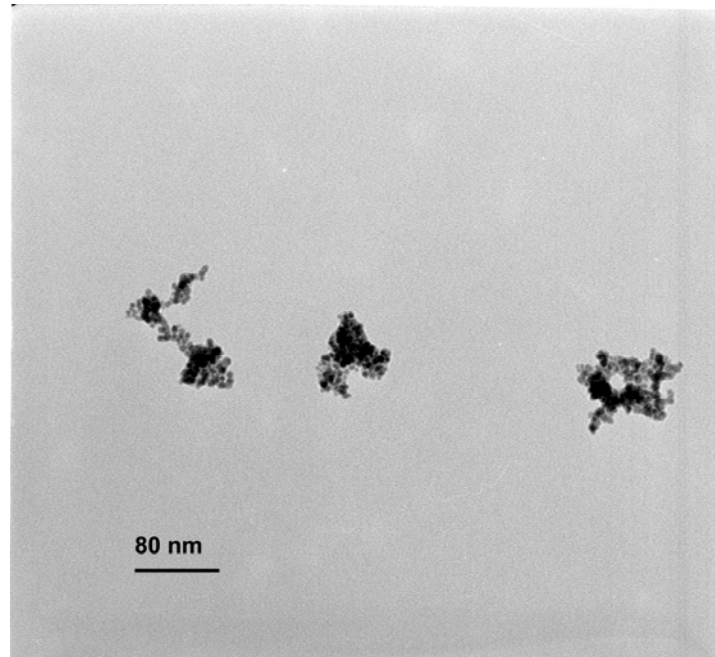
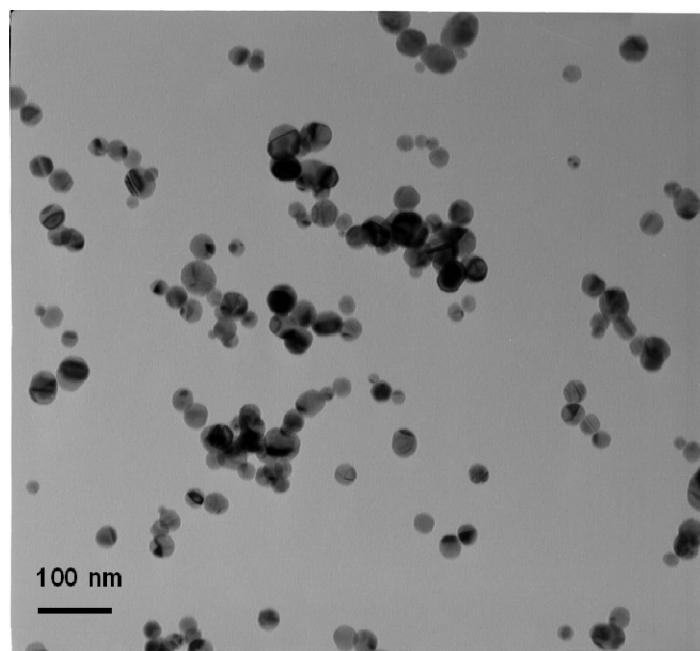


Figure 3: Temperature profile within the quartz flow tube for furnace settings of 500°C
800°C and 1100°C.



(a)



(b)

Figure 4 TEM micrographs of Nickel samples: (a) before sintering (b) after sintering

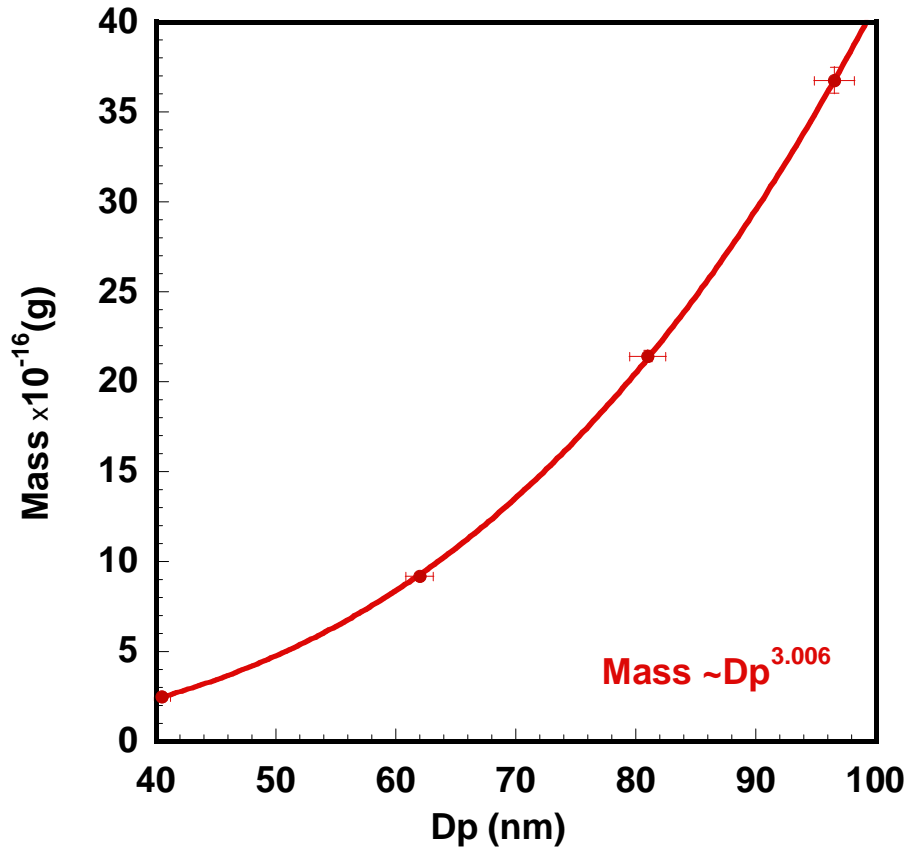


Figure 5 APM measured mass (Y axis) and TDMA measured initial particle size (X-axis).

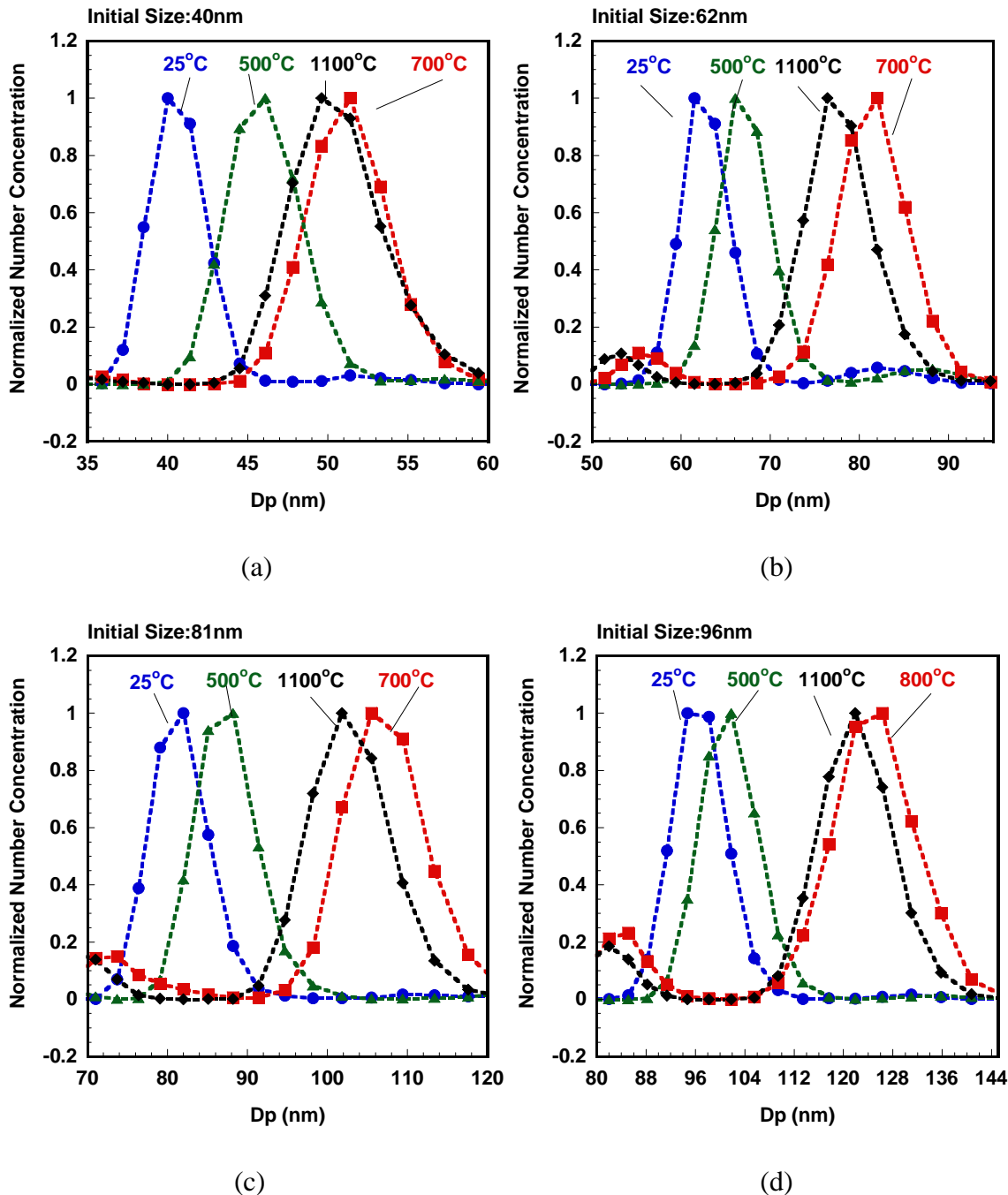


Figure 6 TDMA measured size distribution for initial size of (a) 40 nm, (b) 62 nm (c) 81 nm and (d) 96 nm nickel particles at different oxidation temperatures.

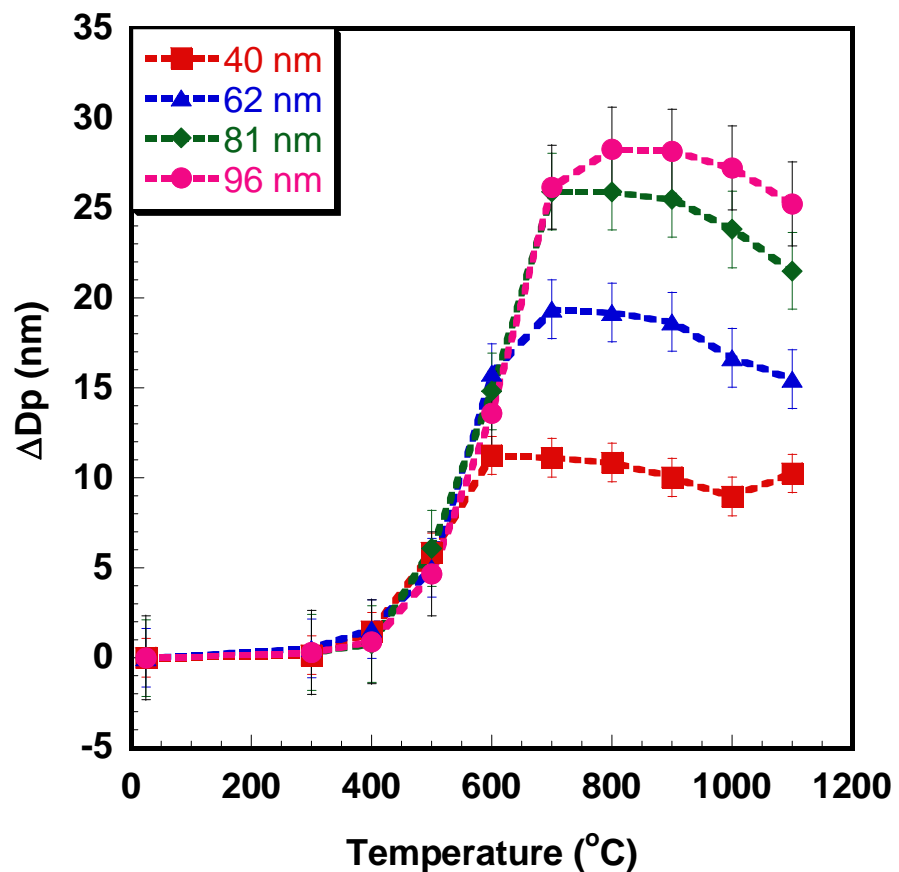


Figure 7. TDMA measured change of particle size as function of oxidation temperature.

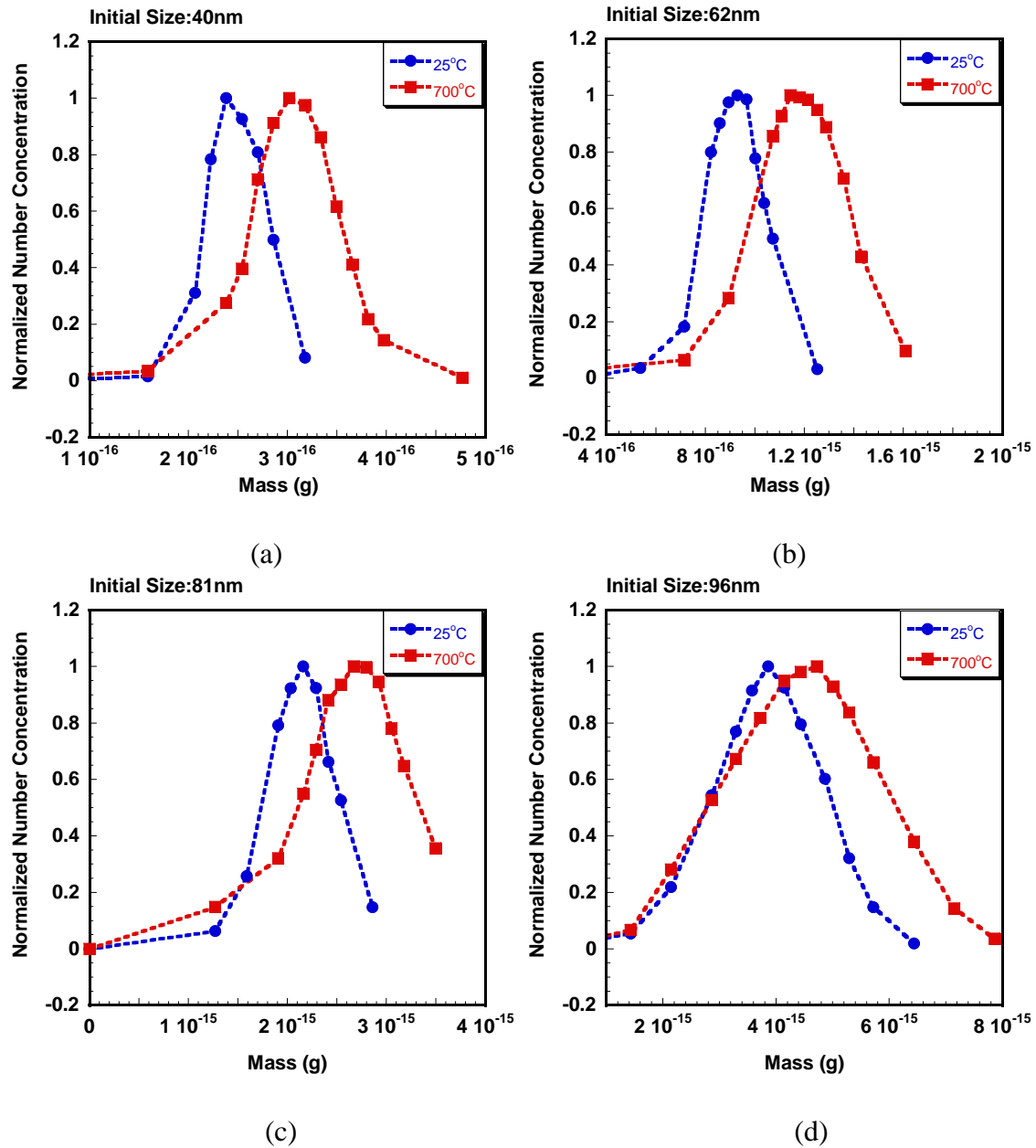


Figure 8 APM measured mass distribution for initial size of (a) 40 nm, (b) 62 nm (c) 81 nm and (d) 96 nm nickel particles at different oxidation temperatures.

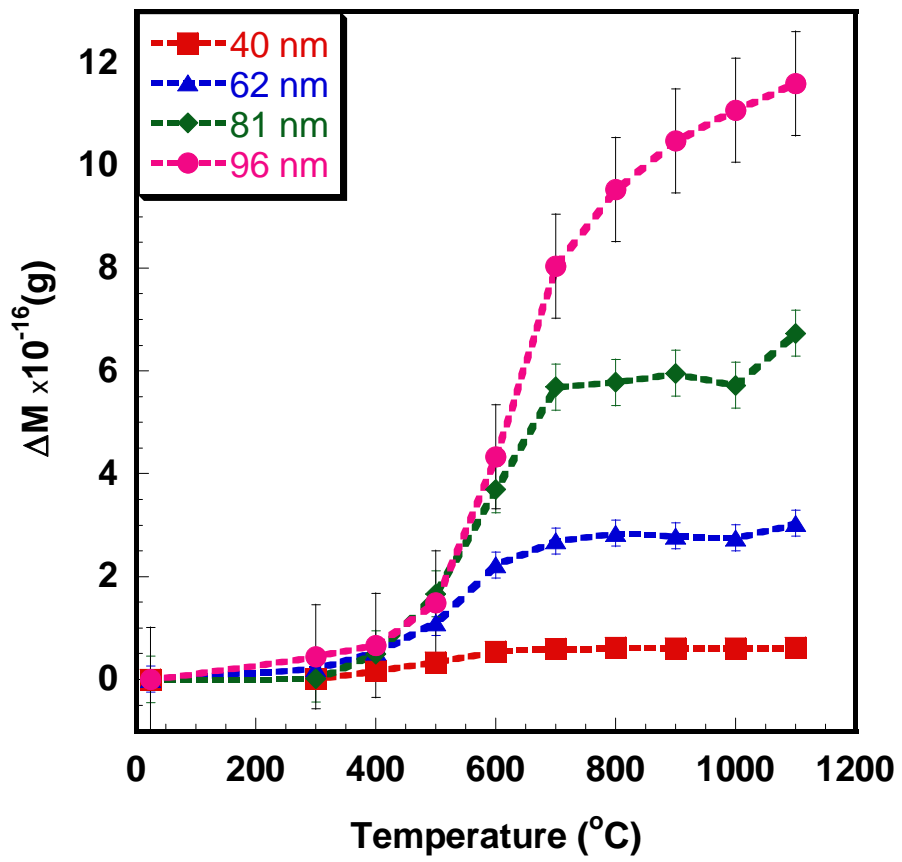


Figure 9. DMA-APM result for change of particle mass as function of oxidation temperature.

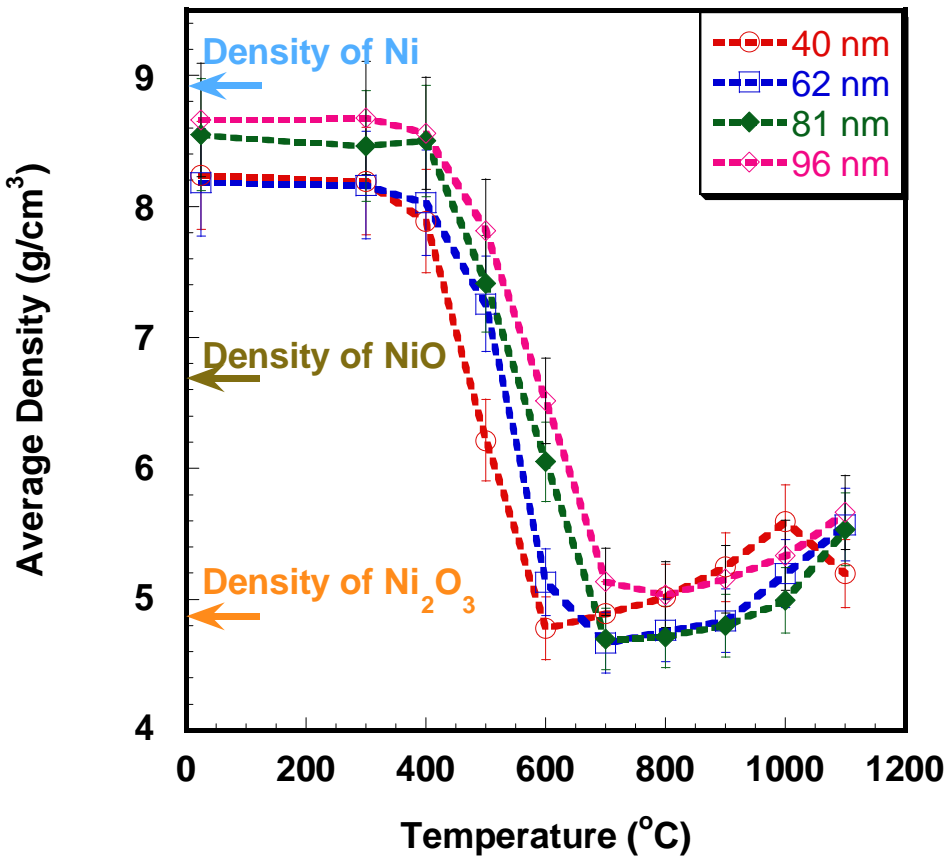


Figure 10 Average density measured using DMA-APM combined experiment.

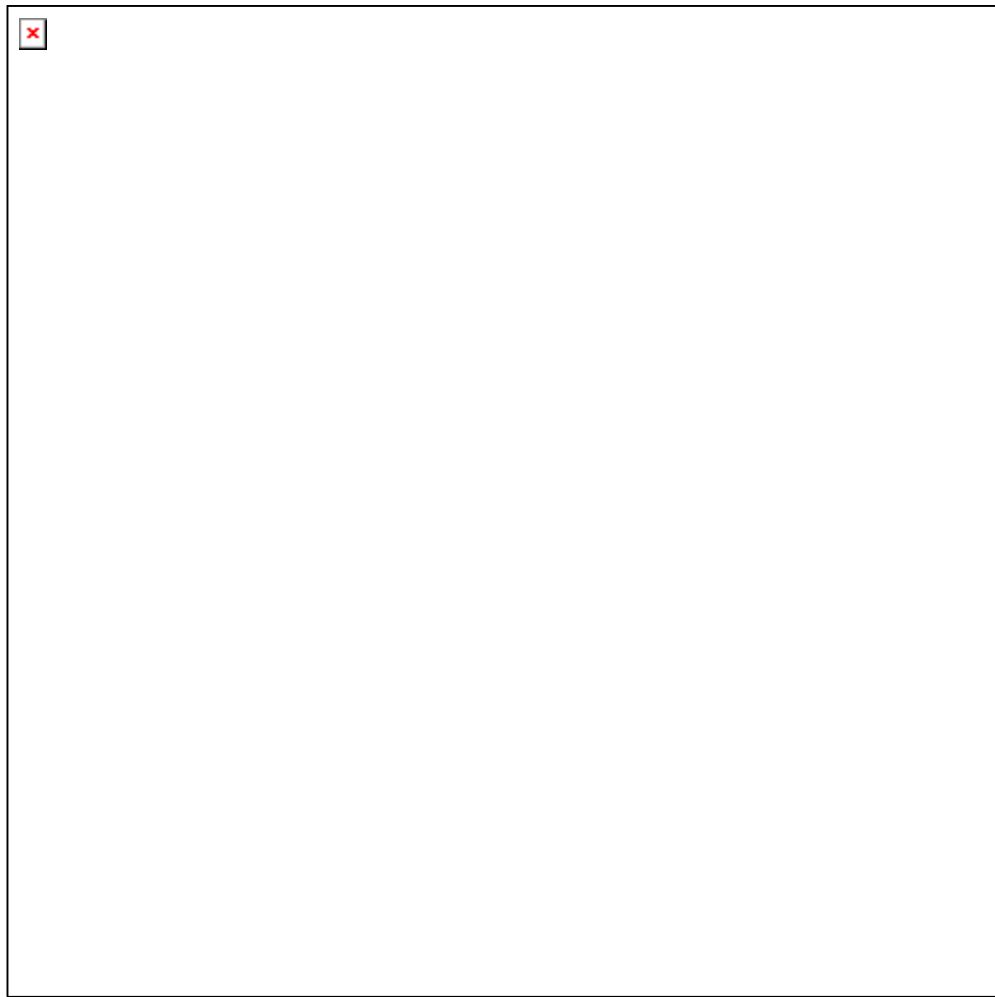


Figure 11 Arrehenius plots of average mass changing rate as a function of inverse temperature. The calculations for activation energy are only for the low temperature region.

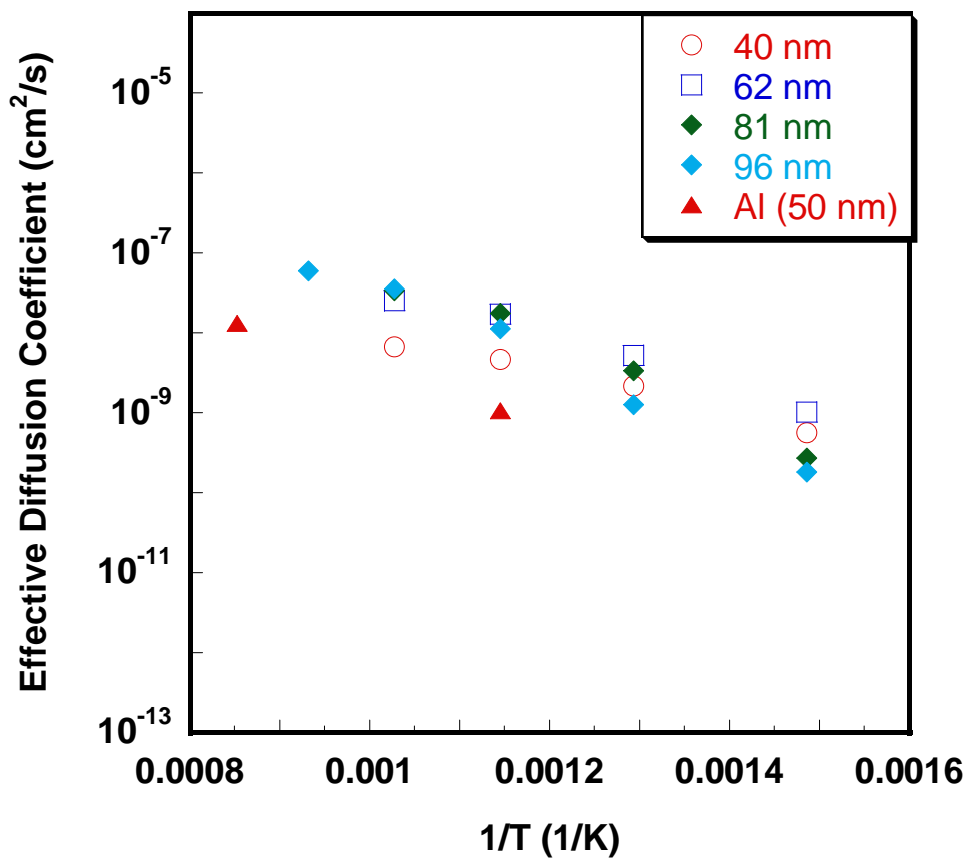


Figure 12 Arrhenius plot of effective diffusion coefficients in the low temperature region for Ni and Al.

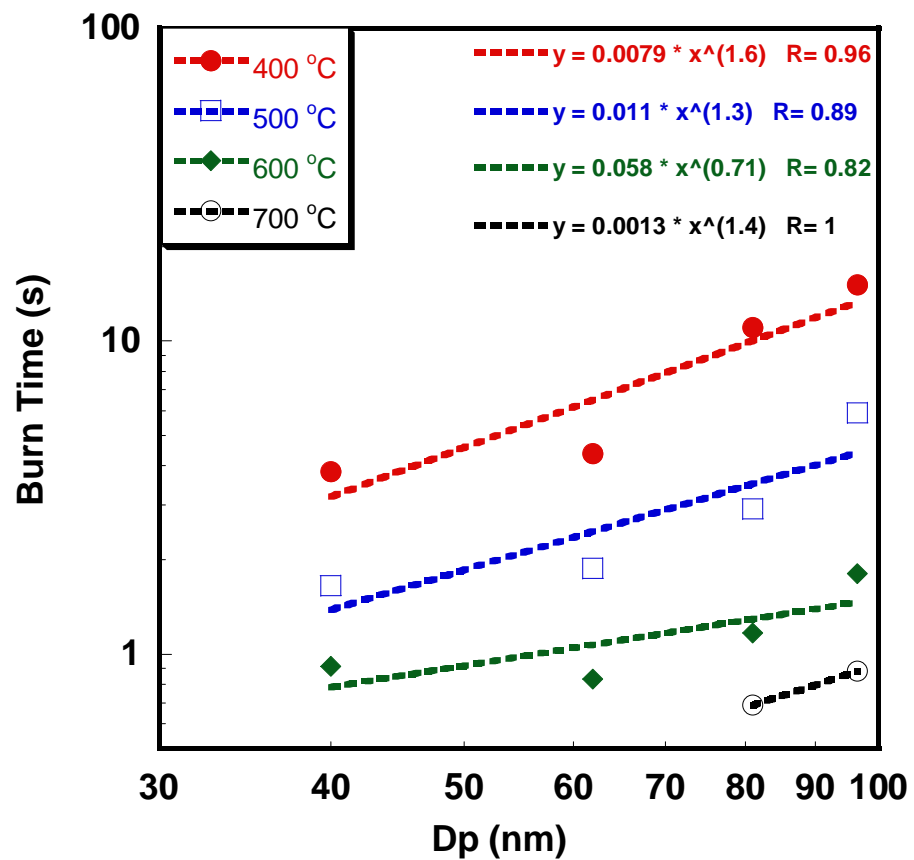


Figure 13 Particle burn time at different temperatures as a function of initial particle size ,

Enhanced Reactivity of Nano-B/Al/CuO MIC's

K. Sullivan, G. Young, and M. R. Zachariah*

To appear in Combustion and Flame

ABSTRACT

Aluminum is traditionally used as the primary fuel in nanocomposite energetic systems due to its abundance and high energy release. However, thermodynamically boron releases more energy on both a mass and volumetric basis. Kinetic limitations can explain why boron rarely achieves its full potential in practical combustion applications, and thus has not replaced aluminum as the primary fuel in energetic systems. In particular, the existence of the naturally-formed boron oxide (B_2O_3) shell is believed to play a major role in retarding the reactivity by acting as a liquid barrier if it cannot be efficiently removed. In this paper we demonstrate from constant-volume combustion experiments that nanoboron can be used to enhance the reactivity of nanoaluminum-based Metastable Intermolecular Composites (MICs) when the boron is <50 mol% of the fuel. It was also observed that an enhancement was not achieved when micronboron (700nm) was used. Thermodynamic calculations showed that the aluminum reaction with CuO was sufficient to raise the temperature above ~2350 K in those mixtures which showed an enhancement. This is above both the boiling point of B_2O_3 (2338 K) and the melting point of boron (2350 K). A heat transfer model investigates the heating time of boron for temperatures >2350 K (the region where the enhancement is achieved), and includes three heating times; sensible heating, evaporation of the B_2O_3 oxide shell, and the melting of pure boron. The model predicts the removal of the B_2O_3 oxide shell is fast for both the nano and micron boron, and thus its removal alone cannot explain why

nanoboron leads to enhancement while micronboron does not. The major difference in heating times between the nano and micron boron is the melting time of the boron, with the micronboron taking a significantly longer time to melt than nanoboron. Since the oxide shell removal time is fast for both the nano and micron boron, and since the enhancement is only achieved when the primary reaction (Al / CuO) can raise the temperature above 2350 K, we conclude that the melting of boron is also necessary for fast reaction in such formulations. Nanoboron can very quickly be heated relative to micronboron, and on a timescale consistent with the timescale of the Al / CuO reaction, thus allowing it to participate more efficiently in the combustion.

The results indicate that sufficiently small boron can enhance the reactivity of a nanoaluminum-based MIC when added as the minor component (<50% by mole) of the fuel.

INTRODUCTION

Energetic materials consisting of a metal as a fuel and a metal oxide as an oxidizer with particle sizes in the nanometer range are termed Metastable Intermolecular Composites (MICs) and give rise to thermite reactions upon ignition. Such materials have received considerable attention due to their high energy densities and reaction temperatures, and their potential use in explosives, pyrotechnics, and propellants is currently being investigated. Perhaps the single most attractive feature of a MIC is that the reactivity can be tuned through easily-adjustable parameters (i.e. particle size, stoichiometry, etc.) making them prime candidates for a wide range of end-user applications, such as initiators for explosives or enhancers for propellants. Traditionally, aluminum has been used as the fuel in thermites due to a combination of its high energy release and its abundance. However, thermodynamically boron is an attractive alternative since it has higher heating values on both a mass and volumetric basis. Table 1

shows the heating values of some metals which could be potential candidates. Other than beryllium, which is not practical due to its toxicity, boron shows higher heating values than all of the other metals.

When exposed to air, aluminum and boron form an oxide shell around the elemental core of fuel. The shell is typically only a few nanometers thick and, on a supermicron level, is an insignificant amount of the particle mass. However, as the particle size transitions into the nanometer regime, the shell becomes a larger portion of the total mass and can play a critical role in the combustion process. Though the heating values clearly suggest that boron should outperform aluminum, the burning mechanisms of these two materials are speculated to be quite different when one takes into consideration the core-shell structure.

Different theories have been suggested to explain the burning of an aluminum particle with its elemental core and oxide shell. Initially, Glassman^{1, 2} proposed that metal combustion is similar to droplet combustion, and therefore a D² model could be employed to describe the burn time. He further suggested that the ignition and combustion processes would be governed by the melting and boiling points of the metal and metal oxide. Price³ suggested two possible mechanisms for the breakdown of the aluminum oxide shell and ignition of aluminum particles. The first mechanism involves the very different melting temperature of aluminum oxide (2327 K) and pure aluminum (930 K). As a result, upon particle heating, the elemental core melts and the molten aluminum expands. This induces thermal stresses in the oxide shell, leading to cracks that expose molten aluminum to the oxidizing species. The other possibility is that the

oxide layer undergoes melting itself, which would require much higher temperatures for ignition.

More recently, Trunov et al⁴ studied the effects of phase transformations in the oxide shell upon heating. They used thermogravimetric analysis and X-ray diffraction to study the oxidation of aluminum particles with various sizes and morphologies, and found that aluminum combustion can be explained by a four stage process. During the first stage, the thickness of the initial amorphous oxide shell increases until it reaches a critical value of about 5nm. The next stage involves the transformation of the oxide layer into denser $\gamma\text{-Al}_2\text{O}_3$, exposing some of the core aluminum. In the third stage, the $\gamma\text{-Al}_2\text{O}_3$ layer grows and partially transforms into $\theta\text{-Al}_2\text{O}_3$ and $\delta\text{-Al}_2\text{O}_3$. Finally, stage four involves the transformation of the shell into stable $\alpha\text{-Al}_2\text{O}_3$. In recent work by our group on nanoaluminum, Rai et al⁵ found that aluminum melting was necessary for fast reaction, and was due to the counter diffusion of aluminum metal out rather than oxidizer to the core. This results in the formation under some conditions of a hollow alumina product. Olsen et al⁶ also showed the formation of a hollow product in combustion studies of micron-sized particles.

In boron, a different observation is made during particle heating. Similar to aluminum, a boron particle has an oxide shell (B_2O_3) which surrounds the elemental boron core. The oxide layer, however, melts at a much lower temperature (722 K) than the core (2375K), rendering a different burning scenario than aluminum. Upon heating, the oxide shell will melt before the solid core, thus leading to a diffusion-controlled process through the molten shell. The pioneering work of Macek and Semple⁷ suggested that boron combustion always happens in a two-step process, separated by a dark period.

The first step involves the removal of the oxide layer, while the second step involves the burning of a bare boron particle in air. Ulas *et al.*⁸ also support that the combustion of boron particles is defined by a two-stage process. Again, the first stage of boron combustion was considered as the removal of the oxide layer. This process is a slow, kinetic and/or diffusion controlled process, which constitutes a significant portion of the overall burning time of the particle. After removal of the oxide layer, the second stage begins with the combustion of the pure boron.

Contradicting theories about the treatment of diffusion through the molten B_2O_3 layer have been proposed, with Glassman⁹ suggesting that elemental boron dissolves into the molten B_2O_3 layer and diffuses outward to the $B_2O_3(L)/$ gas interface, while King¹⁰⁻¹³ suggested that O_2 dissolves into the molten layer and inwards to the $B/B_2O_3(L)$ interface. This argument has been more recently addressed in a review article by Yeh and Kuo¹⁴, where they report that the diffusion of boron into the molten $B_2O_3(L)$ dominates the diffusion process. They also report the formation of a polymeric vitreous $(BO)_n$ complex in the reaction between dissolved boron and molten B_2O_3 . These results were used to develop a reaction mechanism for boron combustion.

Aluminum and boron differ in their combustion mechanisms primarily due to the inherent properties of the pure material and their oxides. Based upon Glassman's Criterion¹⁵, aluminum will combust in a vapor phase in an oxygen environment since its oxide's volatilization temperature is higher than the boiling point of pure aluminum. On the other hand, boron will not combust in the vapor phase since the boiling point of pure boron is significantly higher than the volatilization temperature of its oxide. In fact, since

boron oxide melts at a much lower temperature than pure boron, it covers the particle and creates a substantial diffusive barrier between the oxidizer and pure fuel.

Despite the great potential of boron as a fuel, it has rarely achieved its potential in systems that require fast and complete combustion. Ulas *et al.*⁸ suggest there are two major reason for this; 1) the ignition of boron particles is significantly delayed due to the presence of an oxide layer on the particle surface, and 2) the energy release is during the combustion process of boron particles in hydrogen containing gases is significantly lowered due to the formation of HBO₂. Yetter¹⁶ adds to these issues the idea of an energy trap. Hydrogen containing species can accelerate the gas-phase combustion process. Unfortunately they promote the formation of HBO₂, which is thermodynamically favored over gaseous B₂O₃ as the temperature is lowered, which can result in the boron being “trapped” as HBO₂ and therefore not releasing all of its available energy. The energy trap arises from the fact that from an energetic standpoint, the best product of boron combustion is liquid boron oxide. Even in non-hydrogen containing environments, the quickest way to remove the oxide layer and combust the pure boron material is at temperatures above the B₂O₃ boiling point of 2338 K. However, combustion at these temperatures would result in the formation of B₂O₃(g) whose heat of formation is approximately one third of the liquid form. Furthermore, in early studies Macek¹⁷ showed that boron particles had burn times up to four times longer than similar sized aluminum in similar environments.

Most recently, an effort has been made to address the issue of oxide layer removal. Difluoroamino-based oxidizers have been developed, and have rejuvenated the hopes for boron combustion. With fluorine as an oxidizing agent, an increase in gas-phase combustion products can be realized; a desired effect for energetic materials. Ulas *et al.*⁸ combusted single boron particles in fluorine-containing environments by injecting particles into the post flame region of a multi-diffusion flat-flame burner. Their results show the disappearance of the apparent “two-step” combustion process in the presence of fluorine, along with decreased burning times. This is a major result for boron combustion since the removal of the oxide layer adds significantly to the overall burning time, and if

the oxide layer can be removed more efficiently, then boron might be able to be practically used in energetic formulations.

The primary work on boron particle burning has been studied with particle sizes in the micron range, and few works have investigated the use of nanoboron in composite systems. In separate works, Hunt et al.¹⁸ and Park et al.¹⁹ have shown decreasing activation energies with decreasing particle sizes, leading to increased reactivity. A lower activation energy should also imply a lower ignition temperature, and this was indeed corroborated by various authors such as Parr²⁰ and Bazyn²¹. When nanoaluminum is used in place of its micron-sized counterpart in composite systems, an increase of 1000 in the reactivity has been reported²², therefore, we wanted to investigate the performance of nanoboron in such systems. It will be demonstrated from constant-volume combustion experiments that nanoboron, while very unreactive itself, can be used to enhance the reactivity of nanoaluminum-based MICs. We develop a heat transfer model for boron particles surrounded by an aluminum thermite reaction, and propose that the aluminum reaction augments the burning of the boron by providing a high-temperature environment for fast ignition and combustion of the boron..

EXPERIMENTAL

Sample Preparation

For this work, stoichiometric samples (MICs) were prepared with the fuel being composites of boron and aluminum, and the oxidizer always being copper oxide. We will refer to the samples in terms of the molar percentage of boron in the fuel. For example, a 30%B sample means that 30% of the fuel atoms are boron, 70% are aluminum, and the corresponding amount of copper oxide is added to make the overall mixture stoichiometric assuming complete conversion to Al_2O_3 and B_2O_3 . The aluminum used was obtained from the Argonide Corporation, and designated as “50 nm ALEX” by the supplier. ALEX is a nano-sized aluminum formed from the electroexplosion of an aluminum wire²³. The nanoboron utilized in this study was termed SB99 and was obtained from the SB Boron Corporation. The average primary particle diameter is given to be 62 nm²⁴. A second boron sample designated as SB95 was also obtained from the SB Boron Corporation. SB95 is an amorphous boron powder with particles sizes ranging up to 700 nm, as measured by a Fisher Sub-Sieve Sizer (FSSS). The oxidizer was copper (II) oxide nanopowder purchased from Sigma Aldrich, and had an average primary particle diameter specified by the supplier to be <50 nm. Thermogravimetric Analysis (TGA) was performed (using a 50/50 Ar/O₂ environment and a heating rate of 5 K/min up to 1200 C) on both the aluminum and SB99 boron samples to determine the amount of elemental metal (active content or activity) in the particles. TGA showed the aluminum to be 82% active, while the SB99 boron was found to be 72% active by mass. The SB95

active content was 96%, specified by the supplier. A summary of the materials used is given below in Table 2.

MICs were prepared by first weighing out the fuel and oxidizer and adding the contents to a ceramic crucible. Approximately 10 mL of hexane was then added, and the mixture was sonicated for 20 minutes to ensure intimate mixing of the fuel and oxidizer particles. The hexane was then allowed to dry and then the samples were placed in a furnace at 100 C for a few minutes to drive off any remaining hexane. The powders were then very gently broken apart with a spatula until the consistency for each sample was that of a loose powder.

Measurement of Reactivity

The reactivity of a MIC has been shown to be closely correlated to two properties; the flame propagation velocity in open-channel burn tests, and the constant-volume pressurization rate. Both are relative measurements which are used by several authors to determine the reactivity²⁵⁻²⁸. In this work, we use the pressurization rate inside a small combustion cell as a measurement of the reactivity. A fixed mass (25 mg) of the sample powder was placed inside a constant-volume (~13 mL) pressure cell. A schematic and more details of the pressure cell can be found in a previous publication²⁹. A nichrome wire coupled to a voltage supply was placed in contact with the top of the powder, and served as an ignition source through resistive heating of the wire. A piezoelectric pressure sensor was used in series with an in-line charge amplifier and a signal conditioner, and the resultant voltage trace was captured on a digital oscilloscope upon ignition of the sample. The pressurization rate was calculated by converting the voltage

rise to pressure ($1 \text{ mV} = 0.237 \text{ psi}$), and dividing by the rise time in microseconds. This was repeated three times for each sample, and the average pressurization rate (psi/usec) was recorded.

Pressure signals of various samples are shown in Figure 1 as an example of the kind of typical data obtained for the combustion tests. We show two “slow” reactions (90% and 70% B) along with two “fast” reactions (50% and 30% B), and the reader should note that the time scale is very different. Decreasing the time scale causes a noisier signal, but is necessary in order to capture the first peak with finer time resolution. Another thing to point out in the signal is shock waves “ringing” off the walls, seen in the data as oscillatory behavior of the signal after the first peak. In all of these pressure traces, the first oscillation can be seen around 120usec after the first major peak (this is most obvious in the 70% B trace). This corresponds to the approximate time it takes for a pressure wave to reflect off the wall directly opposite the sensor. In the two “fast” pressure traces, there are some new peaks (i.e. around 50 μsec). These could be caused by some secondary burning within the system, and we should not rule this out as a possibility. However, it may also be simply an artifact of the geometry and/or ejection of the powder after the pressure wave reflects off other walls of the cell or the sample holder.

In order to extract the rise time in a consistent way, we always take the first major peak in the system (usually the maximum voltage) and apply a linear fit. We report the average of three tests, and the uncertainty is calculated from the standard deviation of the data.

Results and Discussion

Shown in Figure 2 is the pressurization rate as a function of %B in an Al / B / CuO mixture for both 62 nm and 700 nm boron, along with data from a MIC of Al / CuO for comparison. It can be seen that, when compared to pure Al / CuO, an enhancement in reactivity is achieved for the cases where nanoboron is added as the minor component of the fuel (<50% by mol). It is also clear that a MIC comprised of boron as the primary fuel is quite ineffective and considerably underperforms an aluminum-based MIC. It can also be seen that, not only is 700 nm boron less reactive than its nano-counterpart, but there is no enhancement effect when added to nanoaluminum in any amount.

Given that the data suggests that an enhancement in MIC burning occurs only when boron is the minor component, it is reasonable to speculate that the primary reaction (Al / CuO) is allowing for efficient ignition and combustion of the boron. The enhancement begins at <50% B by mol, and so we sought an explanation as to why this point was important. In order to examine this, an appropriate thermodynamic calculation is to look at the adiabatic flame temperature assuming that the aluminum reacts with the copper oxide, while the boron is acting as an inert material. The CHEETAH code (using the JCZS product library³⁰ as recommended by Sanders et al.²⁸) was used to calculate the adiabatic flame temperature for the various mixtures (assuming the boron to be inert) and the results are shown in Figure 3. From Figure 3 we see that the mixtures with <50% B can reach temperatures higher than 2350 K, which is above the boiling point of B₂O₃ (2338 K) and the melting point of B (2350 K). Given that the experiment also showed an enhancement in this regime, it suggests that the primary reaction (Al / CuO) provides the

energy necessary to remove the oxide shell and/or melt the boron, and thus enable it to participate in the combustion and enhance the reactivity. The removal of the oxide shell was discussed earlier as being necessary, while the melting of a nanoparticle can increase its reactivity significantly by allowing the fuel to become more mobile, as was seen by Rai et al.⁵ for nanoaluminum.

Shown in Figure 4 are the experimentally measured rise times, and included are the 62 nm and 700 nm boron along with the 17 μ sec rise time for the Al / CuO reaction. Clearly, addition of the smaller boron decreases the rise time below that of Al / CuO when added as the minor component, while the larger boron only slows the reaction down. The data indicates that the 62 nm boron is participating in the combustion, and so an appropriate calculation should compare the timescale of the Al / CuO reaction (17 usec) to the timescale of heating a boron particle up to the surrounding temperature so that it can combust. A heat transfer model is developed to investigate these time scales when the surrounding temperature is above 2350 K, the point where the experimental enhancement is observed.

Phenomenological Heat Transfer Model:

Here we develop a simple heat transfer model for a boron particle in a high temperature (>2350 K) environment. Several assumptions are made to simplify the problem:

- 1) The Al and CuO particles are evenly distributed about single boron particles.

- 2) The B_2O_3 shell thickness is 3.1 nm and 4.5 nm for the 62 nm and 700 nm particles, respectively. This is calculated by using the particle size, active content by mass, and bulk densities of B and B_2O_3 (2.34 g/cm^3 and 2.46 g/cm^3 , respectively).
- 3) The convective term only considers energy transferred through collisions with gas molecules.
- 4) Interparticle radiation was found to make little difference to the model results, and thus was not included.

With the above assumptions in place, heat is convectively transferred to the particle by the gaseous species present during the Al / CuO reaction. The convection term can be written as the product of the heat transfer coefficient, h , the particle surface area, and the temperature difference between the surrounding environment and the particle.

$$\dot{q}_{conv} = h \cdot A \cdot (T - T_p) \quad (1)$$

The heat transfer coefficient for a solid sphere in a gaseous environment can be written in terms of the particle Nusselt number, Nu , the thermal conductivity of the gas, k_G , and the particle diameter as:

$$h = \frac{Nu \cdot k_G}{d_p} \quad (2)$$

For particles with diameters much greater than the mean free path of the gas, the Nusselt number approaches a constant value of 2. However, the particle sizes in this work are comparable to the mean free path, and thus are in a transitional regime between continuum and free-molecular heat transfer. In this regime, the Nusselt number is a function of the particle Knudsen number³¹. The adiabatic flame temperature and the experimental peak to peak pressure rise, shown in Figure 5, are used to estimate the mean

free path, and thus the particle Knudsen numbers. The corresponding Nusselt numbers are then obtained from Figure 4 in Fillippov et al.³¹, and a polynomial fit is applied to write the Nusselt number as a function of temperature for the range of adiabatic flame temperatures achieved in the mixtures. This gives a range of Nusselt numbers from 0.06 to 0.13 for the 62 nm boron, and 0.34 to 0.54 for the 700 nm boron.

The thermal conductivity also changes as a function of the gas temperature and composition. The CHEETAH calculations (assuming B to be inert) were used to obtain the equilibrium species distribution. Since only nitrogen, oxygen and copper are in the product vapor an effective thermal conductivity is obtained as a molar average. For oxygen and nitrogen, the thermal conductivity as a function of temperature is given in Incropera and DeWitt³² up to 3000 K, and we extrapolate it to 3500 K. For copper, the thermal conductivity can be estimated as a function of temperature using kinetic theory for a monatomic gas in terms of the atomic mass (m) and diameter (σ):

$$k(T) = \left(\frac{k_B \cdot T}{\pi^3 \cdot m \cdot \sigma^4} \right)^{1/2}$$

(3)

The convection term has now been completely formulated as a function of temperature and particle properties. To calculate the total heating time, we calculate three individual processes.

- 1) Sensible heating from room temperature to the surrounding temperature (Eq 5)
- 2) Time to evaporate the initial B_2O_3 shell (constant $T_p = 2338$ K) (Eq 6)
- 3) Time to melt the boron (constant $T_p = 2350$ K) (Eq 7)

(Note: The time to melt the B_2O_3 shell is insignificant).

We have included radiation heat loss by assuming the boron particles transfer energy to the pressure cell wall at 300 K (T_{wall}). Here, ε is the emissivity of B_2O_3 (assumed to be 1), σ_B is the Stefan-Boltzmann constant, and A is the particle surface area.

$$\dot{q}_{\text{Rad}} = \varepsilon \cdot \sigma_B \cdot A \cdot (T_P^4 - T_{\text{Wall}}^4) \quad (4)$$

The individual heating times for the above three cases can be obtained by integration of Equations 5-7, respectively:

$$\frac{dT_P}{dt} = \frac{(\dot{q}_{\text{conv}} - \dot{q}_{\text{Rad}})}{m \cdot C_p} \quad (5)$$

$$\frac{dm}{dt} = \frac{(\dot{q}_{\text{conv}} - \dot{q}_{\text{Rad}})}{H_{\text{Vap}, \text{B}_2\text{O}_3}} \quad (6)$$

$$\frac{dm}{dt} = \frac{(\dot{q}_{\text{conv}} - \dot{q}_{\text{Rad}})}{H_{\text{Fus}, \text{B}}} \quad (7)$$

Here T_P is the particle temperature, m is the particle mass, C_p is the heat capacity, $H_{\text{Vap}, \text{B}_2\text{O}_3}$ is the latent heat of vaporization of B_2O_3 at 2338 K (5.19 MJ/kg), and $H_{\text{Fus}, \text{B}}$ is the latent heat of fusion for boron at 2350 K (4.64 MJ/kg). The heat capacity used was weighted (since both B and B_2O_3 are present in the particle), and was calculated as a function of particle temperature using the Shomate approximation of the coefficients in the NIST-JANAF thermochemical tables³³. Equations 5-7 were numerically integrated, and the results of the model are shown for 62 nm boron and 700 nm boron in Figures 6 and 7, respectively. The calculations indicate that the total time to heat the 62 nm boron

up to the surrounding temperature is faster than 17 usec, the Al / CuO time scale, at temperatures above 2370 K while for the 700 nm boron, the time always lags and does not become faster until the surrounding temperature is above 2800 K. It also is evident that the removal of the oxide shell alone cannot explain why 700 nm boron does not enhance the reactivity, since it is removed almost as quickly as in the case of 62 nm boron. However, we see that the sensible heating time for the micronboron is significantly longer than for the nanoboron, and we also see that the time required to melt the micron boron is over an order of magnitude longer than for the nanoboron. Thus, from the experimental and model results, it's reasonable to conclude that for boron to enhance the reactivity, the particles must be heated, have their oxide shell removed, and be melted on a timescale shorter than that for the thermite reaction in order to participate in the combustion and enhance the reactivity.

Boron's ability to enhance the reactivity is most likely due to the increased gas production when boron is present as a fuel. If the boron is able to participate in the combustion, it should oxidize to gaseous B_2O_3 , along with sub-oxides such as BO and BO_2 . As a result, the absolute pressure rise could be higher than that observed for Al / CuO, where the temperature is below the Al_2O_3 boiling point and thus the oxide product is molten. To investigate this, CHEETAH calculations were again performed, but now the boron was assumed to be reactive. The adiabatic temperature and gas species distribution as a function of %B are shown in Figure 8, and the formation of a significant amount of boron oxide species (BO , BO_2 , B_2O_3) in the products can be seen. The calculation predicts the total gas production to increase relative to an Al / CuO mixture,

where copper is the only major gas product. The increase in gaseous products increases the total pressure, and this was consistent with the experimental data (Figure 5).

Not only does gas production affect the pressure rise, it can also affect the rise time. This is because the mode of energy propagation through a loose powder MIC is speculated to be primarily via convection of gaseous intermediate species³⁴. Other experimental works²⁸ show a correlation between the peak reactivity and the peak gas production, but this does not necessarily correspond to the maximum temperature. In this work, the pressure rise time does become faster (see Figure 4) for the cases where the enhancement was seen. This is likely a result of the increased gas production aiding in the convective energy propagation through the loose powder.

A major assumption in our model was that the convective heat transfer to the particle only happened through collisions with gaseous species. However, additionally there could be condensation of intermediate gaseous species, such as copper, onto the particles. This heat of condensation would enhance the heat transfer to the particles, and decrease the time to heat the boron even further than predicted by the model. However, a layer of condensed material on the particles would serve as a barrier to oxidation much like the B₂O₃ does if it is not removed. The complexities of that effect are beyond the scope of this investigation.

CONCLUSIONS

It has been demonstrated from constant-volume combustion studies that the addition of nanoboron to a MIC of Al / CuO can enhance the reactivity when the boron is

<50 mol% of the fuel, while an enhancement was not observed when micronboron was used instead. Thermodynamic calculations assuming the boron to be inert showed that the aluminum reaction with CuO was able to raise the mixture temperature above 2350 K, above the boiling point of B₂O₃ and melting point of boron. This led to the development of a phenomenological heat transfer model which investigated the sensible and latent heating time for boron particles surrounded by a high-temperature environment. The model shows the heating time becomes faster than the Al / CuO reaction time, 17 usec, at temperatures above 2370 K for the nanoboron and above 2800 K for the larger boron. The heating time for the micronboron severely lags because of the very large time to melt the boron. From the experimental and model results, we speculate that not only is the sensible heating and removal of the oxide shell necessary for fast reaction, the melting of the boron is also critical.

1. T. A. Brzustowski; I. Glassman, **1964**, (IAA Accession No. A65-10970), 33 pp.
2. I. Glassman, *Metal Combustion Process*. American Rocket Society Preprint: New York, 1959.
3. E. W. Price, *Combustion of Metallized Propellants*. Progress in Astronautics and Aeronautics: 1983; Vol. AIAA 90.
4. M. A. Trunov; M. Schoenitz; X. Zhu; E. L. Dreizin, *Combustion and Flame* **2005**, 140, (4), 310-318.
5. A. Rai; K. Park; L. Zhou; M. R. Zachariah, *Combustion Theory and Modelling* **2006**, 10, (5), 843-859.
6. S. E. Olsen; M. W. Beckstead, *Journal of Propulsion and Power* **1996**, 12, (4), 662-671.
7. A. Macek; J. M. Semple, *Combustion Science and Technology* **1969**, 1, (3), 181-91.
8. A. Ulas; K. K. Kuo; C. Gotzmer, *Combustion and Flame* **2001**, 127, (1/2), 1935-1957.
9. I. Glassman, Williams, F.A. and P. Antaki in: The Combustion Institute, Pittsburgh, PA, 1984; Pittsburgh, PA, 1984.
10. M. K. King in: *CPIA Publication 529*, 26th JANNAF Combustion Meeting, 1989; 1989.

11. M. K. King in: *CPIA Publication 366*, 19th JANNAF Combustion Meeting, 1982; 1982.
12. M. K. King, *Combustion Science and Technology* **1974**, 8, (5-6), 255-73.
13. M. K. King, *Combustion Science and Technology* **1972**, 5, (4), 155-64.
14. C. L. Yeh; K. K. Kuo, *Progress in Energy and Combustion Science* **1997**, 22, (6), 511-541.
15. I. Glassman, *Combustion*. 3rd ed.; Academic Press: San Diego, CA, 1996.
16. R. A. Yetter; H. Rabitz; F. L. Dryer; R. C. Brown; C. E. Kolb, *Combustion and Flame* **1991**, 83, (1-2), 43-62.
17. A. Macek; J. M. Semple, *Symp. (Int.) Combust., [Proc.]*, **13th 1971**, 859-68.
18. E. M. Hunt; M. L. Pantoya, *Journal of Applied Physics* **2005**, 98, (3), 034909/1-034909/8.
19. K. Park; D. Lee; A. Rai; D. Mukherjee; M. R. Zachariah, *Journal of Physical Chemistry B* **2005**, 109, (15), 7290-7299.
20. T. Parr; C. Johnson; D. Hanson-Parr; K. Higa; K. Wilson in: JANNAF Combustion Subcommittee Meeting, December, 2003; 2003.
21. T. Bazyn; H. Krier; N. Glumac, *Combustion and Flame* **2006**, 145, (4), 703-713.
22. C. E. Aumann; G. L. Skofronick; J. A. Martin, *Journal of Vacuum Science & Technology, B: Microelectronics and Nanometer Structures* **1995**, 13, (3), 1178-83.
23. J. Katz, Tepper, F., Ivanov, G.V., Lerner, M.I. and V. Davidovich in: *CPIA Publication 675*, JANNAF Propulsion Meeting, 1998; 1998.
24. Y. Yang; S. Wang; Z. Sun; D. D. Dlott, *Propellants, Explosives, Pyrotechnics* **2005**, 30, (3), 171-177.
25. S. F. Son; J. R. Busse; B. W. Asay; P. D. Peterson; J. T. Mang; B. Bockmon; M. L. Pantoya, *Proceedings of the International Pyrotechnics Seminar* **2002**, 29th, 203-212.
26. B. S. Bockmon; M. L. Pantoya; S. F. Son; B. W. Asay; J. T. Mang, *Journal of Applied Physics* **2005**, 98, (6), 064903/1-064903/7.
27. J. Y. Malchi; T. J. Foley; S. F. Son; R. A. Yetter, *Combustion, Science, and Technology* **2007**.
28. V. E. Sanders; B. W. Asay; T. J. Foley; B. C. Tappan; A. N. Pacheco; S. F. Son, *Journal of Propulsion and Power* **2007**, 23, (4), 707-714.
29. A. Prakash; A. V. McCormick; M. R. Zachariah, *Advanced Materials (Weinheim, Germany)* **2005**, 17, (7), 900-903.

30. M. L. Hobbs; M. R. Baer; B. C. McGee, *Propellants, Explosives, Pyrotechnics* **1999**, 24, (5), 269-279.
31. A. V. Filippov; D. E. Rosner, *International Journal of Heat and Mass Transfer* **1999**, 43, (1), 127-138.
32. F. P. Incropera; D. P. DeWitt, *Fundamentals of Heat and Mass Transfer*. 3rd ed.; John Wiley and Sons, Inc.: 1990.
33. M. W. Chase, Jr., *J. Phys. Chem. Ref. Data Monograph 9* **1998**, 1-1951.
34. B. W. Asay; S. F. Son; J. R. Busse; D. M. Oschwald, *AIP Conference Proceedings* **2004**, 706, (Pt. 2, Shock Compression of Condensed Matter--2003, Part 2), 827-830.

TABLE I. Heating values per mass and volume for various metals.

Metal	ΔH per unit Mass (Kcal/g)	ΔH per unit Volume (Kcal/cc)
Boron	-14.12	-33.19
Beryllium	-15.88	-29.38
Aluminum	-7.41	-20.01
Titanium	-4.71	-21.20
Vanadium	-3.64	-21.69
Magnesium	-5.91	-10.28
Nickel	-0.98	-8.72

TABLE II. A summary of nanopowders used in this work, including average primary particle diameter and active amount by mass.

Fuel	Source	Avg primary particle diameter	Measured by	Active Content	Measured by
Al	ALEX	50 nm	TEM Reference	82%	TGA
B	SB-99	62 nm	23	72%	TGA
B	SB-95	700 nm	FSSS	96%	Supplier
Oxidize					

r			
CuO	Sigma-Aldrich	<50 nm	Sigma-Aldrich

List of Captions for Figures

Figure 1: From top to bottom: Pressure traces for 90%(slowest), 70%, 50%, and 30%(fastest) B.

Figure 2: Experimental pressurization rate as a function of %Boron in an Al / B / CuO MIC for both nano and micron-sized boron. The horizontal line is Al / CuO data, included for comparison. Error bars represent the standard deviation of the experimental data.

Figure 3: Adiabatic flame temperature calculations for Al / B / CuO mixture. B is considered inert in these calculations. Boiling temperature of $B_2O_3 = 2338$ K.

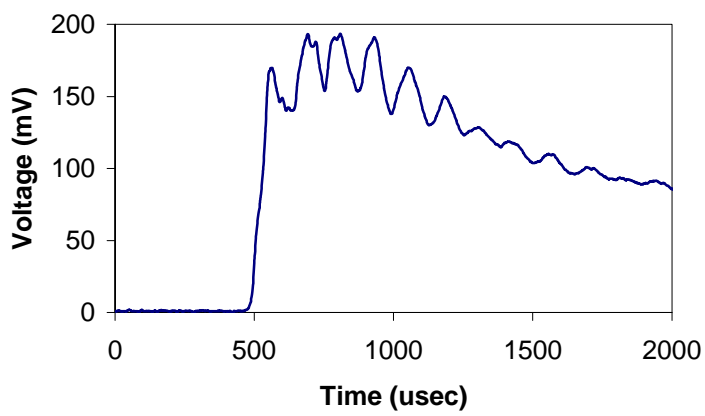
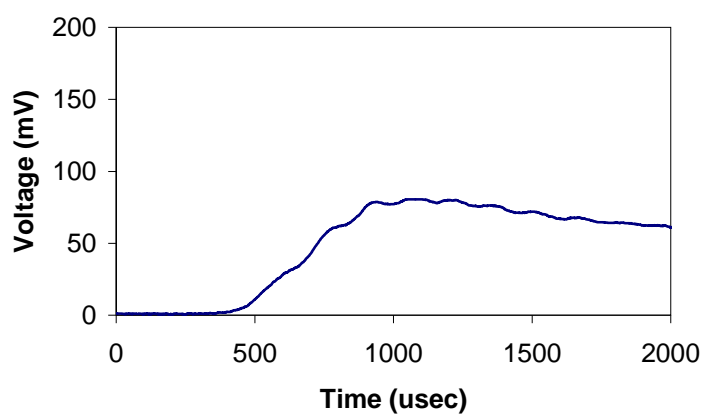
Figure 4: Experimental rise times as a function of %B in an Al / B / CuO MIC for both nano and micron-sized boron. The horizontal line is Al / CuO data, included for comparison. Error bars represent the standard deviation of the experimental data.

Figure 5: Experimentally measured pressure rise in the region where an enhanced reactivity is observed (<50% B by mol).

Figure 6: Model predictions of the timescales as a function of surrounding temperature for a 700 nm boron particle.

Figure 7: Model predictions of the timescales as a function of surrounding temperature for a 700 nm boron particle.

Figure 8: Adiabatic temperature and equilibrium gas species composition assuming boron to be reactive.



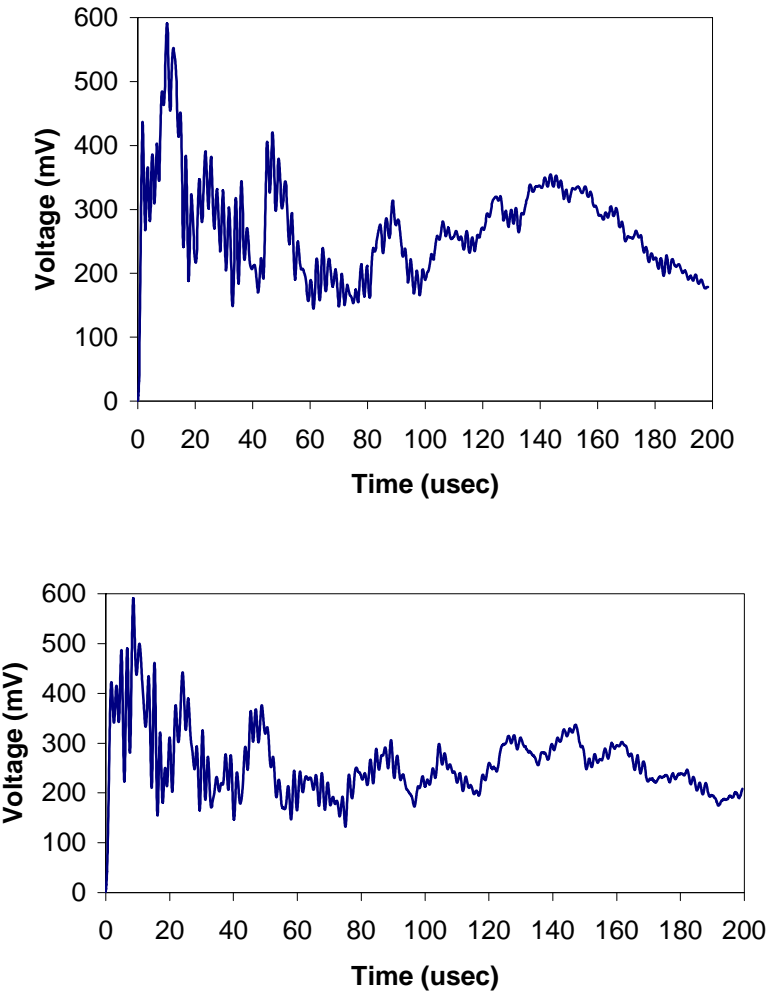


Figure 1: From top to bottom: Pressure traces for 90%(slowest), 70%, 50%, and 30%(fastest) B.

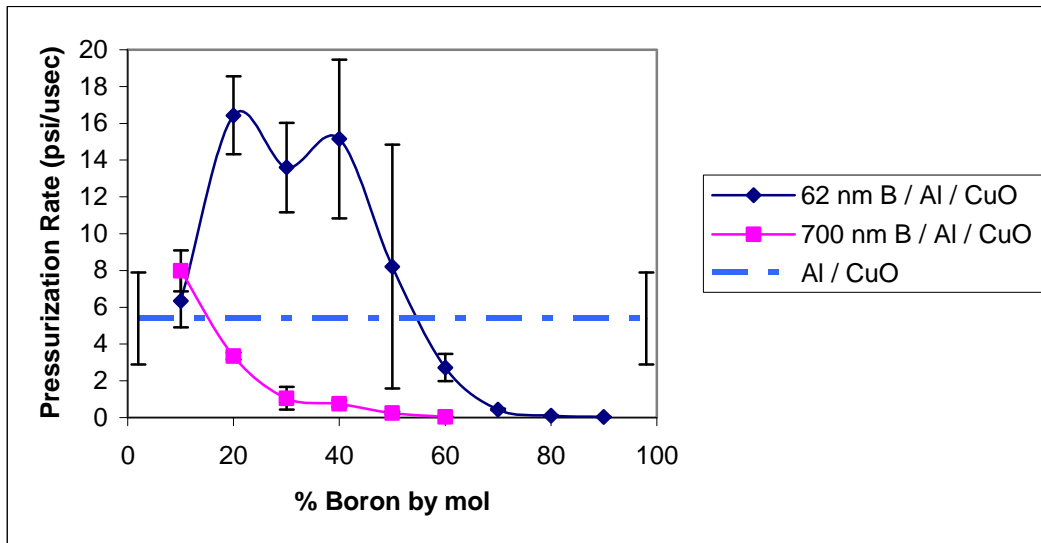


Figure 2: Experimental pressurization rate as a function of %Boron in an Al / B / CuO MIC for both nano and micron-sized boron. The horizontal line is Al / CuO data, included for comparison. Error bars represent the standard deviation of the experimental data.

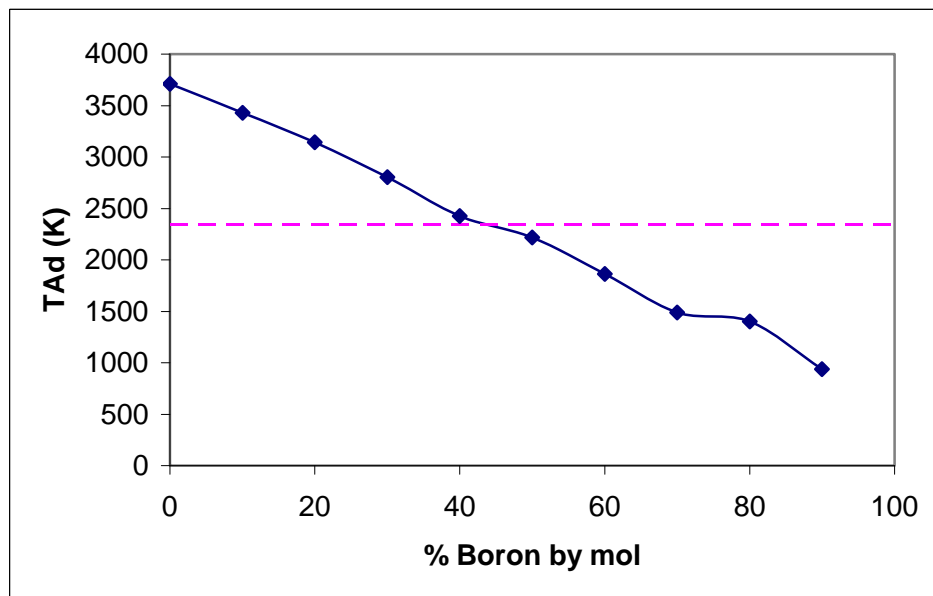


Figure 3: Adiabatic flame temperature calculations for Al / B / CuO mixture. B is considered inert in these calculations. The dotted line is 2350 K, the melting temperature of boron and above the boiling point of B_2O_3 .

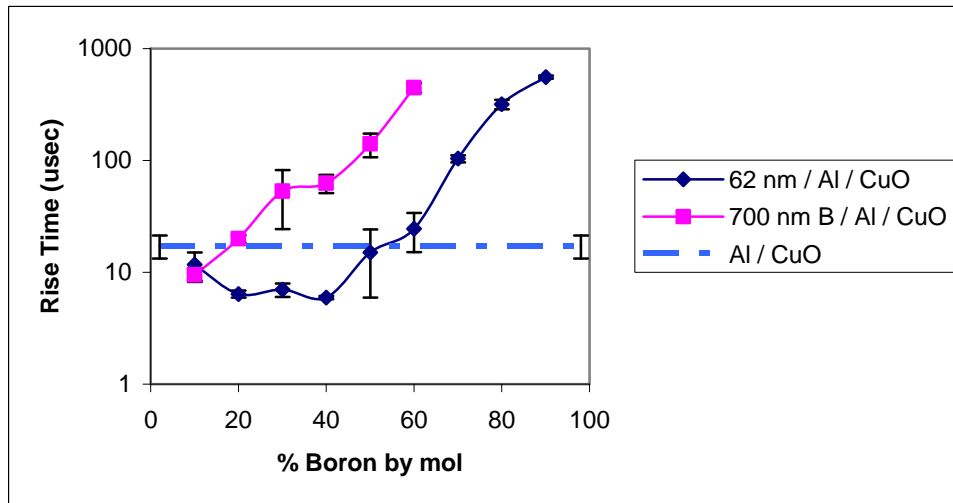


Figure 4: Experimental rise times as a function of %B in an Al / B / CuO MIC for both nano and micron-sized boron. The horizontal line is Al / CuO data, included for comparison. Error bars represent the standard deviation of the experimental data.

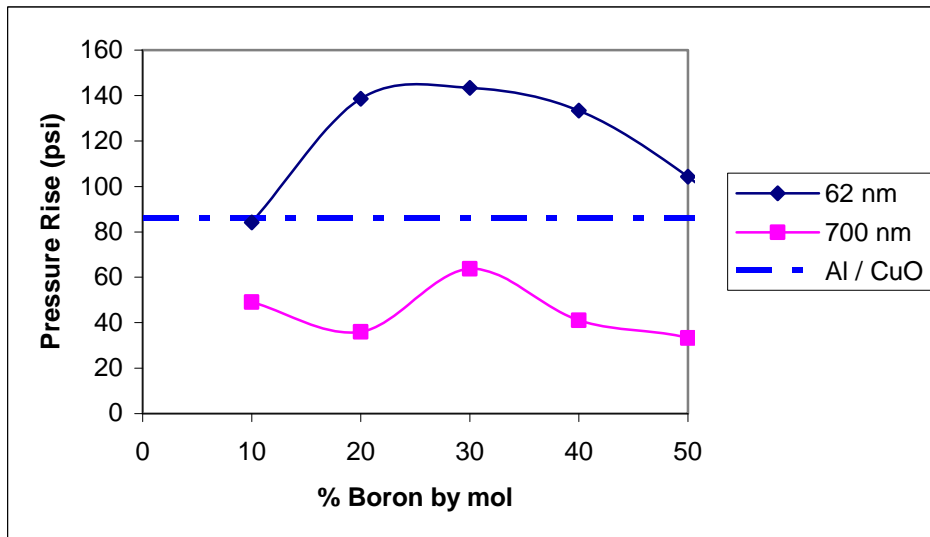


Figure 5: Experimentally measured pressure rise in the region where an enhanced reactivity is observed (<50% B by mol).

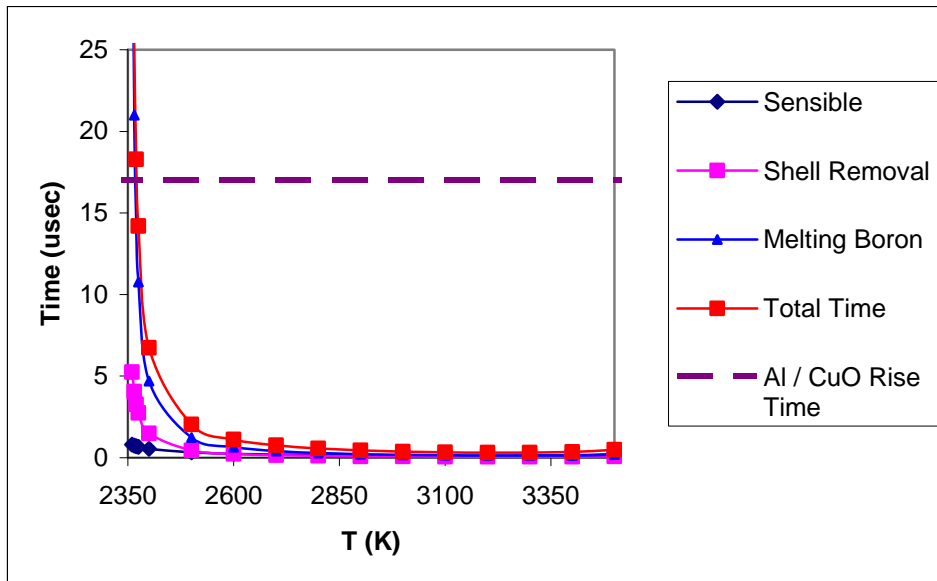


Figure 6: Model predictions of the timescales as a function of surrounding temperature for a 62 nm boron particle.

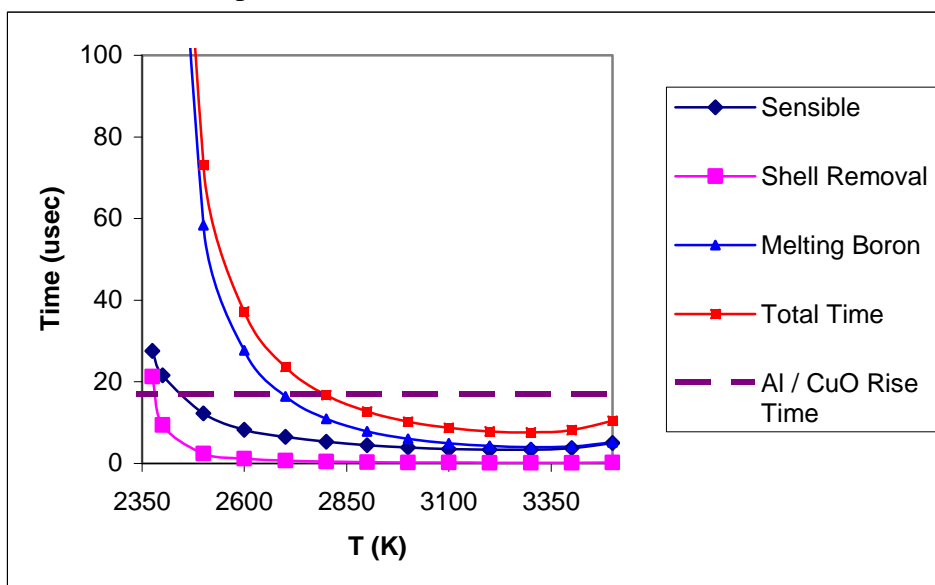
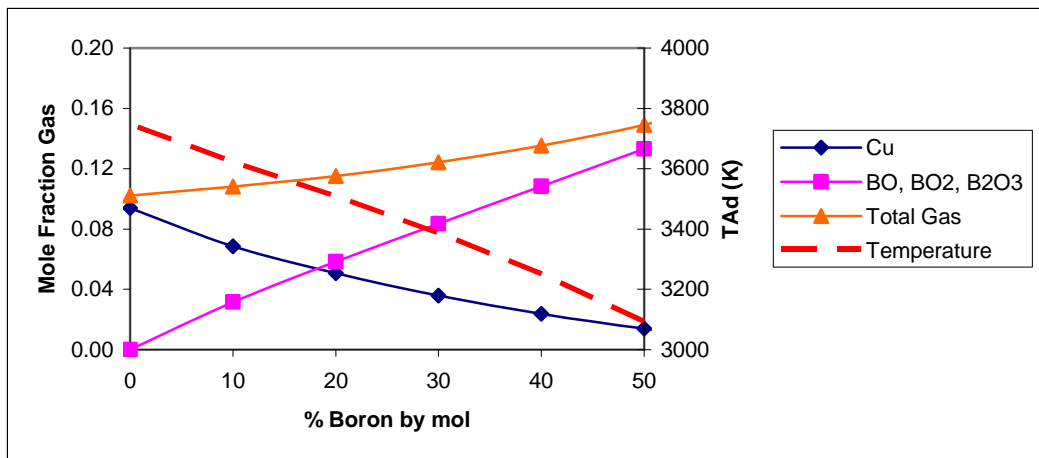


Figure 7: Model predictions of the timescales as a function of surrounding temperature for a 700 nm boron particle.



Figure

8: Adiabatic temperature and equilibrium gas species composition assuming boron to be reactive.

Combustion Characteristics of Boron Nanoparticles

ABSTRACT

An experimental investigation of the combustion characteristics of boron nanoparticles in the post flame region of a flat flame burner has been conducted. Boron is attractive as a fuel or a fuel supplement in propellants and explosives due to its high heats of combustion on both a gravimetric and volumetric basis. A relatively large database exists for combustion characteristics of large (greater than 1 μm) boron particles, but very little exists for nano-sized boron. Ignition and combustion characteristics have been studied in the post flame region of a fuel lean $\text{CH}_4/\text{Air}/\text{O}_2$ flame, with burner temperatures ranging from about 1600 K to 1900 K, and oxygen mole fractions ranging between 0.1 and 0.3. As in earlier investigations on boron combustion, a two-stage combustion phenomenon was observed. Ensemble-averaged burning times of boron nanoparticles were obtained, while the ignition time measurements for boron nanoparticles were extended into a lower temperature range previously unavailable in the literature. The measured burning times were between 1.5 msec and 3.0 msec depending on both the temperature and oxygen mole fraction. The ignition times were relatively insensitive to oxygen concentration in the range studied, and were affected only by temperature. The measured ignition times were inversely related to the temperature, ranging from 1.5 msec at 1810 K to 6.0 msec at 1580 K. The burning time results were compared to both diffusion and kinetic limited theories of particle combustion. It was found that the size dependence on particle burning times did not follow either theory.

INTRODUCTION

Metal additives are common in solid rocket propellants and explosives due to their ability to increase energy density. In particular boron has been studied for many years because it has the highest volumetric heating value of any element. Although Boron exhibits exceptional performance characteristics, it has rarely achieved its potential in propulsion systems. Ulas and Kuo[1] suggest there are two major reason for this; 1) the ignition of boron particles is significantly delayed due to the presence of an oxide layer on the particle surface, and 2) the energy release during the combustion process of boron particles in hydrogen containing gases is significantly lowered due to the formation of HBO_2 . Early studies on boron particle combustion by Macek[2-4] describe a two-stage combustion process. The first stage is associated with particle burning while the particle is still coated with an oxide layer. As the particle heats up to above the B_2O_3 boiling point and the oxide layer is completely removed by evaporation, the second stage of boron combustion begins. Since pure boron has relatively high melting and boiling temperatures, 2350 K and 4139 K respectively, the initial reactions in the consumption of the boron particle involve heterogeneous reactions between the gas phase oxidizer and solid or liquid phase boron. The second stage is essentially the standard combustion of the bare boron particle. Therefore, the removal of the liquid oxide layer plays an important role in the ignition and combustion of boron[5]. Numerous studies[2,6,7] involving micron-sized

and larger boron identified a critical ignition temperature ranging between about 1500 K and 1950 K in oxygenated environments. Dreizen[8] suggests that the ignition event at these temperatures could be associated with polymorphic phase transitions of the boron particle.

Several studies[9,10,11] found that the presence of water vapor greatly enhanced boron oxide gasification rates. In addition, hydrogen-containing species can accelerate the gas-phase combustion process[12]. Unfortunately the presence of water vapor promotes the formation of HBO_2 , which is thermodynamically favored over gaseous B_2O_3 as the temperature is lowered. This results in the boron being “trapped” as HBO_2 and therefore not releasing all of its energy. This “energy trap” arises from the fact that from an energetic standpoint, the best product of boron combustion is liquid phase $\text{B}_2\text{O}_3(\text{l})$.

Introduction

Yeh and Kuo[5] showed that when the combustion process is limited by diffusion, the combustion rate is governed by a D^2 -law, while the combustion rate is governed by a D^l -law when the combustion process is limited by kinetics. They suggest that the dominant mechanism can be determined by evaluation of the Damkohler number, and that large particles at high pressures experience diffusion controlled combustion, while small particles at low pressures are limited by kinetic controlled combustion.

Because of its great potential, boron has been the subject of many studies spanning many years. The vast majority of studies however were conducted with particles larger than 1 μm . Only a limited amount of data exists for studies involving nano-sized boron. Several studies[13,14,15,16] have been conducted on nano-sized aluminum, and even in bulk sample testing the material behaves differently than that of its micron-sized analog. Through thermal gravimetric analysis (TGA), Mench[13] found that aluminum

nanoparticles react at lower temperatures than micron-sized particles. In single particle testing Park[14] also demonstrated that the reactivity of the particles increased with decreasing particle size. Parr[15] demonstrated that for some types of nano-aluminum the critical ignition temperature could be decreased significantly compared to larger particles. These parameters have not been studied thoroughly for nano-sized boron. If boron nanoparticles exhibit similar characteristics to nanoaluminum, i.e reduced ignition temperatures, increased particle reactivity, and reduced combustion times, perhaps it would provide hope that the limitations imposed by HOBO formation can be overcome in time limited systems, and the full potential of boron could be realized in propellants and explosives.

EXPERIMENTAL APPROACH

Flat Flame Burner

A commercially available McKenna Flat Flame Burner using a mixture of methane/air/oxygen was used to provide a test bed for determining critical parameters in the ignition and combustion processes of boron nanoparticles. Since the burner was water cooled, it provided repeatable and stable premixed laminar flames for long durations. In each case a fuel lean mixture was used. Therefore, the products of combustion in the burner post flame region were used in order to provide an environment for particle combustion. The particles were placed in distilled water to create a solution of 1 weight percent of boron. A home-built sonicating atomizer was used to generate droplets of the solution by means of a vibrating film. The droplets were carried away by compressed air in the form of an aerosol. The aerosol was then passed through a series of silica gel dryers to remove all water, leaving only boron particles in the aerosol. Finally, the aerosol was injected in the transverse direction across the flame zone as depicted in figure 1. The particles were injected 5 mm above the burner surface. Figure 2 shows a schematic diagram of the entire test set up.

Particle Image Velocimetry (PIV)

In earlier studies[1,2,5] of boron particle combustion using the post flame region of a flat flame burner to provide the environment for particle combustion the particles were injected in the direction of the burner flow and generally assumed to travel at the flame velocity. In this study the particles were injected perpendicular to the burner flow, such that they would traverse the diameter of the burner. Since the particles were injected perpendicular to the burner flow, it was very important to have detailed knowledge of the particle velocity in order to provide reasonable estimates of ignition and burning times. Therefore, a series of PIV experiments were employed to provide the velocity profiles of the particles after injection into the post flame region of the burner. All of the PIV experiments were conducted in “cold flow”, i.e. non-reacting. However, wide ranges of momentum flux ratios were covered, such that the momentum flux ratios in the reacting flow were matched.

In order to minimize changes in the experimental set-up, the silica gel dryers were removed and the water droplets created by the atomizer were used as the lone seed particles. The droplets averaged $\sim 5 \mu\text{m}$ in size. An important parameter to consider when choosing seed particles for PIV experiments is the Stokes Number, which provides a measure of how well a particle follows the flow. By definition, the Stokes Number is the ratio of the characteristic particle stopping distance (Eq. 1) or time and a characteristic fluid length scale or time. In this case, the characteristic fluid length was taken as the jet core length, which was six times the inner diameter of the injection tube. By this definition, the Stokes Number in these experiments ranged from 0.16 – 0.31. Since the Stokes number was less than unity in each case the droplets were considered suitable seed particles for the experiment.

$$S_{particle} = \frac{\rho_p D^2 U}{18\mu}$$

Eq. 1

By matching the momentum flux ratios we have ensured that the fluid in the jet will follow the same trajectory in both the hot and cold flow. A small Stokes number ensures that the particles will follow the carrier gases very closely. Considering the current experiment and a conservative estimate of 1000 nm for our largest boron particle size, in a worst case scenario the particles have a Stokes number of 0.02. Therefore, we can be assured that not only are the water droplets suitable seed particles for the PIV

experiments, but our boron particles were also subjected to the same momentum flux ratio and were able to follow the carrier gas just as well as the water droplets.

For the experiments an LA Vision PIV set up was employed. This includes an ND:Yag Laser and an ICCD camera. The laser sheet was passed through the injector flow and the camera was placed perpendicular to the laser sheet. For data processing, the standard PIV sum of correlation was used. In total three different injection flow rates were studied under 12 different burner crossflows. Figure 3 shows an example of a collected image pair. For each test condition, 50 images were collected and processed to determine the velocity vectors, an example of which can be seen in figure 4. Since the data collection for this study results in spatial locations of the boron combustion process, only the axial-component of velocity was important in later data analysis. Figure 5 shows the averaged axial-component of velocity for the selected injection flow rate under the highest crossflow condition used in this experiment. The centerline velocity was extracted from all of the experiments and plotted in Figure 6, which shows that under these conditions, the crossflow does not significantly affect the centerline velocity. The location of the centerline does change, but the magnitude of the centerline velocity at a given axial location does not vary by significant amounts with changing crossflow.

An analytical expression to describe the centerline axial component of velocity can be derived based upon a laminar jet exhausting into a quiescent atmosphere. The expression is seen in equation 2. Using this expression for guidance, a correlation was extracted to provide one velocity profile for all crossflows in subsequent data analysis. Therefore the centerline velocity may be represented by a piecewise function. For the first 6 mm from the injection location, the velocity is a constant determined by taking the average of all of the maximum velocities collected for a given injection flow rate. After 6 mm the correlation is used to represent the velocity of the particles. This piecewise function is illustrated in figure 6.

$$u_{x,CL} (m/s) = [a * u_e^2] * x^b$$

Eq. 2

The solution for a jet exhausting into a quiescent atmosphere has an exponent, b , equal to -1. The results obtained here in a moderate crossflow, show a spatial dependence $u_{x,CL} \sim x^{-1.11}$, which is relatively consistent with the quiescent atmosphere solution.

Particle Characterization

SB99 boron particles were obtained from the SB Boron Corporation and used in all of the combustor testing during this study. As previously mentioned, most boron particles contain some oxide layer on the outside of the particles. When nanoparticles are considered, even a small oxide layer may be a significant portion of the total mass/volume of the particle. This layer not only impedes combustion, but also essentially removes the available energy from a given particle. In order to estimate how much of the boron particle is occupied by the oxide layer; a thermal gravimetric analysis (TGA) was performed. The TGA was conducted in a 50% Oxygen/50% Argon environment with a heating rate of 5 °C per minute. Essentially, the assumption is that the available boron undergoes complete oxidation since it is in an oxygen environment. Therefore the mass added to the sample during oxidation is exclusively the result of oxygen reacting with the boron[17]. Knowing the stoichiometric ratio and the mass gained during the test, one can deduce the amount of active boron in the sample. From the TGA results, the elemental boron content in the SB99 particles was found to be 72.2% by mass.

Reference 18 suggests that the primary particle size of the SB99 particles is 62 nm[18]. In this study however, the particles tended to be quite agglomerated. The particles were added to distilled water to create a solution for atomization. In order to understand the size distribution of the particles as they were injected into the post flame region, two different measurements were made. The first measurement, while not entirely quantitative allowed for visualization of the condition of the particles as they entered the burner and was made by Transmission Electron Microscopy (TEM). The particles were collected at the end of the injection system, as they would be when injected into the post flame region during the actual experiment. Figure 7 is a representative TEM image. As was mentioned earlier, the image reveals that the particles that were injected are in fact agglomerations of smaller primary particles. In general the agglomerations we observed through TEM were approximately 200 nm in size.

The second measurement to understand the size distribution utilized a commercial Differential Mobility Analyzer (DMA)[19] purchased from TSI inc. This device serves to construct a size distribution in a polydisperse aerosol by electrostatically separating particles by mobility size and then recording the concentration by means of a Condensation Particle Counter (CPC). This method allows for a very sensitive (< 1nm resolution) online sampling of an aerosol. The boron particles were redirected at the injection location for sampling and figure 8 shows the size distribution determined by the DMA. The results indicate that the mean mobility diameter of the “particles” was approximately 200 nm. In other words, the “particles” behaved aerodynamically as a spherical particle of 200 nm in diameter. Unfortunately, the range of the DMA truncated the measurement to less than 500 nm. According to Friedlander[20], aerosol size distributions often have large standard deviations caused by a long upper “tail” for particles larger than the peak in the distribution. Such distributions can be represented approximately by the lognormal distribution function:

$$n_d(D_p) = \frac{N_\infty}{(2\pi)^{1/2} D_p \ln \sigma_g} \exp\left[-\frac{(\ln D_p - \ln d_{pg})^2}{2 \ln^2 \sigma_g}\right]$$

Eq. 3

Where N_∞ refers to the total concentration of particles at a given point and time, d_{pg} refers to the geometric mean diameter, and σ_g refers to the geometric standard deviation. Equation 3 was used fit to the data collected by the DMA and used to extrapolate the aerosol properties during data processing. The curve fit can be seen in Figure 8 along with the original DMA data.

Test Conditions

A mixture of Methane/Air/Oxygen created the environment used to study the ignition and combustion characteristics of the SB99 nanoparticles. B-type (Platinum/Rhodium) thermocouples were used to measure the temperature of the flat flame burner under steady state conditions. Measurements were made at three locations, $x = 10, 30, 50$ mm, from the injection source 5 mm above the burner surface. The measurements were corrected for radiation loss. The method for correction is the same as explained in reference 21. After correction, the three measurements were averaged together for data analysis purposes. The test matrix for this study as well as the results of the temperature measurements can be seen in Table 1. The measured temperatures were considerably below the adiabatic flame temperatures for a given condition. This is primarily a result of significant heat loss to the water-cooled burner. Under the conditions considered in this study, the burner temperature was fairly insensitive to equivalence ratio; rather the temperature was driven by fuel flow rate. A similar finding was observed using this burner in references 22 and 23. The product mole fractions listed in Table 1 represent the nominal values based upon complete combustion of the fuel.

RESULTS AND DISCUSSION

Ignition and Combustion Time Results

A Cooke Dicam Pro Intensified CCD camera (ICCD) with a minimum shutter speed of 1 ms and typical framing rates around 11 Hz was used to visualize the combustion properties of the SB99 particles. Similar to previous observations, when appropriate temperature and or burner product composition requirements were met, a two-stage combustion phenomenon was observed, which is consistent with observations from other researchers[2,24]. Initially,

as the particles were injected into the post flame region, there was no visible phenomenon occurring. Further downstream, a yellowish/orange region appeared for some duration and if appropriate burner conditions were met, the yellowish region was followed by an abrupt change to a bright white glow region. Li and Williams[24] concluded that the yellow region can be considered the ignition region, or first stage of boron combustion, culminating in complete removal of the oxide layer, while the white glow region signified full fledged combustion, or the second stage of boron combustion.

In order to extract usable data from the observed phenomenon, two sets of images were taken for each test condition; the first image was an unfiltered image, while the second utilized a narrow-band interference filter, centered at 546 ± 2 nm and had a full width half maximum (FWHM) value of 10 nm. In each case 50 images were collected and averaged together for data analysis. In addition, background images were taken, i.e. no particles flowing, and were subtracted from the original averaged images to remove any background emission associated with hydrocarbon combustion. Typically though, no emission of any significance was detected during the collection of the background images for the camera settings that we employed. 546 nm corresponds to a band of emission for the BO_2 molecule, which is a reactive intermediary gas-phase species, formed throughout boron particle ignition and combustion[25]. Li and Williams[26] examined the two-stage combustion behavior of boron particles spectrally. In this study they describe a yellow region, which they attributed to ignition, and a bright green region, which they've attributed to combustion. They found that none of the yellow region contributed to the spectra that they were analyzing in the green region, while they observed broad maxima at several wavelengths with 542 nm being the strongest. Li and Williams[26] attributed the peaks of their broad maxima to BO_2 emission.

Similarly Spalding et. al[27] studied boron suboxides during ignition and combustion through emission spectroscopy and verified a two stage combustion process in nitrogen containing atmospheres. Spalding[27] also found maxima at multiple wavelengths with the strongest being near 546 nm in atmospheres in which no fluorine was included. This observation is certainly in agreement with that of Li and Williams[26] and verifies the idea of a two-stage combustion process.

Figure 9 shows an unfiltered image of the complete combustion process, while figure 10 shows the filtered image where only the second stage of combustion was observed. Figure 11 shows a series of processed images, as BO_2 intensity contours collected for an oxygen mole fraction, X_{O_2} , of 0.3. This shows the location of stage two combustion and as would be expected as the temperature is increased the location shifts closer to the origin.

Although Spalding[28] suggests that the BO_2 spectrum is readily observable during both the full-fledged combustion and ignition stages of boron combustion, the yellow ignition region was not observed in the filtered images. This does not necessarily suggest that BO_2 was not present, only that the level of emission was not strong enough for the camera settings used in the testing. Furthermore, as mentioned earlier Li and Williams[26] did not detect any BO_2 emission at a similar wavelengths during the ignition stage. This behavior allowed for a clear distinction between the first and second stage of boron combustion. For data analysis purposes, the filtered images provided the spatial location of stage two combustion. The starting boundary of stage two combustion also served as the ending boundary for stage one combustion. Finally, the unfiltered

images gave the starting location for stage one combustion. This was defined as the first instance that visible emission was detected.

In order to verify that BO₂ was being detected and not just black body radiation, an experiment was conducted in which a 532 nm filter replaced the 546 nm filter, since there are no BO₂ bands in the direct vicinity of 532 nm. Figure 12 shows the emission intensity contours for each filter. The integrated intensity levels for the 546 nm filter image are typically at least 50% higher than the image obtained with the 532 nm filter. If we consider Planck's Law:

$$I_b(\lambda, T) = \frac{C_1 / \pi}{\lambda^5 \cdot (\exp[C_2 / (\lambda \cdot T)] - 1)}$$

Eq. 4

Where $C_1 = 2 \cdot \pi \cdot h \cdot c_0^2 = 37,413 \frac{W \cdot \mu m^4}{cm^2}$ and $C_2 = \frac{h \cdot c_0}{k_B} = 14,388 \mu m \cdot K$ and integrate the black

body radiation intensity over the full width half maximum value (10 nm) of the filter, we find that the black body radiation should be about 35% higher at 546 nm than at 532 nm for 1600K and about 25% higher at 2000K. Thus suggesting that the emission detected at 546 nm must be more than just the contribution associated with black body radiation and must be attributed to Boron combustion. Furthermore we can rule out the idea of black body radiation further by inspection of the intensity profiles. There is a clear beginning and end luminescence in the filtered images. If we were detecting primarily black body radiation we would expect to continue to see black body radiation after consumption of the boron particles since the products of combustion are primarily condensed phase B₂O₃ at these temperatures. This suggests that while black body radiation certainly would exist in this system, between the camera settings used and the effects of filtering we have minimized its effect on what we have visualized. It should also be noted, that we did not detect any significant emission when particles were absent in the system at either wavelength (532 nm

or 546 nm). While hydrocarbon emission would normally be expected at these wavelengths, with the camera settings we employed we did not detect anything of significance. Furthermore, we conducted similar experiments with nano aluminum and were unable to detect anything above blackbody radiation levels. Therefore, it is reasonable to conclude that the intensity levels detected at 546 nm with the boron particles can be directly attributed to boron combustion processes.

As figure 11 shows, the “shape” of the stage two combustion was not consistent for differing test conditions, making the problem two-dimensional and difficult to evaluate. As such, a technique for evaluating the spatial boundaries needed to be developed. Thus, the problem was made one-dimensional by summing the columns of the images (or the y-dimension) and then plotting the profile in the x-direction. Once this was accomplished an area rule was utilized for determining the boundaries of stage two combustion. An area-based method was chosen since area based methods provide the most unambiguous determination of burn time[29] In this case the burning time was defined as occupying 95% of the area of the original profile as shown in figure 13, where the blue line represents the original profile, while the red line represents 95% of the total area, and therefore the burning time. The boundary on the left side of figure 13 identifies the start of stage two combustion and the end of stage one combustion. Therefore, with spatial locations of the beginning and

ending of each stage of combustion, and the velocity measurements, the ensemble average ignition and combustion times of the SB99 particles can now be extracted.

Figure 14 shows the results of the stage one, or ignition stage times, defined here as t_I . Typical ignition stage times ranged from about 6 ms to about 1.5 ms. In figure 14, the data shown is for the conditions in which both stage 1 and stage 2 combustion were completed within the post flame region. As the figure indicates, the ignition time was relatively insensitive to oxygen mole fraction under these conditions. At the lower oxygen mole fraction conditions, $X_{O_2} \leq 0.15$, stage two combustion was either not completed or not even achieved at the lower temperature conditions. For $X_{O_2} = 0.1$ stage 2 combustion was not achieved until temperatures approached 1800 K. Table 2 provides a summary of which test conditions achieved and completed both stages of combustion. Temperature was found to have a dramatic effect on the ignition time, for example t_I decreases by more than a factor of 2 with an increase of about 200 K in burner temperature. Other studies have shown that the presence of water vapor can greatly alter the ignition process of boron[2,11]. In this study oxygen mole fraction was the primary variable investigated, and the amount of water vapor in the burner combustion products was relatively constant. Figure 14 also shows a comparison of ignition time measurements made by Yeh and Kuo[5] for 2-3 μm boron particles, which shows that the ignition times for the different particle sizes are relatively independent of size. The most likely reason for the lack of size dependence can be attributed to a combination of two issues, 1) Particle agglomeration, and 2) Elemental or pure content of the particles. As our previous measurements showed, our size distribution can be represented by a log-normal distribution. From equation 3 we can extract the mass mean diameter, which is defined in equation 5.

$$d_{mm} = \frac{\sum n_i D_i^4}{\sum n_i D_i^3}$$

Eq. 5

The mass mean diameter was selected as the appropriate scale rather than the geometric mean diameter since the emission intensity scales as a function of D^3 . Given that the aerosol follows a log-normal

distribution, the majority of the mass of the particles will come from the upper “tail” of the distribution. More than 90% of the particles in the distribution are less than or equal to 679 nm. Thus we can reasonably conclude that the emission detected is well represented by the selection of the mass mean diameter.

When comparing the ignition time data of this study to that of Yeh and Kuo’s[5] we must take into account the elemental or pure boron content of the particles. Since the primary particles making up the agglomerates in this study are on the nanoscale, the oxide shell thickness takes up a much larger fraction of the volume/mass of the particles. This means that our 679 nm agglomerates are only comprised of 72% by weight pure boron, which is not representative of a typical particle in that size range. For instance, SB Boron Corporation also sells a product named SB95 which is measured by Fisher Sub-Sieve Sizer (FSSS) as being 700 nm in size and has an elemental content of 95-97%. In the case of Yeh and Kuo’s[5] data, they used particles that ranged from 2-3 μm in size and estimated that the oxide layer thickness was 20 nm. This would result in particles having about 87% by weight pure boron. If we consider an idealized case in which the agglomerates under consideration in this study can be represented by a single spherical particle, this would result in an oxide layer thickness of about 34 nm, or more than 50% thicker than that of Yeh and Kuo’s[5]. Furthermore, if we consider the volume that the oxide layer would occupy in each particle and then calculate the mass of each oxide layer we find that they are of the same order of magnitude ($1.1 * 10^{-13}$ grams for our agglomerates compared to $6.1 * 10^{-13}$ grams for Yeh and Kuo’s⁵ particles). Since by definition the first stage of combustion is not completed until all of the oxide layer has been removed and the agglomerates studied here have a comparable oxide shell to that of Yeh and Kuo’s[5], it is not surprising that the ignition times are quite comparable as well.

Since the primary variable affecting the ignition times was temperature an analytical expression to describe the ignition time was developed based upon an energy balance. The analysis assumed that the lumped capacitance assumption was appropriate, i.e. the temperature of the particle was spatially uniform at any instant during a transient process. In order to verify the validity of the lumped capacitance method, the Biot number, should be much less than unity. In this case the typical Biot number was approximately 0.005, thus validating the lumped capacitance assumption.

The energy balance for the particle is given by:

$$\dot{E}_{st} = \dot{E}_{in} - \dot{E}_{out} + \dot{E}_{gen}$$

Eq. 6

where, \dot{E} refers to the rate of change of energy, and the subscripts *st*, *in*, *out*, and *gen* refer to stored, in, out, and generated respectively. In this analysis, we assume that heat release due to chemical reaction is negligible until the point of ignition. Since the convective heat flux was typically three orders of magnitude larger than that of the radiation heat flux, we neglected radiation terms. With those simplifications, the energy balance reduces to only the storage term and a convective term as an energy input:

$$\dot{E}_{st} = \dot{E}_{in} \Rightarrow \rho_p V C_p \frac{dT}{dt} = h_\infty A_s (T - T_\infty)$$

Eq. 7

The solution for which is given by equation 8.

$$t = \frac{\rho_p D_p C_p}{6h_\infty} \ln\left(\frac{T_{initial} - T_\infty}{T_c - T_\infty}\right)$$

Eq. 8

From this analytical solution a correlation was developed (seen in equation 9) for the ignition times for the two highest oxygen mole fraction conditions, $X_{O2} = 0.2, 0.3$, in which the constants were lumped together into one “time constant”, τ_c , and T_c is the critical temperature to complete ignition in the burner. Figure 15 shows the results of the correlation. Critical temperatures were 1610 K and 1550 K for $X_{O2} = 0.2, 0.3$ respectively. We estimate the uncertainty of the critical temperatures at ± 40 K. This results in a sensitivity of Eq. 9 less than 10% at the higher temperatures and approximately 30% on the lower temperature end. These temperatures are consistent with previously observed ignition temperatures for larger sized boron[2,6,7,11]. Unlike nanoaluminum, which has been shown to ignite at lower temperatures than micron-sized aluminum, no such phenomenon was observed here.

$$t_1 = \tau_c \ln\left(\frac{T_{initial} - T_\infty}{T_c - T_\infty}\right)$$

Eq. 9

Figure 16 shows a summary of the results for the second stage burning times, t_2 , obtained in this study. On the burning time, t_2 , axis (Y-axis) the error bars represent our estimate for the uncertainty in the burning time. In this case this takes into account uncertainty in the piece-wise velocity profile used for the particle velocity as well as the spatial error detected in our emission images. For example when using the 95% area rule to determine burning time we selected ± 1 pixel for spatial resolution. Therefore the velocity profile determined the uncertainty in the particle velocity and the ± 1 pixel was selected as the spatial resolution. The two combined then determined the burning time uncertainty. Typical burning times range from about 3 milliseconds down to about 1.5 milliseconds. Oxygen mole fraction, X_{O_2} , had a clear effect on the burning time particularly at the lower range of the temperatures examined in this study. For example the burning time at a temperature of about 1625 K was approximately 50% longer for $X_{O_2} = 0.2$ than for $X_{O_2} = 0.3$. As the temperature was increased, the effect of X_{O_2} was less pronounced although there was still a significant difference between the two highest oxygen mole fractions, 0.2 and 0.3. For $X_{O_2} \leq 0.2$ there was no clear effect of oxygen mole fraction on the second stage burning time. However, the effect of temperature became more pronounced at low X_{O_2} . In the case of $X_{O_2} = 0.15$ at the lowest temperature condition second stage combustion was not completed before the flow left the burner area. For $X_{O_2} = 0.1$, second stage combustion was not even reached at all except for the highest temperature condition.

Figure 17 shows a comparison of the t_2 burning times obtained in this study with those obtained with larger particles in other studies[2,4,5,24]. The data collected by Macek^{2,4} used particles ranging from about 30 μm to 100 μm . The data from Li and Williams[24] came from 7 and 10 μm boron particles, while the data from Yeh and Kuo[5] came from particles that were 2-3 μm . Again, the data collected in this study was plotted considering its mass mean diameter, 679 nm, which was determined by extrapolating equation 3.

Here, a modified burning time, the product of oxygen mole fraction and burning time ($X_{O_2} * t_2$), is plotted against particle size. These coordinates were chosen since both kinetic and diffusion limited reaction times

are inversely proportional to X_{O_2} , therefore the product of $X_{O_2} * t_2$ should be approximately independent of X_{O_2} , and should only be dependent on pressure and particle size[24].

From figure 17 it can be seen that the burning time of the largest particles studied by Macek[2,4] are dependent on the particle diameter by a factor of approximately 2, which would be consistent with diffusion limited burning, or the D^2 -*law*. The intermediate sized particles studied by Li and Williams[24], and Yeh and Kuo[5] have burning times that approach the kinetic limited regime where the burning time follows a D^1 -*law*. As the size of the particles continue to decrease into the nanometer range, the particle size dependence continues to decrease, to well below unity ($t_b \sim D^{0.48}$), beyond what traditional theories have explained. The selection of another size scale such as the count mean or the geometric mean diameter only decreases the size dependence further.

In order to investigate whether or not boron nanoparticles exhibit significantly different properties than micron-sized particles, as nanoaluminum has, an Arrhenius burning rate law was obtained by plotting the reciprocal of the modified burning time with the reciprocal of burner temperature in figure 18. For comparison purposes, Yeh and Kuo's[5] data has also been plotted in the same manner. In this case, only the data collected for $X_{O_2} = 0.2$ and 0.3 have been included so that the conditions could be most comparable to the Yeh and Kuo[5] data. In this range, the activation energies between the two studies, and two very different particle sizes, are comparable considering experimental error and data scatter. This is in great contrast to similar data for nanoaluminum. For instance, Park[14] found that the activation energy of aluminum significantly decreases with decreasing particle size.

The Damkholer Number analysis of Yeh and Kuo[5] suggests that the burning of these boron nanoparticles should be kinetically controlled. Huang et al.[30] proposed a burning time correlation based on a kinetically controlled system in the form of equation 10 for nanoaluminum. This correlation was applied to the present data set using the Arrhenius parameters obtained above, the results of which can be seen in figure 19.

$$t_2 = \frac{aD^n}{X_{O_2} A \exp\left(\frac{-E_a}{R_u T}\right)}$$

Eq. 10

The correlation takes the activation energy determined for the nanoparticles in this study, and ranges from the nanoparticle data collected in this study up through the data collected by Yeh and Kuo[5] and can be seen in figure 19. This correlation reduces some of the scatter seen in the correlations developed earlier. With the Arrhenius parameters included, the size dependence decreases even further to $t_b \sim D^{0.29}$. Therefore, only a small benefit in burning time was obtained when going from 2-3 μm down into the nanometer range for boron. The nanoaluminum data correlated by Huang[30] resulted in a size dependence of approximately $t_b \sim D^{0.3}$. Similarly, Bazyn[16] found a size dependence $t_b \sim D^{0.6}$ for nanoaluminum at higher pressures.

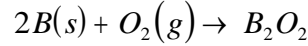
Traditional burning rate theories, i.e. Diffusion or Kinetic limited schemes generally apply to a droplet, or single particle. In this case however, agglomerates are being introduced into the post flame region. Similarly the data correlated by Huang[30], likely suffered from agglomeration. The effects of agglomeration are not well understood at this point. Heat transfer estimates, namely Biot number estimates, suggest that the entire agglomerate should be at a uniform temperature. Li and Williams[24] performed a heat transfer analysis that suggested that as the particle size and partial pressure of oxygen were decreased that boron particles might extinguish. The data collected in this study does not indicate particle extinguishment. If particle extinguishment were occurring, we might expect to observe shorter burn times at the lower temperatures, yet our data shows that the combustion time decreases with increasing temperature which is what would be expected for a boron particle which is being completely consumed. A similar heat transfer analysis has been applied here. However, instead of specifying a particle surface temperature and solving for a quenching diameter as Li and Williams[24] did, here the particle surface temperature was solved for directly by solving the energy balance given in equation 11 (using Li and Williams' notation).

$$Q_5 \omega_5 = \frac{2k(T_p - T_\infty)}{D_p} + \varepsilon \sigma (T_p^4 - T_\infty^4)$$

Eq. 11

The term on the left hand side of equation 11 refers to the heat released by the surface reaction given in equation 12, while the terms on the right hand side of equation 11 refer to the convective and radiative heat transfer. ω_5 is the kinetic rate constant for the surface reaction the values of which are temperature

dependent and can be found in reference 24. For the purpose of the analysis the oxygen mole fraction was assumed to be 0.2.



Eq. 12

Figure 20 shows the results of this analysis for several particle sizes. Clearly, the calculations suggest that the particle (or agglomerate) temperature will be very close to the ambient temperature for very small particles, which in this case is well below the melting temperature of pure boron ($T_m \sim 2340$ K). As the particle size becomes small, the heat generation cannot overcome the heat losses due to radiation and convection, therefore the particle surface is essentially limited to the ambient temperature. It is not until the particle size approaches 1 μm that the heat generation can significantly heat the particle above the ambient temperature. Once the particle size approaches 2 μm , the particle surface temperature reaches the melting temperature of pure boron. This result demonstrates a significant difference in the burning behavior of the particles used in this study compared to those other researchers[2-5,24] and may help to explain the deviation from traditional theory on size dependence. Although the particles under question in this study are in agglomerated form, once the oxide shell has been removed the remaining boron is in solid phase. Whereas, considering Yeh and Kuo's[5] data, once the oxide layer has been removed, the remaining boron is in liquid phase. The increased particle temperature of larger particles due to heat generation overcoming convective and radiation losses at these lower ambient temperatures would certainly enhance both kinetic and diffusion rates. Another potential explanation for the deviation from traditional theory on size dependence is that this could be an artifact of agglomeration. Once the agglomerate is heated up, the original oxide layer removed, and the pure "particle" begins to oxidize, the newly formed B_2O_3 may begin condensing onto or very close to neighboring particles within the agglomerate further restricting oxidation of pure material. Essentially this creates a situation in which there may never be a true second stage, i.e. clean boron combustion, but rather a mixture of stage 1 and stage 2 combustion throughout the consumption of the agglomerate. These two issues are the likely cause of the observed lack of size dependence in this study.

CONCLUSION

Ignition and burning time characteristics of nano-sized boron were studied in the post flame region of a flat flame burner. Unlike previous studies, the particles were injected in the transverse direction across the flame cross-section. Particle Image Velocimetry measurements coupled with ICCD images allowed for measurements of ensemble average ignition and burning time measurements of boron nanoparticles. The particles injected into the post flame region were agglomerates of smaller primary particles, with mean mass diameters of 679 nm. The effect of oxygen concentration and temperature were investigated.

Under appropriate temperature and oxygen mole fraction (X_{O_2}) conditions a two-staged combustion phenomenon was observed for the SB99 particles. Just after injection there was no visible signature of combustion, however, depending on flame conditions, a yellow/orange glow developed further downstream and was attributed to the first stage of boron combustion. The first stage of boron combustion, normally referred to as the ignition stage, is related the removal of the oxide (B_2O_3) layer. Following the first stage, a bright white glow zone was observed, and attributed to the second stage of boron combustion. The second stage combustion was considered full-fledged combustion of the “clean” pure boron particle.

The ignition stage time of nano boron combustion, t_I , was determined for a wide range of parameters, such as oxygen mole fraction X_{O_2} ranging from 0.1-0.3, and temperatures ranging from 1580 K to 1810 K. t_I was found to be a strong function of temperature, but relatively insensitive to oxygen mole fraction in the ranges studied, while ranging from 1.5 milliseconds at the highest temperatures, to about 6 milliseconds at the lowest temperatures. When compared to available data from other researchers[5] employing micron-sized particles, the ignition stage of the boron nanoparticles was not substantially different from particles of approximately 2-3 μm in size. This is a result of the comparable initial oxide shell that is created by agglomerations of nano-sized particles whose elemental content of pure boron is significantly lower than those of larger particles.

Stage 2 combustion of boron nanoparticles was studied for $0.1 \leq X_{O_2} \leq 0.3$, and temperatures ranging from 1580 K to 1870 K. At the lowest temperatures, the oxygen mole fraction played a large role in the t_2 burning time and affected the ability of the particles to achieve stage 2 combustion. For $X_{O_2} \geq 0.2$ stage 2 combustion was achieved for temperatures as low as 1578 ± 31 K. At the lowest temperature condition,

and $X_{O_2} = 0.15$, stage two combustion was achieved but was not completed while the particles remained in the post flame region of the burner. For $X_{O_2} = 0.1$, and the two lowest temperatures conditions, second stage combustion was not achieved while the particles were in the post flame region. Comparison with other researchers data revealed that the t_2 burning times did not follow a diffusion limited D^2 -*law* or a kinetic limited D^I -*law*. Instead the t_2 burning time was found to be far less dependent on particle size than observations for larger particles. At this point we believe that this is a result of a significant difference in particle temperature between sub-micron sized particles and micron-sized particles due to heat losses by convection and radiation. Below 2000 K, particles below 1 μm are unable to generate enough heat to melt the pure material. Whereas, larger boron particles (greater than 2 μm) are able to generate enough heat to be converted into liquid phase at temperatures near 2000 K. This observation may also be related to affects of particle agglomeration, and further studies are certainly warranted particularly at higher temperatures. An Arrhenius Burning Rate law was obtained which showed that the measured activation energy of the particles was consistent with other data[5] employing micron-sized particles. Similarly, the temperature range in which ignition was obtained for the nanoparticles was consistent with that of larger boron particles.

ACKNOWLEDGMENTS

This research effort was sponsored through A) Center for Energetic Concepts Development (CECD); a collaborative effort between the Naval Surface Warfare Center – Indian Head Division (NSWC-IHD), and the University of Maryland (UMD) and B) The Army Research Office. The authors would specifically like to thank Mr. Gary Prybyla, Mr. Kevin Gessner, Mr. Bob Kaczmerak, Mr. Chris Fawls, and Mr. Bob Kavetsky of NSWC-IHD, along with Dr. David Anand, director of the CECD at UMD.

References

- [1] A. Ulas; K.K. Kuo, *Combustion and Flame* **2001**, 127, (1/2), 1935-1957.
- [2] A. Macek; J.M. Semple, *Combustion Science and Technology* **1969**, 1, 181-191.
- [3] A. Macek; J.M. Semple, *Symp. (Int.) Combust., [Proc.]*, **13th 1971**, 859-868.
- [4] A. Macek, *Symp. (Int.) Combust., [Proc.]*, **14th 1972**, 1401-1411.
- [5] Yeh, C.L., Kuo, K.K., *Progress Energy Combustion Science*, 22 (6) (1996) 511-541
- [6] S. Yuasa; H. Isoda, *Combustion and Flame* **1991**, 86, (3), 216-222.

- [7] S.N. Pen'kov, in: K.K. Kuo, R. Pein, (Eds.), Combustion of Boron Based Solid Propellants and Fuels, CRC Press, Boca Raton, 1993, p. 218
- [8] E.L. Dreizen; D.G. Keil; W. Felder; E.P. Vicenzi, *Combustion and Flame* **1999**, 119, (3), 272-290.
- [9] Y.I. Vovchuk; A.N. Zolotko; L.A. Klyachko; D.I. Polishchuk; V.G. Schevchuk, *Combustion Explosion and Shockwaves* **1974**, 10, (4), 538-540.
- [10] S.R. Turns; J.T. Holl; A.S.P. Solomon; G.M. Faeth, *Combustion Science and Technology* **1985**, 43, (5/6), 287-300.
- [11] T. Yoshida; S. Yuasa, *Symp. (Int.) Combust., [Proc.] 38th* **2000**, 2735-2741.
- [12] R.A. Yetter; H. Rabitz; F.L. Dryer, *Combustion and Flame* **1991**, 83, (1/2), 43-62.
- [13] M.M. Mench; K.K. Kuo; C.L. Yeh; Y.C. Lu, *Combustion Science and Technology* **1998**, 135, (1-6), 262-292.
- [14] K. Park; D. Lee; A. Rai; D. Mukherjee; M.R. Zachariah, *Journal of Physical Chemistry* **2005**, 109, (15), 7290-7299.
- [15] T. Parr; C. Johnson; D. Hanson-Parr; K. Higa; K. Wilson in: JANNAF Combustion Subcommittee Meeting, December, 2003; 2003.
- [16] T. Bazyn; H. Krier; N. Glumac, *Combustion and Flame* **2006**, 145, (4), 703-713.
- [17] G.A. Risha, E. Boyer, B.J. Evans, K.K. Kuo, in: Materials Research Symposium, Boston, MA, USA, 2003
- [18] Y. Yang; S. Wang; Z. Sun; D. Dlott, *Propellants, Explosives, and Pyrotechnics* **2005**, 30, (3), 171-177.
- [19] S.H. Kim; B. Y.H. Liu; M.R. Zachariah, *Journal of Colloid and Interface Science* **2005**, 282, (1), 46-57.
- [20] Friedlander
- [21] G. Young, R. Balar, K. Yu, in: 42nd Joint Propulsion Conference and Exhibit, Sacramento, CA, USA, 2006, AIAA 2006-4401
- [22] R.M. Mihalcea; D.S. Baer; R.K. Hanson, *Applied Optics* **1997**, 36, (33), 8745-8752.
- [23] R.M. Mihalcea; D.S. Baer; R.K. Hanson, *Measurement Science and Technology* **1998**, 9, (3), 327-338.
- [24] Li, S.C., Williams, F.A., in: K.K. Kuo, R. Pein, (Eds.), Combustion of Boron Based Solid Propellants and Fuels, CRC Press, Boca Raton, 1993, p. 248
- [25] R.O. Foelsche; R.L. Burton; H. Krier, *Combustion and Flame* **1999**, 117, (1/2), 32-58.
- [26] S.C. Li; F.A. Williams; F. Takahashi, *Symp. (Int.) Combust., [Proc.] 22nd* **1988**, 1951-1960.
- [27] M.J. Spalding; H. Krier; R.L. Burton, *Combustion and Flame* **2000**, 120, (1/2), 200-210.
- [28] M.J. Spalding, H. Krier, R.L. Burton, in: 35th Aerospace Sciences Meeting and Exhibit, Reno, NV, USA, 1997, AIAA 97-0119
- [29] T. Bazyn; H. Krier; N. Glumac, *Journal of Propulsion and Power* **2005**, 21, (4), 577-582.
- [30] Y. Huang; G.A. Risha; V. Yang; R.A. Yetter, *Symp. (Int.) Combust., [Proc.] 31st* **2007**, 2001-2009.

Table 1: Test Conditions

Test Condition	Volumetric Flow Rates (L/min)			Product Mole Fractions				Average Burner Temperature (K)
	O ₂	Air	CH ₄	O ₂	H ₂ O	CO ₂	N ₂	
1	16.8	30.2	5.8	0.200	0.234	0.117	0.450	1684
2	21.0	29.8	7.3	0.200	0.266	0.133	0.400	1808
3	24.8	27.5	8.7	0.200	0.300	0.150	0.350	1854
5	28.6	24.5	10.1	0.200	0.234	0.117	0.450	1637
6	23.2	30.2	5.6	0.300	0.200	0.100	0.400	1630
7	28.9	29.8	7.3	0.300	0.233	0.117	0.350	1797
8	33.2	26.8	8.8	0.300	0.267	0.133	0.300	1872
9	19.2	24.9	4.6	0.300	0.200	0.100	0.400	1578
10	14.0	26.5	5.8	0.150	0.267	0.133	0.450	1718
11	17.7	33.4	7.3	0.150	0.267	0.133	0.450	1814
13	11.0	20.7	4.5	0.150	0.267	0.134	0.449	1596
14	8.5	28.9	4.5	0.100	0.233	0.117	0.550	1614
15	11.0	28.3	5.6	0.100	0.267	0.134	0.499	1712
16	13.7	35.3	6.9	0.100	0.267	0.134	0.499	1791

Table 2: Summary of Results

Test Condition	Product Mole Fractions				Average Burner Temperature (K)	Stage 1 Reached	Stage 2 Reached	Stage 2 Completed
	O ₂	H ₂ O	CO ₂	N ₂				
1	0.200	0.234	0.117	0.450	1684	yes	yes	yes
2	0.200	0.266	0.133	0.400	1808	yes	yes	yes
3	0.200	0.300	0.150	0.350	1854	yes	yes	yes
5	0.200	0.234	0.117	0.450	1637	yes	yes	yes
6	0.300	0.200	0.100	0.400	1630	yes	yes	yes
7	0.300	0.233	0.117	0.350	1797	yes	yes	yes
8	0.300	0.267	0.133	0.300	1872	yes	yes	yes
9	0.300	0.200	0.100	0.400	1578	yes	yes	yes
10	0.150	0.267	0.133	0.450	1718	yes	yes	yes
11	0.150	0.267	0.133	0.450	1814	yes	yes	yes
13	0.150	0.267	0.134	0.449	1596	yes	yes	no
14	0.100	0.233	0.117	0.550	1614	yes	no	no
15	0.100	0.267	0.134	0.499	1712	yes	no	no
16	0.100	0.267	0.134	0.499	1791	yes	yes	yes

List of Captions for Figures

- Fig. 1 Schematic Diagram of Burner and Injection Scheme
- Fig. 2 Schematic Diagram of Burner Test Setup
- Fig. 3 Image Pair Collected in PIV Experiment
- Fig. 4 Velocity Vectors Obtained Using PIV
- Fig. 5 Average Axial-Component of Velocity
- Fig. 6 Correlation for Centerline Jet Velocity
- Fig. 7 TEM Image at Particle Injection Location
- Fig. 8 Size Distribution Determined by DMA
- Fig. 9 Unfiltered Image of SB99 Combustion
- Fig. 10 Filtered Image of SB99 Combustion
- Fig. 11 Sequence of Processed Images for $X_{O_2} = 0.3$
- Fig. 12 Intensity Contours Using Different Filters
- Fig. 13 Example of t_2 Burn Time Determination ($X_{O_2} = 0.2$, $T = 1808$ K)
- Fig. 14 t_1 Ignition Stage Times
- Fig. 15 Correlation for Ignition Time, t_1
- Fig. 16 t_2 Burning Times for SB99
- Fig. 17 t_2 Burning Time Comparison to Larger Particles
- Fig. 18 t_2 Arrhenius Burning Rate Law for SB99
- Fig. 19 t_2 Burning Time Correlation
- Fig. 20 Effect of Ambient Temperature on Particle Surface Temperature

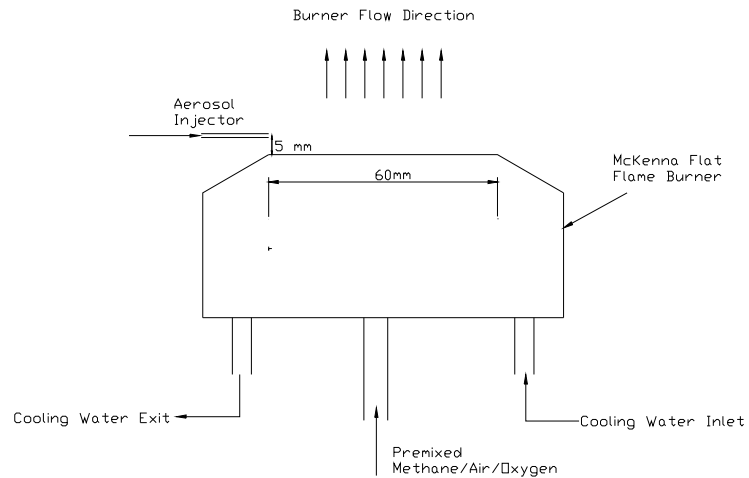


Fig. 1 Schematic Diagram of Burner and Injection Scheme

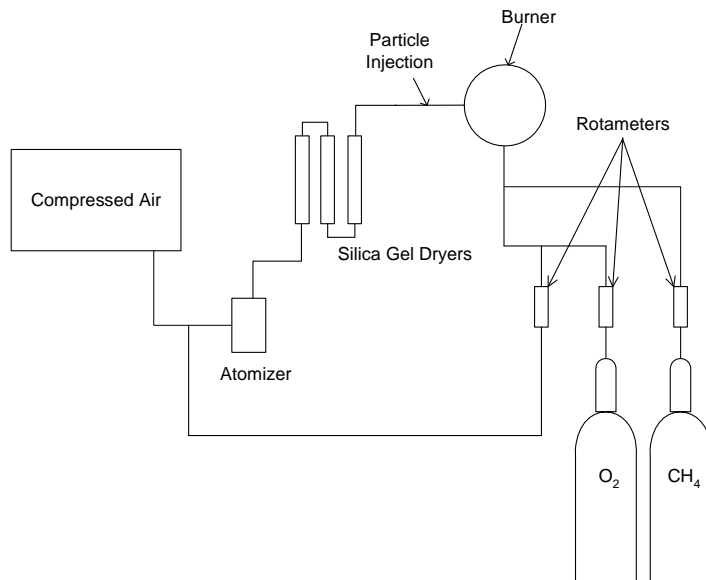


Fig. 2 Schematic Diagram of Burner Test Setup

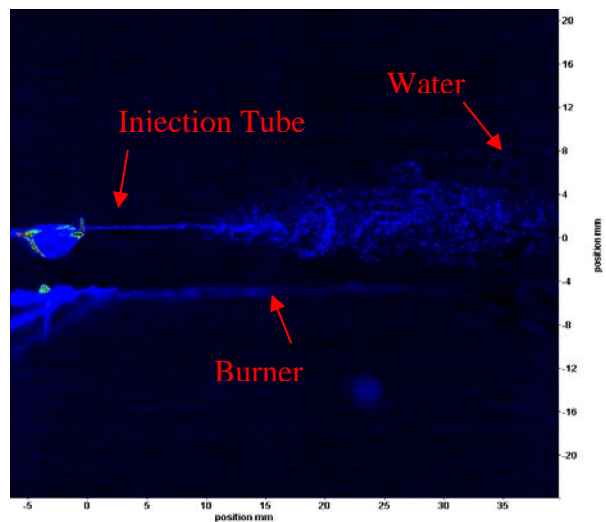


Fig. 3 Image Pair Collected in PIV Experiment

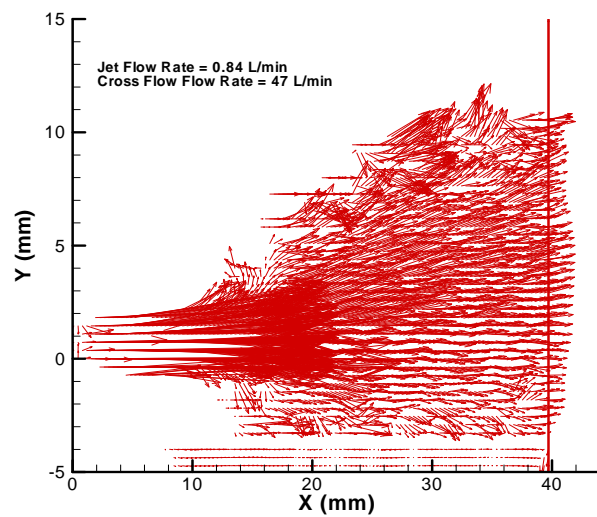


Fig. 4 Velocity Vectors Obtained Using PIV

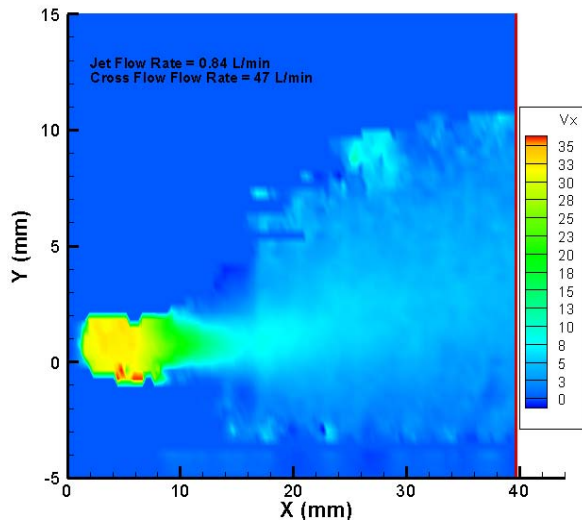


Fig. 5 Average Axial-Component of Velocity

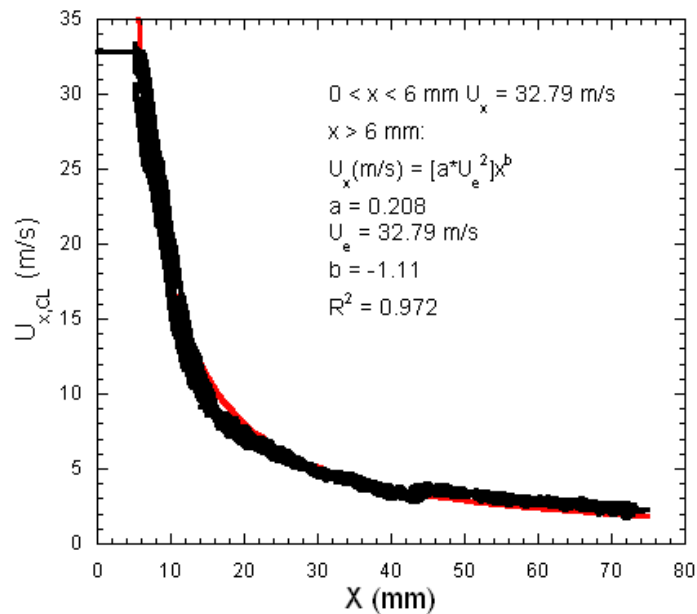


Fig. 6 Correlation for Centerline Jet Velocity

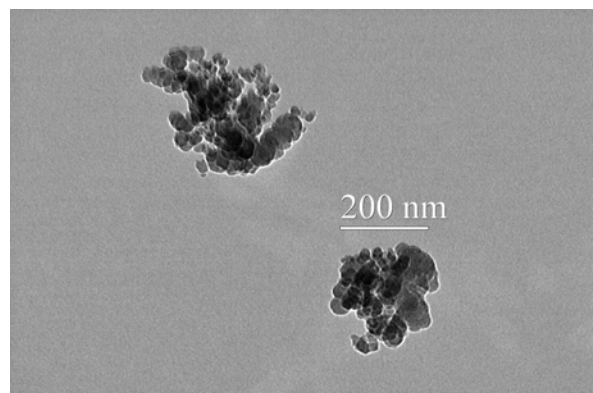


Fig. 7 TEM Image at Particle Injection Location

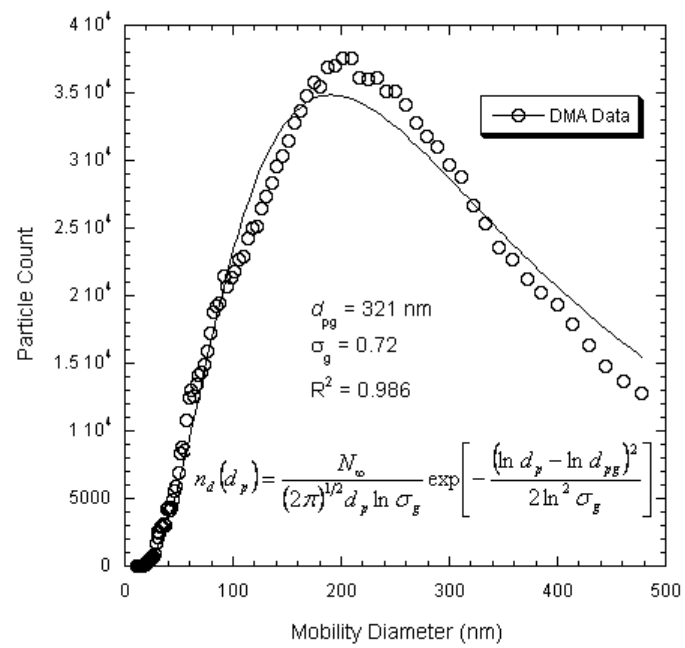


Fig. 8 Size Distribution Determined by DMA

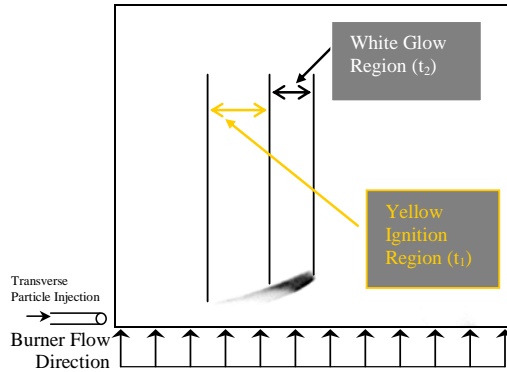


Fig. 9 Unfiltered Image of SB99 Combustion

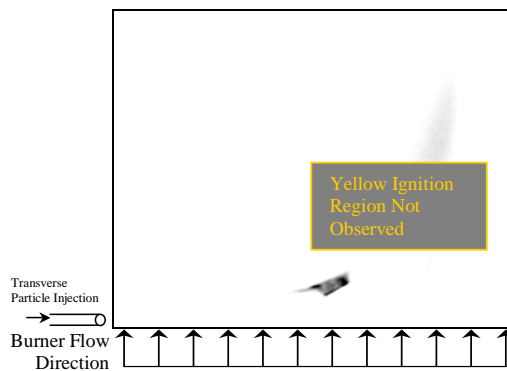


Fig. 10 Filtered Image of SB99 Combustion

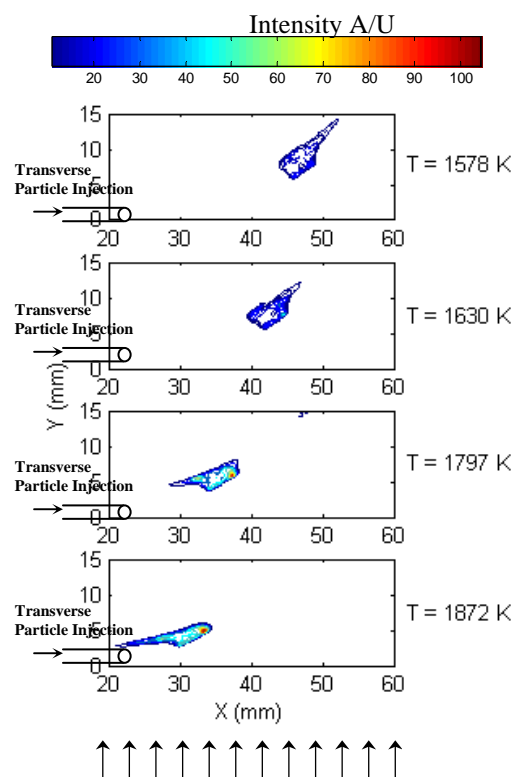


Fig. 11 Sequence of Processed Images for $X_{O_2} = 0.3$

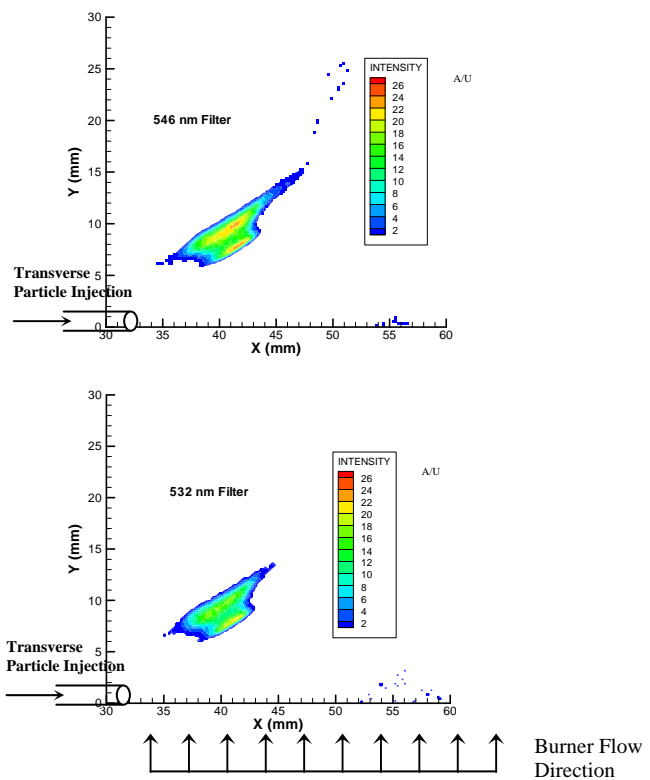


Fig. 12 Intensity Contours Using Different Filters

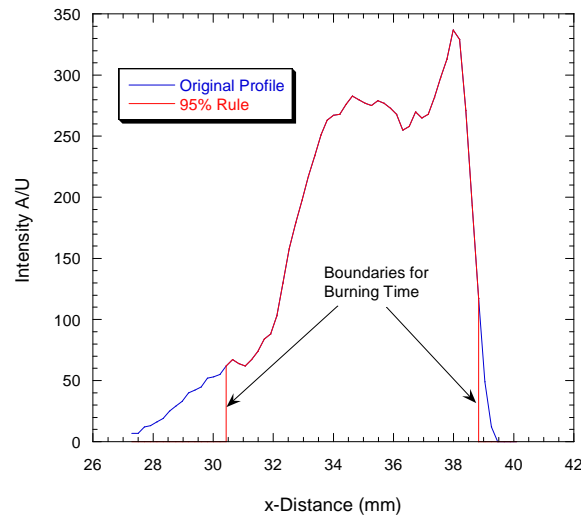


Fig. 13 Example of t_2 Burn Time Determination ($X_{O_2} = 0.2$, $T = 1808$ K)

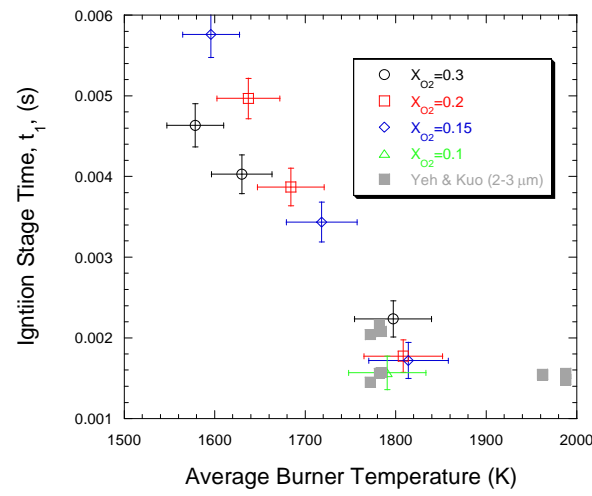


Fig. 14 t_1 Ignition Stage Times

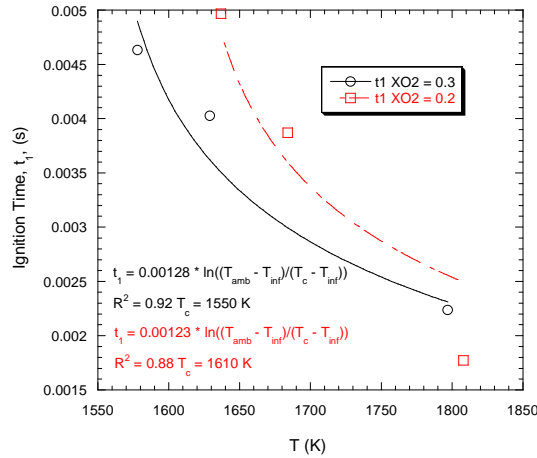


Fig. 15 Correlation for Ignition Time, t_1

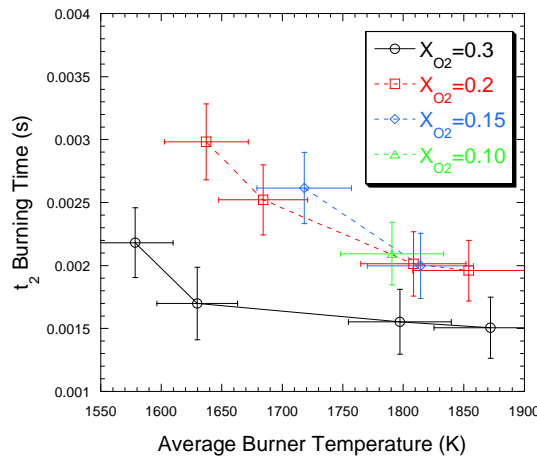


Fig. 16 t_2 Burning Times for SB99

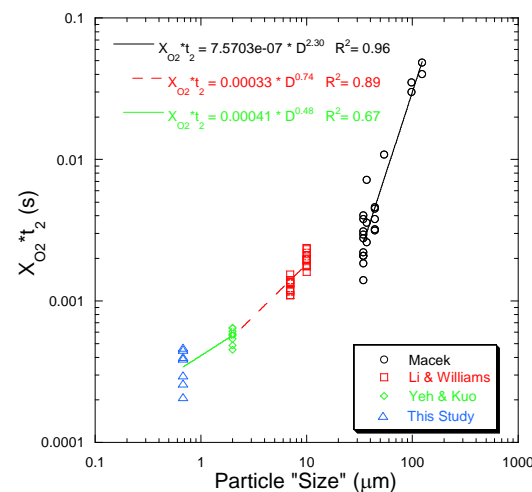


Fig. 17 t_2 Burning Time Comparison to Larger Particles

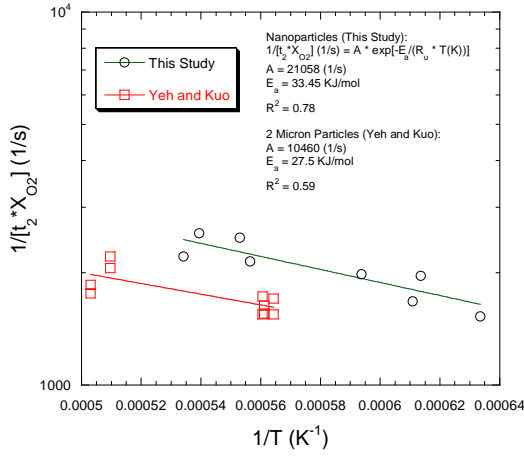


Fig. 18 t_2 Arrhenius Burning Rate Law for SB99

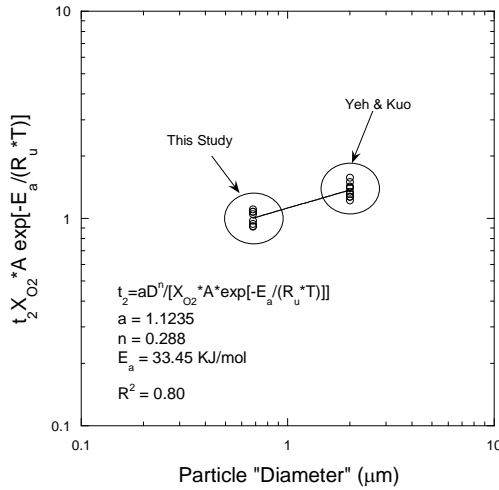


Fig. 19 t_2 Burning Time Correlation

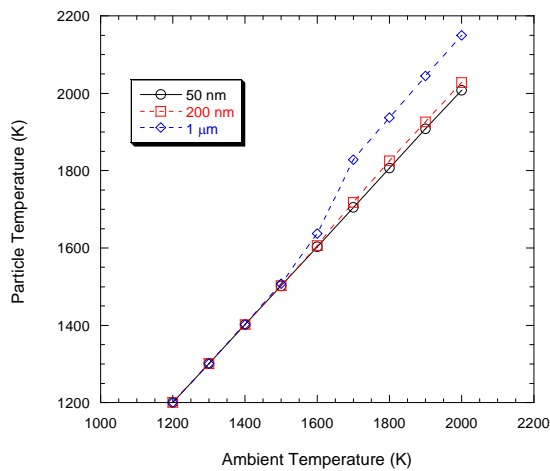


Fig. 20 Effect of Ambient Temperature on Particle Surface Temperature

Molecular Dynamics Simulation of the Kinetic Reaction between Ni and Al Nanoparticles

Abstract

Molecular dynamics simulations are used to simulate the kinetic reaction of Ni and Al particles at the nanometer scale. The affect of particle size on reaction time and temperature for separate nanoparticles has been considered as a model system for a powder metallurgy system. Coated nanoparticles in the form of Ni-coated Al nanoparticles and Al-coated Ni nanoparticles are also analyzed as a model for nanoparticles embedded within a matrix. The differences in melting temperature and phase change behavior, e.g. the volumetric expansion of Al, between Al and Ni are expected to produce differing results for the coated nanoparticle systems. For instance, the volumetric expansion of Al upon melting is expected to produce large tensile stresses and possibly rupture in the Ni shell for Ni-coated Al. Simulation results show that the sintering time for separate and coated nanoparticles is nearly linearly dependent upon the number of atoms or volume of the sintering nanoparticles. We have also found that nanoparticle size and surface energy is an important factor in determining the adiabatic reaction temperature for both systems at nanoparticle sizes of less than 10nm in diameter.

* Corresponding Author: mrz@umd.edu

Introduction

Nanoparticles have interesting physical properties that often vary from the bulk material. Some of these properties, including increased reactivity [1], are due to the high surface area to volume ratio of nanoparticles. With that in mind nanoparticles may provide enhanced energy release rates for explosive and propellant reactions [2].

There is considerable interest in the self-propagating high-temperature synthesis (SHS) reactions of intermetallic compounds because of the associated energy release that takes place [3] during the alloying reaction. In addition to the energetic reaction observed in these materials it is possible to produce structural materials that contain this energy release property. Once ignited, the SHS reaction releases a large amount of energy in a short period of time. One significant difference between SHS and typical combustion processes is that the reactants and products are confined to the condensed state [4]. The SHS process has many potential applications where heat generation is required and oxygen is not available or gaseous products are not desirable. These include alloy formation, net-shape processing, propellants, and as initiators. One of the compounds formed from the SHS reaction, and studied here, is NiAl or nickel aluminide. NiAl is an important alloy because of its desirable high temperature strength and oxidation resistance [5] and the high energy of formation [6]. Recently Weihs and coworkers have also used the NiAl nanolaminate systems in applications of reactive welding [7].

Not surprisingly since the reaction involves solid starting materials, particle size has a significant affect on the properties of the reaction product and the SHS reaction itself [8]. The simulation and analysis of nanoparticle coalescence without the SHS reaction for like materials is extensive [9-14] and involves surface passivation [10], size differences [9,11], and phase change [9] considerations. The analysis here includes all of the previously listed concerns with an additional energy release term from the heat of formation.

The focus of this paper is to use atomistic simulation to model the reactive behaviour of Ni-Al nanoparticles in various configurations. Fortunately, there have been numerous efforts to determine accurate empirical potentials for simulating the Ni-Al material system [15]. Prior simulations using these potentials have investigated the diffusion of Ni and Al atoms [15], point-defect concentrations in NiAl [16], and plasticity [17] in addition to many other mechanical and chemical properties. These efforts have primarily focused on bulk materials rather than nanoparticle systems [18], even though there are many manufacturing processes that produce nanometer sized powders for SHS reactions [19]. For this simulation effort we have chosen a set of embedded atom method (EAM) parameters that reproduce reasonably well the properties of Ni, Al, and NiAl in the temperature range of interest.

Simulation Approach

In this work we employ classical molecular dynamics (MD) with an EAM interatomic potential to study the SHS reaction. The EAM is used because of its accuracy and capability to scale up to material systems with over 10^6 atoms. The MD simulations are compared with thermodynamic analyses in order to provide validation of the simulation results and assess the expected energy release.

The MD simulation was conducted using the LAMMPS software package [20]. For the Ni-Al interactions the Finnis-Sinclair EAM potential [21] from Angelo et al. [22]

was used. The Finnis-Sinclair EAM potential allows for non-symmetric embedding potential terms, potentially providing improved accuracy for metallic alloys [23]. In addition to the parameters for NiAl from Angelo et al. other authors have also developed parameters for the Ni-Al system [16] that may also be described by using the Finnis-Sinclair EAM.

Three primary nanoparticle sizes were considered in this work from smallest to largest are nanoparticles with 1289, 5635, and 36523 atoms each, which correspond approximately to 3nm, 5nm, and 10nm, respectively. The range of sizes was chosen because it represents nanoparticles that may be produced in the laboratory, and which offers reasonable computational time to conduct parametric studies. For the largest system studied, the 10nm diameter nanoparticle kinetic reaction simulation requires approximately two days and 64 processor cores to complete a few nanoseconds of simulated time on 3.0 GHz Intel Woodcrest processors.

Thermodynamic Analysis of Separate Nanoparticles

The separate nanoparticle system is used as a model for powder metallurgy systems where Ni and Al particles are compressed into a structural component. In addition to mechanical properties, the structural component will contain stored energy for future release through a SHS reaction. A thermodynamic analysis of the SHS reaction for the separate Ni and Al nanoparticle system is used here to determine the expected trends and data points for simulation validation. In the thermodynamic analysis we are interested in determining the system parameters of the Ni-Al nanoparticle system that contribute to the combustion temperature and reaction time. Here we have assumed an adiabatic process so that energy released to the surroundings can be ignored. This is a good approximation since the reaction occurs on relatively short time scales and the nanoparticles are expected to be included in a much larger system where the overall surface to volume ratio is small, limiting convective and radiative heat loss. The validity of this assumption is explored in a later section. The SHS reaction of an equimolar Ni and Al mixture is written as



In order to compute the adiabatic temperature for the synthesis reaction the enthalpy of the products and reactants must be equal.

$$H_{prod}(T_{ad}) = H_{reac}(T_0) \quad (2)$$

Assuming that the reaction begins with the reactants at 600K, above the simulated melting temperature of the Al nanoparticles, the enthalpy of the reactants is computed as,

$$H_{reac} = (0.5)(H_{Al,fusion}) + (0.5)(H_{Al,600K} + H_{Ni,600K}) = 11.85 \text{ kJ/mol} \quad (3a)$$

This enthalpy result includes the enthalpy of solid Ni and liquid Al [6]. The Al nanoparticle is assumed to be liquid because for small nanoparticles the melting temperature is known to be appreciably below the bulk melting temperature [24].

Additionally, for the EAM potential used here [22] the aluminum is liquid for these nanoparticle sizes at 600K. The choice of initial temperature will have a nearly linear affect on the adiabatic temperature as long as the temperature is between the melting temperature of the Al and Ni nanoparticles. This linear affect has been observed in experiments [25], and is a reasonable assumption so long as the heat capacities of the solid phases of Ni and NiAl are relatively insensitive to temperature in the ranges studied.

For the products of the SHS process the enthalpy calculation must take into account contributions from the melting of the nickel and the NiAl nanoparticle, enthalpy of formation for the NiAl alloy, and changes in surface energy. The first of these, the enthalpies of melting for Ni and NiAl is experimentally determined to be 17.2 kJ/mol and 31.4 kJ/mol , respectively. The enthalpy of mixing for Ni and Al has garnered close scrutiny in the experimental community with a wide range of reported values. The enthalpy of formation that is used here is approximately in the middle of the reported values at about -65 kJ/mol [6,26,27].

The last contribution to the enthalpy of the products, results from the change in surface energy, due to the reduced total surface area of the combined nanoparticle [28]. The contribution to the change in system energy from the change in surface area is given as equation 4.

$$\Delta E_{surf} = \sigma_{NiAl} \cdot a_{NiAl} - (\sigma_{Ni} \cdot a_{Ni} + \sigma_{Al} \cdot a_{Al}) \quad (4)$$

In equation 4, a_{NiAl} , a_{Ni} , and a_{Al} are the surface area of the NiAl, Ni, and Al nanoparticles, respectively. For the 3nm, 5nm, and 10nm Al nanoparticles the reactant surface area is computed from the Gibbs surface [29] as 36.32 nm^2 , 98.17 nm^2 , and 343.7 nm^2 , respectively. For the associated Ni nanoparticles the surface area is 27.15 nm^2 , 73.59 nm^2 , and 257.87 nm^2 , respectively. The surface energy is approximately 1115 mJ/m^2 for Al and 2573 mJ/m^2 for Ni at 600K [30]. The surface area of the sintered NiAl nanoparticles is 50.77 nm^2 , 137.18 nm^2 , and 480.25 nm^2 for the 3nm, 5nm, and 10nm nanoparticle case, respectively. In experimental analysis of the free surface energy of NiAl near its melting point, the free surface energy has been reported as 1400 mJ/m^2 [31]. The approximate change in energy versus nanoparticle size is tabulated in table I. In table I the trend is for a lower surface energy contribution to the reaction as the nanoparticle size increases. Intuitively, one may expect this because the surface area to volume ratio is also decreasing with increasing particle size, and therefore has less influence on the sintering process. With the enthalpy of formation for NiAl around -65 kJ/mol , the surface energy contribution to the change in enthalpy for coalescence of 10nm diameter nanoparticles is less than 10% of the total enthalpy change. This means that even at relatively small nanoparticle sizes, e.g. 10nm, the affect of nanoparticle size on energy release is minimal.

With the preceding discussion it is possible to take into account many of the sources of enthalpy change in the reaction products including phase and surface area changes. The enthalpy of the products is now estimated as

$$H_{prod} = H_{form,NiAl} + \Delta H_{surf} + \int_{298K}^{T_{ad}} C_{p,NiAl}(T) dT + H_{melt,Ni} \quad (6)$$

The heat capacity for solid and liquid NiAl is given in Kubaschewski et al [21]. For the 3nm case, assuming the NiAl nanoparticle melting temperature to be about 1350K, or the melting point of a similarly sized Ni nanoparticle it is possible to compute the adiabatic reaction temperature, table II. Notice in table II that if no surface energy contribution is considered, i.e. infinitely large spheres, the final adiabatic temperature is computed to be 1599K. In the simulation section we will observe that these results are reasonable and accurately predict the simulated increase in temperature attributable to the contribution from the surface energy.

The Coalescence Processes

For Ni and Al nanoparticles the SHS reaction consists of two processes, namely coalescence and alloying. In this work we have considered the coalescence of a two nanoparticle system with an Al and a Ni nanoparticle with an atomic ratio of unity. A complete SHS reaction of this system will result in a single NiAl nanoparticle. The MD simulations used to work model adiabatic conditions with constant number of atoms and total system energy. The purpose of these simulations is to analyze the affect of nanoparticle size on sintering time, adiabatic combustion temperature, and to visualize the process. The assumed process is illustrated in figure 1. In figure 1 the nanoparticles are initially in contact at a point (a) and the Al nanoparticle is larger than the Ni nanoparticle because of the longer Al-Al bond length. The simulations are initialized at 600K so that the Al nanoparticle is liquid and the Ni nanoparticle is solid. In figure 1 the sintering process proceeds with the liquid Al nanoparticle initially coating the solid Ni nanoparticle while forming some Ni-Al bonds on the surface (b-d). Next, the alloying process proceeds with the Ni nanoparticle being heated above its melting point and becoming liquid so that mixing may occur (e). The formation of Ni-Al bonds beyond the interfacial surface requires diffusion of Al into the Ni nanoparticle or Ni into the liquid Al. Either of these processes is possible but since diffusion is a relatively slow process in solid materials it is expected that the Ni nanoparticle must melt before the coalescence process proceeds appreciably.

The nanoparticle sintering process is driven by two sources of energy as previously discussed. The first of these is a decrease in surface area that lowers the total surface energy of the system. This energy release mechanism is also observed in the sintering of homogeneous material systems such as silicon nanoparticles [28,32]. The second source of energy is from the reactive synthesis that occurs initially at the interface between the nanoparticles and later throughout the entire system. The energy release from the surface sintering is proportional to the surface area of the Ni nanoparticle that is coated by Al and in the whole system to the total number of Ni and Al atoms. Additionally, with the temperature increase there is a decrease in the viscosity of the liquid aluminum that will affect the predicted coalescence time.

The coalescence of nanoparticles in the liquid and solid phases has been examined extensively [9-11]. These studies are primarily concerned with the coalescence of two liquid or two solid nanoparticles. The analysis for the Ni-Al system requires considering the coalescence of a liquid Al nanoparticle and a solid Ni nanoparticle. Lewis et al [9]

considered the coalescence of a liquid and a solid gold nanoparticle, this is similar to the situation here except that the material system considered was homogeneous.

In Lewis et al [9] the author is able to simulate two phases occurring simultaneously for a single material by choosing the size of each nanoparticle such that at a specific temperature the phase of the nanoparticles is different. Lewis found that coalescence proceeded in two stages, first the contact area was maximized and secondly “sphericization” took place driven by surface diffusion. The first stage is much faster than the second and is very similar to the process observed here where the Al nanoparticle maximizes the contact area and partially coats the Ni nanoparticle. In this case there is an added driving force in addition to the surface energy, specifically the energy release on forming of Ni-Al bonds as compared to the Al-Al and Ni-Ni bonds. During the second stage the atoms in the two nanoparticles diffuse and rearrange until the system becomes a single spherical nanoparticle. This stage is driven strongly by the formation of Ni-Al bonds and is expected to occur on a much shorter time scale than for two nanoparticles of the same material. The analytical model and MD simulation results shown in the following sections will explore this assumption.

Phenomenological Model of Nanoparticle Reactive Sintering

To gain further insight we have developed a phenomenological model for the reactive sintering of Ni and Al nanoparticles. The model includes energy release from surface energy, bond formation, and viscous dissipation through deformation. Frenkel [33] has developed a model for the coalescence of two homogeneous nanoparticles, however his model did not account for any phase change, kinetic sintering, or heterogeneous materials. Here we extended Frenkel’s model to consider the coalescence of two liquid drops to consider the coalescence of a liquid and a solid drop with reactive synthesis.

The analytical model is initialized with the Al and Ni nanoparticles in contact at a point. The distance from nanoparticle center to center is equal to the sum of the respective radii, denoted as D in figure 2. The sintering process initially proceeds by the liquid Al nanoparticle coating the solid Ni nanoparticle, as illustrated in figure 1. During this phase of the sintering process, two sources of energy release are occurring; the first of these is related to the decrease in surface area and proportional to the respective surface tension values. The second source of energy release is from the formation of Ni-Al bonds at the interfacial region. Figure 3 is an illustration of the parameters used to model the coalescence time.

In figure 2, $2a$ is the diameter of a circle circumscribed by the contact circumference of the two nanoparticles. v_{Al} and v_{Ni} are the distance from the Al and Ni nanoparticle surface to the surface of the contact circle, respectively. θ is the contact angle as measured from the center of the Ni nanoparticle and ranges from 0 to π radians. In order to model the change in energy of the coalescing nanoparticle system, three energy change mechanisms must be considered. These mechanisms are energy release due to change in surface area, energy release due to kinetic reactions at the interface, and energy loss due to viscous dissipation. The rate of energy change due to all three must balance at all times.

The first energy term considered, namely the surface energy of the nanoparticle system, is simply the surface tension times the total exposed surface area. This energy term is written as a sum of the Al and Ni nanoparticle contributions.

$$E_{surf} = \sigma_{Ni}^s \cdot S_{Ni,exposed} + \sigma_{Al}^l \cdot S_{Al,exposed} \quad (10)$$

The exposed area of the Ni nanoparticle can be written as

$$S_{Ni,exposed} = S_{Ni} - 2\pi r_{Ni} v_{Ni} = 4\pi r_{Ni}^2 - 2\pi r_{Ni} v_{Ni} \quad (11)$$

where

$$v_{Ni} = r_{Ni} (1 - \cos(\theta)) \quad (12)$$

Initially during the sintering process the Ni nanoparticle is assumed to remain in the solid phase thus maintaining a constant radius. This assumption is reasonable because of the higher melting temperature of the Ni nanoparticle.

The exposed surface area of the Al nanoparticle is written as

$$S_{Al,exposed} = S_{Al} - 2\pi r_{Al} v_{Al} = 4\pi r_{Al}^2 - 2\pi r_{Al} v_{Al} \quad (13)$$

where

$$v_{Al} = r_{Al} - \sqrt{r_{Al}^2 - a^2} \quad (14a)$$

$$a = \sqrt{v_{Ni} (2r_{Ni} - v_{Ni})} \quad (14b)$$

The radius of the Al nanoparticle is computed numerically by using conservation of volume for the Al nanoparticle. The exposed surface area of each nanoparticle versus the center to center distance is plotted in figure 3a. Notice that although the surface area of the Al nanoparticle increases during most of the coalescence process the combined total surface area of the Ni and Al nanoparticles decreases monotonically throughout the entire coalescence process. In figure 3 the center-to-center distance never reaches zero because the coalescence is considered complete once the Ni nanoparticle is completely enveloped by the Al nanoparticle.

The second source of energy release, namely the reactive synthesis term is considered by assuming a constant surface density of the Ni nanoparticle and the transient contact area of the Ni-Al interface.

$$E_{reactive} = \rho_{Ni,surface} \cdot a_{interface} \cdot V_{bondenergy} \quad (15)$$

The surface density term, $\rho_{Ni,surface}$, is proportional to the number of Ni-Al bonds at the contact interface. The surface density and bond energy terms, $V_{bondenergy}$, can be combined into a single constant that defines the energy release per unit area of interface.

$$\beta_{density} = \rho_{Ni,surface} \cdot V_{bondenergy} \quad (16)$$

The interfacial contact area is a function of the distance between nanoparticle centers, figure 4. The interfacial area increases monotonically up until the Ni nanoparticle surface is completely covered. This result is expected since the reactive energy term is negative, or releases energy during the entire process, in addition to the minimization of surface energy that is driven by the surface tension of Ni and Al. The interfacial area is written as

$$a_{\text{interface}} = 2\pi v_{Ni} r_{Ni} \quad (17)$$

where v_{Ni} is a function of θ as given in equation 12.

The third energy term represents the viscous dissipation due to deformation of the Al nanoparticle. This viscous dissipation is a function of the viscosity in the liquid Al nanoparticle and the rate of deformation. The extent of the viscous flow can be specified by the decrease in distance between the center of each drop, and the surface of contact with the Ni nanoparticle. A velocity gradient, γ , can be defined as $(\frac{d}{dt}D)/r_{Al}$. The energy dissipated in the whole body per unit time is therefore approximately

$$\frac{dE_{\text{viscous}}}{dt} = 2\eta \int_0^{r_{Al,0}} \gamma^2 (4\pi r^2) dr = \frac{8}{3}\pi r_{Al,0}^3 \eta \left(\frac{dD}{dt} \right)^2 \quad (18)$$

where η is the viscosity of liquid aluminum and $r_{Al,0}$ is the initial radius of the Al nanoparticle.

By conservation of energy the rate of coalescence can now be computed.

$$\frac{dE_{\text{viscous}}}{dt} = \frac{dE_{\text{surf}}}{dt} + \frac{dE_{\text{reactive}}}{dt} \quad (19a)$$

$$\frac{8}{3}\pi r_{Al,0}^3 \eta \left(\frac{dD}{dt} \right)^2 = \frac{d}{dt} [\sigma_{Ni}^s \cdot S_{Ni,\text{exposed}} + \sigma_{Al}^l \cdot S_{Al,\text{exposed}}] + \frac{d}{dt} [2\beta\pi v_{Ni} r_{Ni}] \quad (19b)$$

After writing equation 19b in terms of $d\theta/dt$ and simplifying the right and left hand sides we find that equation 19b is only linearly dependent on $d\theta/dt$. Even with this simplification, equation 19, is most easily solved numerically using an iterative solver. In order to solve equation 19b we need some physical properties of Al, Ni, and NiAl. The dynamic viscosity of bulk molten Al at the melting temperature is about $\eta = 1.3 \cdot 10^{-3} \text{ Pa} \cdot \text{s}$ [34]. Based upon a comparison of the configurational energy in MD simulations of separate nanoparticles and Al-coated Ni nanoparticles the energy release per unit area, β_{density} , is estimated to be 20.7 eV/nm^2 . This number is computed by subtracting the system energy of an Al coated Ni nanoparticle system from the energy of a system with separate nanoparticles and dividing by the interfacial surface area. This method results in the net change in energy during coating of the Ni surface with Al since some Al-Al bonds are lost during the coating process while some Ni-Al bonds are formed at the interface. By numerically solving equation 19b we are able to compute the contact angle, θ , as a function of time and relate this to total exposed surface area of the coalescing nanoparticles. This result is presented in figure 5 along with a comparison to the MD simulation results.

Although qualitatively the results in figure 5 show similar trends the absolute rate of coalescence is slightly under predicted by the model. This difference can be attributed to the obvious simplicity of the model and more specifically to the difficulty in obtaining accurate material parameters. For instance, it is difficult to compare the viscosity of a nanoparticle to the bulk material [12] and since the coalescence time is linearly dependent upon the viscosity a change in viscosity is directly proportional to a change in modeled coalescence time. Additionally, the energy release per unit area term assumes that the net change in energy due to the addition of Ni-Al bonds at the interface is a constant value. This is likely not completely accurate since fewer Al bonds must be broken to form new Ni-Al bonds during the initial contact of the nanoparticles. However, the deviation in this energy release term is likely to be minimal. The deviation of the model time from the simulation results at about 50 ps is due to the switch from stage 1 to stage 2 in the kinetic coalescence process as described by Lewis et al [9]. As described by Lewis, during stage 2, surface diffusion is the predominant factor in continued coalescence and is a much slower process than contact area maximization. The actual simulation results, as compared with the illustration in figure 1, of the observed coalescence process are given in figure 6.

In figure 6 each of the steps in the coalescence process are shown with plots from an MD simulation of the coalescence of 10nm diameter Al and Ni nanoparticles. The correlation of the sintering stages to the reaction temperature and time is illustrated in figure 8 for the sintering of separate 10nm diameter nanoparticles. In the initial step the liquid Al nanoparticle, blue atoms in figure 6, has melted and is spherical in shape. The solid Ni nanoparticle, red atoms, has large faceted sides and is a single crystal, a typical configuration for a crystalline nanoparticle at low temperatures. During stage 1 the Al nanoparticle is attracted to the Ni surface because of the dual driving forces of surface energy minimization and Ni-Al bond formation. This period lasts about 50 ps in this simulation as noted in figures 6 and 7. Between stages 1 and 2 the driving forces associated with the surface energy are counteracted by a resistance to flow in the Al nanoparticle, causing the coalescence process to slow down dramatically. During stage 2, lasting about 450 ps, the surface area is not changing so that energy release from the surface energy terms has ceased to contribute to the change in system potential energy. The subsequent energy release is entirely attributable to the formation of Ni-Al bonds. This stage lasts a much longer time than the initial nanoparticle coalescence stage and is governed by the material diffusion coefficients. Initially at stage 2 the Ni nanoparticle is still solid and the formation of Ni-Al bonds is only possible by Al diffusing into the Ni core or Ni on the surface of the core melting and diffusing away from the interface. This process proceeds until the Ni core has reached its melting point and mixing of the remaining Ni and Al atoms occurs more rapidly, driven by the enthalpy of formation of NiAl. From stage 2 until complete alloying has occurred, taking approximately 400 ps, diffusion and mixing of Ni and Al atoms is the primary driving force.

MD Simulation Results of Separate Nanoparticle Reactivity

We have previously predicted the adiabatic temperature and sintering time for the reactive sintering process of separate equimolar nanoparticles of Al and Ni. In figure 8, the MD simulation results for the equimolar nanoparticles are plotted along with the computed adiabatic temperature for each considered particle size.

From figure 8 it is apparent that the predicted adiabatic temperature is in close agreement with the simulated temperature. Variability of the computed temperature arises from the wide range of experimental results for the surface tension for liquid Al and solid Ni, the reported enthalpy of formation for NiAl, and the assumed melting temperature for the Ni and NiAl materials at this scale. Each of these experimental data points are used in the thermodynamic analysis and contribute to the small inaccuracies in the predicted temperature.

The characteristic time for reactive synthesis that we use here is defined by Zhao et al [35] as t when

$$T(t) = T_0 + 0.8(T_1 - T_0) \quad (20)$$

where T_0 is the initial temperature, T_1 is the maximum size dependent temperature reached, and $T(t)$ is the transient temperature. The computed reaction times are given in figure 9 and illustrate that the time required for separate nanoparticles to react has a power law relationship that is between nanoparticle volume (3), and surface area (2). This implies that not only will the reaction temperature be higher, but will occur more rapidly with decreases in particle size, to a power of about 2.5. This is important because a high rate of energy release is desirable for many applications.

By observing the MD simulations and analyzing the shape of the curves in figure 8 for temperature versus time we have surmised that there are two reaction rates to consider. The first is during the coalescence process (called the growth rate (see 0 to 500 ps for Al₃₆₅₂₃ curve in figure 8)) and Ni nanoparticle melting, and the second is the rapid formation of the NiAl alloy from liquid Al and Ni (convergence rate (see 500 ps and later for the Al₃₆₅₂₃ curve in figure 8)). The temperature at which the transition occurs is size dependent because the melting temperature of the Ni nanoparticle is also size dependent. If the process is not perfectly adiabatic, and some heat is lost to the surroundings it is also possible that the first process would not precede far enough for the Ni nanoparticle to melt and thus the reaction would halt. This would only occur with larger nanoparticles that require longer reaction times during which some energy loss to the surroundings is likely. This is an important consideration in real world applications that are not perfectly adiabatic, but when complete alloying is desired. One reason for this observed increase in reaction rate is because the heat generated from the formation of Ni-Al bonds will conduct into the core nanoparticle so that when the reaction front reaches the inner atoms they will have a higher diffusion coefficient, which in turn increases the reaction rate.

Reactive Sintering of Core-Shell Nanoparticles

Aluminum Coated Nickel

In this section we will discuss the sintering process for an Al-coated Ni nanoparticle followed by a discussion of a Ni-coated Al nanoparticle. Both of these systems can be used as a model for highly compacted Ni and Al nanoparticles or one material serving as a matrix for nanoparticles of the other. In the first model system we assume that a Ni nanoparticle has been coated with Al and equilibrated without the Ni melting, or any further reaction occurring. Results for the reaction time and temperature will be presented and a comparison with the separate nanoparticle case will be given. Here again we have considered three system sizes with 1289, 5635, and 36523 atoms each of Al and Ni.

An initial estimate is that the coalescence process for the fully coated nanoparticle system will be a truncated version of the separate nanoparticle case. In the coated nanoparticle system we do not have the first stage of coalescence occurring and only observe the second stage, namely diffusion of Ni and Al atoms to form Ni-Al bonds. The sintering temperature versus time plot is given in figure 10 and shows an interesting result. Whereas the maximum temperature reached increases with decreasing nanoparticle size for coalescence of separate nanoparticles, the opposite is true here, the temperature decreases with decreasing nanoparticle size.

In figure 10 the observed decrease in adiabatic temperature is due to the fact that the ratio of atoms near the interfacial region to the atoms in the bulk nanoparticle decreases as the nanoparticle size increases. Atoms in the interfacial region have already formed Ni-Al bonds and are therefore already at a lower configurational energy than if they were contained in a homogeneous nanoparticle of either pure Al or Ni. If we extend the adiabatic temperature relationship to infinitely large particles we would approach the result obtained from the analysis of separate nanoparticle as they increase in size. The thermodynamic analysis is similar except that the surface energy term is zero and the enthalpy of formation is lowered by a factor proportional to the ratio of surface area to volume. The enthalpy of the products, equation 6, modified for coated nanoparticles becomes

$$H_{prod} = \left(1 - \frac{t \cdot A_{surface}}{V}\right) H_{form, NiAl} + \int_{298K}^{T_{ad}} C_{p, NiAl}(T) dT + H_{melt, Ni} \quad (21)$$

where t is a computed thickness value for the interfacial layer, $A_{surface}$ is the area of the interfacial region, and V is the volume of the Ni core. In order to determine the correct empirical thickness value, t , for equation 21 we have used the adiabatic temperature computed in the MD simulation results for the Al-coated Ni nanoparticle. These results indicate that an interface thickness of 0.07nm is able to accurately predict the adiabatic temperature observed in the MD simulations, figure 11. In figure 11 it is apparent that the adiabatic combustion temperature is highly size dependent for nanoparticles of less than 10nm in diameter. For very small nanoparticles, less than 1nm diameter, there is little predicted change in temperature from the initial temperature of 600K since most of the potential Ni-Al bonds have already been formed.

From the sintering of separate nanoparticles it is expected that the reaction time will be linearly related to the radius of the nanoparticle to a power of about 2.5. In figure 12 this appears to be the case for this range of nanoparticle sizes. A slight deviation from the separate nanoparticle result is probably related to the fact that the coalescence process, stage 1, is not included in this model system and diffusion takes longer to initialize the kinetic reaction process.

The results for the Al-coated Ni nanoparticle indicate the trends that one might expect from a material system that included an Al matrix with embedded Ni nanoparticles. From the results in figures 11 and 12 there are two competing reaction results, namely reaction time and maximum temperature. In figure 12 we see that as the Ni nanoparticle size decreases the reaction time decreases, causing the energy release rate to increase. A second observation that can be made from figure 11 is that the reaction temperature decreases with decreasing Ni nanoparticle size, potentially minimizing the effect of the rapid energy release.

Looking more closely at the reaction time versus number of atoms for the separate nanoparticle and Al-coated Ni nanoparticle cases we observe a similar relationship of reaction time to nanoparticle size as that found in separate nanoparticles. In both cases the reaction time appears to have a power law relationship with radius, with an exponent of 2.5. The accelerated temperature increase in figure 10 after about 900ps for the Al_{36523} curve is the convergence rate discussed previously.

Nickel Coated Aluminum

The Ni-coated Al nanoparticle system has garnered some interest because when Al melts there is an experimentally observed increase in volume of about 6.5%. This increase in volume creates a large stress in the Ni coating and may result in catastrophic failure and fragmentation of the nanoparticle [18]. In the work by Delogu [18], the fragmentation is only observed for a specific set of conditions including Ni shell thickness. In this work, even with the appropriate Ni shell thickness, fragmentation of the nanoparticle is not observed. With the empirical potentials and parameters considered here the kinetic alloying reaction is fast and results in a liquid NiAl nanoparticle without fragmentation.

In the first set of analyses the Ni shell contains the same number of atoms as the Al core. This results in an Al core with a radius of 2.8 nm and a Ni shell of about 0.7 nm. Since the bond length of Ni is less than Al the shell is thinner and the contact area is initially greater than observed in similarly sized Al-coated Ni nanoparticles. As with the nanoparticle coalescence simulations, the temperature of the system is raised to 600K at which time a constant energy simulation is used to analyze the energy conversion rate and the adiabatic temperature rise of the system.

In the initial simulations with an atomic ratio of unity there are more Ni-Al bonds in the Ni-coated nanoparticle than the Al-coated nanoparticle. It may therefore be expected that the total system energy would initially be lower in the Ni-coated Al nanoparticle system than the Al-coated Ni system. In fact, the opposite is true, because although there are more Ni-Al bonds in the Ni-coated system there are fewer Ni-Ni bonds than in the Al-coated nanoparticle. Since Ni-Ni bonds are stronger than Al-Al bonds the total initial energy is lower in the Al-coated Ni nanoparticle system. Since the final configuration of both systems is a completely alloyed NiAl nanoparticle, the system energy change for the Ni-coated nanoparticle is greater than the Al-coated system. This greater change in potential energy, results in the computed adiabatic temperature for the Ni-coated Al nanoparticle being higher than the Al-coated nanoparticle, figure 13, although the difference is not large.

In the two following simulations we simulated an approximately 5nm diameter Al nanoparticle coated with either a 1 nm or a 2 nm thick Ni coating. For these simulations the temperature was controlled using an NVT ensemble. This temperature control was used in order to rapidly increase the temperature from about 300K to above the melting point of the Al nanoparticle, at a rate of 0.1 K/ps. When the Al nanoparticle melts and expands, a large sudden increase of stress in the Ni coating is observed. For the 2nm thick Ni coating the increase in stress is not high enough to cause failure of the coating. In this case the outer shell expands slightly but does not crack. For the 1nm thick case the stress in the Ni shell is high enough to cause failure. When the shell fails the Al begins to leak out onto the surface of the nanoparticle but no fragmentation is observed. If the

nanoparticle were surrounded by oxygen this may initiate the Al oxidation reaction, releasing additional energy as Al oxides are formed.

The cracking and leaking of Al onto the surface of the Ni shell is very different from what Delogu [18] observed using a semi-empirical tight-binding (TB) potential. Another difference from the work by Delogu is the choice of Al core radius. For both of the shell cases here the core has a radius of 2.8nm, this is in contrast to the core radius of 3.0nm and 2.0nm for the 1.0 nm and 2.0 nm shell cases, respectively used by Delogu [18]. Since the 1nm shell case is the most interesting and the radii are very close (2.8nm vs. 3.0nm) the choice of core size is not expected to have had an appreciable affect on the results for this case.

Throughout this simulation effort, oxygen in the form of free molecules or metal oxides is not considered. This is primarily due to the fact that including oxygen in the simulations would require computing charge transfer [36,37] which would limit the size and scope of the model configurations considered. From knowledge of the binding energy for Al and Ni oxides it is possible to estimate what affect an oxide coating will have on the various configurations considered here. For the sintering of separate particles an oxide coating would act as a passivating layer because of the high melting points of these oxides, 2327K for Al_2O_3 and 2257K for NiO. This passivation layer will likely need to be removed by mechanical failure or melting before complete sintering could take place, increasing the temperature required for activation of the sintering process. A similar affect will likely be observed in the coated nanoparticle models if an oxide layer is present between the two metals. For free oxygen molecules surrounding sintering nanoparticles the oxidation reaction would take precedence over the SHS reaction where competition exists on exposed surfaces, because of the much higher enthalpies of formation for the oxides over the formation of Ni-Al bonds.

Conclusions

We have analyzed two model systems for the energetic reaction of Ni and Al. In the first case we considered the coalescing and sintering of separate nanoparticles and found that the energy release from the change in surface area is only significant at small, less than 10 nm diameter, nanoparticles. These separated nanoparticle reaction simulations and thermodynamic analyses show that the reaction time will decrease and the adiabatic reaction temperature will increase with decreasing nanoparticle sizes. This may be important for applications where high energy release rates are desired. The simulation data closely match a classical thermodynamic analysis.

In the second part of this work we considered the sintering of Al-coated Ni nanoparticles and Ni-coated Al nanoparticles as a model material system for nanoparticles embedded in a matrix of the other metal. This work revealed that the reaction time is again inversely related to nanoparticle size but the adiabatic temperature decreases with decreasing nanoparticle size. Mechanically the Al-coated Ni nanoparticle system is a model system for a light weight Al matrix with embedded Ni nanoparticles, a system with relatively high strength compared to a loosely bonded powder of Al and Ni nanoparticles. This Al matrix system could be used in systems where mechanical strength is important in addition to energy release from kinetic sintering of the Ni and Al atoms. In the Ni-coated Al nanoparticle system we investigated possible rupture and fragmentation of the Ni shell but were unable to observe any fragmentation.

References

1. X. Phung, J. Groza, E. A. Stach, L. N. Williams, and S. B. Ritchey. “Surface characterization of metal nanoparticles”, *Materials Science and Engineering A*, **359**, 261–268, 2003.
2. A. Rai, D. Lee, K. Park, and M. R. Zachariah. “Importance of Phase Change of Aluminum in Oxidation of Aluminum Nanoparticles”, *Journal of Physical Chemistry B*, **108**, 14793–14795, 2004.
3. H. P. Li. “Influence of ignition parameters on micropyretic synthesis of NiAl compound”, *Materials Science & Engineering A*, **404**, 146–152, 2005.
4. S. Gennari, U. A. Tamburini, F. Maglia, G. Spinolo, and Z. A. Munir. “A new approach to the modeling of SHS reactions: Combustion synthesis of transition metal aluminides”, *Acta Materialia*, **54**, 2343–2351, (2006).
5. P. Nash, and O. Kleppa. “Composition dependence of the enthalpies of formation of NiAl”, *Journal of Alloys and Compounds*, **321**, 228–231, 2001.
6. R. Hu, and P. Nash. “The enthalpy of formation of NiAl”, *Journal of Materials Science*, **40**, 1067–1069, 2005.
7. J. C. Trenkle, T. P. Weihs, and T. C. Hufnagel. “Fracture toughness of bulk metallic glass welds made using nanostructured reactive multilayer foils”, *Scripta Materialia*, **58**, 315–318, 2008.
8. S. Dong, P. Hou, H. Cheng, H. Yang, and G. Zou. “Fabrication of intermetallic NiAl by self-propagating high-temperature sysnthesis reaction using aluminum nanopowder under high pressure”, *Journal of Physics: Condensed Matter*, **14**, 11023–11030, 2002.
9. L. J. Lewis, P. Jensen, and J.-L. Barrat. “Melting, freezing, and coalescence of gold nanoparticles”, *Physical Review B*, **56**(4), 2248–2257, 1997.
10. T. Hawa, and M. R. Zachariah. “Coalescence kinetics of bare and hydrogen-coated silicon nanoparticles: A molecular dynamics study”, *Physical Review B*, **71**, 165434, 2005.
11. T. Hawa, and M. R. Zachariah. “Coalescence kinetics of unequal sized nanoparticles”, *Aerosol Science*, **37**, 1–15, 2006.
12. M. R. Zachariah, and M. J. Carrier. “Molecular Dynamics Computation of Gas-Phase Nanoparticle Sintering: A Comparison with Phenomenological Models”, *Journal of Aerosol Science*, **30**(9), 1139–1151, 1999.
13. S. H. Ehrman. “Effect of Particle Size on Rate of Coalescence of Silica Nanoparticles”, *Journal of Colloid and Interface Science*, **213**, 258–261, 1999.
14. S. Arcidiacono, N. R. Bieri, D. Poulikakos, and C. P. Grigoropoulos. “On the coalescence of gold nanoparticles”, *International Journal of Multiphase Flow*, **30**, 979–994, 2004.
15. S. Yu, C.-Y. Wang, T. Yu, and J. Cai. “Self-diffusion in the intermetallic compounds NiAl and Ni₃Al: An embedded atom method study”, *Physica B*, **396**, 138–144, 2007.
16. Y. Mishin, M. J. Mehl, and D. A. Papaconstantopoulos. “Embedded-atom potential for B2-NiAl”, *Physical Review B*, **65**, 224114, (2002).

17. J. Mei, B. R. Cooper, and S. P. Lim. “Many-body atomistic model potential for intermetallic compounds and alloys and its application to NiAl”, *Physical Review B*, **54**(1), 178–183, 1996.
18. F. Delogu. “Numerical simulation of the thermal response of Al core/Ni shell nanometer-sized particles”, *Nanotechnology*, **18**, 505702, 2007.
19. H. X. Zhu, and R. Abbaschian. “Reactive processing of nickel-aluminide intermetallic compounds”, *Journal of Materials Science*, **38**, 3861–3870, 2003.
20. S. J. Plimpton. “Fast Parallel Algorithms for Short-Range Molecular Dynamics”, *Journal of Computational Physics*, **117**, 1–19, 1995.
21. M. W. Finnis and J. E. Sinclair. “A simple empirical N-body potential for transition metals”, *Philosophical Magazine A*, **50**, 45–55 (1984).
22. J. E. Angelo, N. R. Moody, and M. I. Baskes. “Trapping of hydrogen to lattice defects in nickel”, *Modelling Simul. Mater. Sci. Eng.*, **3**, 289–307, (1995).
23. G. J. Ackland, and V. Vitek. “Many-body potentials and atomic-scale relaxations in noble-metal alloys”, *Physical Review B*, **41**(15), 10324–10333, 1990.
24. P. Pawlow. *Z Phys. Chem.*, **65**, 545, 1909.
25. P. Zhu, J. C. M. Li, and C. T. Liu. “Adiabatic temperature of combustion synthesis of Al-Ni systems”, *Materials Science and Engineering A*, **357**, 248–257, 2003.
26. R. Arroyave, D. Shin, and Z.-K. Liu. “Ab initio thermodynamic properties of stoichiometric phases in the Ni-Al system”, *Acta Materialia*, **53**, 1809–1819, 2005.
27. F. Z. Chrifi-Alaoui, M. Nassik, K. Mahdouk, and J. C. Gachon. “Enthalpies of formation of the Ni-Al intermetallic compounds”, *Journal of Alloys and Compounds*, **364**, 121–126, 2004.
28. M. R. Zachariah, M. J. Carrier, and E. Blasiten-Barojas, *J. Phys. Chem.* **100**, 14856 (1996).
29. M. P. Allen and D. J. Tildesley. Computer Simulation of Liquids. New York: Oxford, 1996.
30. V. I. Nizhenko. “Free Surface Energy as a Criterion for the Sequence of Intermetallic Layer Formation in Reaction Couples”, *Powder Metallurgy and Metal Ceramics*, **43**(5–6), 273–279 (2004).
31. A. Y. Lozovoi, A. Alavi, and M. W. Finnis. “Surface Stoichiometry and the Initial Oxidation of NiAl(110)”, *Physical Review Letters*, **85**(3), 610–613, 2000.
32. D. Mukherjee, C. G. Sonwane, and M. R. Zachariah. “Kinetic Monte-Carlo Simulation of the Effect of Coalescence Energy Release on the Size and Shape Evolution of NanoParticles Grown as an Aerosol”, *Journal of Chemical Physics*, **119**, 3391, 2003.
33. J. Frenkel. *J. Phys.*, **9**, 385, (1945).
34. M. A. Assael, K. Kakosimos, R. M. Banish, J. Brillo, I. Egry, R. Brooks, P. N. Quested, K. C. Mills, A. Nagashima, Y. Sato, and W. A. Wakeham. “Reference Data for the Density and Viscosity of Liquid Aluminum and Liquid Iron”, *J. Phys. Chem. Ref. Data*, **35**(1), 285–300, (2006).
35. S. Zhao, T. C. Germann, and A. Strachan. “Atomistic simulations of shock-induced alloying reactions in Ni/Al nanolaminates”, *Journal of Chemical Physics*, **125**, 164707, (2006).

36. Q. Zhang, T. Çağın, A. van Duin, W.A. Goddard III, Y. Qi, and L.G. Hector, Jr. “Adhesion and Nonwetting-Wetting Transition in the Al/α-Al₂O₃ Interface”, *Physical Review B*, **69**, 045423, 2004.
37. F.H. Streitz and J.W. Mintmire. “Electrostatic potentials for Metal-Oxide Surface and Interfaces”, *Physical Review B*, **50**(16), 11996–12003, 1994.

Table I. change in surface energy versus nanoparticle size.

<u>Nanoparticle Radius (nm)</u>	<u>ΔE_{surf} (kJ/mol)</u>
3	-18.35
5	-11.41
10	-6.17

Table II. Computed adiabatic temperature versus nanoparticle radius, including contact of flat surfaces or infinitely sized spheres.

<u>Nanoparticle Radius (nm)</u>	<u>T_{ad} (K)</u>
3	2115
5	1920
10	1772
∞	1599

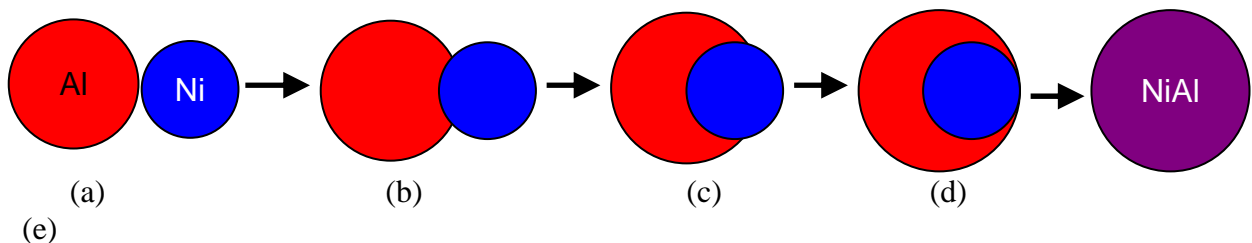


Figure 1. Illustration of sintering process showing liquid Al nanoparticle first coating the solid Ni nanoparticle and then complete alloying after the Ni nanoparticle has melted.

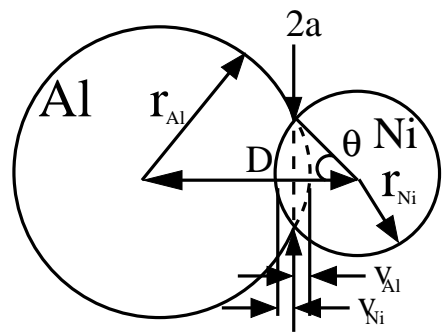


Figure 2. Illustration of parameters used in analytical model of reactive coalescence of Ni and Al nanoparticles.

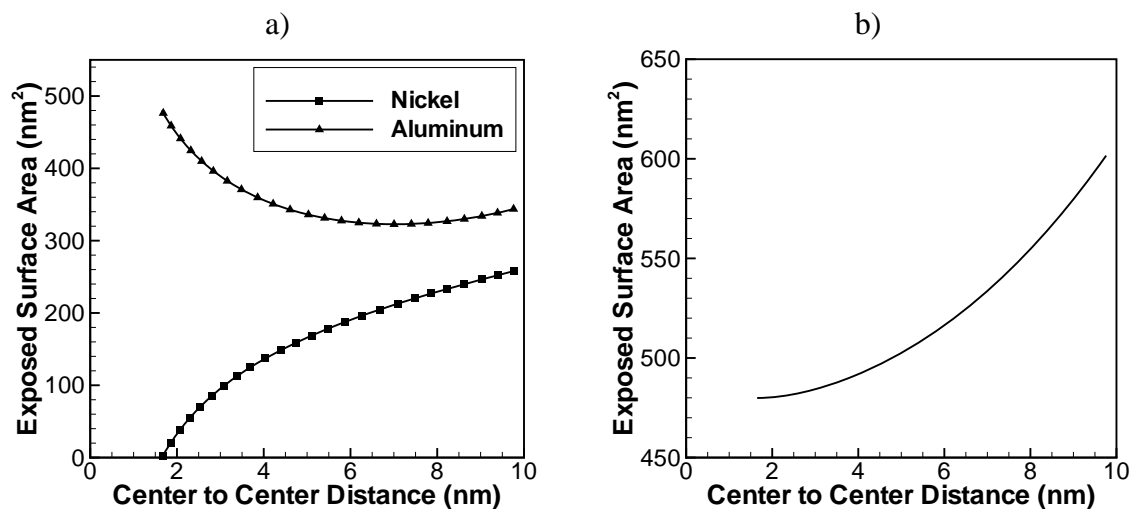


Figure 3. a) Plot of exposed Ni and Al nanoparticle surface area as a function of distance between nanoparticle centers. b) Plot of total exposed surface area as a function of distance between nanoparticle centers. These results assume a Ni nanoparticle of radius 4.53 nm and an Al nanoparticle of 5.23 nm. Notice that the total exposed surface area is monotonically decreasing, indicating that the surface energy is also decreasing monotonically

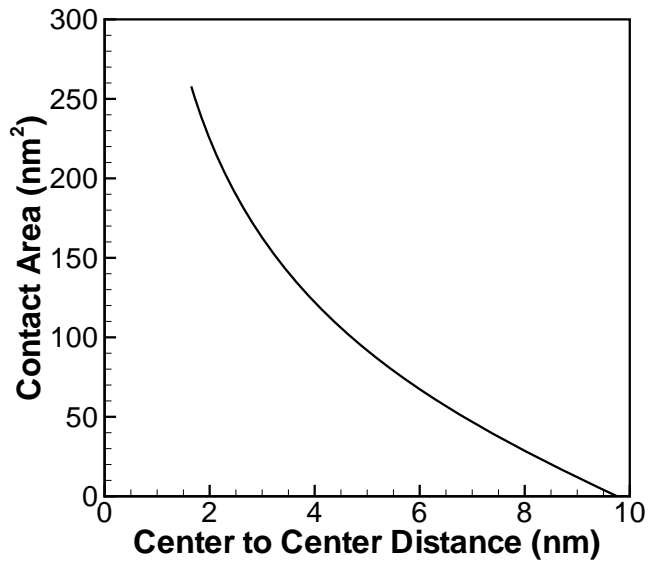


Figure 4. Contact or interface area as a function of center-to-center distance. The contact area is increasing as the nanoparticles move closer together (right to left on x-axis).

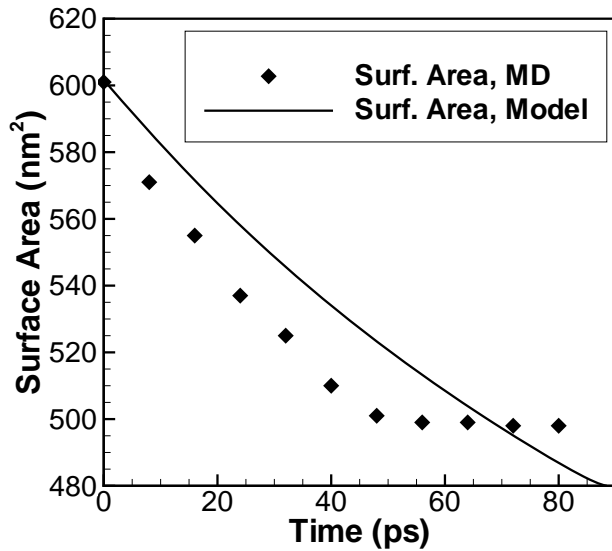


Figure 5. Total system surface area versus time from mathematical model and MD simulations for the sintering of 10nm diameter nanoparticles, where the final surface area of the NiAl nanoparticle is approximately 480 nm².

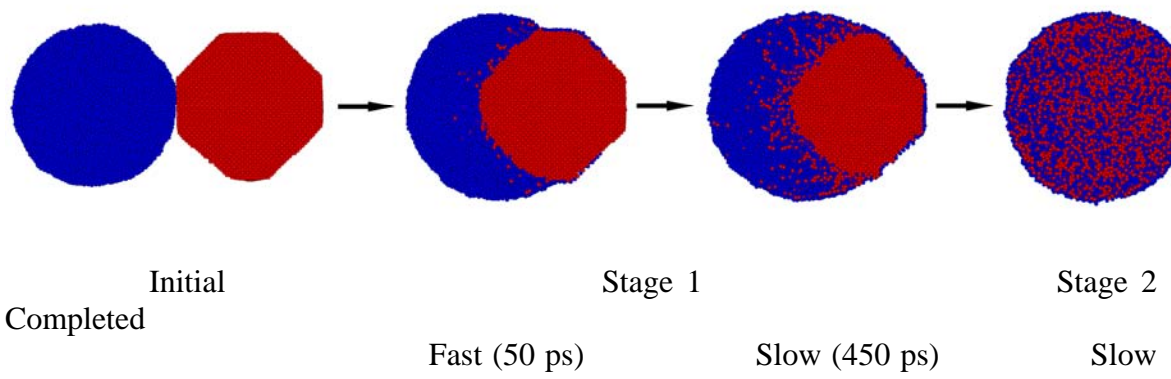


Figure 6. Cross sectional view from MD simulations of Ni/Al nanoparticle sintering process showing the start of the second stage of coalescence where diffusion is the driving force as opposed to contact area maximization. Aluminum atoms are blue and nickel atoms are red.

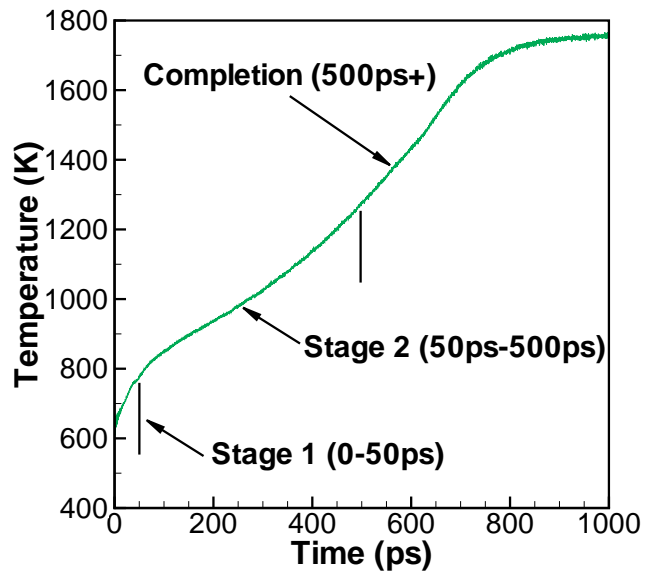


Figure 7. Time versus temperature plot for sintering of separate 10nm diameter Al and Ni nanoparticles. The various stages of the coalescence processes are denoted on the curve, including the final completion stage that occurs after the Ni nanoparticle has melted.

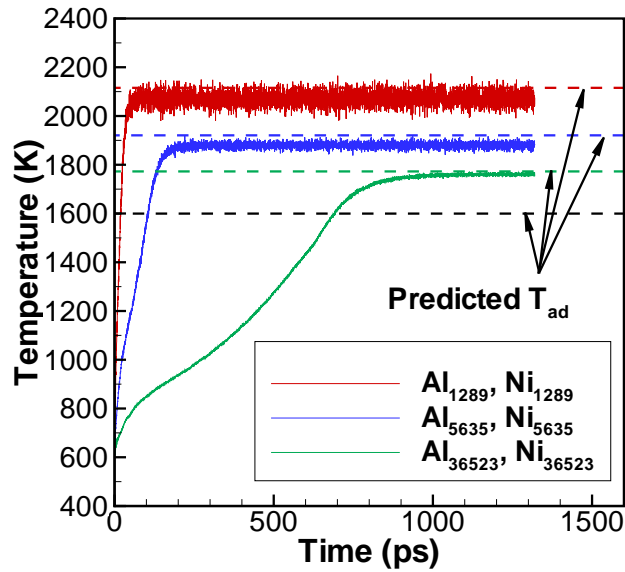


Figure 8. Temperature versus time in the sintering of nanoparticles with an Ni:Al ratio of 1:1. The subscripts in the legend refer to the number of atoms of each material and correspond to nanoparticles of diameter approximately 3nm, 5nm, and 10nm. The color coded dashed lines are the computed adiabatic temperature from the thermodynamic analysis. The black dashed line is the predicted temperature for coalescence of bulk Al and Ni.

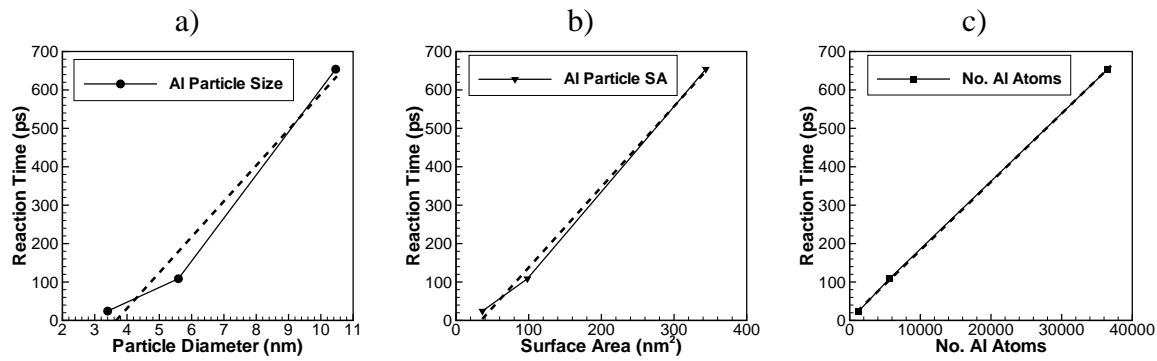


Figure 9. Reaction time versus Al nanoparticle diameter (a), Al nanoparticle surface area (b), and number of Al atoms (c). Note the nearly linear relationship (dashed line) of reaction time between number of atoms (volume) and surface area.

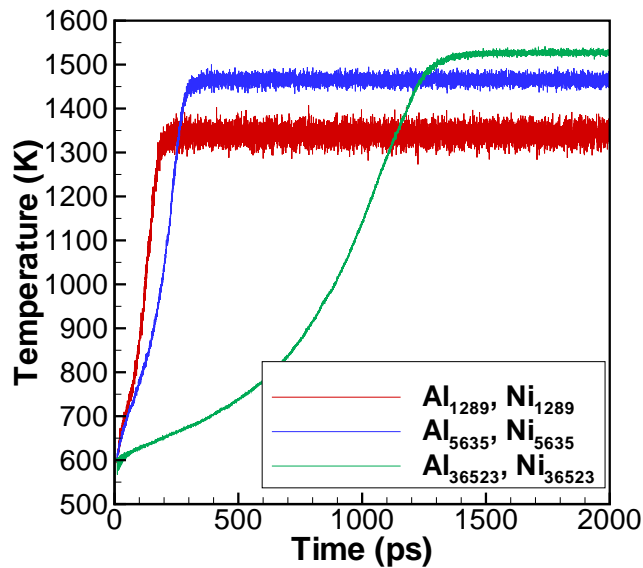


Figure 10. Temperature versus time in the sintering of Al-coated Ni nanoparticles with an Ni:Al ratio of 1:1.

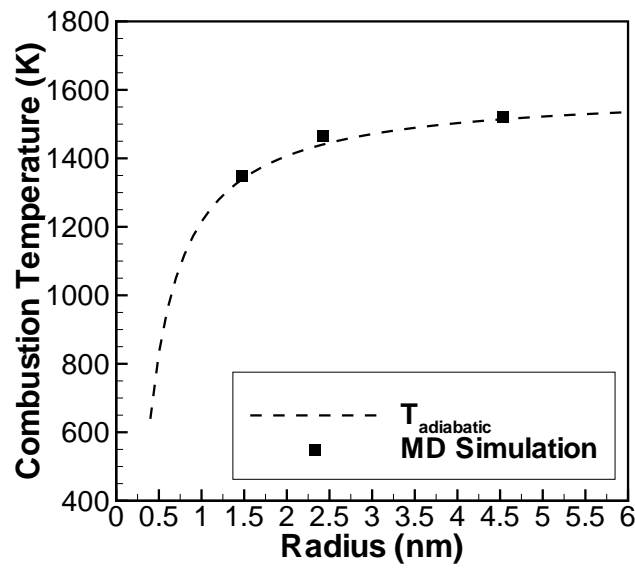


Figure 11. Comparison of thermodynamically determined adiabatic temperature for Al-coated Ni nanoparticle and results from MD simulation.

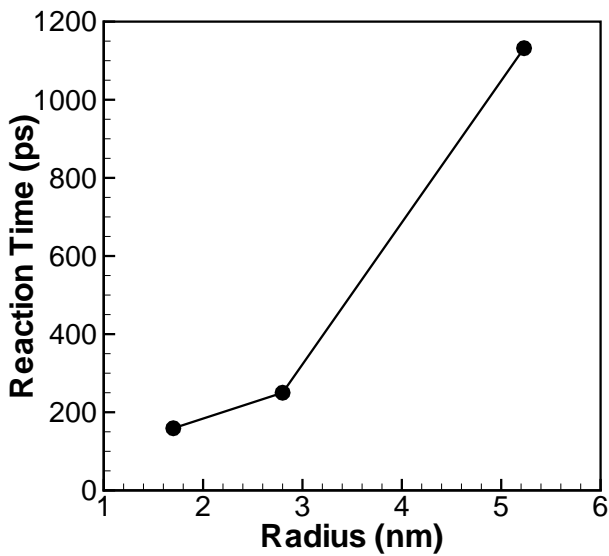


Figure 12. Reaction time versus number of Al atoms in the Al-coated Ni nanoparticle system.

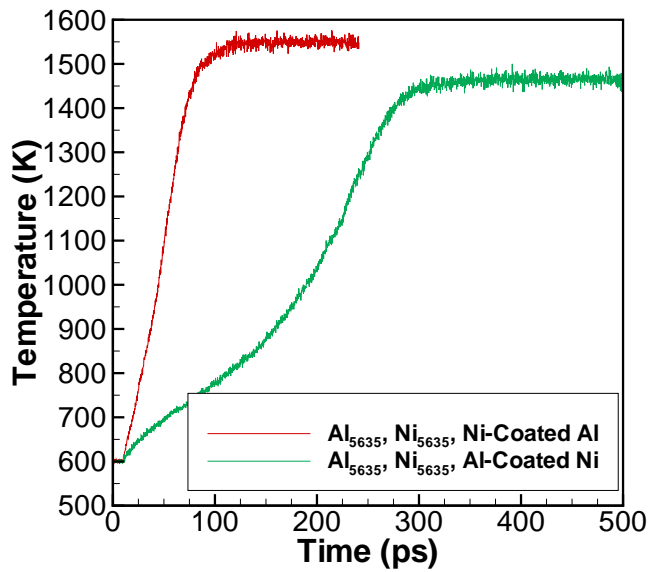


Figure 13. Comparison of combustion temperature for Ni-coated Al nanoparticle versus Al-coated Ni nanoparticle.

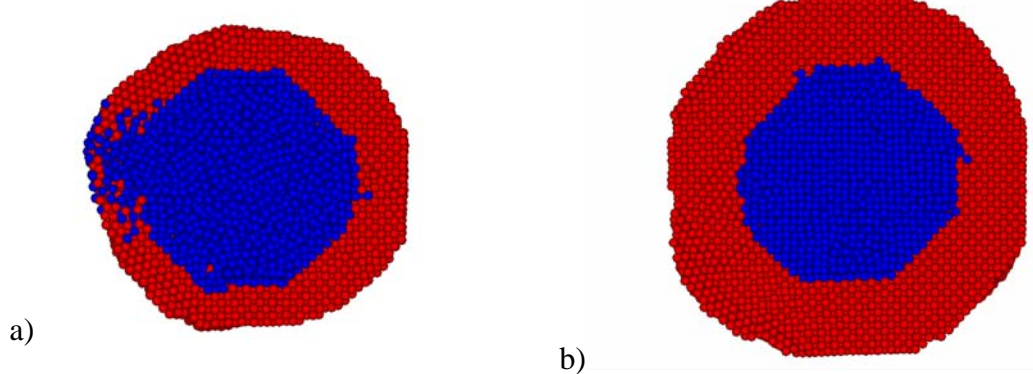


Figure 14. Cross sections of the Ni-coated Al nanoparticle simulation model just after melting of the Al core for the 1nm (a) and 2nm (b) thick Ni shells.

T-Jump/Time-of-Flight Mass Spectrometry for Time Resolved Analysis of Energetic Materials

ABSTRACT:

We describe a new T-jump/time-of-flight mass spectrometer for time-resolved analysis of rapid pyrolysis chemistry of solids and liquids, with a focus on energetic materials. The instrument employs a thin wire substrate which can be coated with the material of interest, and can be rapidly heated (10^5 K/s). The T-Jump probe is inserted with the extraction region of a linear-TOF, which enables multiple spectra to be obtained during a single reaction event. By monitoring the electrical characteristics of the heated wire, the temperature could also be obtained and correlated to the mass-spectra. As example, we present time-resolved spectra for the ignition of nitrocellulose and RDX. The fidelity of the instrument is demonstrated in the spectra presented which show the temporal formation and decay of several species in both systems. A simultaneous measurement of temperature enables us to extract the ignition temperature and the characteristic reaction time. The time resolved mass spectra obtained show that these solid energetic material reactions, under a rapid heating rate, can occur on a time scale of milliseconds or less. While the data sampling rate of 10000 Hz were used in the present experiments, the instrument is capable of a maximum scanning rate of up to \sim 30 kHz. The capability of high speed time resolved measurements offers an additional analytical tool for characterization of the decomposition, ignition, and combustion of energetic materials.

INTRODUCTION

Here we report on a new Time-of-Flight mass spectrometer (TOFMS) electron ionization (EI) source that can obtain time resolved mass-spectra during the ignition of energetic materials. The unique feature of this apparatus is a) implementation of TOFMS/EI with a Temperature Jump (T-Jump) technique to monitor highly reactive condensed state-samples at high heating and decomposition rates, and 2) measurement of the chemistry in a bi-molecular gas-phase-free kinetic environment. Due to its low detection limits and fast time response, the instrument developed here allows for a time resolved characterization of the decomposition, ignition, and combustion of solid energetic materials.

Quantitative measurement of the condensed phase reaction kinetics are usually performed using conventional thermal analysis techniques¹ such as TGA (Thermogravimetric Analysis) and DSC (Differential Scanning Calorimetry). However, those methods fail in the measurement of fast chemistry processes such as rapid thermal decomposition, ignition and combustion of energetic materials where high heating rates are involved. It is well established that the high heating rates in those processes are critical and must be attained in order to study rapid condensed phase reactions.²⁻⁴ In recent years, many experimental diagnostic methods have been developed to characterize rapid reaction processes.^{1, 5-12} In particular, T-Jump (Temperature Jump)/FTIR (Fourier Transform Infrared Spectroscopy) was developed for studying reaction kinetics of condensed-phase propellants.^{2, 13} In the T-Jump/FTIR the sample is placed on a Pt filament and rapidly heated to a chosen temperature and the gaseous species are detected and quantified using FTIR spectroscopy. The thermal decomposition behavior of

numerous energetic materials under isothermal conditions have been studied using this technique.¹⁴⁻¹⁶ However, for rapid condensed phase reactions especially those associated with an ignition event, the relevant time scale can be on the order of milliseconds or less. The nominally low IR spectra scanning rate greatly limits the application of the T-Jump/FTIR spectroscopy in characterizing ignition, and combustion.

Mass Spectrometry (MS) is widely used to study condensed phase reactions.^{11, 17} For decades, the use of MS alone or in conjunction with other techniques has become a powerful tool for thermal analysis.^{9, 18-23} Blais and co-workers developed a TOFMS/EI apparatus capable of measuring the intermediates and products of chemical reactions from detonation of explosives.^{9, 24} The decomposition of thermite based aluminum/iron (III) oxide energetic material was also studied using the Matrix-Assisted Laser Desorption/Ionization (MALDI)-TOFMS technique, and the products of laser initiated thermite reactions were identified.^{25, 26} Time resolved measurements for condensed phase reactions have also been conducted using MS techniques. Dauerman and co-workers developed a scanning sector mass spectrometer which directly attaches to a low pressure strand burner to study the thermal decomposition and combustion of nitrocellulose.^{8, 21} The sample is heated by exposure to the radiation of an arc image furnace and the gaseous species as well as the surface temperature are continuously analyzed by a mass spectrometer and thermocouple as a function of time. Behrens developed a thermogravimetric modulated beam mass spectrometer that combine thermogravimetric analysis, differential thermal analysis, and modulated beam mass spectroscopy. This instrument is capable of quantitative measurement, and has been used to study thermal decomposition mechanisms and kinetics of many compounds.²⁷⁻²⁹ Korobeinichev and co-

workers developed a pulse heated mass spectrometer to studied the high temperature decomposition of ammonium perchlorate.³⁰

Common to all these methods has been that the studies were conducted at either slow heating rate, e.g. the thermal decomposition took place in minutes, or the mass spectrometer sampling rates were slow, e.g. ~ 0.1 sec. Recently, confined thermolysis FTIR spectroscopy with a TOFMS system has allowed for the gaseous products from a high pressure thermolysis chamber.³¹ Although the time resolution of the mass spectra measurement can be ~ 1 ms, the system time respond is limited by the slow sampling rate of the FTIR probe.

Despite the many efforts directed to characterizing condensed phase reactions, time resolved characterization of very rapid condensed phase reactions, particularly those associated with ignition and combustion have proved to be a formidable task. These processes, where the heating rates are usually of the order of $10^3\text{--}10^6$ K/s, are beyond the limit of current thermal analysis techniques.^{7, 32}

One additional consideration is that for many of the MS and FTIR studies, experiments were conducted in an open tube condition, such that much of the chemistry occurred in the gas-phase. However to gain a mechanistic understanding one would like to separate the condensed vs. gas phase contribution. Thus, in order to understand the decomposition mechanism or the combustion process of energetic materials, it is necessary to separate the primary and secondary processes, and investigate the condensed phase reaction under the condition of rapid heating.

Our objective in developing the T-Jump-MS system was first be able to characterize chemistry under high heating rate conditions (i.e. fast chemistry), and second to conduct the experiments under conditions where the secondary gas phase chemistry can be minimized. In the former case high heating rates correspond more closely to the environment usually encountered by energetic materials but more profoundly one should expect reaction channels to increasing favor the higher activation channels possessing the lowest entropy constraints. The later emphasis of minimizing gas-phase chemistry eliminates the possibility of bi-molecular gas phase reaction and likely much unimolecular decomposition. As a result the rapid pyrolysis of energetic materials in vacuum should be dominated by condensed phase reactions, which should ultimately allow for a more direct probe of condensed phase chemistry. The essence of the experiment is that the T-Jump probe is directly inserted into the Electron Ionization chamber of the mass spectrometer, and the species from T-Jump excitation are monitored by the TOF mass spectrometer continuously. The time-resolved mass spectrometric capabilities of the instrument enable the characterization of rapid solid state reactions, which should provide an insightful complement to conventional thermal analysis. The purpose of this initial paper is to describe the operation and capabilities of this new instrument.

EXPERIMENTAL SECTION

a. EI/TOF Mass Spectrometer.

The EI/TOF mass spectrometer is comprised of a linear Time-of-Flight chamber, adapted from a previously developed Single Particle Mass Spectrometer (SPMS)^{11,33} and includes an electron gun for ionization, and the T-Jump probe with an electrical feedthrough, as shown in figure 1. The sample loading chamber is separated from the ionization chamber by a gate valve, which enables the T-Jump probe to be rapidly changed without the need to break vacuum in the TOF chamber. An electron gun (R. M. Jordan Company, Grass Valley, CA, US) is mounted between the extraction plates of the TOF, and perpendicular to the orientation of the T-jump probe. The electron beam is nominally operated at 70 eV, and 1 mA, with the background pressure in the TOF chamber at $\sim 10^{-7}$ Torr.

b. T-Jump Sample Probe.

For the T-Jump we have primarily used a 76 μ m diameter platinum wire, with a total heated length of ~ 1 cm, which is replaced after each heating event. In each experiment, the wire is coated with a thin layer of either sample powder as in the case of particulates, or solution dipped to prepare organic coatings. Using an in-house built power source, the heating rate of the T-Jump probe can be varied by changing the pulse voltage or pulse width, at a rate of up to $\sim 5 \times 10^5$ K/s for the present filament configuration.

c. Control and Data Acquisition System. The schematic of the control and data acquisition system for the T-Jump/TOF mass spectrometer is shown in Figure 2. The present design is based on a previously developed Single Particle Mass Spectrometer (SPMS) which is configured for a standard laser ionization source.^{11,34} To ensure a field-

free region for EI ionization, one DC high voltage power supply is used with a “T” splitter to bias both the repeller plate, and the extraction plate (V1 and V2 shown in figure 2). In the presence of a field-free region, electrons are injected between the plates and ionization takes place. After a predetermined ionization period the voltage on the extraction plate is changed by a high voltage pulser, to create the field for ion extraction region between the plates. The extracted ions drift in the linear TOF tube, and are counted at the MCP (Microchannel Plate) detector. Following the ion extraction period, the voltage on the extraction plate is pulsed back, and a new ionization period begins. Serial pulses generated from a pulse generator (DG535, Stanford Research System, Sunnyvale Inc, CA, USA) are used to trigger the high voltage pulser so that the ionization and extraction processes occur continuously. The pulse timing sequence of the high voltage pulse is also traced from the monitor signal output of the high voltage pulser. Both the detector signal and the monitor signal are recorded with a 500 MHZ digital oscilloscope and transferred to a PC for further analysis.

The heating of the T-Jump probe is also synchronized with the time-of-flight measurement system by triggering the probe power supply from the pulse generator as shown in the timing sequence diagram (There is ~2 μ s delay between trigger and monitor signal, for illustration purpose we show them as the same pulse in figure 3). The temporal voltage and current of the T-Jump probe during the heating event is recorded, so that a resistivity measurement can be obtained, and related to the instantaneous temperature, which can be mapped against the mass spectra.

RESULT AND DISCUSSION

Before testing the T-Jump/TOF mass spectrometer, T-Jump probe heating experiments were conducted by heating an un-coated wire to evaluate the performance of T-Jump probe. The heating rate of the probe can be varied by changing the heating pulse width and the output pulse intensity. The pulse width can be varied from ~1 ms to ~100 ms, with a maximum output voltage of ~50 V. Figure 4 (a) shows a typical current, voltage trace, while figure 4 (b) shows the resulting temporal temperature of the platinum wire. Since the rise time of the heating pulse is in the range of 10 to ~100 us depending on the output pulse voltage, the resistance and the corresponding temperature is calculated after the rise time of the heating pulse. Thus the filament temperature is estimated to be ~400 K initially, and reaches ~1800 K after the 2.5 ms; i.e. a heating rate ~640,000 K/s.

Another important factor to consider in the design of the T-Jump/TOF mass spectrometer is the nature of the ion extraction in the presence of the T-jump probe. The nominal configuration of the ion extraction electrode assembly ensures a uniform extraction field between the plates³⁴. However the presence of the probe and in particular its location was found experimentally to be a sensitive parameter to both signal sensitivity and resolution. One might reasonably expect that placing the probe too close to the extraction plates would distort the electric field, and result in a decrease in the mass spectrometer's resolution. Placing the probe too far away from the ionization region would lower the concentration of reaction product species in the ionization region, and consequently decrease the sensitivity of the measurement. The effect of the T-Jump probe position was examined experimentally by inserting the probe at different distances from the plates, and monitoring the ion signal from the background gas. The relative water

(H₂O) ion intensity are plotted in figure 5 (a) as a function of probe position. Each experimental data point is an average of 40 mass spectrum measurements, and normalized by the ion intensity measured without the presence of the T-Jump probe. As a comparison to the experimental data, the effect of the T-Jump probe on the electric field and ion detection was also evaluated by conducting ion-trajectory simulations using Simion.³⁵ In the simulation, water ions with +1 charge were placed in the center plane of the ion extraction region with a uniform distribution, and their flight trajectories were calculated for the voltages used in the experiment. The relative ion abundance calculated from trajectory simulation is also plotted as the function of probe position in figure 5 (a). Both simulation and experimental data show that the ion signal is significantly decreased when the probe is placed close to the extraction plates. As the probe moves away from the plates, the ion signal increases, and reaches a plateau at a distance of 1.3 cm, suggesting that the presence of the grounded probe significantly perturbs the electric potential in the ion source region. Figure 5 (b) shows the calculated electric potential and ion trajectories for T-Jump probe placed 1.3 cm from the ionization region. When compared with the no-probe case in figure 5(c), it is clear that the probe induces considerable distortion to the electric potential, and ion trajectories in the region closest to the T-Jump probe, but very little change for ion trajectories in the central region. As we further move the probe away from the ionization region, even though the effect of the probe on the electric field is minimized, a slight decrease of the ion signal in the experimental data was observed. This implies that at larger distances sensitivity will be lost for material originating from the probe, and that a distance 1.3 cm would seem to be a near optimal for this system.

Nitrocellulose and hexahydro-1,3,5-trinitro-1,3,5-triazine (RDX) samples were used to test the performance of the T-Jump/TOF mass spectrometer as examples of a slow and fast “burners”. In these experiments, Nitrocellulose sample (Mallinckrodt Baker Inc. Phillipsburg, NJ, USA) or RDX was mixed with diethyl ether or acetone, and a small amount of solution (~0.07ml) is coated on the T-Jump filament surface using a dropper. While the eventual goal of this instrument is to use the temporal mass spectra, and temperature, to extract mechanistic information, the purpose of the present results is focus on illustrating the capabilities of the instrument.

The mass spectra obtained for rapid pyrolysis of nitrocellulose are shown in figure 6. The heating duration is about 9 ms with a heating rate of $\sim 1.3 \times 10^5$ K/s, with a total of 95 spectra sampled with a temporal resolution of 100 μ s per spectrum (10000Hz). Out of the 95 spectra obtained in the experiment, we plot 17 of them in figure 6, along with a more, detailed view of a spectrum at $t = 2.5$ ms. Since the heating pulse is synchronized with the first EI duration, the mass spectrum at $t = 0$ ms is actually the background in the ion source region, which consists of water (m/z 18), N₂ (m/z 28), N (m/z 14), OH (m/z 17), O₂ (m/z 32), and H (m/z 1). We sampled up to $m/z \sim 300$ for each spectrum, but no heavy ions were observed, and major ions are only seen for $m/z < 100$. At $t = 1.7$ ms, the estimated temperature of the probe is ~ 575 K, and a new ion of m/z 31 appears which suggest the start of the reaction. At $t = 1.8$ ms which corresponds to a probe temperature ~ 590 K, the ion signal intensity of m/z 31 increases along with ions at m/z of 15, 27, 29, 45 and 59. As the reaction time advances to $t = 1.9$ ms ($T \sim 600$ K), ion m/z 31 achieves its maximum intensity, and now ions at m/z 30 and 46 appear, along with m/z 16, 43, and 44. These species last for the whole duration of the heating pulse (~9ms), and some

species are still present well after the end of the wire heating due to the self-burning of nitrocellulose. The time-resolved feature of the spectra allows us to extract the characteristic time of the reaction. As the highest ion intensity for most of major ions were achieved at $t = 2.3$ ms, following which the ion signals gradually decreases with no noticeable changes after 4 ms, it is suggested that the most aggressive reaction (ignition) happens within ~ 4 ms, and the whole reaction lasts ~ 9 ms. We compare our results for nitrocellulose thermal decomposition with experiments done at lower heating rates. Chen et al used a SMATCH (Simultaneous MAss and Temperature Change)/FTIR system to examine decomposition products of a nitrocellulose film heated at a rate of up to 320°C/s . The reaction products are noted as, NO, CO, CH_2O , CO_2 , HCOOH, and NO_2 .³⁶ which we also see, although we are unable to distinguish HCOOH from NO_2 . It should also be noted that although m/z 28 is part of our background signal of N_2 , there is significant increase for this peak during the heating event, which most likely can be attributed to CO. We also compare work with that of Dauerman and co-workers who used a mass spectrometer paired with a low-pressure strand burner to examine nitrocellulose combustion.²¹ This work shows multiple spectra at different times during heating, which include significant ions that are consistent with our work. The major ions cited are m/z of 14, 15, 16, 17, 18, 27, 28, 29, 30, 31, 43, 44, 45, 46, which are all seen in our experiment excepting m/z 14, 17, 18. We are currently continuing our studies in developing a mechanism and its comparison with theoretical work by Melius which suggests possible condensed-phase initial reaction steps in nitrate ester decomposition.³⁷ The reaction pathway shows consistencies to our findings, and will be more fully addressed in a subsequent publication.

RDX was used as a second example to test the T-Jump/TOF mass spectrometer. RDX decomposition has been the subject of investigation under different conditions. Behrens and co-workers have studied RDX decomposition using the simultaneous thermogravimetric modulated beam mass spectrometry (STMBMS).^{27, 38, 39} The results via STMBMS provide detail information about both mechanisms and rates of reaction of RDX decomposition under low heating rate (~1K/min). The combustion like decomposition of RDX has been studied using a T-jump/FTIR method^{2-4, 13, 16, 40} with a heating rate at $\sim 10^3$ K/s. In our experiments, a heating rate of $\sim 10^5$ K/s was used to study the ignition and combustion of RDX. Similar to the nitrocellulose experiment, we use a sampling rate of 100 μ s per spectrum (10,000Hz) to capture the progression of the reaction. The heating pulse is about 8 ms at a heating rate of $\sim 1.5 \times 10^5$ K/s, and a total of 95 spectra obtained. Figure 7 shows that species, other than background species (water/N₂/O₂), only appear from 0.7 ms - 2.6 ms, which corresponds to a wire temperature of 370K to 670K. These results clearly show as expected that RDX is more reactive than Nitrocellulose, and occurs over an interval of only ~2 ms. Although a m/z range up to 400 was recorded for each spectrum, no heavy ions were observed above m/z 150. The major ions from RDX decomposition observed are m/z 15, 28, 29, 30, 42, 46, 56, 75 and 127. Small ions of m/z 14, 16, 41, 43, 81, 120 are also found in some spectra. The RDX mass spectra in terms of m/z values observed and their most likely ions structures are tabulated in table 1. Similar to the T-jump/FTIR method,^{2-4, 13, 16, 40} species of NO₂, CH₂O, NO, CO, HNCO are also observed by our T-jump/TOF mass spectrometer. Using gas phase CO₂ laser photolysis of RDX, which provided extremely high heating rates, Zhao et al. observed ions at 42, 56, 75, 81, 120 and 127, which we

also see in our experiments⁴¹. However, HONO, HCN and N₂O which are reported in both T-jump/FTIR and gas-phase infrared multiphoton dissociation experiments were not detected under our conditions. The differences point to the complex nature that heating rate and ambient environment may play in probing the decomposition pathways. For example, it is believed that two global reactions are responsible for the decomposition of RDX under flash heating condition.^{13, 40} The reaction channel which leads to the formation of N₂O is dominant at lower temperatures, while the reaction channel to NO₂ favors the higher temperatures. Our heating rate is much higher than the heating rate employed in T-jump/FTIR experiments ($\sim 10^5$ K/s vs. $\sim 10^3$ K/s) it is possible that the chemistry is dominated by the NO₂ channel and N₂O is not favored under these conditions. Moreover, as one of the motivations in developing this T-jump mass spectrometer, was to minimize or eliminate the gas phase chemistry, the failure to detect species such as HCN and HONO and possibly N₂O suggests these may be formed primarily in the gas phase.

Since the purpose of this paper is to demonstrate of the operation and capabilities of the instrument, we defer further analysis on rates of reactions and mechanisms to the future. Based on the experimental results presented above, it is clear that the characteristic reaction time for energetic materials decomposition/combustion is in the order of milliseconds or even less. We note that while a time resolution of 100 μ s was used to test and demonstrate the instrument, the T-Jump/TOF mass spectrometer can be operated with a scanning rate up to ~ 30 kHz. The experimental results suggest that the time-resolved spectra obtained using T-jump/TOF mass spectrometer shoud have sufficient

sensitivity, and time resolution to probe the reaction dynamics of extremely fast condensed state reactions at high heating rates.

CONCLUSION

A new Time-of-Flight mass spectrometer (TOFMS) combined with a temperature jump technique is described. The instrument allows for the time resolved characterization of the decomposition, ignition, and combustion of solid energetic materials or other highly reactive condensed state reactions. Using heating rates of up to 10^5 K/sec, samples of nitrocellulose and RDX were ignited, and time resolved mass spectra were obtained. By monitoring the electrical characteristics of the heated wire, the temperature could also be obtained and correlated to the mass-spectra. When combined with the time dependent temperature information, the results indicate that the instrument can capture the signature of rapid condensed phase reactions in a time resolved manner.

REFERENCES

- (1) Vyazovkin S. *Analytical Chemistry* **2006**; *78*: 3875.
- (2) Brill TB, Brush PJ, James KJ, Shepherd JE, Pfeiffer KJ. *Applied Spectroscopy* **1992**; *46*: 900.
- (3) Brill TB, Arisawa H, Brush PJ, Gongwer PE, Williams GK. *J. Phys. Chem.* **1995**; *99*: 1384.
- (4) Thynell ST, Gongwer PE, Brill TB. *Journal of Propulsion and Power* **1996**; *12*: 933.
- (5) Furutani H, Fukumura H, Masuhara H, Kambara S, Kitaguchi T, Tsukada H, Ozawa T. *J. Phys. Chem. B* **1998**; *102*: 3395.
- (6) Roberts TA, Burton RL, Krier H. *Combustion and Flame* **1993**; *92*: 125.
- (7) Ward TS, Trunov MA, Schoenitz M, Dreizin EL. *International Journal of Heat and Mass Transfer* **2006**; *49*: 4943.
- (8) Dauerman L, Salser GE, Tajima YA. *Aiaa Journal* **1967**; *5*: 1501.
- (9) Blais NC, Fry HA, Greiner NR. *Review of Scientific Instruments* **1993**; *64*: 174.
- (10) Makashir PS, Mahajan RR, Agrawal JP. *Journal of Thermal Analysis* **1995**; *45*: 501.
- (11) Mahadevan R, Lee D, Sakurai H, Zachariah MR. *J. Phys. Chem. A* **2002**; *106*: 11083.
- (12) Trunov MA, Schoenitz M, Dreizin EL. *Propellants Explosives Pyrotechnics* **2005**; *30*: 36.
- (13) Kim ES, Lee HS, Mallory CF, Thynell ST. *Combustion and Flame* **1997**; *110*: 239.
- (14) Brill TB, Gongwer PE. *Propellants Explosives Pyrotechnics* **1997**; *22*: 38.
- (15) Brill TB, Ramanathan H. *Combustion and Flame* **2000**; *122*: 165.
- (16) Hiyoshi RI, Brill TB. *Propellants Explosives Pyrotechnics* **2002**; *27*: 23.
- (17) Morelli JJ. *Journal of Analytical and Applied Pyrolysis* **1990**; *18*: 1.
- (18) Park K, Lee D, Rai A, Mukherjee D, Zachariah MR. *J. Phys. Chem. B* **2005**; *109*: 7290.
- (19) Yang M, Ramsey JM, Kim BJ. *Rapid Communications in Mass Spectrometry* **1996**; *10*: 311.
- (20) Jones DEG, Turcotte R, Acheson B, Kwok QSM, Vachon M. *International Annual Conference of ICT* **2003**; *34th*: 46/1.
- (21) Dauerman L, Tajima YA. *Aiaa Journal* **1968**; *6*: 1468.
- (22) Farber M, Srivastava RD. *Combustion and Flame* **1978**; *31*: 309.
- (23) Fowler AHK, Munro HS. *Polymer Degradation and Stability* **1985**; *13*: 21.
- (24) Blais NC, Engelke R, Sheffield SA. *J. Phys. Chem. A* **1997**; *101*: 8285.
- (25) Mileham ML, Kramer MP, Stiegman AE. *J. Phys. Chem. C* **2007**; *111*: 16883.
- (26) Stiegman AE, Mileham ML, Kramer MP. *Abstracts of Papers, 233rd ACS National Meeting, Chicago, IL, United States, March 25-29, 2007* **2007**: INOR.
- (27) Maharrey S, Behrens R. *J. Phys. Chem. A* **2005**; *109*: 11236.
- (28) Minier L, Behrens R, Bulusu, S. *Journal of Mass Spectrometry* **1996**; *31*: 25.
- (29) Behrens R. *Review of Scientific Instruments* **1987**; *58*: 451.
- (30) Korobein Op, Boldyrev VV, Karpenko YY. *Combustion Explosion and Shock Waves* **1968**; *4*: 19.

- (31) Chowdhury A, Thynell ST. *Thermochimica Acta* **2006**; *443*: 159.
- (32) Umbrajkar SM, Schoenitz M, Dreizin EL. *Thermochimica Acta* **2006**; *451*: 34.
- (33) Lee D, Park K, Zachariah MR. *Aerosol Science and Technology* **2005**; *39*: 162.
- (34) Wiley WC, McLaren IH. *Review of Scientific Instruments* **1955**; *26*: 1150.
- (35) Dahl DA, V.8.0 ed.; Scientific Instrument Services, Inc. www.simion.com: Ringoes, NJ.
- (36) Chen JK, Brill TB. *Combustion and Flame* **1991**; *85*: 479.
- (37) Melias CF, Piqueras MC. *Proceedings of the Combustion Institute* **2002**; *29*: 2863.
- (38) Behrens R, Bulusu S. *J. Phys. Chem.* **1992**; *96*: 8891.
- (39) Behrens R, Bulusu S. *J. Phys. Chem.* **1992**; *96*: 8877.
- (40) Brill TB, Brush PJ, Kinloch SA, Gray P. *Philosophical Transactions of the Royal Society of London Series a-Mathematical Physical and Engineering Sciences* **1992**; *339*: 377.
- (41) Zhao X, Hintsa JE, Lee YT. *The Journal of Chemical Physics* **1988**; *88*: 801.

Table 1. ions observed from mass spectra of RDX pyrolysis and their possible assignments.

m/z	Species
14	N [#]
15*	CH ₃ , NH
16	O
17	OH [#]
18*	H ₂ O [#]
28*	N ₂ [#] , CH ₂ N, CO
29*	HCO
30*	NO, CH ₂ O
32	O ₂ [#]
41	CHN ₂
42*	C ₂ H ₄ N, CH ₂ N ₂ , CNO
43	HCNO
46*	NO ₂
56*	C ₂ H ₄ N ₂
75*	CH ₃ N ₂ O ₂
81	C ₃ H ₃ N ₃ (1,3,5-triazine)
120	CH ₂ N ₃ O ₄

127*

 $C_3H_3N_4O_2$

(*) major ions

(# species also observed in background MS

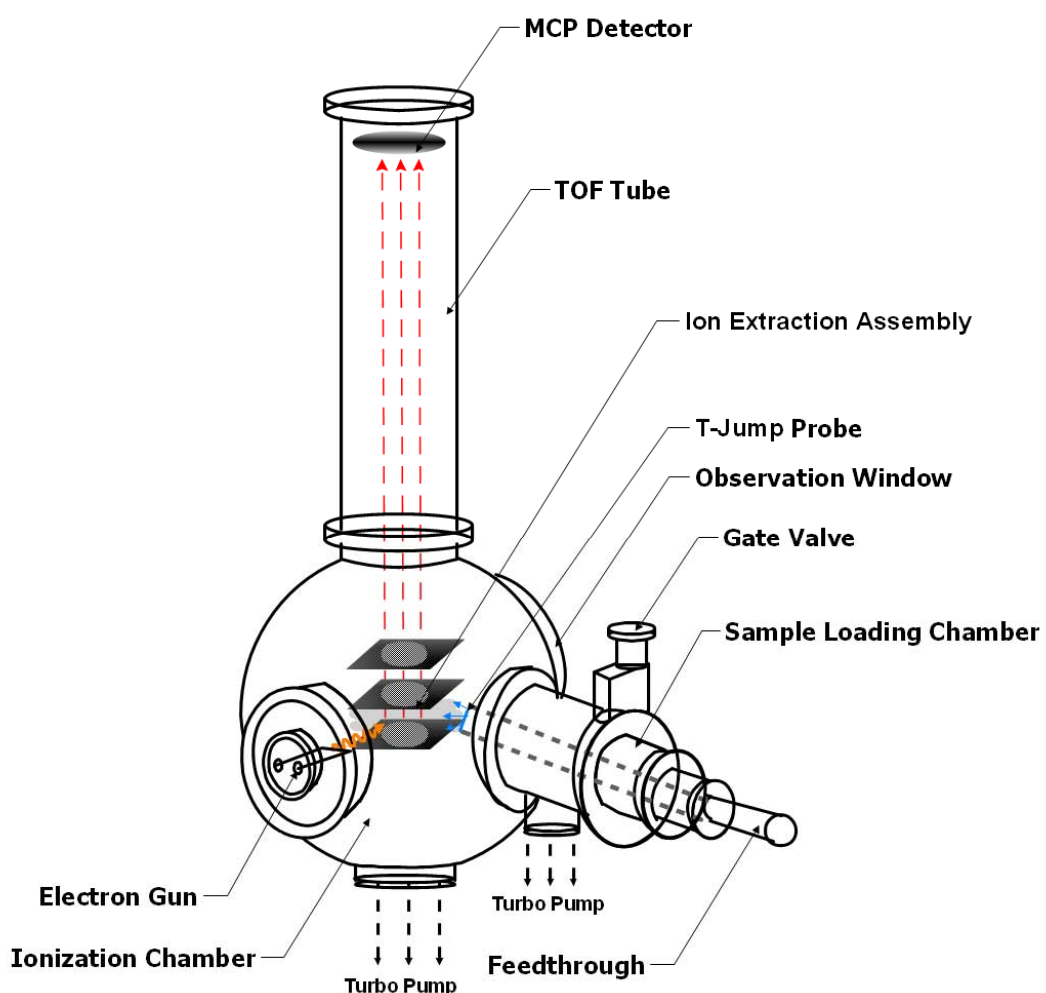


Figure 1. Schematic of T-Jump/TOF mass spectrometer.

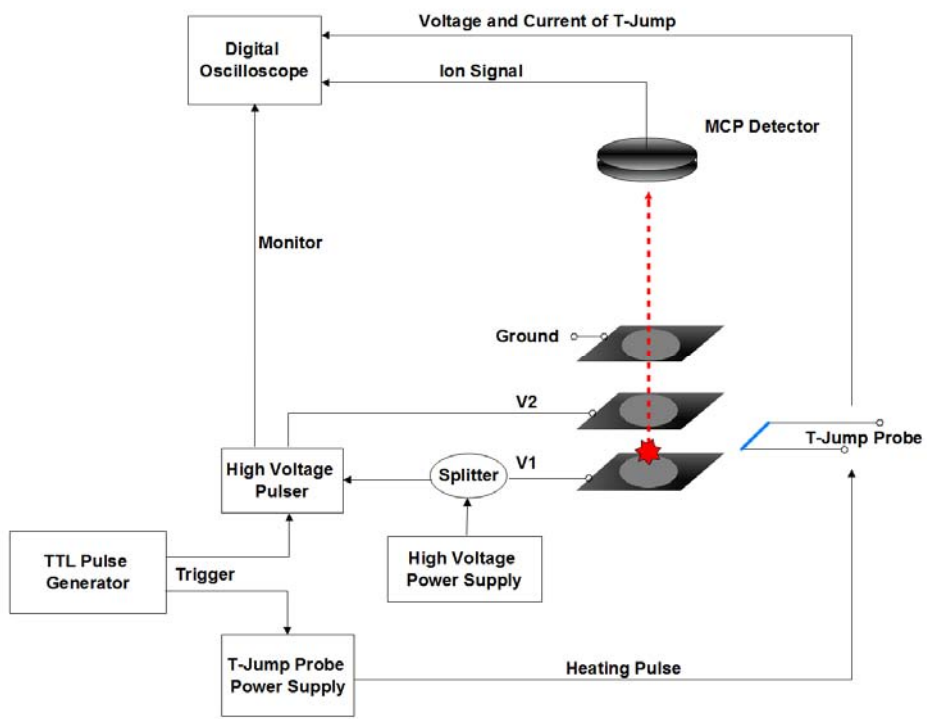


Figure 2. Schematic of the control and data acquisition system for the T-Jump/TOF mass spectrometer.

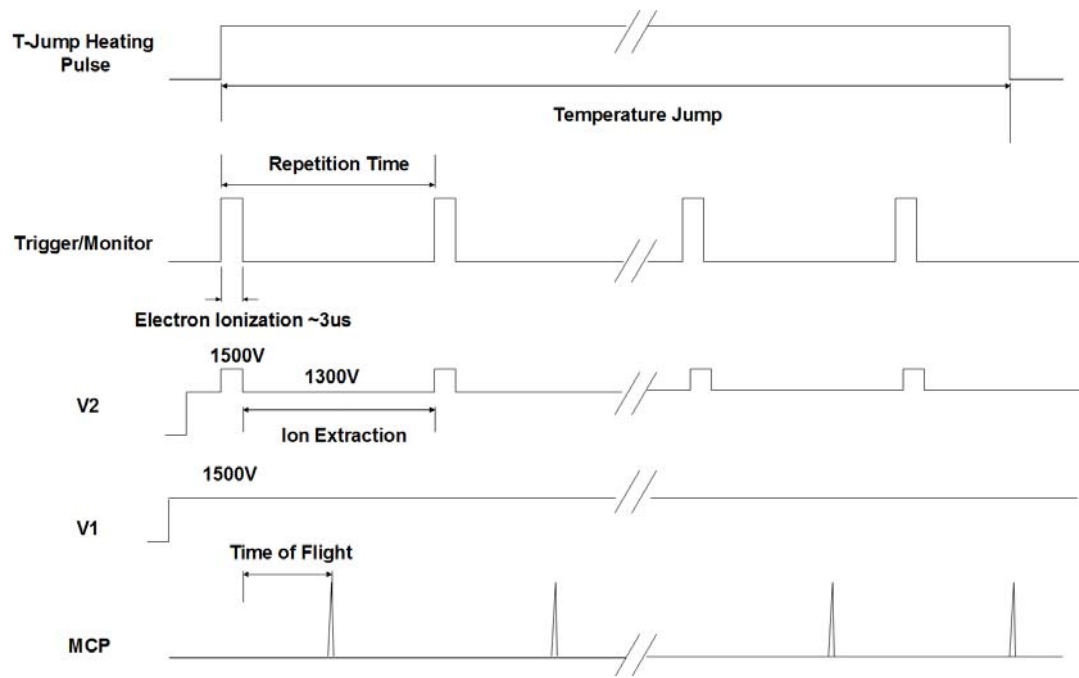


Figure 3. Pulse sequence used for EI ionization and ion extraction in the T-jump/TOF mass spectrometer.

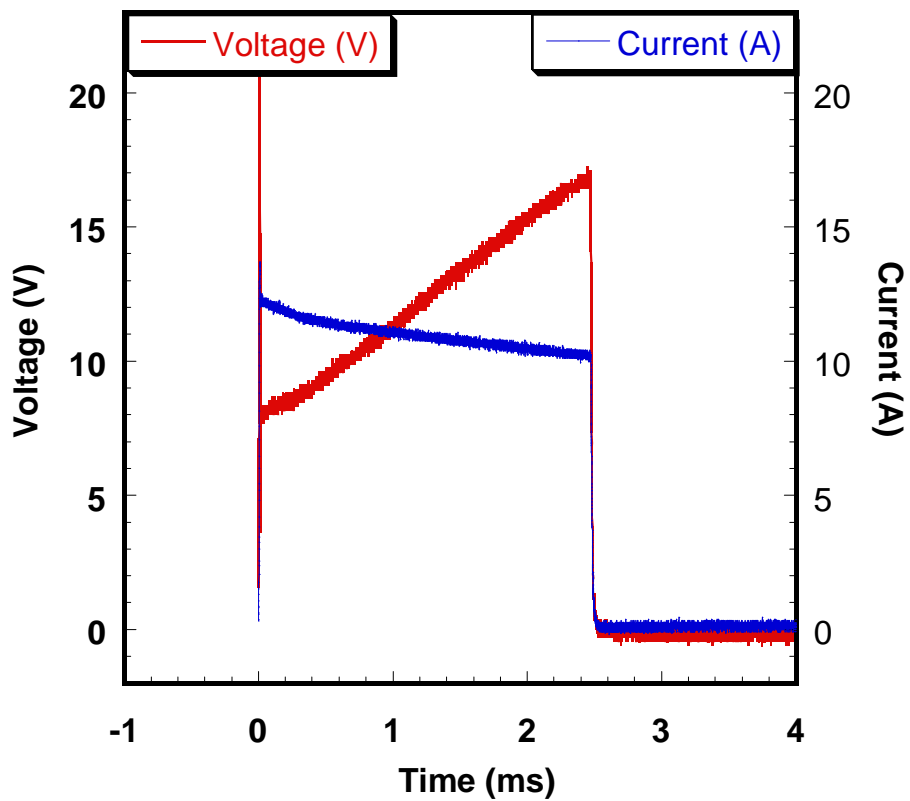


Figure 4 (a). Voltage and current across the T-Jump probe.

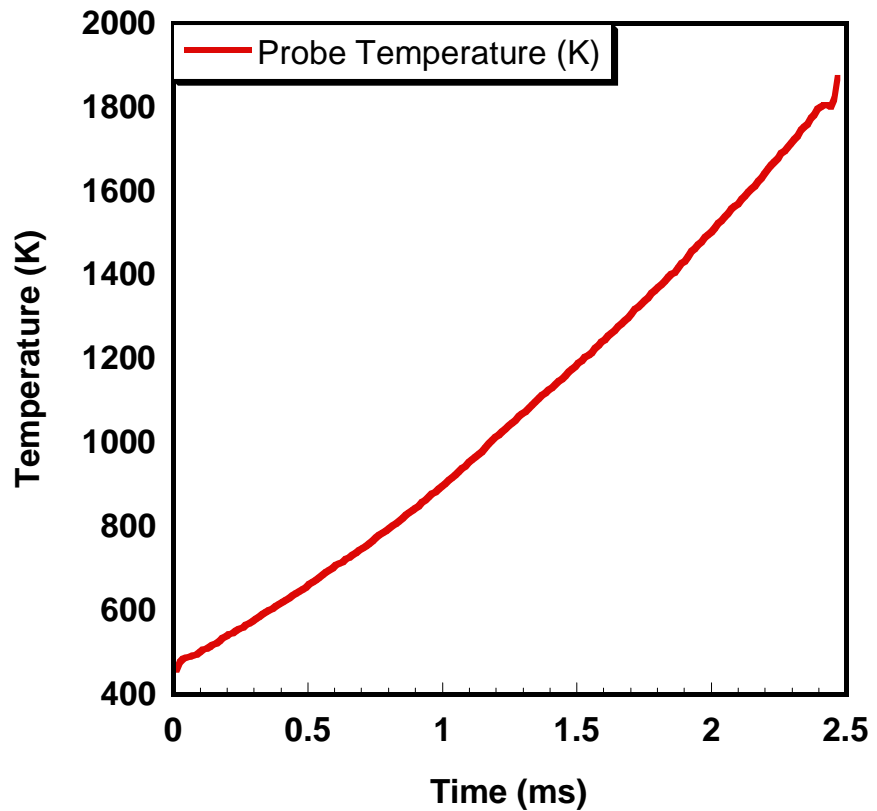


Figure 4 (b). Estimated probe temperature from electrical resistance

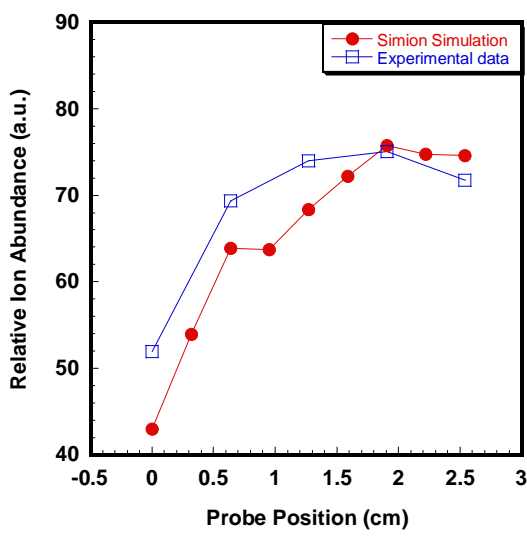


Figure 5 (a)

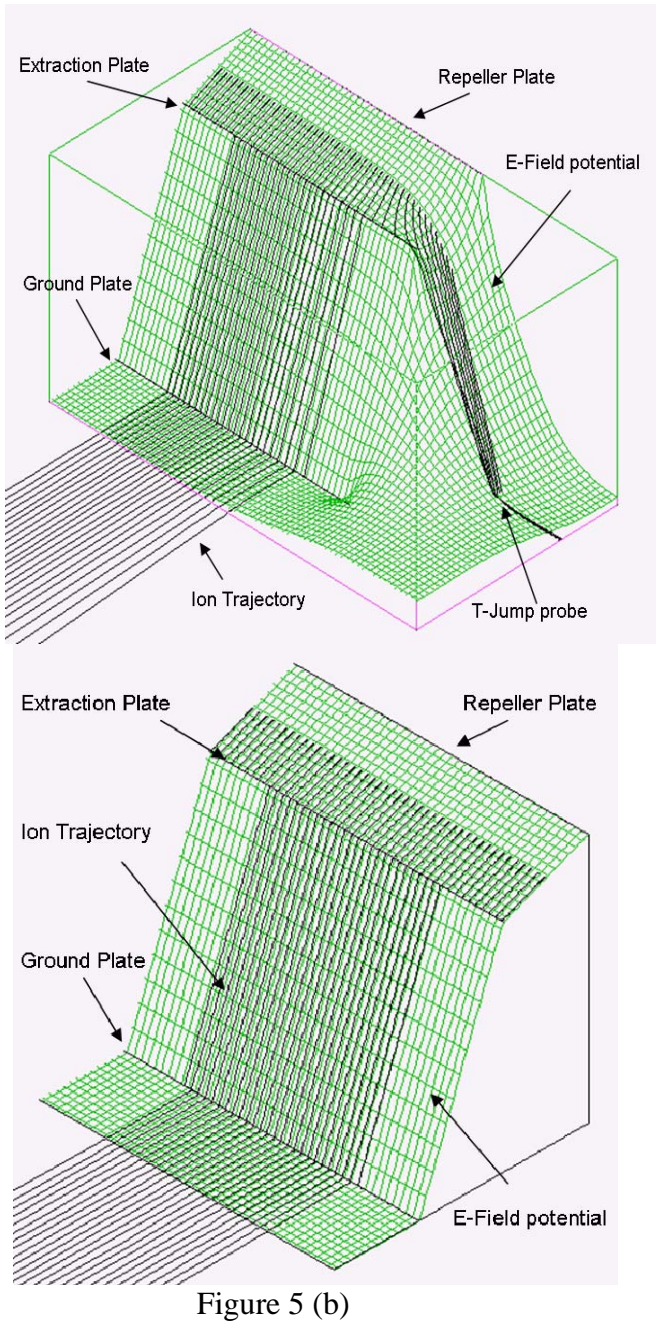


Figure 5 (b)

Figure 5 (c)

Figure 5 (a). Relative water ion abundance as a function of the probe filament position.

(b). Ion trajectory and electric potential at ion source region with the presence of T-Jump probe. **(c)** Ion trajectory and electric potential calculation at ion source region without probe.

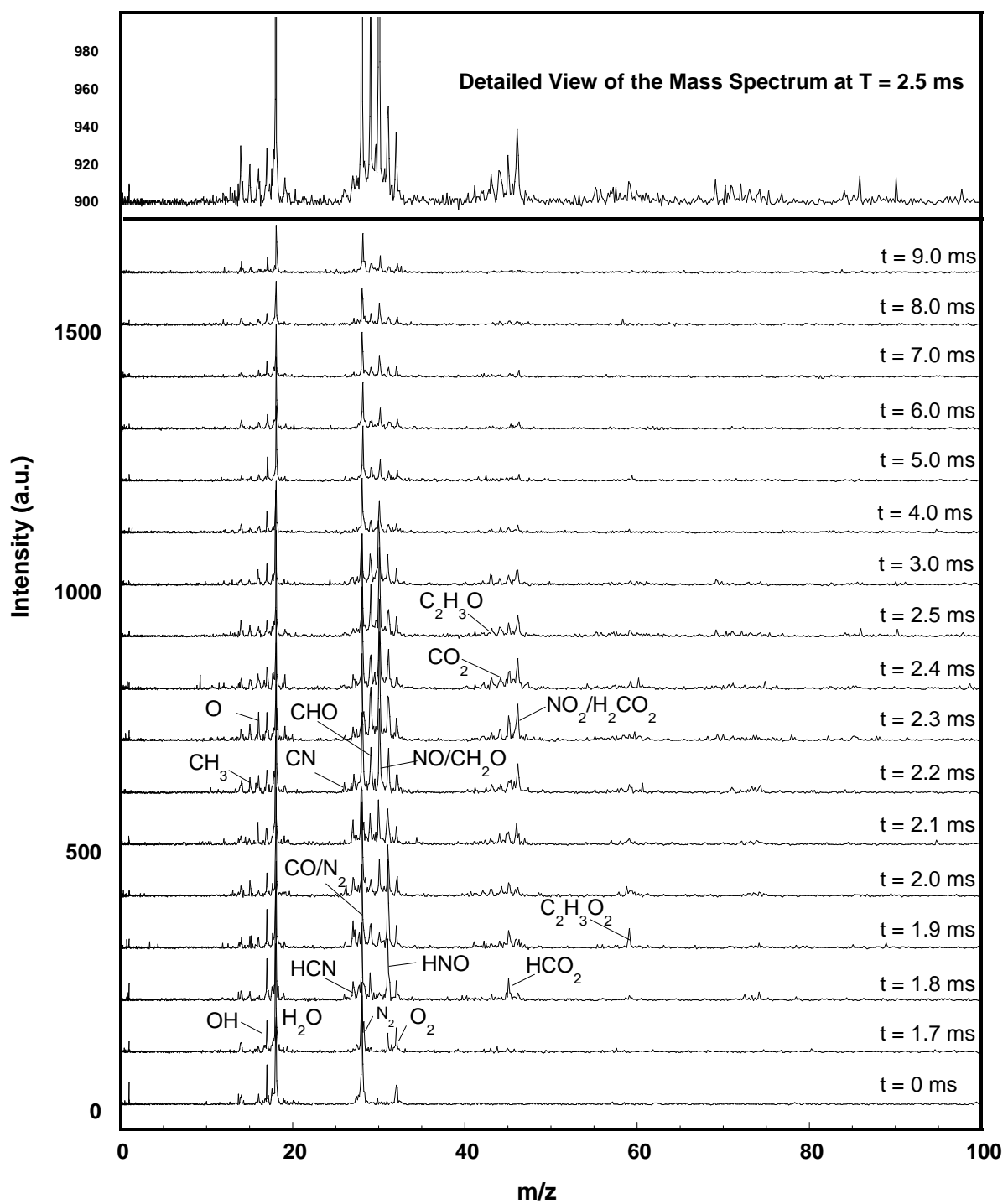


Figure 6. Time resolved mass spectrum from rapid heating of nitrocellulose. Heating rate $\sim 1.3 \times 10^5$ K/s

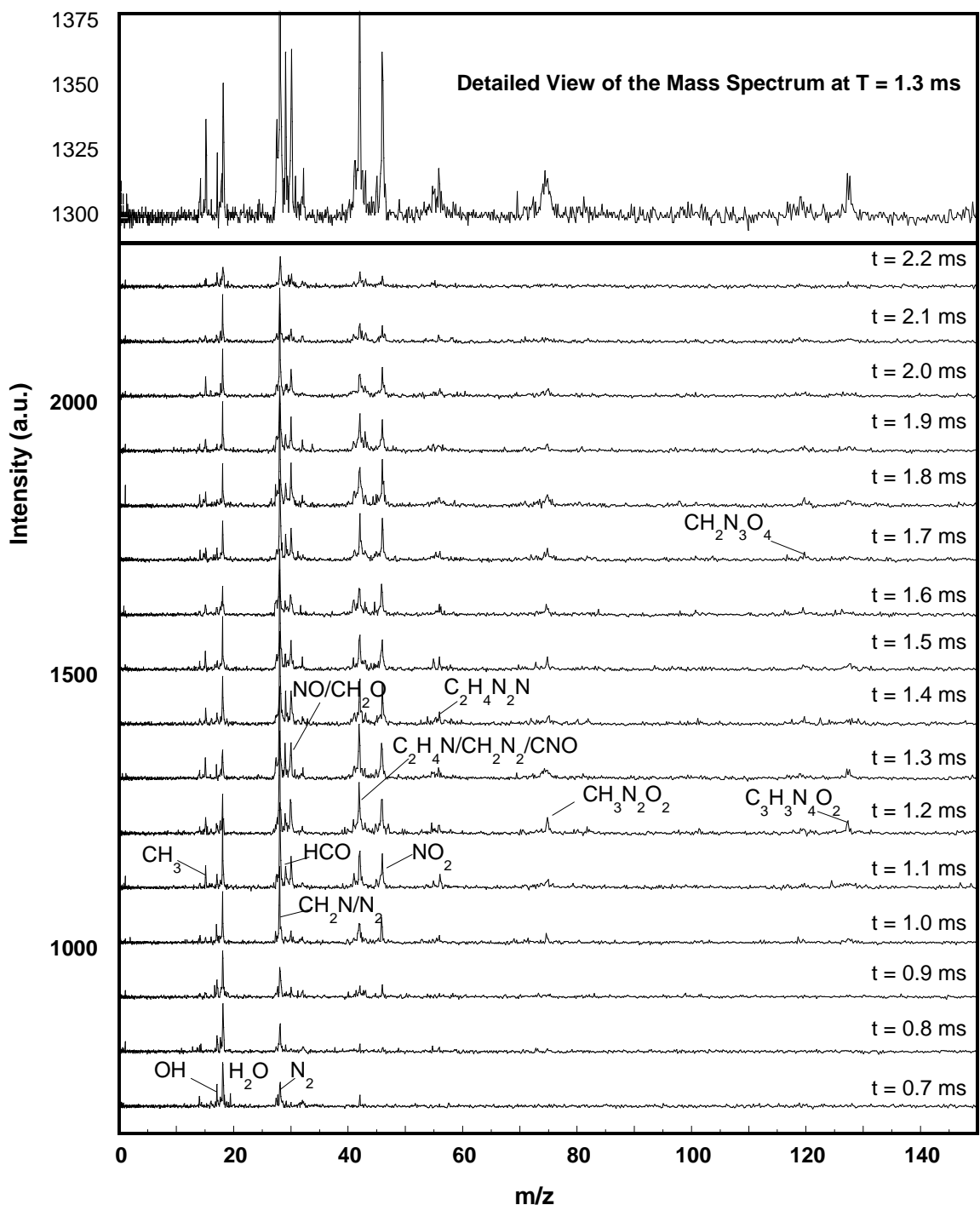


Figure 7. Time resolved mass spectrum from rapid heating of RDX. Heating rate $\sim 1.5 \times 10^5$ K/s

Diffusive vs. Explosive Reaction at the Nanoscale

Snehaunshu Chowdhury, Kyle Sullivan, Nicholas Piekiel, Lei Zhou and Michael R.

Zachariah *

University of Maryland at College Park, MD 20742

Email: mrz@umd.edu.

*Corresponding author. Phone: 301-405-4311. Fax: 301-314-9477

ABSTRACT. Solid-Solid reactions at the nanoscale between a metal passivated with a nascent oxide, and another metal oxide can result in a very violent reaction. The natural question is what mechanism is responsible for such a rapid reaction. The ignition of nanoscale Al/CuO thermites with different aluminum oxide shell thicknesses was investigated on a fast heated Pt wire. ($\sim 10^5 \text{ K/s}$). Ramping the wire temperature to $\sim 1250 \text{ K}$, and then shutting off the voltage pulse results in ignition well after the pulse it is turned off- i.e. and ignition delay is observed. The delay is used as a probe to extract effective diffusion coefficient of the diffusing species, which is confirmed by fast time-resolved mass spectrometry. The results of this experiment are consistent with a diffusion controlled ignition mechanism.

KEYWORDS. Solid-solid reactions, ignition mechanism, mass spectrometry of Al-CuO nanothermite reactions, diffusion mechanism.

1. Introduction

Nanoscale particles composed of a metal and metal oxide can undergo a violent thermite reaction. Furthermore it is well known that making the particles smaller increases the reaction rate dramatically. An example of such a system is Al + CuO, which under stoichiometric conditions yield an adiabatic reaction temperature of 2840 K, with an energy density more than a factor of 3 over TNT on a volumetric basis. Nevertheless because of the interrelationship between many complex processes occurring, considerable debate continues as to the nature of initiation of the thermite event. Close proximity of the fuel and oxidizer reduces the diffusion length and increases the reaction rate¹. Fuel nanoparticles usually have lower melting point than their micron size counterparts^{2,3} making them easier to ignite. However, for very small particles, heat transfer rates are extremely fast and hence reaction characteristics such as onset of reaction, ignition temperature, ignition delays etc. are known to depend on the particle size⁴⁻⁶.

We consider the Al/CuO nanoscale thermite system as representative of the wide class of such reactions. The aluminum fuel component is actually a core shell structure of an aluminum core with an aluminum oxide passivation layer. Typically such layers are on

the order of a few nanometers⁷. The interaction between the low melting core and high melting shell is critical in understanding the ignition mechanism at the nanoscale. Nominally, we consider the nanoscale regime to be those where both components (metal and metal oxide) are below 100 nm in diameter.

It is important, before proceeding further, to define some terminologies. Ignition temperature is defined as the temperature at which a particle/mixture can sustain chemical reaction on its own, without the aid of an external heat source. Ignition temperature is a strong function of experimental conditions as well as material property.

Several researchers have reported that the ignition temperature of micron sized aluminum is very close to the melting point of the metal oxide (Al_2O_3) shell⁸⁻¹⁴. On the other hand, nano-sized aluminum exhibits much lower ignition temperatures closer to the melting point of aluminum¹⁵⁻¹⁹. In other cases reaction (but not ignition) occurs at well below the melting point when probed by low heating rate experiments (10's K/min). For example, Umbrajkar et al.¹⁶ reports evidence of reaction occurring at temperatures as low as 400 K in thermal analysis experiments. However, the reaction rate in such systems is not high enough to lead to thermal runaway and ignition. In shock tubes with heating rates of $\sim 10^6$ K/s the ignition temperature of nanoaluminum has been observed to be in the range 1200-2100 K at elevated pressures¹³. Nanoaluminum, thus, has been reported to have a wide range of ignition temperatures as compared to micron sized aluminum. Studies also report the effect of the type of shell and its thickness on the chemical reactivity of the particle. Jones et al.²⁰ found that aluminum nanoparticles with aluminum oxide and Teflon coatings have a remarkable difference in its reactivity towards water. Levitas et al.²¹ has suggested that an initiation event via the melt dispersion mechanism

(described below) would be promoted if the temperature of formation of the oxide shell is increased.

Two different mechanisms have been proposed in the literature to explain the observed behavior for nanoaluminum. These mechanisms differ significantly in the way ignition occurs. The first mechanism states that the ignition and reaction of nanoaluminum has a diffusion based mechanism where participating species diffuse across the oxide shell. Rai et al.²² has shown that even with low heating rate, the aluminum core melts and exerts pressure on the oxide shell causing it to crack (not violently). In contrast, the melt dispersion mechanism, proposed by Levitas et al.²¹, requires the mechanical rupture of the shell and thereby release of the aluminum for ignition/reaction. According to this mechanism, under high heating rates the core melts very quickly and volumetrically expands while the oxide shell remains solid. If the stress on the shell becomes high enough, it causes the oxide shell to suddenly rupture explosively followed by the ejection of small molten aluminum clusters²¹. However, the current knowledge about the exact physical mechanism is still unclear.

A resolution of the two opposing views is the subject of this letter. The assessment of the prevailing mechanism is done by systematically changing the thickness of the oxide shell to determine the ignition temperature and characteristic reaction time. Our studies will show that this highly violent reaction is likely based on a diffusion mechanism.

2. Experiment

In this study we prepare mixtures of Al/CuO nanoparticles that are coated onto a fine wire. The wire is rapidly joule heated using a pre-programmed voltage pulse and the

point of ignition is recorded with a photomultiplier tube. In addition, time resolved time-of-flight mass-spectrometry enables us to obtain temporal speciation of the reaction. The key point is the preparation of metal with different oxide thicknesses, and our ability to accurately measure temperature during heating rates of $\sim 10^5$ K/sec.

a) Sample Preparation

Commercially available aluminum powder ALEX procured from Argonide Corporation has been used in this study. The particles have a nominal size of ~ 50 nm with an active aluminum content of $\sim 70\%$ determined by thermogravimetric analysis (TGA). This would indicate an aluminum oxide shell thickness of ~ 2 nm which is consistent with TEM analysis. To increase the oxide thickness, particles were oxidized at 500 $^{\circ}\text{C}$, (i.e. below the melting point of aluminum) for various lengths of time, and subsequently weighed to determine the oxide growth. This ensures that the oxide shell thicknesses are formed at the same temperature, an important criterion in the melt dispersion mechanism. The shell thickness is calculated based on the weight gain and assuming spherical particles and bulk densities for Al and Al_2O_3 . The process was repeated until the gain in weight corresponded to thickening of the oxide shell to ~ 3 nm and 4 nm. The active aluminum content in those samples is thus changed to 59 and 50 % respectively. These measurements have an accuracy of $\pm 3\%$ limited by precision of the balance (0.1 mg). Appropriate amount of copper (II) oxide nanopowders (< 100 nm size) from Sigma Aldrich is weighed and mixed with the aluminum powders with different shell thicknesses to make 3 stoichiometric mixtures. Hexane is then added to the samples and sonicated for ~ 30 minutes to intimately mix the fuel and oxidizer. Table 1 below shows the preparation and composition of the three samples.

Table 1 Samples used in experiments and their preparation

Sample	Time in preheated furnace at 500 °C (mins)	Shell Thickness calculated from weight gain (nm)	Activity (%)
1	-	2	70
2	5	3	59
3	10	4	50

b) Experimental Setup

A thin platinum wire (length ~ 12 mm, diameter ~ 76 um) is joule-heated by a tunable voltage pulse generated by a home built power source. For any applied voltage (i.e. heating rate) the temperature to which the wire is heated can be controlled by varying the amplitude of the pulse, and the current passing through the circuit is measured transiently by a current probe. A small portion of the central region of the wire (~ 3-4 mm) is coated with the samples using a micropipette and the hexane is allowed to evaporate leaving a dense coating on the wire. The ignition event is recorded using a photomultiplier tube (PMT), and is identified by the appearance of a sudden emission of light above the background signal from the heated wire. In the context of this paper, ignition delay is defined as the time difference between the appearance of the ignition signal, identified as a sharp spike in the optical detector, and the end of the applied voltage pulse.

From the recorded voltage and current data, the temperature of the wire at the point of ignition can be calculated from the well known Callender- Van Dusen equation²³. A new wire is used each time a sample is heated.

3. Results

Figure 1 (a) shows the temperature of the wire and the PMT signal recorded as a function of time for such an event, for the three samples in Table 1 under condition of a heating rate of 1.7E5 K/sec. Heating rates were fairly repeatable with uncertainty $\sim 10^4$ K/s. The uncertainty associated with the measurement of maximum temperature is ± 50 K, based on several factors including contact resistance, length of wire, etc. The sharp rise in the PMT signal indicates the start of the reaction. The results show an apparent increase in ignition temperature from 1275 K to 1450 K as the shell thickness is increased. Please note that in this case, the wire temperature is being ramped past the ignition temperature. In a second experiment we vary the heating rate of 1.7e5 and 5.2e5 K/s and plot the result in Figure 1(b) for a particle with a 2 nm shell. Clearly observed is that the ignition temperature is heating rate independent in the range of heating rates carried out in this study. Similar behavior is observed for sample 2 and 3. The maximum heating rate is limited by the power supply and the shortest pulse duration that would not melt the platinum wire.

A next set of experiments are conducted in which we shut off the off the voltage pulse at a temperature below where the optical emission was observed in Figure 1(a). What we observed was that the powders could still be ignited even after the pulse had been shut off - *there is a very clear delay associated with ignition*. We define the ignition

delay as the time difference between when the pulse is shut off and the onset of optical emission. The maximum temperature of the wire is 1250K in all runs, and was decided by iteratively lowering the maximum temperature until just before no ignition was seen. Therefore, we are only heating the particles just to their ignition temperature and then observing as the ignition subsequently occurs.

The experimental data for the three different oxide shell thicknesses are shown in Figure 2. In all three samples, the wire was heated to 1250K at 3.2E5 K/s and then shut off. This temperature is just around the lowest ignition temperature of any particle determined in Figure 1(a). The ignition delays were fairly repeatable, with samples 1 (~20 μ s) and 2 (~50 μ s) showing lesser variability than sample 3 (~100 μ s). Since the heating pulses for the three samples are the same, in the absence of any reaction the system would be cooling. Despite this, a reaction event occurs, and the event time correlates with oxide shell thickness. *This is the key result of this paper which we will interpret.*

Finally time resolved time of flight mass spectrometry of Al-CuO MIC is also conducted on the samples as a qualitative tool to verify the delay in ignition. A description of the instrument, its operating procedures and verification could be found elsewhere²⁴. Figure 3 shows time resolved mass spectra taken at 100 μ s intervals for sample 1, the 2 nm shell thickness case. Species with strong signals, such as H_2O^+ ($m/z = 18$) and N_2^+ ($m/z = 28$) are background species while HCHO^+ ($m/z = 30$) and CO_2^+ ($m/z=44$) appears from small amount of copper carbonate formed on the surface of CuO. In this experiment, the heating pulse was turned off around 2.35 ms. Very relevant is that no Al^+ ($m/z = 27$) is seen before 2.35 ms, but appears at ~ 2.4 ms. Cu^+ ($m/z = 63.0$) starts

appearing at \sim 2.5 ms, suggesting an ignition delay of \sim 150 μ s. This compares very closely to the optical measurement which has better time resolution. Cu is never observed when CuO alone is heated and its appearance in mass spectrometry is analogous to the sharp rise in the PMT signal, as Cu is present only as a product species, and indicates start of the reaction. O_2^+ (m/z = 32) appears from the decomposition of CuO, $2CuO \rightarrow Cu_2O + \frac{1}{2} O_2$ and is seen before the pulse is turned off. Cu always appears in the same or after one spectrum of the appearance of Al. Another product species Al_2O^+ (m/z =70) appears around the same time as copper. A more detailed description of the mass spectrometric measurements on Al-CuO thermites is available in Zhou et al²⁵. Similar results were seen for sample 2 and 3, except that copper seemed to appear even later in the spectrum with increase in shell thickness.

4. Discussion

The independence of ignition temperature on heating rate for any given shell thickness is possibly a first suggestion against the melt dispersion mechanism, as it is expected be very sensitive to heating rate. However, the range of heating rates is fairly small in our case, which is restricted by the power supply. The change in ignition temperature in Figure 1(a) with oxide thickness could be explained as due to a longer path to diffusion through the oxide shell, rather than an increase in temperature. This point is most reinforced by the key observation in this work (Figure 2), that ignition occurs after the wire is turned off, and thus energy input to the system has ceased. Furthermore, the thicker the oxide shell, the greater the ignition delay - again consistent with a diffusion mechanism. According to the melt dispersion mechanism, reaction would occur at the

melting point of aluminum owing to the maximum mismatch in thermal expansion coefficient between the molten aluminum core and the solid oxide shell.

A simplified model simulation was carried out to estimate the actual powder temperature based on the model developed by Ward et al²⁶. Results show that the powder temperature is <5 K from the wire temperature. Also, once the pulse is shut off, the heat loss from the wire due to convection and radiation is minimal, which over the relevant time of the experiment decreases no more than ~ 50 K. This would indicate the ignition temperature of the powder exceeds the melting point of aluminum (~ 933 K) and contrary to what is expected according to the melt dispersion mechanism. The characteristic heat transfer time across a nanoparticle is on the order of a few nanoseconds, so that melting should occur essentially instantaneously once the melting point is exceeded. This would cause a huge buildup in internal pressure, and hence explode violently, in time scales ~ ns. However, we see no evidence of reactions at such time scales, rather we see delay times of ~100's of microseconds.

The melt dispersion mechanism is expected to happen at very high heating rates of 10^6 - 10^8 K/s²⁷. This was phenomenologically suggested from the rise time observed in pressure traces in burn tube experiments¹. However, in those experiments, the powder was set off by an electrical igniter. The external heating rate is thus unknown and hence, the above mentioned rate is clearly the “intrinsic” heating rate once the powder has ignited. The adiabatic flame temperature of Al-CuO mixture is ~2840K and the ignition temperature seen in this study is ~1200 K. The rise time (time for the optical signal to go from 0 to 1 in Fig. 2) observed in the optical signal is ~ 100 μ s. This would suggest an intrinsic heating rate of ~ 1.6e7 K/s, which is within the range of the melt dispersion

mechanism. As a result, we would assume that the “intrinsic” heating rate of the powder is sufficient to observe the melt dispersion mechanism if it were to happen.

An order of magnitude estimate of the effective diffusion coefficient ($= L^2/t_{\text{delay}}$) is presented in Table 2, with the delay times reported as an average of 2 experiments and the characteristic diffusion length (L) is assumed to be the thickness of the shell. The extracted diffusion coefficients, assuming a transport mechanism controlling seem quite reasonable²⁸.

Table 2 Ignition delay and effective diffusion coefficient with oxide shell thickness

Oxide shell thickness, L (nm)	t _{delay} (us)	D _{eff} (cm ² /s)
2	100	4.0E-10
3	500	1.8E-10
4	2000	8.0E-11

The appearance of Cu⁺ signal in mass spectrometry follows the same trend that we see in our optical experiments. We use Cu as evidence of reaction since it does not appear when we heat pure CuO, but rather only when the aluminum is present. Cu gas is a major reaction product of stoichiometric Al/CuO under vacuum, and so its signature is a strong indicator that the reaction is occurring. The appearance of copper later in the spectrum for samples 2 and 3 (relative to sample 1) indicates a delay in the initiation of those reactions and supports the diffusion controlled mechanism.

Based on the ignition temperature, the aluminum core would be molten. Although the purpose of this paper is not to determine the diffusion species, it is the aluminum ions from the molten core which are more likely to diffuse because of their smaller size

relative to oxygen ions. Evidence of the dominance of the diffusion of aluminum has been observed in other studies too. Rai et al.²⁸ have shown the formation of hollow particles during aluminum oxidation where the molten aluminum in the core has leaked out and reacted. Similar hollow particle formation has also been reported by Nakamura et al.²⁹ Henz et al.³⁰ has also recently showed that intrinsic electric fields within the nanoparticle promote the movement of aluminum ions through the oxide shell, which significantly enhance the initial transport over Fickian diffusion.

Once the reaction starts, an increase in temperature will cause enhancement in diffusion of all diffusing species. Although, based on Ref 28 and 29, we would expect all the aluminum in the core to leak out faster. However, we do not have direct evidence of this, and cannot from this set of experiment conclude more on the nature of the diffusing species.

Finally in Figure 4 we summarize the ignition delay observed for the various cases tested. Ignition delay increases with increase in shell thickness, with the 4 nm shell showing the longest delay. The mass spectrometric data compares well qualitatively with the optical data, and shows the same trend as identified by the appearance of the Cu signal. These observations point to an initiation mechanism governed by diffusion across the oxide shell.

5. Conclusions

Experiments were conducted at high heating rates to investigate the ignition mechanism of nano-thermites. Aluminum nanoparticles were prepared with varying oxide shell thicknesses, and were mixed with CuO to investigate the ignition behavior at

high heating rates of $\sim 10^5$ K/s. We find the ignition temperature is well above the melting point of aluminum, and ignition was not observed below 1250K. Furthermore *an ignition delay consistent with a diffusion limited reaction is observed*. The delay increased with increase in shell thickness of aluminum particles in the samples, and from this effective diffusion coefficients were extracted. Fast time-of-flight mass spectrometry shows that the appearance of copper, which is a product species, is progressively delayed in the mass spectra with increase in the shell thickness and agrees with the order of ignition delay observed. Based on our data, we would conclude that ignition under the heating rates investigated has a *diffusion governed mechanism*.

Figures

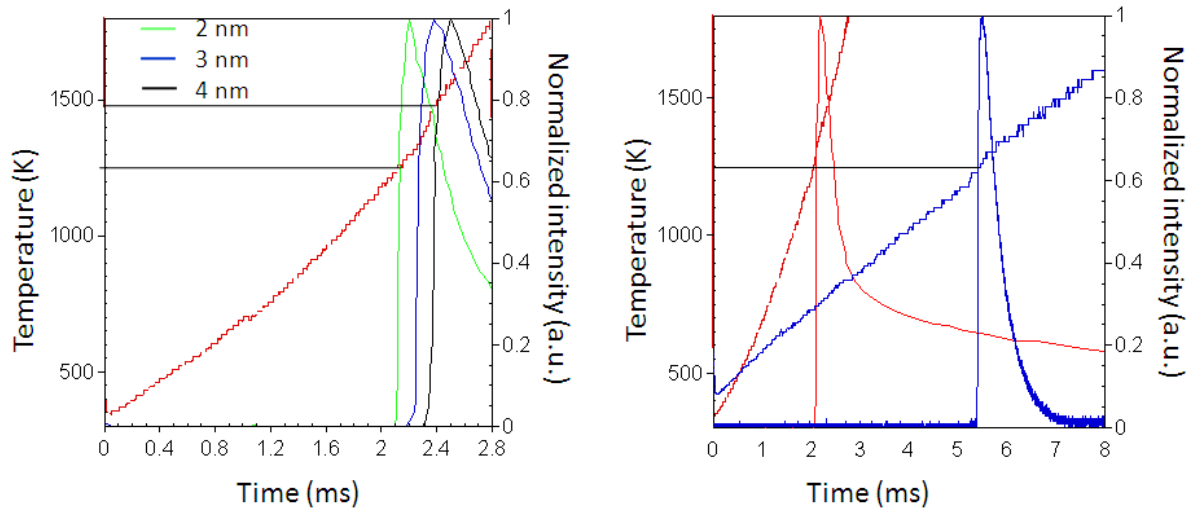


Figure 1(a) Ignition temperature for sample 1, 2 and 3 at $5.3\text{e}5$ K/s and 1(b) Effect of heating rate - $1.7\text{e}5$ K/s (blue) and $5.2\text{e}5$ K/s (red) on ignition temperature of sample 1.

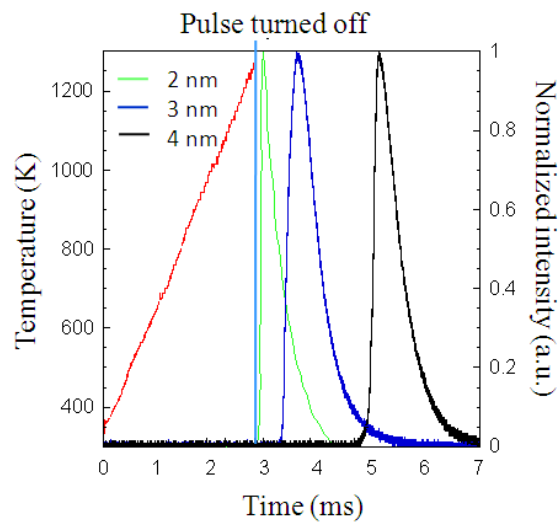


Figure 2 Ignition delay as observed with samples having different oxide shell thickness on aluminum. The maximum temperature attained by the wire is 1250 K as indicated by

the red curve. The wire cools down ~ 50 K in the longest times scales seen here after the pulse is turned off. Heating rate is $\sim 3.2\text{e}5$ K/s.

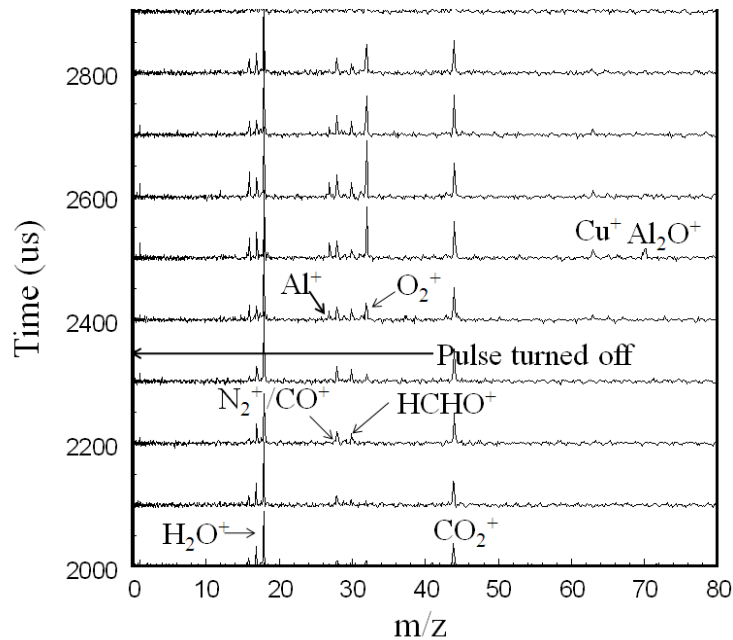


Figure 3 Time of flight mass spectrometric measurements for sample 1. The temperature of the wire when the pulse is turned off is around 1300 K. Species mentioned before the pulse is turned off emanates from background²⁵.

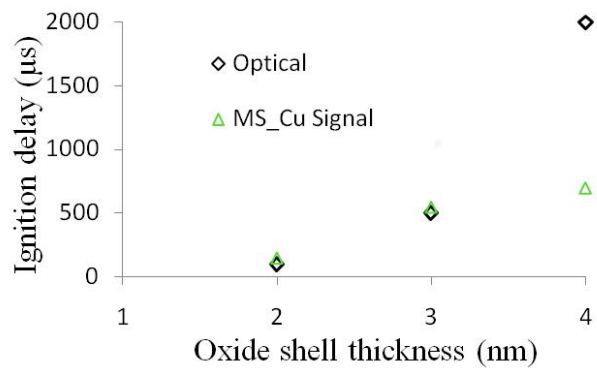


Figure 4 Ignition delay time as a function of various oxide shell thicknesses

References

1. B.S. Bockmon, M.L. Pantoya, S.F. Son, B.W. Asay and J.T. Mang, *J. of App. Phys.* 98, 064903, 2005.
2. P. Puri and V. Yang, *J. of Phys. Chem. C* 111, 2007.
3. S. Alavi and D.L. Thompson, *J. of Phys. Chem. A*, 2005.
4. K. Moore and M.L. Pantoya, *J. of Prop. and Power* 23, No. 1, 2007.
5. J. Sun, M.L. Pantoya and S.L. Simon, *Thermochimica Acta* 444, 2006, 117-127.
6. C.J. Bulian, T.T. Kerr and J.A. Puszynski, 31st International Pyrotechnics Seminar, Fort Collins, CO, USA, July 12-14, 2004, pp. 237.
7. D.E. Wilson and K. Kim, 30th AIAA/ASME/SAE/ASEE Joint Prop. Conf., 2003, Reno, Nevada.
8. E. L. Dreizin, *Combust. Flame* 105, 541-546, 1996.
9. R. Friedman and A. Macek, *Combust. Flame* 1962, 6, 9.
10. A.G. Merzhanov, Y.M. Grigoriev and Y.A. Galchenko, *Combust. Flame* 1977, 29, 1.
11. M.A. Trunov, M. Schoenitz, X. Zhu and E.L. Dreizin, *Combust. Flame* 2005, 140, 310.
12. M.A. Trunov, M. Schoenitz and E.L. Dreizin, Joint Meeting of the U.S. Sections of the Combustion Institute, Philadelphia, PA, 2005.
13. T. Bazyn, H. Krier and N. Glumac, *Combust. Flame* 145 (2006), 703-714.
14. T. Bazyn, N. Glumac, H. Krier, T.S. Ward, M. Schoenitz and E.L. Dreizin, *Combust. Sci. and Tech.*, 179, 457-476, 2007.
15. C.E. Aumann, G.L. Skofronick and J.A. Martin, *J. of Vac. Sci. Technol. B* 13(3), May/June 1995.

16. S.M. Umbrajkar, M. Schoenitz and E.L. Dreizin, *Thermochimica Acta* **451**, 2006, 34-43.
17. M.L. Pantoya and J.J. Granier, *J. of Thermal Anal. And Calorimetry*, Vol. **85** (2006)1, 37-43.
18. K. Park, D. Lee, A. Rai, D. Mukherjee and M.R. Zachariah, *J. of Phys. Chem B*, Nov 2004.
19. M.A. Trunov, M. Schoenitz and E.L. Dreizin, *Propellants, Explosives, Pyrotechnics* **30** (2005), No. 1.
20. D.E.G. Jones, R. Turcotte, R.C. Fouchard, Q.S.M. Kwok, A.M. Turcotte and Z.A. Qader, *Propellants Explosives Pyrotech.* **28**, 2003, 120-131.
21. V.L. Levitas, B.W. Asay, S.F. Son and M.L. Pantoya, *Appl. Phys. Lett* **89**, 071909 (2006).
22. A. Rai, D. Lee, K. Park and M.R. Zachariah, *J. of Phys. Chem. B*, **108** (39), 2004.
23. P.R.N. Childs, "Practical Temperature Measurement", Butterworth-Heinemann, 2001, Chapter 6, pp 149.
24. L. Zhou, N. Piekiel, S. Chowdhury and M.R. Zachariah, *Rapid Commun. Mass Spectrom.* **2009**; 23:194-202.
25. L. Zhou, N. Piekiel, S. Chowdhury and M.R. Zachariah, (in preparation).
26. T.S. Ward, M.A. Trunov, M. Schoenitz and E.L. Dreizin, *Intl. J. of Heat and Mass Transfer* **49**, 2006, pp 4943-4954.
27. V.I. Levitas, M.L. Pantoya and K.W. Watson, *Appl. Phys. Lett* **92**, 201917 (2008).
28. A. Rai, K. Park, L. Zhou and M.R. Zachariah, *Combustion Theory and Modelling*, Vol. **10**, No. 5, Oct 2006, pp 843-859.
29. R. Nakamura, D. Tokozakura, H. Nakajima, J.G. Lee and H. Mori, *J. of Appl. Physics* **101**,

074303, 2007.

30. B. Henz, T. Hawa and M.R. Zachariah, *J. of Appl. Physics*, in press.

Simultaneous Pressure and Optical Measurements of Nanoaluminum-Based Thermites: An Investigation of the Reaction Mechanism

This work investigates the reaction mechanism of Metastable Intermolecular Composites (MICs) by collecting simultaneous pressure and optical signals during combustion in a constant-volume pressure cell. Nanoaluminum and three different oxidizers are studied; CuO, SnO₂, and Fe₂O₃. In addition these mixtures are blended with varying amount of WO₃ as a means to perturb the gas release in the system. The mixtures with CuO and SnO₂ exhibit pressure signals which peak on timescales faster than the optical signal, while the mixtures containing Fe₂O₃ do not show this behavior. The burn time is found to be relatively constant for both CuO and SnO₂, even when a large amount of WO₃ is added. For Fe₂O₃, the burn time decreases as WO₃ is added and the temperature increases. The results are consistent with the idea that oxidizers such as CuO and SnO₂, which decompose at relatively low temperatures, show an initial fast pressure rise followed by combustion over a longer time scale. In this case the burning is rate limited by the aluminum, and is similar to the burning of aluminum in a pressurized oxygenated environment. For the Fe₂O₃ system, the oxidizer decomposition to release oxygen only occurs significantly at the adiabatic flame temperature, and is the rate limiting step.

I. Introduction

Metastable Intermolecular Composites (MICs) are a class of energetic materials consisting of an intimate mixture of fuel and oxide nanoparticles. Aluminum is primarily used as the fuel, and a variety of metal oxides have been used including, but not limited to, CuO, WO₃, MoO₃, Bi₂O₃ and Fe₂O₃. MICs are a relatively new class of energetic materials, and research efforts to understand them have increased since Aumann[1] reported a ~1000x increase in reactivity when nano-sized Al/MoO₃ particles were used in place of their micro-sized counterparts. The high energy density and wide range of tunability of MICs make them attractive candidates for uses in propellants, pyrotechnics, and explosives. However, the reaction mechanism is still very poorly understood.

MICs can be prepared by several methods, including various techniques such as Arrested Reactive Milling[2], sol-gel chemistry[3, 4], and ordered assembly[5, 6]. Another commonly used technique is to

ultrasonicate the powders in a dispersing liquid, such as hexane or isopropyl alcohol, and then allow the liquid to dry. The remaining powder can be broken up or sieved until it has the consistency of a loose powder. A variety of experimental methods have been used to investigate the reactivity of these powders, including thermal analysis[7, 8], combustion in a shock tube[9], flame propagation in open channels[10-16] and tubes[17-19], heated filament studies[8], and constant-volume pressure cells[11, 20-24]. The pressure signal and/or optical emission can be collected to investigate the reactivity of these materials. The pressurization rate has been shown to correlate with flame propagation velocities[25], and is typically reported as a relative measurement of reactivity. Other authors[17, 19] have shown a correlation between the peak pressure and propagation velocity. Recently, authors[17-19] have used an instrumented burn tube to collect the optical and pressure signals simultaneously. Understanding the reactivity of MICs is complicated not only by the fact that so many experimental techniques are used, but so many parameters are involved, such as aluminum supplier, mixing technique, size distributions, etc.

If the reaction is self-propagating, i.e. a burn tube or pressure cell, then there are three phenomena occurring simultaneously; ignition of the fuel, reaction between the fuel and oxidizer, and energy propagation. None of these phenomena themselves are well understood at the nanoscale or with practical ($>10^6$ K/s) heating rates. Nanoaluminum has been shown to have a much lower ignition temperature than micron-sized aluminum. The reason for this is attributed to the naturally-formed oxide shell surrounding aluminum. For a nanoparticle, the oxide shell can account for a relatively large portion of the particle's mass, and the interaction between the core and shell during heating is critical in understanding the mechanism of ignition. The aluminum core melts at a much lower temperature than the oxide shell (933K vs. 2327K). Upon heating the core will melt and expand, inducing stresses on the oxide shell. What happens next is not clear. Some authors argue that a decomposition or phase change in the shell occur, thus allowing aluminum to diffuse outwards[26-28], while other authors argue that the rapid expansion of the core induces enough stress to completely shatter the shell and unload the aluminum as small liquid clusters[29-31]. The burning mechanism of aluminum thereafter will be quite different depending on what mechanism of ignition happens.

For super-micron sized aluminum, the burning can be described by a droplet burning model, and thus the burn time can be predicted by a “Dⁿ” behavior, where D is the particle diameter. If aluminum

behaved like a liquid droplet, the value of the exponent would be 2, while Beckstead et al.[32] show this value to be 1.5-1.8 (The reduction is explained by the formation of an “oxide cap”[33]). As the particle size transitions into the nanometer regime, the droplet burning model is thought to become invalid and the reaction mechanism is poorly understood. Part of the difficulty in studying nanoaluminum combustion is to use experimental techniques which heat the particles uniformly and with practical heating rates, $\sim 10^6 \text{ K/s}$.

One experimental technique to achieve these heating rates is to use a shock tube. Bazyn et al.[34, 35] studied the combustion of nanoaluminum at elevated temperatures and pressures in a shock tube. The authors combust aluminum at varying temperatures, pressures and oxygen mole fractions, and use three-color pyrometry to measure the particle temperature. The authors show that the ambient temperature plays a significant roll on the aluminum combustion, indicating that heat losses are much more important for nanoparticles than for larger sized particles. Nanoparticles are small thermal loads with relatively fast heat transfer to the surroundings. The same authors[36] show that a transition from a diffusion to a kinetic-limited mechanism begins to occur below a critical particle size. For a kinetic-limited mechanism, the flame sits closer to, if not on, the particle surface and the flame temperature is limited by the boiling point of aluminum.

The third phenomena occurring in the reaction mechanism of a self-propagating MIC is energy propagation. Sanders et al.[17] have shown that the dominant mode of energy propagation through a loose powder is convection. As a result, MICs often exhibit an optimal reactivity which correlates with gas production instead of temperature. For example, Sanders et al.[17] found that Al/CuO has a peak reactivity for an equivalence ratio very near stoichiometric. The authors use equilibrium calculations to show that a stoichiometric mixture produces the maximum amount of Cu gas, and any deviation from this mixture will lower the temperature, hindering the gas production, and hence the convective mode of energy propagation. Conversely, a mixture of Al/Bi₂O₃ exhibits an optimal reactivity at an equivalence ratio of 1.5. Equilibrium calculations are again used to show a correlation with gas production, and in this case the gas is a combination of Al₂O, Al and Bi. It’s interesting to note that the temperature is almost 600 degrees cooler for Al/Bi₂O₃ at an equivalence ratio of 1.5 instead of 1, yet the reactivity is higher. This is counterintuitive, since the reaction rate usually scales exponentially with temperature.

Both Sanders et al.[17] and Malchi et al.[19] show that the peak pressure correlates with the flame propagation velocity. In the two works, an instrumented burn tube is used to simultaneously collect the pressure and optical signals. The authors use equilibrium calculations to show correlations between the predicted equilibrium gas and the experimental trends in pressure. From Figure 9 in Malchi et al.[19], it appears that the optical signal reaches its peak on the same time scale as the pressure does, ~10usec.

II. Thermochemistry of Mixtures

Recent mass spectrometry work by our group has indicated that oxygen release from the metal oxide decomposition is important in the reaction mechanism of thermites, in particular for CuO and Fe₂O₃. The current work expands on this idea to investigate the burning of nanoaluminum composites in a constant-volume pressure cell. The pressure and optical signals are collected simultaneously to have two different measurements of reactivity. The oxides studied are CuO, Fe₂O₃, and SnO₂. These particular oxidizers have adiabatic flame temperatures at or above the boiling point of the metal in the metal oxide, and the gas is predicted to be almost entirely comprised of this metal at equilibrium. These oxidizers also decompose to suboxides and gaseous oxidizers, which will be discussed in more detail later. The calculated equilibrium for stoichiometric mixtures of these oxidizers with aluminum is shown in Table 1. The CHEETAH 4.0 code was used with the JCZS product library[37], as recommended by Sanders et al.[17]. The mixture density was assumed to be 0.00192 g/cc, since we always react 25mg of material in our 13cc cell. The experimental pressurization rate is also given for comparison.

We will start by investigating the simultaneous pressure and optical signals for the three oxidizers mentioned above. We will then go on to perturb the system by adding increasing amounts of WO₃ in place of the metal oxide. We chose WO₃ because, when added as the minor component, the adiabatic temperature remains relatively unchanged. Also, WO₃ is predicted to release very little equilibrium gas and also does not decompose to O₂ or any significant gaseous oxidizing species until >2800K. All blends are stoichiometric and are referred to in terms of the molar %WO₃ in the oxidizer. For example, a 40%WO₃ mixture means that 40% of the oxidizer molecules are WO₃, 60% are the other oxidizer, and the corresponding amount of aluminum is added to make the overall mixture stoichiometric assuming complete conversion to Al₂O₃.

III. Experimental

The aluminum used in this study was 50nm ALEX, purchased from the Argonide Corporation. The aluminum was found to be 70% active by mass, as measured in a TGA. All other materials were purchased from Sigma Aldrich, and have average particle diameters <100nm as specified by the supplier. All samples were prepared by weighing out the powder and adding it to a ceramic crucible. Approximately 10mL of hexane was added and the mixtures were ultrasonicated for 30 minutes to ensure intimate mixing. The samples were then placed in a fume hood until the hexane evaporated and the wetness was gone, and then the samples were put in a 100C furnace for a few minutes to drive off any remaining hexane. The dry powders were very gently broken up with a spatula until the consistency was that of a loose powder.

A fixed mass (25mg) of the powder was weighed out and placed in a small (13cc free volume) combustion cell. Two ports were utilized to collect the pressure and optical signal simultaneously. In one port a lens tube assembly, containing a plano-convex lens ($f=50\text{mm}$), collected light and imaged onto an optical fiber coupled to a high speed Si photo detector (1ns rise time, model DET10A, Thorlabs). In the second port a piezo-electric pressure sensor was employed, the details for which can be found in Prakash et al.[22]. The data collection was triggered by the rising optical signal. There is always a $\sim 60\text{usec}$ delay between the onset of the optical emission and the onset of the pressure signal. This is due to the time delay between the optical triggering and when the pressure wave arrives at the sensor, a few centimeters away. The pressure data was thus shifted in time for the analysis so that the onset of the pressure and light are shown to occur simultaneously.

IV. Results and Discussion

We first show the simultaneous pressure and optical signals for pure Al/CuO, Al/SnO₂, and Al/Fe₂O₃ in Figure 1. Also included is pure Al/WO₃ for comparison. Note that the axes for each plot have all been adjusted to fill the plot area. From Figure 1, we can immediately see that CuO and SnO₂ exhibit a pressure peak well before the optical signal reaches its peak. In the case of Fe₂O₃ and WO₃, the pressure and optical signals occur concurrently.

The experimental data shown in Figure 1 is for a sample mass of 25mg. In order to determine whether the sample mass had any effect on the optical signal, we also repeated this for a sample mass of 10mg. In this case we see a decrease in the pressure signal (as expected) but no change in the optical signal.

This result is important in that it implies that the optical emission reflects the particle burning time, and is not coupled to the flame propagation.

An accurate measurement of temperature is not possible for such a large sample, since the viewing area is optically thick and thus the measurement would be biased to the outermost, or coolest, region of the reaction. However, the optical signal is still useful in that it is a relative measurement of the system temperature. For Al/CuO and Al/SnO₂, the observations in Figure 1 imply that the pressurization is happening well before the system temperature is at its peak value. These systems have adiabatic flame temperatures near the boiling point of the metal (Cu and Sn), and so the vaporization of the metal should not occur until the temperature is near its hottest point. This is clearly not the case for these two systems, and thus the pressure rise is likely caused by something else.

An alternate explanation is that the pressure rise is attributed to the decomposition of the oxidizer. We have recently investigated this idea for the Al/Fe₂O₃ and Al/CuO thermite system using fast-heating wire experiments coupled with mass spectrometry. Upon rapid heating, a significant O₂ signal emerges first, followed by other species indicative of the reaction, i.e. Al₂O, Cu, Fe. The O₂ signal is a product of the thermal decomposition of the metal oxide in the case of both CuO and Fe₂O₃.

To illustrate this we use NASA's CEA code to show the decomposition behavior of the metal oxides in Figure 2, where the equilibrium species distribution is plotted as a function of temperature (Constant TP with P=1atm). The markers indicate the point where no oxygen-containing species remain in the condensed phase (i.e. Cu₂O(L) or Fe₃O₄(L), decomposition products of CuO and Fe₂O₃). For all three oxidizers, we see the emergence of O₂ when the temperature reaches a certain value and the metal oxide decomposes to a suboxide and O₂. In the case of SnO₂ a significant amount of SnO gas is also formed during decomposition, therefore, we have lumped the O₂ and SnO together into one quantity, since both are gaseous decomposition products and are likely important in oxidizing the aluminum.

From Figure 2 we see an interesting observation: CuO and SnO₂ fully decompose to gaseous oxidizing species at temperatures *below* their adiabatic flame temperatures. In contrast, Fe₂O₃ does not fully decompose until >3200K, several hundred degrees above its adiabatic temperature. From the experimental data and the arguments above, it is reasonable to speculate that the decomposition of CuO and SnO₂ is what leads to the first pressure spike, followed by a much longer optical trace as the aluminum continues to burn.

In the case of Fe_2O_3 , the oxidizer cannot efficiently decompose, and therefore the decomposition may in fact be the rate limiting step. To further investigate this, we now turn to the experimental results where WO_3 is added.

The experimental pressurization rate is shown as a function of WO_3 for the three systems in Figure 3. For both the CuO and SnO_2 systems, the optimum reactivity occurs when no WO_3 is added, and drops significantly when even a small amount of WO_3 is introduced. For the Fe_2O_3 , we see a significant enhancement and peak reactivity when the mixture is 80% WO_3 . Clearly something in the blended $\text{Fe}_2\text{O}_3/\text{WO}_3$ system is enhancing the pressurization rate above either system alone.

In order to show whether the trends in experimental pressurization rate could be explained by oxidizer decomposition, we seek some way to estimate the gaseous oxidizer (O_2 and SnO) release rate. Since knowledge of these rates is not well known, we assume the oxidizer decomposition and gas release rate are proportional to the number of moles of the decomposing species in the mixture (CuO , SnO_2 , or Fe_2O_3). Because WO_3 does not show any decomposition products and gas release until $>2800\text{K}$, we are fairly certain that WO_3 does not contribute to the initial pressure rise, at least in the CuO and SnO_2 systems. We chose to use pressurization rate rather than peak pressure as a measure of kinetics, since a peak pressure analysis can most easily be correlated only if one can assume complete decomposition of the oxidizer. The pressurization rate and predicted oxidizer release rate are plotted for the three systems in Figure 4. The values have been normalized by the maximum.

We see that the pressurization rate does indeed correlate with the predicted oxidizer release rate for the CuO and SnO_2 systems, but not for Fe_2O_3 . This is further support that the pressurization rate is attributed to the oxidizer decomposition for the CuO and SnO_2 . For the Fe_2O_3 system, the predicted oxygen release does not correlate with the trend in pressurization rate at all. We see a constant value of the pressurization rate up until about 70% WO_3 , followed by a sharp jump to a peak at 80%, and then a decrease from 90-100% WO_3 . One explanation for this behavior could be that the formation of Fe gas causes this peak, however, this does not explain why the pressurization rate is constant over such a wide range (0-70%). As WO_3 is added, we would expect the amount of Fe gas to change and affect the pressurization rate, but this was not observed. A more likely explanation is that the temperature reaches a high enough value to decompose the Fe_2O_3 efficiently. As discussed previously and shown in Figure 2, the adiabatic flame

temperature of Al/Fe₂O₃ is lower than the point where Fe₂O₃ can fully decompose. As WO₃ is added the adiabatic temperature increases, and it's likely that at 80 and 90% WO₃, the temperature becomes high enough to efficiently decompose the Fe₂O₃. To corroborate this idea, the raw data is shown for 70% and 80%WO₃ in the Al/WO₃/Fe₂O₃ system in Figure 5. What can be seen is that for 80%WO₃, the first pressure peak occurs well before the optical peak, while this is not the case for 70%. This is consistent with the idea that the system temperature reaches a point where the Fe₂O₃ can decompose efficiently, leading to a fast pressure spike relative to the burning.

We can use the results and discussion thus far to make some speculations about the reaction mechanism. For systems where the adiabatic flame temperature is high enough and heat transfer is not limiting, when the fuel begins to burn, the oxidizer can decompose and pressurize the system faster than the reaction timescale. The fuel then continues to burn over a longer period, as can be seen in Figure 1 for the CuO and SnO₂. Systems such as these would thus be rate limited by the mechanism by which the aluminum burns in a gaseous oxidizing environment. For an oxidizer such as Fe₂O₃, the adiabatic flame temperature is below the point where the oxidizer can fully decompose and thus the oxidizer cannot decompose efficiently. The burning mechanism in this case is rate limited by the oxidizer decomposition and oxygen release. The fact that the optical and pressure signals occur concurrently for Fe₂O₃ supports this argument, and indicates that the two are tightly coupled.

To further test these ideas, we can also look at the trends in the optical signals. We assume the burning time to be the full width half max of the optical signal. This is plotted for the three systems in Figure 6. The only system which shows a decrease in the burning time as the temperature increases (see Figure 4 for temperature) is the Fe₂O₃ system. For the other two systems, this is not the case. Instead, we see that the burning time does not change over a very wide range of added WO₃ (0-80%), even when WO₃ becomes the major component and the temperature increases. Also noteworthy is that the burning time is nearly identical for CuO and SnO₂, 185usec and 210usec, respectively. This supports our speculation that the burning is rate limited by the aluminum in these two systems, since the aluminum is the only common factor between the two systems. If we compare these burning times to those reported by Bazyn et al.[35] for the combustion of nanoaluminum in a shock tube, we see that our values compare reasonably well. This similarity suggests that the burning of a MIC may resemble the combustion of aluminum in a pressurized,

oxygenated environment if the oxidizer can decompose efficiently relative to the timescale of the aluminum burning. This behavior was observed for CuO and SnO₂ over almost the entire range of WO₃, and was also seen for the Fe₂O₃ when enough WO₃ is added (80-90%).

Let's discuss this point in the context of a burn tube. As mentioned previously, the pressurization rate has been shown to correlate with the flame propagation velocity. However, this correlation is not quantitative. For example, Al/CuO has a pressurization rate on the order of 10psi/usec with a flame velocity of 550m/s, while Al/Fe₂O₃ has a pressurization rate of 0.02psi/usec with a flame velocity of 25m/s (velocities are from unpublished data of burning in an acrylic burn tube and measuring the 2-point velocity with photodiodes). We can also look at the difference in burning times measured in this work, 170 and 936usec for Al/CuO and Al/Fe₂O₃, respectively. The pressurization rates are different by a factor of 500, the burning times a factor of 5, and the flame velocities a factor of 20. It is evident that neither the pressurization rate nor the burning time alone can quantitatively predict the flame propagation velocity. We believe the reason for this lies in the discussion of what the rate limiting step is.

As was discussed previously, the difference in these two systems is oxygen release relative to the burning. For Al/Fe₂O₃, both occur at the same time and so the pressurization rate should be directly related to the flame velocity. For Al/CuO however, predicting the propagation velocity is more complicated. In this case the system is speculated to pressurize quickly via the release of O₂ gas, followed by the burning of aluminum over a longer time scale. If this is happening, then one would not expect the pressurization rate alone to predict the propagation velocity. Instead, the velocity would be more limited by the aluminum burning. As mentioned in the introduction, convection is considered to be primarily responsible for energy transport through the material. If O₂ gas is being released quickly, then it would contribute largely to the convection. If we consider a self-propagating flame to be a series of ignition sites, then upon ignition, the first layer would begin to burn and transfer energy forward. The subsequent unreacted layer will only need to be heated to the ignition point before the flame can continue propagating. To complicate this further, nanoparticles have small characteristic relaxation times, meaning that they can be easily swept up and carried forward by the gas. This itself may be an important phenomenon to include in modeling such a system. If a pressure rise is happening fast relative to the burning, it's possible that the O₂ can pick up

unreacted particles and carry them forward, leading to a faster flame velocity than would be predicted by simply looking at the aluminum burning time.

V. Conclusion

The reaction mechanism of aluminum-based MICs was investigated by simultaneously collecting the pressure and optical signals from combustion in a constant-volume pressure cell. Three oxidizers were studied, CuO, SnO₂, and Fe₂O₃, and were chosen based on their ability to decompose and release O₂ (and SnO for the SnO₂). WO₃ was blended with the three oxidizers as a means to perturb the system gas release, while keeping the system temperature relatively constant when added as the minor component. The results suggest that CuO and SnO₂ decompose to release gaseous oxidizers, leading to a rapid pressurization followed by a longer burn time which is rate-limited by the aluminum. For the Fe₂O₃, the experimental data show that the optical and pressure signals occur concurrently. The reaction mechanism in this case is speculated to be rate-limited by the oxidizer decomposition. The results suggest that if oxidizer decomposition is fast relative to the reaction timescale, then the burning of an aluminum-based MIC may resemble the burning of aluminum in a pressurized, oxygenated environment.

Table 1 Calculated temperature and gas production for stoichiometric mixtures of various metal oxides with nanoaluminum.

Metal Oxide	Boiling Point Metal (K)	Tad (Cheetah UV) (K)	Moles Gas	Contribution of Metal to the Total Gas	Experimental Pressurization Rate (psi/usec)
CuO	2837	2967	3.5	97%	11.1
SnO ₂	2533	2573	2.2	94%	7.7
Fe ₂ O ₃	3023	2834	0.52	98%	0.017

Table 2 Experimental pressurization rate and flame velocity for Al/CuO and Al/Fe₂O₃.

Thermite	Pressurization Rate (psi/usec)	Flame velocity (m/s)
Al/CuO	11.1	~550
Al/Fe ₂ O ₃	0.017	~25

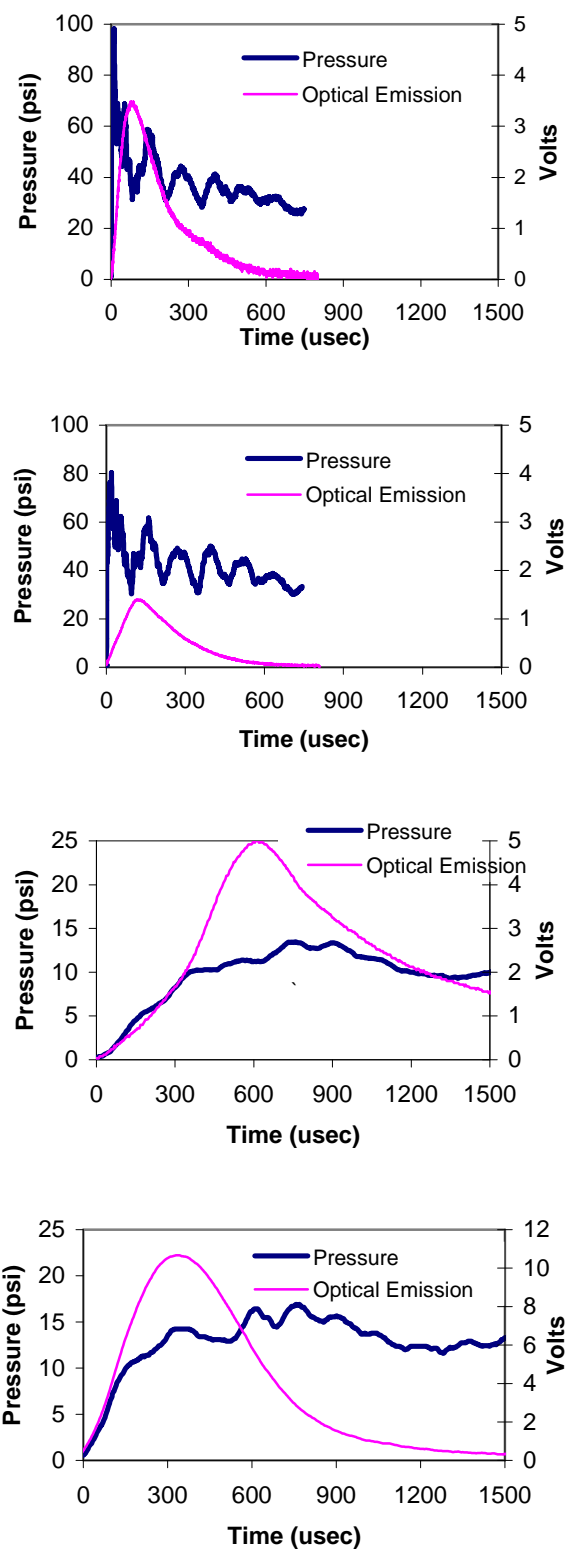


Figure 1 Simultaneous optical and pressure signals from top to bottom: Al/CuO, Al/SnO₂, and Al/Fe₂O₃. Also shown is Al/WO₃(bottom).

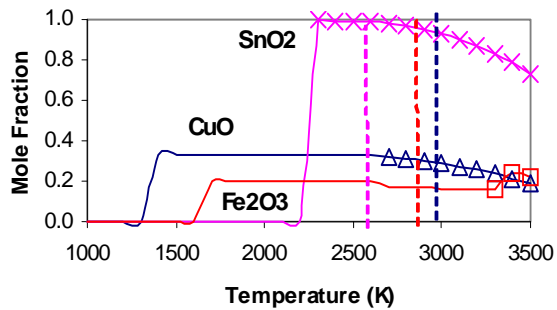


Figure 2 Gaseous oxidizer release as a function of temperature. The markers indicate the points where no oxygen remains in the condensed phase. The vertical line shows the adiabatic temperature for reference, from left to right; SnO_2 , Fe_2O_3 , and CuO . Constant TP calculations assuming $P=1\text{ atm}$ for all runs.

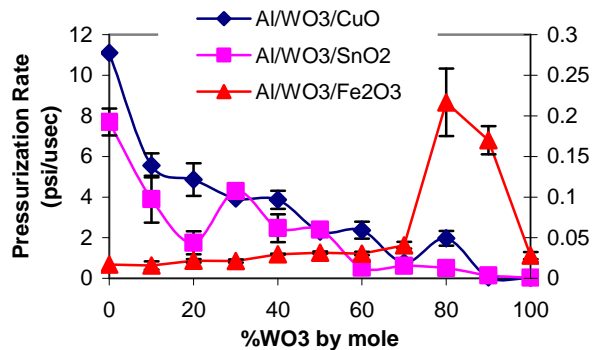
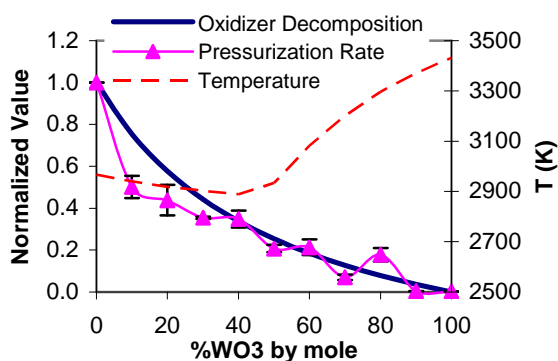


Figure 3 Experimental pressurization rate as a function of the molar % of WO_3 in the oxidizer. The $\text{Al}/\text{WO}_3/\text{Fe}_2\text{O}_3$ data is plotted on the secondary axis.



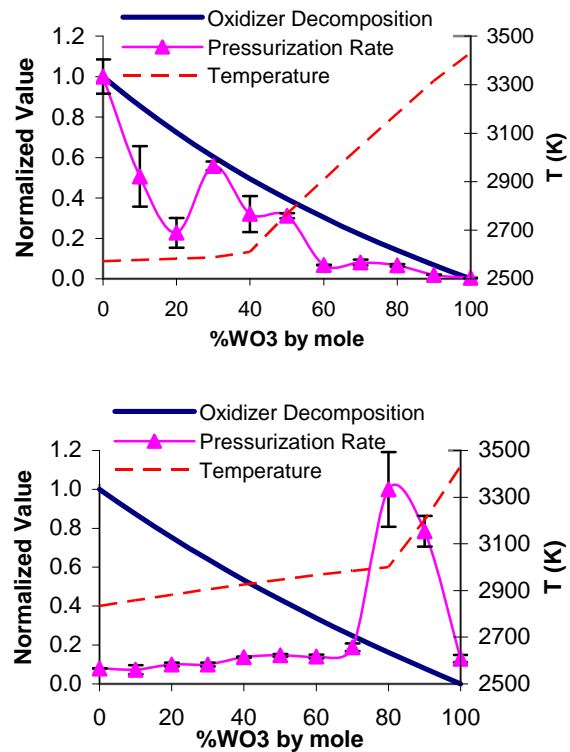


Figure 4 Gas release prediction and experimental pressurization rate (both normalized by the maximum value), along with the adiabatic temperature. Systems from top to bottom are Al/WO₃/CuO, Al/WO₃/SnO₂, and Al/WO₃/Fe₂O₃.

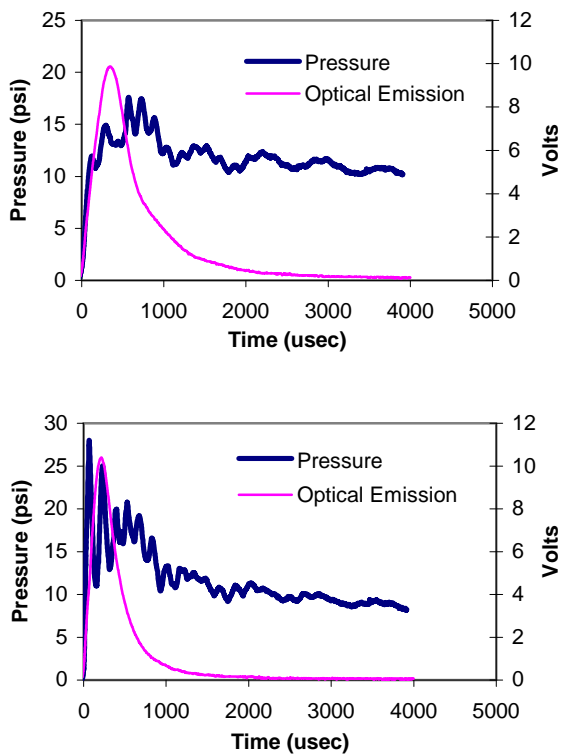


Figure 5 Raw data for the 70% (top) and 80% (bottom) WO_3 mixtures of $\text{Al}/\text{WO}_3/\text{Fe}_2\text{O}_3$. Note how the pressure peak occurs earlier than the optical peak for the 80% WO_3 mixture.

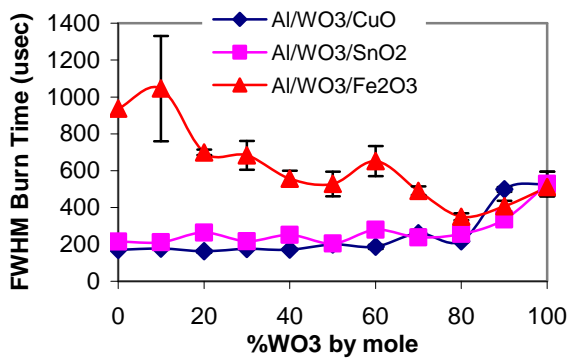


Figure 6 Experimental FWHM burn time for the three systems as a function of % WO_3 .

1. Aumann, C. E., Skofronick, G. L., and Martin, J. A. "Oxidation behavior of aluminum nanopowders," *Journal of Vacuum Science & Technology, B: Microelectronics and Nanometer Structures* Vol. 13, No. 3, 1995, pp. 1178-83.
2. Dreizin, E. L., Schoenitz, M., Shoshin, Y. L., and Trunov, M. A. "Highly-energetic nanocomposite powders produced by arrested reactive milling," *International Annual Conference of ICT* Vol. 36th, No. Energetic Materials, 2005, pp. 138/1-138/12.

3. Gash, A. E., Satcher, J. H., Jr., Simpson, R. L., and Clapsaddle, B. J. "Nanostructured energetic materials with sol-gel methods," *Materials Research Society Symposium Proceedings* Vol. 800, No. Synthesis, Characterization and Properties of Energetic/Reactive Nanomaterials, 2003, pp. 55-66.
4. Prakash, A., McCormick, A. V., and Zachariah, M. R. "Aero-sol-gel synthesis of nanoporous iron-oxide particles: A potential oxidizer for nanoenergetic materials," *Chemistry of Materials* Vol. 16, No. 8, 2004, pp. 1466-1471.
5. Apperson, S., Shende, R. V., Subramanian, S., Tappmeyer, D., Gangopadhyay, S., Chen, Z., Gangopadhyay, K., Redner, P., Nicholich, S., and Kapoor, D. "Generation of fast propagating combustion and shock waves with copper oxide/aluminum nanothermite composites," *Applied Physics Letters* Vol. 91, No. 24, 2007, pp. 243109/1-243109/3.
6. Kim, S. H., and Zachariah, M. R. "Enhancing the rate of energy release from nanoenergetic materials by electrostatically enhanced assembly," *Advanced Materials* Vol. 16, No. 20, 2004, pp. 1821-+.
7. Umbrajkar, S. M., Schoenitz, M., and Dreizin, E. L. "Exothermic reactions in Al-CuO nanocomposites," *Thermochimica Acta* Vol. 451, No. 1-2, 2006, pp. 34-43.
8. Schoenitz, M., Umbrajkar, S., and Dreizin, E. L. "Kinetic analysis of thermite reactions in Al-MoO₃ nanocomposites," *Journal of Propulsion and Power* Vol. 23, No. 4, 2007, pp. 683-687.
9. Bazyn, T., Glumac, N., Krier, H., Ward, T. S., Schoenitz, M., and Dreizin, E. L. "Reflected shock ignition and combustion of aluminum and nanocomposite thermite powders," *Combustion Science and Technology* Vol. 179, No. 3, 2007, pp. 457-476.
10. Prentice, D., Pantoya, M. L., and Clapsaddle, B. J. "Effect of Nanocomposite Synthesis on the Combustion Performance of a Ternary Thermite," *Journal of Physical Chemistry B* Vol. 109, No. 43, 2005, pp. 20180-20185.
11. Schoenitz, M., Ward, T. S., and Dreizin, E. L. "Fully dense nano-composite energetic powders prepared by arrested reactive milling," *Proceedings of the Combustion Institute* Vol. 30, No. Pt. 2, 2005, pp. 2071-2078.
12. Moore, D. S., Son, S. F., and Asay, B. W. "Time-resolved spectral emission of deflagrating nano-Al and nano-MoO₃ metastable interstitial composites," *Propellants, Explosives, Pyrotechnics* Vol. 29, No. 2, 2004, pp. 106-111.

13. Plantier, K. B., Pantoya, M. L., and Gash, A. E. "Combustion wave speeds of nanocomposite Al/Fe₂O₃: the effects of Fe₂O₃ particle synthesis technique," *Combustion and Flame* Vol. 140, No. 4, 2005, pp. 299-309.
14. Clapsaddle, B. J., Zhao, L., Gash, A. E., Satcher, J. H., Jr., Shea, K. J., Pantoya, M. L., and Simpson, R. L. "Synthesis and characterization of mixed metal oxide nanocomposite energetic materials," *Materials Research Society Symposium Proceedings* Vol. 800, No. Synthesis, Characterization and Properties of Energetic/Reactive Nanomaterials, 2003, pp. 91-96.
15. Kwon, Y.-S., Gromov, A. A., Ilyin, A. P., Popenko, E. M., and Rim, G.-H. "The mechanism of combustion of superfine aluminum powders," *Combustion and Flame* Vol. 133, No. 4, 2003, pp. 385-391.
16. Perry, W. L., Smith, B. L., Bulian, C. J., Busse, J. R., Macomber, C. S., Dye, R. C., and Son, S. F. "Nano-scale tungsten oxides for metastable intermolecular composites," *Propellants, Explosives, Pyrotechnics* Vol. 29, No. 2, 2004, pp. 99-105.
17. Sanders, V. E., Asay, B. W., Foley, T. J., Tappan, B. C., Pacheco, A. N., and Son, S. F. "Reaction propagation of four nanoscale energetic composites (Al/MoO₃, Al/WO₃, Al/CuO, and Bi₂O₃)," *Journal of Propulsion and Power* Vol. 23, No. 4, 2007, pp. 707-714.
18. Bockmon, B. S., Pantoya, M. L., Son, S. F., Asay, B. W., and Mang, J. T. "Combustion velocities and propagation mechanisms of metastable interstitial composites," *Journal of Applied Physics* Vol. 98, No. 6, 2005, pp. 064903/1-064903/7.
19. Malchi, J. Y., Foley, T. J., Son, S. F., and Yetter, R. A. "The Effect of Added Al₂O₃ on the Propagation Behavior of an Al/CuO Nano-Scale Thermite," *Combustion, Science, and Technology* Vol. 180, 2008, pp. 1278-1294.
20. Puszynski, J. A., Bulian, C. J., and Swiatkiewicz, J. J. "The effect of nanopowder attributes on reaction mechanism and ignition sensitivity of nanothermites," *Materials Research Society Symposium Proceedings* Vol. 896, No. Multifunctional Energetic Materials, 2006, pp. 147-158.
21. Puszynski, J. A., Bulian, C. J., and Swiatkiewicz, J. J. "Processing and ignition characteristics of aluminum-bismuth trioxide nanothermite system," *Journal of Propulsion and Power* Vol. 23, No. 4, 2007, pp. 698-706.
22. Prakash, A., McCormick, A. V., and Zachariah, M. R. "Synthesis and reactivity of a super-reactive metastable intermolecular composite formulation of Al/KMnO₄," *Advanced Materials (Weinheim, Germany)* Vol. 17, No. 7, 2005, pp. 900-903.

23. Moore, K., Pantoya, M. L., and Son, S. F. "Combustion behaviors resulting from bimodal aluminum size distributions in thermites," *Journal of Propulsion and Power* Vol. 23, No. 1, 2007, pp. 181-185.
24. Perry, W. L., Tappan, B. C., Reardon, B. L., Sanders, V. E., and Son, S. F. "Energy release characteristics of the nanoscale aluminum-tungsten oxide hydrate metastable intermolecular composite," *Journal of Applied Physics* Vol. 101, No. 6, 2007, pp. 064313/1-064313/5.
25. Son, S. F., Busse, J. R., Asay, B. W., Peterson, P. D., Mang, J. T., Bockmon, B., and Pantoya, M. L. "Propagation studies of metastable intermolecular composites (MIC)," *Proceedings of the International Pyrotechnics Seminar* Vol. 29th, 2002, pp. 203-212.
26. Rai, A., Park, K., Zhou, L., and Zachariah, M. R. "Understanding the mechanism of aluminum nanoparticle oxidation," *Combustion Theory and Modelling* Vol. 10, No. 5, 2006, pp. 843-859.
27. Trunov, M. A., Schoenitz, M., and Dreizin, E. L. "Effect of polymorphic phase transformations in alumina layer on ignition of aluminum particles," *Combustion Theory and Modelling* Vol. 10, No. 4, 2006, pp. 603-623.
28. Trunov, M. A., Schoenitz, M., Zhu, X., and Dreizin, E. L. "Effect of polymorphic phase transformations in Al₂O₃ film on oxidation kinetics of aluminum powders," *Combustion and Flame* Vol. 140, No. 4, 2005, pp. 310-318.
29. Levitas, V. I., Asay, B. W., Son, S. F., and Pantoya, M. "Mechanochemical mechanism for fast reaction of metastable intermolecular composites based on dispersion of liquid metal," *Journal of Applied Physics* Vol. 101, No. 8, 2007.
30. Levitas, V. I. "Burn time of aluminum nanoparticles: Strong effect of the heating rate and melt-dispersion mechanism," *Combustion and Flame* Vol. 156, No. 2, 2009, pp. 543-546.
31. Levitas, V. I., Pantoya, M. L., and Dikici, B. "Melt dispersion versus diffusive oxidation mechanism for aluminum nanoparticles: Critical experiments and controlling parameters," *Applied Physics Letters* Vol. 92, No. 1, 2008.
32. Beckstead, M. W., Newbold, B. R., and Waroquet, C. "A summary of aluminum combustion," *CPIA Publication* Vol. 701, No. JANNAF 37th Combustion Subcommittee Meeting, 2000, Vol. 1, 2000, pp. 485-504.
33. Law, C. K. "Simplified theoretical model for the vapor-phase combustion of metal particles," *Combustion Science and Technology* Vol. 7, No. 5, 1973, pp. 197-212.

34. Bazyn, T., Krier, H., and Glumac, N. "Shock Tube Measurements of Combustion of Nano-Aluminum," *44th AIAA Aerospace Sciences Meeting and Exhibit*. Reno, Nevada, 2006, pp. 1-8.
35. Bazyn, T., Krier, H., and Glumac, N. "Combustion of nanoaluminum at elevated pressure and temperature behind reflected shock waves," *Combustion and Flame* Vol. 145, No. 4, 2006, pp. 703-713.
36. Bazyn, T., Krier, H., and Glumac, N. "Evidence for the transition from the diffusion-limit in aluminum particle combustion," *Proceedings of the Combustion Institute* Vol. 31, No. Pt. 2, 2007, pp. 2021-2028.
37. Hobbs, M. L., Baer, M. R., and McGee, B. C. "JCZS: an intermolecular potential database for performing accurate detonation and expansion calculations," *Propellants, Explosives, Pyrotechnics* Vol. 24, No. 5, 1999, pp. 269-279.

On the Role of Built-in Electric Fields on the Ignition of Oxide Coated NanoAluminum: ion mobility versus Fickian Diffusion.

Abstract

Using the classical molecular dynamics method we simulate the mechanochemical behavior of small (i.e. core diameter < 10nm) oxide coated aluminum nanoparticles. Aluminum nanoparticles with core diameters of approximately 5nm and 8nm are simulated with 1nm and 2nm thick oxide coatings or shells. In addition to thickness the shells are parameterized by varying degrees of crystallinity, density, and atomic ratios in order to study their affect on the ignition of nanoparticle oxidation. The oxide shells are parameterized to consider oxide coatings with the defects that commonly occur during the formation of an oxide layer and for comparison with a defect free crystalline oxide shell. Computed results include the diffusion coefficients of aluminum cations for each shell configuration and over a range of temperatures. The observed results are discussed and compared with the ignition mechanisms reported in the literature. From this effort we have found that the oxidation ignition mechanism for nanometer sized oxide coated aluminum particles is the result of an enhanced transport due to a built-in electric field induced by the oxide shell. This is in contrast to the currently assumed pressure driven diffusion process. This induced electric field accounts for approximately 90% of the mass flux of aluminum ions through the oxide shell. The computed electric fields show good agreement with published theoretical and experimental results.

Introduction

Much of the interest in nanoparticles is derived from an appreciation that chemical/physical properties often vary from that of the bulk material. Some of these properties, including increased reactivity [1], can simply be attributed to the high surface area to volume ratio of nanoparticles, however it is known that catalytic activity can be significantly changed from that of the corresponding bulk [2,3]. It is also well known that metal nanoparticles are pyrophoric and have enhanced energy release rates, which make them attractive in propulsion [4].

Virtually all metal nanoparticles will nominally have a native oxide shell, which for aluminum is ~2-3 nm thick. Thus any oxidative reaction or vigorous combustion must proceed by transport of either the aluminum or oxidizer through the oxide shell. The ignition temperature of oxide coated aluminum nanoparticles has been observed to decrease with particle size, with a minimum temperature reached for nanoparticles near the melting point of the aluminum core.[5] This suggests to some that a mechanism associated with the melting of the aluminum core is responsible for ignition, whereas in larger particles the ignition temperature is closer to the melting temperature of alumina, namely 2327K. The closeness of the reaction temperature to the melting point of pure aluminum indicates that the melting of the aluminum core is the possible initiator of this reaction for nanoparticles.

It has previously been assumed that either the sudden decrease in density of the aluminum upon melting [6,7] or the lower melting temperature of the nanometer sized oxide shell [8] is the key to initiation of the oxidation process. However, in this paper we explore the possibility that built-in electric fields as opposed to Fickian diffusion drive

aluminum cations through the oxide shell to the nanoparticle surface where it is possible for the oxidation process to proceed. Experimentally produced hollow aluminum oxide nanoparticles provide support for this rapid diffusion hypothesis [9,10]. These observed hollow oxide shells are an indication that the oxidation process is driven by the diffusion of aluminum cations. We will show that field mediated ion-transport is much faster than Fickian diffusion, and will be the dominant transport process in the initiation of the oxidation of nanoaluminum. Anecdotal support for this mechanism comes from numerous numerical [11,12] and experimental studies. [13,14]

Simulation Approach

In this work we have chosen to use the ReaxFF (Reactive Force Field) empirical potential from van Duin [15] implemented within the GRASP (General Reactive Atomistic Simulation Program) MD application. The ReaxFF potential has an advantage over traditional empirical potentials in that it is able to accurately simulate the charge transfer that occurs during metal oxidation. The other empirical potential commonly used for this material system is the Streitz-Mintmire potential [16], however we chose to use the ReaxFF potential because it is available within GRASP which can be executed in parallel. The Al-O potential parameter set used in this work comes from a previous effort that considered the sliding of Al_2O_3 coatings against Al and Al_2O_3 [17]. The computational requirement of this software is high with the largest material system considered here containing nearly 100,000 atoms and requires 96 Intel Woodcrest processor cores running at 3.0 GHz to be simulated efficiently.

Model Description

Two core sizes are considered here, the smaller of these consists of a 5.6nm diameter core of aluminum with either a 1nm or 2nm thick shell of Alumina (Al_2O_3) as illustrated by the example systems in figure 1. The larger model includes an 8nm aluminum core with a 2nm thick crystalline oxide shell. This model is used to consider scaling effects for the electric field and diffusivity.

There are four shell configurations considered for each oxide shell thickness.

1. A defect free crystalline shell that may result from extremely slow or high temperature formation. This shell is modeled by coating a bare aluminum nanoparticle with a crystalline shell made up of $\alpha\text{-Al}_2\text{O}_3$. Although the gamma phase of alumina is more prevalent in oxide coated nanoparticles the alpha form is also observed, and is a limiting case as it is the densest phase that the oxide shell will form. A dense amorphous shell that has an atomic ratio of 2:3 aluminum to oxygen atoms (i.e. Al_2O_3). This shell is formed in the simulation by heating a crystalline oxide shell above its melting temperature while holding the aluminum core atom positions fixed. In this way the oxide layer melts and then is rapidly cooled and trimmed in order to obtain a slightly amorphous oxide layer with the desired thickness.
2. A dense amorphous shell 10% deficient in oxygen atoms, $\text{Al}/\text{O} = 2:2.7$. This shell may form during a faster rate of formation or if the environment during formation was oxygen lean. In the computer simulation this shell is formed by removing 10% of the oxygen from the previous dense oxide shell that is at the stoichiometric ratio of 2:3 aluminum to oxygen atoms.

3. Lastly, a porous amorphous shell with an atomic ratio of 2:3 aluminum to oxygen atoms. This shell has approximately one half of the density of the previously described dense shell with the same atomic ratio. This more porous amorphous shell represents oxide formation that may occur at a very fast rate with a sufficient supply of oxygen. This oxide shell is formed in the computer simulation similarly to the process used for the dense shell except that the shell is repeatedly heated to a higher temperature and rapidly cooled until a much more amorphous configuration is achieved.

Following the creation and equilibration of the oxide shell, the model systems were heated at rates of 10^{11} K/s, 10^{12} K/s, and 10^{13} K/s in order to determine any rate dependencies. We found, similarly to Puri and Yang [8], that at rates below 10^{12} K/s the heating rate appears to have little effect on the simulation results. This is an important result, as lower heating rates would increase the number of MD simulation time steps, which for this work was ~1fs to maintain energy conservation, to a level that would be unreasonable with current computing capacities. The temperature of the model systems was raised from 300K to 1000K and eventually up to 3000K, which is much higher than the melting point of the oxide layer. From experimental data available in the literature [4] it is expected that some reaction should be observed near the melting point of the aluminum core. At the melting point of the core the aluminum density decreases from, 2.7g/cm^3 to 2.4g/cm^3 , resulting in a volumetric expansion of about 12%. Melting of the oxide shell requires heating the nanoparticle to above the melting point of the oxide

which is 2327K for the bulk material or somewhat less for a nanoparticle shell because of the size affect. The results of each of these efforts are detailed in the following sections.

Results of Rapid Heating Simulations

The simulations in this section were carried out in a vacuum so that as Al cations move radially outward towards the oxide surface there are no oxygen molecules available for oxidation reactions. In simulations discussed later we have found the diffusivity of Al through the oxide layer to be more important than oxygen diffusion towards the core. For this reason we are primarily concerned in this work with the mechanism by which Al cations reach the surface of the nanoparticle, therefore limiting the scope of this effort to the ignition process. Initially, the nanoparticles were heated from 300K to about 1000K, which is above the core melting point but below the size dependent oxide melting point reported by Puri and Yang [8]. At around 900K, or slightly below the bulk melting temperature of the aluminum core, a rapid volumetric expansion of the core is observed indicating that the aluminum core has begun to melt. At 1000K the oxide shell still remains intact, with no cracking, even when maintained at that temperature for 100ps. We do see however, as illustrated in Figure 3, the initiation of aluminum cation diffusion to the particle surface.

The results in figure 3 show a slightly inhomogeneous melting of the aluminum core, which is evident in the “1000K, +0ps” plot. Some of the less dense faces of the core begin to melt while the top and bottom remain crystalline, giving the nanoparticle a slightly elongated appearance. The plots in figure 3 also demonstrate the mechanism by which oxidation will be initiated at elevated temperatures. The first observation is that the

oxide shell does not crack as one might expect if diffusion were extremely limited, or the shell were brittle. This suggests that the shell is more elastic at this length scale, or the expansion of the aluminum is insufficient to cause failure in the shell, even at these elevated temperatures. One possible reason for the enhanced elasticity is the lower coordination of the atoms in the oxide shell as compared to the bulk material [18], which is incidentally also a contributing factor to the size dependent melting temperature observed in nanoparticles. In addition, we observe significant diffusion of the core atoms through the oxide shell, thus relieving the potentially high internal pressures. The primary mechanism driving this diffusion is discussed in the following sections.

Aluminum Cation Diffusion through the Oxide Shell

As observed by us and by others [8], at temperatures below the melting point of the oxide shell there is significant diffusion of aluminum cations through the oxide shell. Computation of the diffusivity from the mean square displacement (MSD) of the aluminum cations yields values typically found for liquids. This was unexpected because these measurements were taken at 600K, somewhat below the melting temperature of the relatively small 5.6nm aluminum nanoparticle core. Although the MSD data is somewhat noisy because of the limited simulation time and small nanoparticle sizes, there is an obvious trend of proportionally increasing diffusion rates radially through the shell with increased temperature. To support this observation the radial diffusivity is compared to the overall diffusivity in table I.

The diffusion coefficients in table I are computed using equation 1.

$$\frac{\partial \langle r^2(t) \rangle}{\partial t} = 2dD \quad (1)$$

In equation 1, the number of dimensions, d , available for atomic diffusion, is 3 for overall diffusion, and 1 for radial diffusion [19]. The use of the bulk diffusion equation is reasonable since during the time scales considered the movement of only the atoms initially on the surface are restricted by the particle boundary [20]. For radial diffusion we are only concerned with the MSD directed radially from the center of the nanoparticle. In equation 1, t is the elapsed time, and $\langle r^2(t) \rangle$ is the MSD of the atoms being tracked. The diffusion coefficients reported are for all of the core atoms including those near the center of the nanoparticle. This is important since we would expect the mechanical and electrostatic affects to be larger near the core/shell interface, but because of the small sample sizes available, computing a radial distribution of diffusivity is unreliable.

By comparing the radial and overall diffusivities in table I an interesting trend is observed. As the temperature increases the radial diffusivity becomes a generally more important portion of the overall diffusivity of aluminum cations. This result indicates that once the aluminum core has melted the diffusion of aluminum cations is preferentially in the radial direction, as compared to the results prior to melting. This is possibly due to a high pressure gradient near the core/shell interface pushing atoms out into the shell. Another possibility is that once the core has melted the atoms are more mobile so in addition to pressure, any other effects such as an electric field will increase diffusion. The radial diffusion data that does not correlate with this observation at 600K is for the 2nm thick crystalline oxide shells for both the 5.6nm and 8.2nm aluminum cores. These configurations show diffusion rates that are on par with the overall diffusivity, possibly indicating that one of the drivers of radial diffusion is proportionally stronger for these

shell configurations at 600K. We will show in the following sections that the electric field is indeed strongest in the 2nm thick crystalline shells.

In figure 4 an Arrhenius plot of the diffusivity versus temperature is given for each of the oxide shell configurations used with the 5.6nm aluminum core in this work. From figure 4 we observe that a change in slope occurs near the melting point of the aluminum core, namely 1000K. This indicates that for temperatures above 1000K the activation energy required for cation diffusion is lower than for temperatures below 1000K. The increase in activation energy for the 1nm amorphous and dense oxygen poor shells, is likely due to a lower melting point for these oxide shells. This is not the case, for thicker or more crystalline shells where the oxide remains in the solid phase, and does not undergo any phase transformation. In the remaining model systems the activation energy drops once the melting temperature is reached, indicating a change in diffusion mechanism. The primary change that occurs at around 1000K is the melting of the aluminum core, the associated volumetric expansion, and increased mobility of the aluminum atoms. This expansion is expected to greatly increase the pressure inside of the core, and enhance the diffusion of aluminum cations radially outward through the oxide shell.

Induced Electric Field in Oxide Shell

One possible explanation for the computed rapid diffusion of aluminum atoms through the oxide layer is that they are driven by an induced electric field near the core/shell interface. The theory that oxidation growth proceeds via migration of charged particles is not a new one. In fact Carl Wagner proposed this theory in 1933 [13]. In a 1948 paper by

Cabrera and Mott [11] the authors developed a theory focused on the growth of a thin oxide film on metal surfaces that is driven by an induced electric field. This electric field causes metal ions to migrate to the surface, increasing the oxide thickness until the induced field is prevented by the thickening surface to cause further diffusion of metal cations. The maximum thickness of the oxide layer that is formed with this process increases with temperature, up to a critical temperature above which growth of the oxide layer will continue indefinitely.

Recent theoretical and experimental evidence points to the importance of the induced electric field described by Cabrera and Mott in the oxidation of oxide coated metal nanoparticles. Zhdanov and Kasemo [21] recently performed an analysis of the induced electric field in oxide coated nanoparticles. They found that by considering the size and geometry effect of nanoparticles coated with oxide shells that the induced electric field will be much stronger than observed in a flat surface, thus increasing the associated oxidation rate exponentially in oxide coated nanoparticles. We have also observed the formation of hollow particles [9, Figure 2] during the oxidation of oxide coated aluminum, which we attributed to the faster diffusion of Al cations. Subsequently Nakamura et al [10] also observed formation of hollow metal oxide nanoparticles from oxidation of metals and attributed the rapid diffusion of metal cations through the oxide shell to the induced electric field. In the following sections we investigate the magnitude and effect of the induced electric field on the oxide coated aluminum nanoparticle system.

In the current simulation effort, rapid diffusion of aluminum cations through the oxide layer is observed. An indicator of the strength of the electric field is the radial

charge density. The radial charge density is computed through the nanoparticle at 2Å radial intervals and is averaged over 100ps of simulation time. Although noisy, which is partially caused by atomic diffusion, it is apparent that there is a negative charge gradient throughout the oxide shell. This charge gradient contributes to the out flow of positive charges, and the mass flux of aluminum cations at the core/shell interface.

The difference in charge density between the inner and outer surfaces of the oxide shell indicates that an electric field is induced which will drive aluminum cations near the core/shell interface to the outer surface where they will be exposed to oxygen and oxidize. An approximate interaction between an aluminum cation, with the core and shell can be computed using Gauss's Law. By assuming the atomic charges to be distributed approximately homogeneously in the shell and the core, the electric field on the surface of the core can be estimated as the field from a single point charge at the center of the core, through equation 2. If we assume the charge to be evenly distributed in the oxide shell then the electric field inside of the shell from the atoms in the oxide shell is zero.

$$E = \frac{Q_{core}}{4\pi\epsilon_0 r^2} \quad (2)$$

In equation 2, Q_{core} is the total charge of the core, r is the radial position of the interfacial aluminum atom of interest, and ϵ_0 is the permittivity of a vacuum. Using equation 2 the electric fields from the various oxide coated models are computed in table II.

In figure 6 the volume between the core surface and outer surface of the oxide shell is assumed to be a vacuum. For the purpose of computing the electric field, this assumption is valid so long as the charges in the oxide shell are distributed radially only. With a radially distributed charge the electric field due to the oxide shell is zero everywhere for atoms at the core/shell interface or inside of the aluminum core. The most

obvious trend observed in table II is that of the decreasing core charge and electric field strength with increasing temperature. This is likely due to the fact that as shown in table I, diffusivity increases as temperature increases, and smears the boundary between the core and shell. Another observed trend, albeit weaker, is an increase in the electric field as the shell becomes thicker, and more organized. So in going from an amorphous 1nm thick shell to a 2nm thick crystalline shell we observe a 100% increase in the electric field strength. This observation is supported by the analysis of Zhdanov and Kasemo [21].

A more accurate method of computing the electric field at each ion in the core and shell is to use Coulomb's Law and to sum the discrete contribution from all of the neighboring charges. Using this method is straight forward since there are a finite number of discrete charge carrying atoms. In figure 7 the computed electric field, using equation 3, is plotted at each of the core aluminum atoms.

$$E = \frac{q}{4\pi\epsilon_0 r^2} \hat{e}_r \quad (3)$$

In equation 3 \hat{e}_r is the radial unit vector coming from the neighboring atom and q is the charge associated with the neighboring atom. Summing each of these vectors for all of the core atoms gives the results as shown in figure 7 for 600K, 1000K, and 2000K. The electric field plotted in figure 7 is within one order of magnitude of the simple model results, tabulated in table II, which assumes a homogeneous charge distribution in the core and oxide shell. The direction of the computed electric field indicates that the mass flux due to the electric field is directed out through the oxide shell rather than acting to randomly rearrange the atoms. The positively charged aluminum atoms will therefore be

preferentially directed towards the outer surface of the oxide shell, where they will come into contact with oxygen ions and oxidize.

With the diffusion coefficients previously computed and the electric field results computed here it is possible to analyze the mass flux due to concentration gradients (J_d), the electric field (J_e), and the internal pressure (J_c). The relative magnitude of the effect of the electric field on Al ion diffusion can be computed using the Nernst-Planck equation.

The Nernst-Planck equation is given in equation 4 [22].

$$J = -D \frac{dC}{dx} - \frac{zFDC}{RT} \frac{d\phi}{dx} + Cv \quad (4a)$$

$$J = J_d + J_e + J_c \quad (4b)$$

If we assume a zero molar concentration of Al cations in the shell and the bulk concentration at the interface then the parameters for equation 4a are given as the following.

$$C = 0.1 \text{ mol/cm}^3$$

$$\frac{dC_{1nm}}{dx} = 1.0 \cdot 10^6 \text{ mol/cm}^4$$

$$R = 8.314 \text{ J/mol}\cdot\text{K}$$

$$F = 96485 \text{ C/mol} \quad (5)$$

The electric field computed in table II is the negative of the charge gradient $d\phi/dx$.

The convective flux, J_c in equation 4 is the drift velocity of metal ions through the core/shell interface due to constant force acting on the ions. The force on these ions comes from the pressure gradient which is due to the expanding aluminum melt. When considering J_c only the radial drift velocity, and therefore the radial pressure gradient, in equation 4a is considered so that J_c can be rewritten as $C(Df_r/k_B T)$, where f_r is defined as

$$f_r = -\frac{\partial V}{\partial r} = -\nabla p v_{Al} \quad (6)$$

In equation 6, ∇p is the pressure gradient in the radial direction and v_{Al} is the solubility of Al in the Al_2O_3 network [23]. The maximum pressure gradients observed in the simulations range from less than 1GPa/nm at 600K to 2GPa/nm at 1000K and above. For the solubility of Al in Al_2O_3 we have assumed a value that comes from previous analysis of oxygen and Al diffusion through Al_2O_3 and should therefore be a reasonable value. Assuming a value of about 0.02nm^3 for the solubility of Al, v_{Al} , it is possible to estimate the mass flux due to each term in equation 4. The diffusivity due to the drift velocity is directly proportional to v_{Al} but variations here by less than one order of magnitude and would have little effect on the results in table III.

From the final column in Table III, listing the ratio of J_e to J , it is apparent that in all cases except for two, over 90% of the mass flux through the oxide shell is due to the induced electric field present at the core/shell interface. The exceptions to this 90% observation are the 1nm amorphous and 1nm dense $\text{Al}_2\text{O}_{2.7}$ shells at 2000K, which from previous analysis appear to have undergone a phase change at this temperature. This illustrates the importance of considering the electric field in the oxide shell for any oxidation analysis of the oxide coated aluminum nanoparticle system. Another interesting trend is that the importance of the electric field in diffusion increases, as both the shell thickens and the temperature decreases. The trend associated with temperature is expected since diffusion without an electric field is strongly temperature and pressure dependent, and at low temperatures diffusion would be very slow without an electric field. The trend associated with shell thickness requires some more thoughtful analysis. By considering the computed electric fields in table II, we observe that the magnitude

does indeed increase with shell thickness while the overall mass flux decreases, Table II and figure 8.

In figure 8 we observe some interesting trends not necessarily apparent in Table III. For nanoparticle systems at 600K and 1000K the degree of crystallinity in the oxide shell does not appear to have a noticeable effect on the mass flux of the aluminum cations through the oxide shell. This result is interesting because we can conclude that the reaction rate for oxide coated aluminum nanoparticles in this size range will not be dependent on how the coating was formed or upon its thickness, up to 2nm.

The most apparent trend in figure 8 is that the mass flux of aluminum atoms through the shell at 2000K decreases with increasing shell crystallinity and thickness. This result is likely due to the increased dependence of total mass flux on the concentration gradient and drift velocity terms in equation 4 as opposed to being solely due to the electric field. This decreased mass flux is observed as lower values in the last column in Table III for 2000K versus 600K and 1000K. Since the heating rate required to reach 2000K before an appreciable amount of the core has diffused into the shell is so high, greater than 10^{12} K/s, we would not expect this to be an experimentally observable result without some sort of very rapid heating method.

Formation of Hollow Aluminum Oxide Shells

Recent experimental efforts by Rai et al [9] and Nakamura et al [10] have both observed the formation of hollow aluminum oxide nanoparticles as a result of the oxidation of oxide coated aluminum nanoparticles. In the work by Rai et al [9] we observed the formation of hollow spheres of aluminum oxide subsequent to the oxidation of aluminum

nanoparticles at about 727K. We expected that these hollow oxide shells are produced by the outward diffusion of aluminum through the oxide shell as opposed to inward diffusion of oxygen. This observation is supported here by the high measured diffusion coefficients for aluminum cations and mass flux due to the electric field in the nanoparticle.

In order to better compare the inward diffusion of oxygen versus the outward diffusion of aluminum we have simulated a 5.6nm aluminum core with a 2nm crystalline oxide shell in a high density oxygen gas as shown in figure 9. The diffusion of oxygen ions through the shell has the potential to limit the mass flux of aluminum cations emanating from the core, producing reactions inside of the oxide shell and at the core/shell interface as opposed to on the nanoparticle surface. Oxidation in the core would potentially increase the internal pressure of the nanoparticle from volumetric expansion resulting in mechanical failure of the oxide shell, but would be unlikely to result in the hollow shells observed by Rai et al [9].

In figure 9 it is apparent that the diffusivity of aluminum cations through the oxide shell is observably higher than the diffusion rate of oxygen anions towards the core. This result indicates that oxidation will occur on or near the outer surface of the oxide shell rather than at or near the core/shell interface. By the oxidation reaction occurring on the outer shell surface an outward growth of the oxide shell is observed which ultimately results in a hollow aluminum oxide shell as observed experimentally [9,10]. One effect that may limit the mass flux of oxygen atoms into the oxide shell is that at higher temperatures the sticking probability of the gas molecules is lower than for temperatures <623K [24].

Conclusions

For small oxide coated aluminum nanoparticles we have found that ignition of the oxidation process is likely to occur by rapid diffusion of aluminum cations through the oxide shell as opposed to mechanical failure or melting of the shell, for heating rates as high as 10^{12} K/s. The high level of measured aluminum cation diffusivity is driven not only by the volumetric expansion of the aluminum core, but primarily by the induced electric field in the oxide shell. This enhanced diffusivity due to the induced electric field is supported by theoretical analysis of the Cabrera-Mott effect for oxide coated nanoparticles [21]. Oxidation initiation by rapid diffusion of aluminum ions to the nanoparticle surface is in agreement with published experimental efforts that have observed the formation of hollow aluminum oxide nanoparticles [9,10]. Diffusion of oxygen ions into the shell has also been considered but does not contribute appreciably when compared to the flux of aluminum to the nanoparticle surface.

References

38. X. Phung, J. Groza, E. A. Stach, L. N. Williams, and S. B. Ritchey. “Surface characterization of metal nanoparticles”, *Materials Science and Engineering A*, **359**, 261–268, 2003.
39. J.H. Sinfelt. *Bimetallic Catalysis: Discoveries, Concepts and Applications*. Wiley, New York, 1983.

40. J. Uppenbrink and David J. Wales. “Structure and energetic of model metal clusters”, *Journal of Chemical Physics*, **96**(11), 8520–8534, 1992.
41. A. Rai, D. Lee, K. Park, and M. R. Zachariah. “Importance of Phase Change of Aluminum in Oxidation of Aluminum Nanoparticles”, *Journal of Physical Chemistry B*, **108**, 14793–14795, 2004.
42. M.A. Trunov, M. Shoenitz, and E.L. Dreizin. “Effect of polymorphic phase transformations in alumina layer on ignition of aluminum particles”, *Combustion Theory and Modelling*, **10**(4), 603–623, 2006.
43. V.I. Levitas, B.W. Asay, S.F. Son, and M. Pantoya. “Melt dispersion mechanism for fast reaction of nanothermites”, *Journal of Applied Physics*, **89**, 071909, 2006.
44. V.I. Levitas, B.W. Asay, S.F. Son, and M. Pantoya. “Mechanochemical mechanism for fast reaction of metastable intermolecular composites based on dispersion of liquid aluminum”, *Journal of Applied Physics*, **101**, 083524, 2007.
45. P. Puri and V. Yang. “Thermo-Mechanical Behavior of Nano Aluminum Particles with Oxide Layers”, 46th AIAA Aerospace Sciences Meeting and Exhibit, Reno, NV, 7-10 January 2008.
46. A. Rai, K. Park, L. Zhou, and M.R. Zachariah. “Understanding the mechanism of aluminum nanoparticle oxidation”, *Combustion Theory and Modelling*, **10**(5), 843–859, 2006.
47. R. Nakamura, D. Tokozakura, H. Nakajima, J.-G. Lee, and H. Mori. “Hollow oxide formation by oxidation of Al and Cu nanoparticles”, *Journal of Applied Physics*, **101**, 074303, 2007.

48. N. Cabrera and N.F. Mott. “Theory of the Oxidation of Metals”, *Rep. Prog. Phys.*, **12**, 163–184, 1948.
49. A.T. Fromhold, jr, and E.L. Cook. “Kinetics of Oxide Film Growth on Metal Crystals: Thermal Electron Emission and Ionic Diffusion”, *Physical Review*, **163**(3), 650–664, 1967.
50. C. Wagner. “Beitrag zur Theorie des Anlaufvorgangs”, *Z. Phys. Chem.*, **B21**, 25, 1933.
51. L.P.H. Jeurgens, W.G. Sloof, F.D. Tichelaar, and E.J. Mittemeijer. “Growth kinetics and mechanisms of aluminum-oxide films formed by thermal oxidation of aluminum”, *Journal of Applied Physics*, **92**(3), 1649–1656, 2002.
52. A.C.T. van Duin, S. Dasgupta, F. Lorant, and W.A. Goddard III. “ReaxFF: A Reactive Force Field for Hydrocarbons”, *Journal of Physical Chemistry A*, **105**, 9396–9409, 2001.
53. F.H. Streitz and J.W. Mintmire. “Electrostatic potentials for Metal-Oxide Surface and Interfaces”, *Physical Review B*, **50**(16), 11996–12003, 1994.
54. Q. Zhang, T. Çağın, A. van Duin, W.A. Goddard III, Y. Qi, and L.G. Hector, Jr. “Adhesion and Nonwetting-Wetting Transition in the Al/α-Al₂O₃ Interface”, *Physical Review B*, **69**, 045423, 2004.
55. N. Pradeep, D.I. Kim, J. Grobelny, T. Hawa, B.J. Henz, and M.R. Zachariah, “Ductility at the nano scale: Deformation and fracture of adhesive contacts using atomic force microscopy”, *Applied Physics Letters*, **91**, 203114, 2007.
56. S. Ogata, H. Iyetomi, K. Tsuruta, F. Shimojo, A. Nakano, R.K. Kalia, and P. Vashishta. “Role of atomic charge transfer on sintering of TiO₂ nanoparticles:

- Variable-charge molecular dynamics”, *Journal of Applied Physics*, **88**(10), 6011–6015, 2000.
57. P.P. Mitra, P.N. Sen, L.M. Schwartz, P. Le Doussal. “Diffusion Propagator as a Probe of the Structure of Porous Media”, *Physical Review Letters*, **68**(24), 3555–3558, 1992.
58. V.P. Zhdanov and B. Kasemo. “Cabrera–Mott kinetics of oxidation of nm-sized metal particles”, *Chemical Physics Letters*, **452**, 285–288, 2008.
59. C.G. Zoski. *Handbook of Electrochemistry*. Elsevier, 2007.
60. J. Dalla Torre, J.–L. Bocquet, Y. Limoge, J.–P. Crocombe, E. Adam, G. Martin, T. Baron, P. Rivallin, and P. Mur. “Study of self-limiting oxidation of silicon nanoclusters by atomistic simulations”, *Journal of Applied Physics*, **92**(2), 1084–1094, 2002.
61. V. Zhukov, I. Popova, and J.T. Yates. *Surface Science*, **441**, 251, 1999.

Table I. Effective diffusion coefficients for core aluminum atoms with various oxide shell configurations. The effective diffusion coefficients are for general diffusion (D_{eff}) and radial diffusion (D_{radial}).

Shell Thickness	Type	Temperature	D_{eff} (cm²/s*10⁻⁷)	D_{radial} (cm²/s*10⁻⁷)
1nm	Amorphous	600K	53	5.9
1nm	Amorphous	1000K	420	300
1nm	Amorphous	2000K	7100	8300
1nm	Dense	600K	11	4.0
1nm	Dense	1000K	340	280
1nm	Dense	2000K	1300	1300
1nm	Dense, Al ₂ O _{2.7}	600K	2.6	2.1
1nm	Dense, Al ₂ O _{2.7}	1000K	380	190
1nm	Dense, Al ₂ O _{2.7}	2000K	6000	6700
1nm	Crystalline	600K	31	6.7
1nm	Crystalline	1000K	330	240
1nm	Crystalline	2000K	1000	1300
2nm	Amorphous	600K	23	4.6
2nm	Amorphous	1000K	400	320
2nm	Amorphous	2000K	770	660
2nm	Dense	600K	8.1	6.9
2nm	Dense	1000K	360	250
2nm	Dense	2000K	490	520

2nm	Dense, Al ₂ O _{2.7}	600K	4.2	3.3
2nm	Dense, Al ₂ O _{2.7}	1000K	370	180
2nm	Dense, Al ₂ O _{2.7}	2000K	270	100
2nm	Crystalline	600K	8.3	7.8
2nm	Crystalline	1000K	330	190
2nm	Crystalline	2000K	490	520
2nm, 8nm Core	Crystalline	600K	6.9	9.9
2nm, 8nm Core	Crystalline	1000K	190	160
2nm, 8nm Core	Crystalline	2000K	1300	920

Table II. Total charge of aluminum core and associated electric field are given here for all of the core/shell configurations considered. Note on electric field units, N/C = 0.01 V/m.

Shell Thickness	Type	Temperature	$Q_{core} (C \cdot 10^{-18})$	$E (N/C \cdot 10^{10})$
1nm	Amorphous	600K	8.28	1.10
1nm	Amorphous	1000K	5.67	0.75
1nm	Amorphous	2000K	1.47	0.20
1nm	Dense	600K	11.4	1.52
1nm	Dense	1000K	8.86	1.18
1nm	Dense	2000K	4.01	0.53
1nm	Dense, $Al_2O_{2.7}$	600K	7.91	1.05
1nm	Dense, $Al_2O_{2.7}$	1000K	6.38	0.85
1nm	Dense, $Al_2O_{2.7}$	2000K	1.09	0.14
1nm	Crystalline	600K	12.7	1.69
1nm	Crystalline	1000K	10.8	1.44
1nm	Crystalline	2000K	3.04	0.40
2nm	Amorphous	600K	13.3	1.77
2nm	Amorphous	1000K	11.9	1.58
2nm	Amorphous	2000K	4.61	0.61
2nm	Dense	600K	13.8	1.83
2nm	Dense	1000K	12.7	1.69
2nm	Dense	2000K	4.21	0.56
2nm	Dense, $Al_2O_{2.7}$	600K	11.6	1.54
2nm	Dense, $Al_2O_{2.7}$	1000K	11.1	1.47

2nm	Dense, Al ₂ O _{2.7}	2000K	7.80	1.04
2nm	Crystalline	600K	15.6	2.08
2nm	Crystalline	1000K	13.9	1.85
2nm	Crystalline	2000K	4.39	0.58
2nm, 8nm Core	Crystalline	600K	43.9	2.47
2nm, 8nm Core	Crystalline	1000K	42.6	2.40
2nm, 8nm Core	Crystalline	2000K	30.4	1.71

Table III. Diffusion coefficient and mass flux computed at 600K, 1000K, and 2000K for all shell configurations with the 5.6nm core unless noted. The last column labeled Ratio J_e to J , is the fraction of the total mass flux due to the induced electric field, with the balance due to the concentration gradient and drift velocities.

Shell Thickness	Configuration	Temperature	J (mol/cm ² ·s)	D (cm ² /s *10 ⁻⁸)	Ratio J_e to J
1nm	Amorphous	600K	4.20	1.97	0.98
1nm	Amorphous	1000K	11.97	13.6	0.96
1nm	Amorphous	2000K	53.45	424.0	0.83
1nm	Dense	600K	3.03	1.03	0.99
1nm	Dense	1000K	11.49	8.33	0.97
1nm	Dense	2000K	35.18	110.8	0.93
1nm	Dense, Al ₂ O _{2.7}	600K	2.13	1.03	0.98
1nm	Dense, Al ₂ O _{2.7}	1000K	8.06	7.88	0.96
1nm	Dense, Al ₂ O _{2.7}	2000K	46.27	426.0	0.78
1nm	Crystalline	600K	5.08	1.55	0.99
1nm	Crystalline	1000K	14.72	8.75	0.98
1nm	Crystalline	2000K	35.58	147.0	0.91
2nm	Amorphous	600K	3.31	0.97	0.99
2nm	Amorphous	1000K	18.49	10.0	0.98
2nm	Amorphous	2000K	23.73	65.2	0.94
2nm	Dense	600K	1.26	0.35	0.99
2nm	Dense	1000K	6.13	3.11	0.98

2nm	Dense	2000K	11.34	33.8	0.93
2nm	Dense, Al ₂ O _{2.7}	600K	3.69	1.23	0.99
2nm	Dense, Al ₂ O _{2.7}	1000K	7.99	4.58	0.98
2nm	Dense, Al ₂ O _{2.7}	2000K	5.27	8.38	0.96
2nm	Crystalline	600K	7.83	1.94	0.99
2nm	Crystalline	1000K	15.06	6.98	0.98
2nm	Crystalline	2000K	6.81	19.6	0.93
2nm, 8nm Core	Crystalline	600K	17.27	3.59	0.99
2nm, 8nm Core	Crystalline	1000K	24.31	8.61	0.99
2nm, 8nm Core	Crystalline	2000K	31.27	30.8	0.98

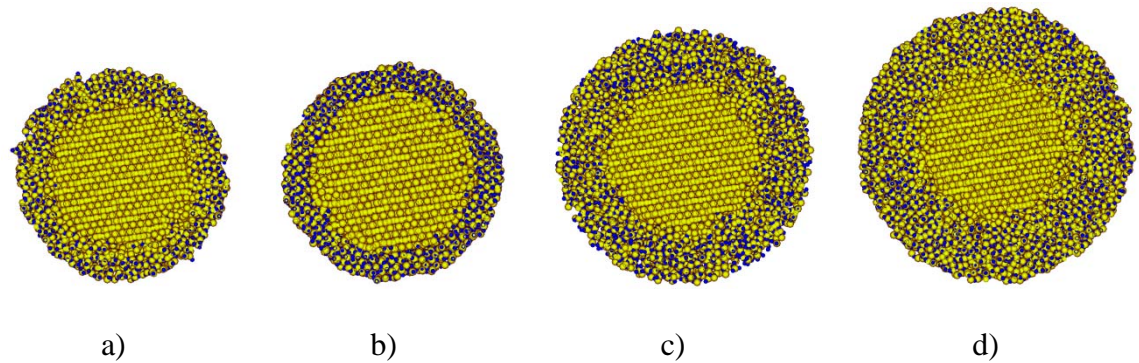


Figure 1.

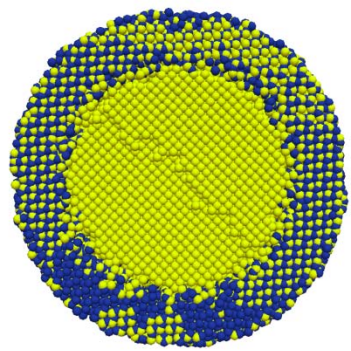


Figure 2.

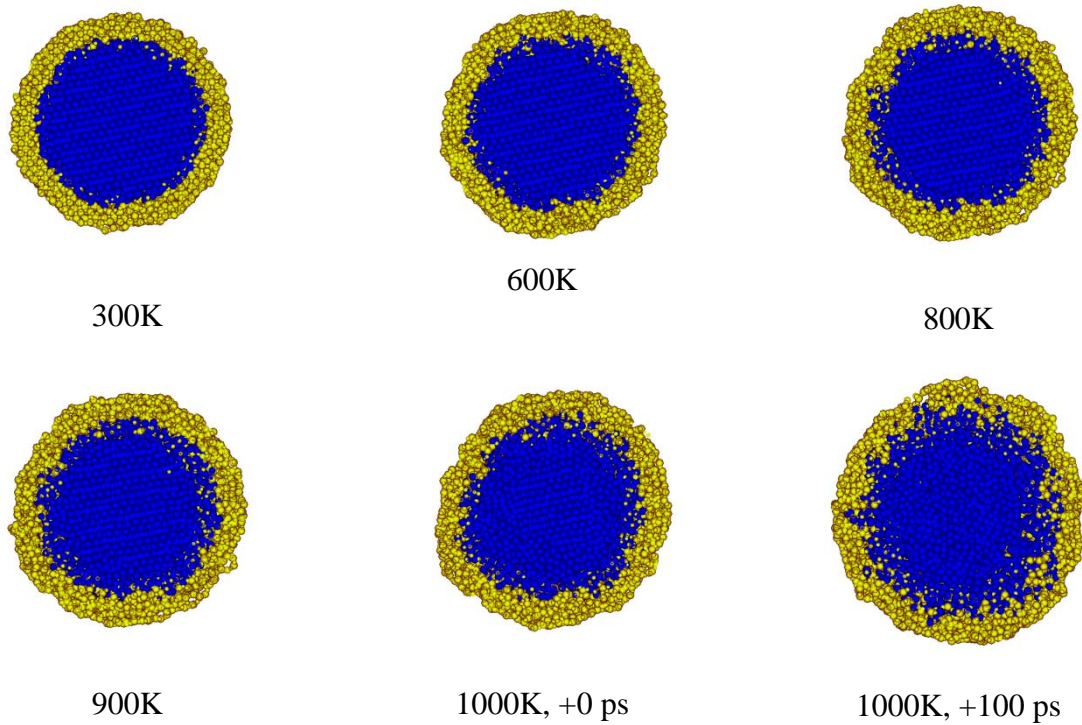


Figure 3.

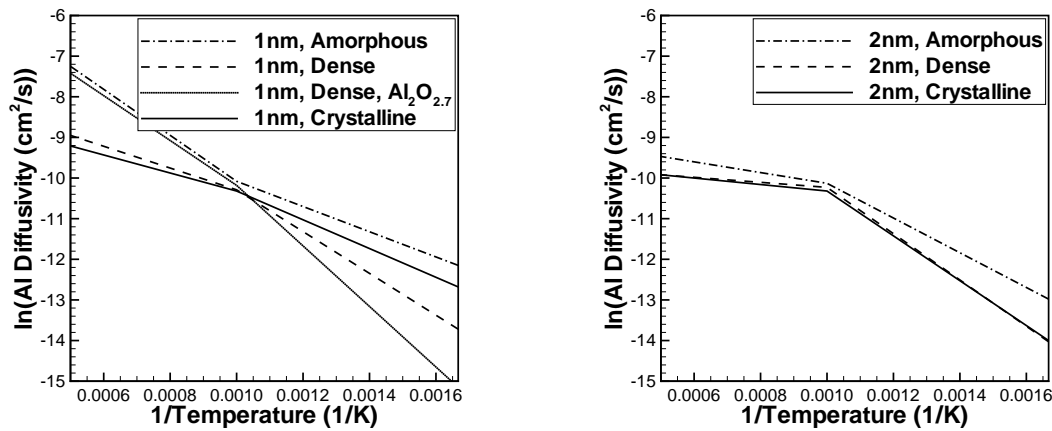


Figure 4.

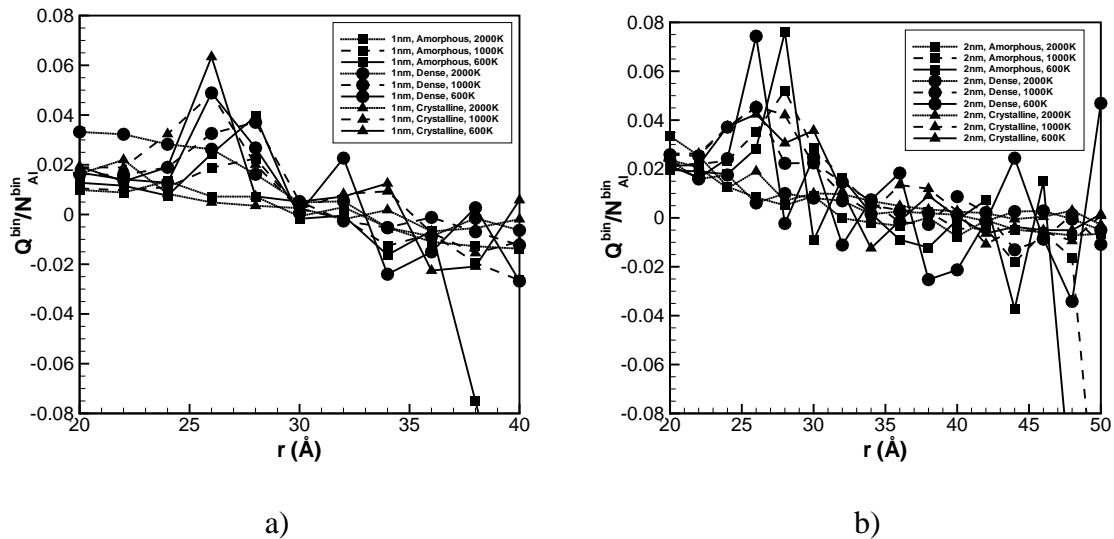


Figure 5.

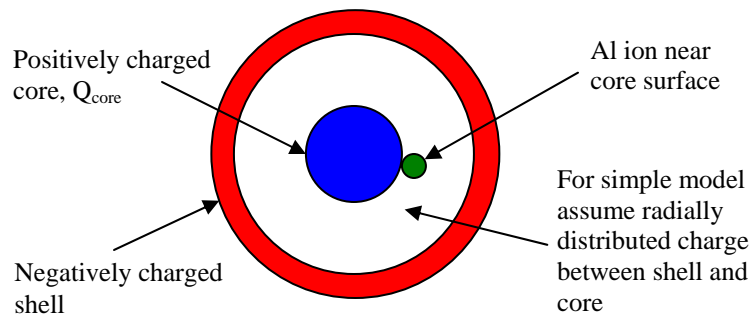


Figure 6.

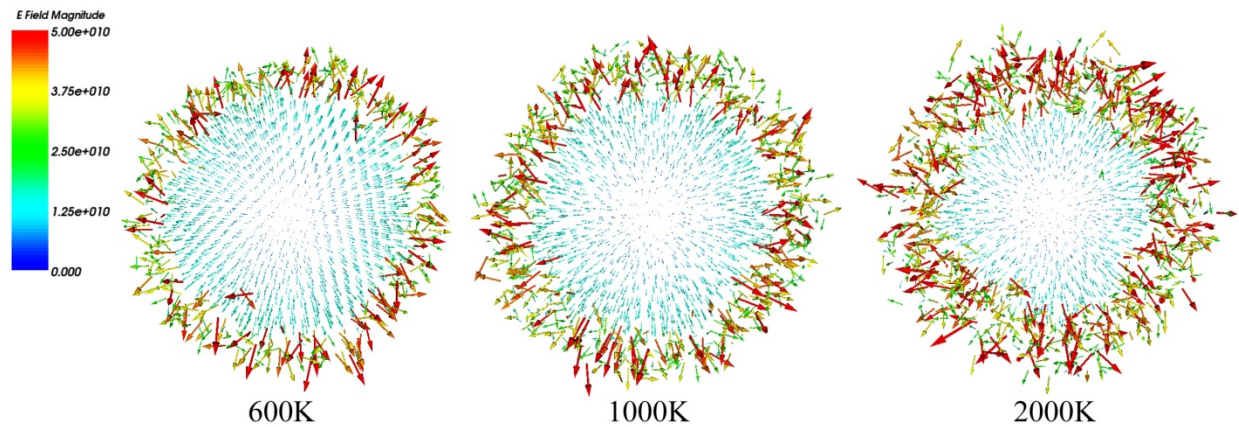


Figure 7.

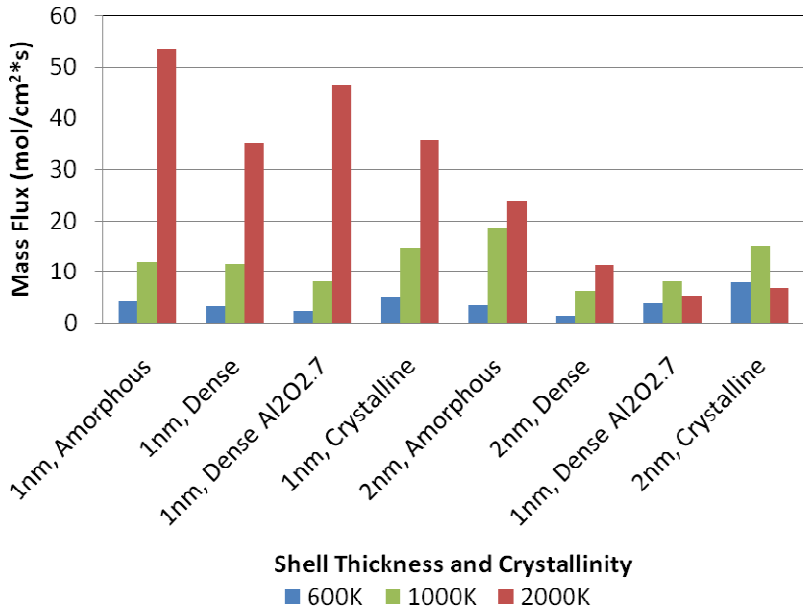
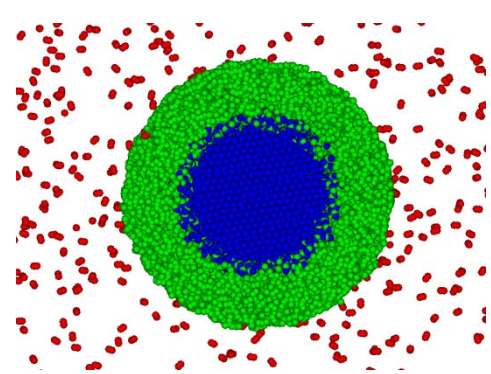
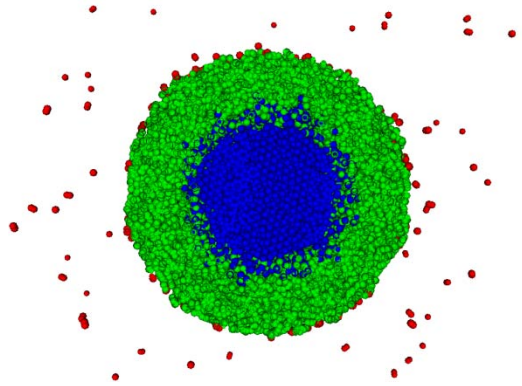


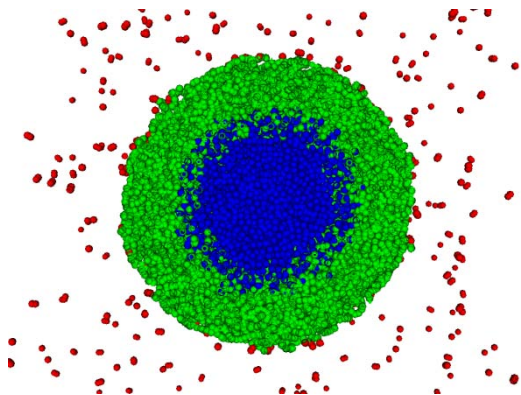
Figure 8.



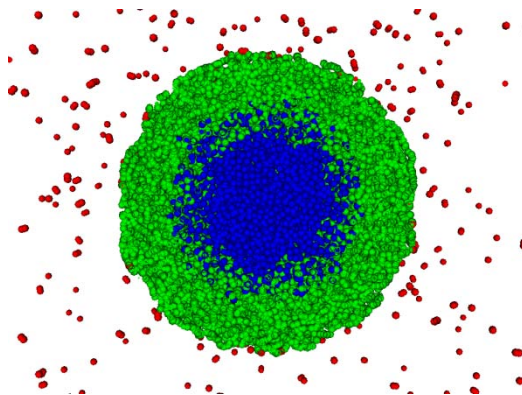
600K, 10ps



600K, 100ps



1000K, 10ps



1000K, 100ps

Figure 9.

Captions

Figure 1. Cross sections of some of the oxide coated aluminum nanoparticle models used in this work. a) 1nm thick, dense oxide shell. b) 1nm thick, crystalline oxide shell. c) 2nm thick, amorphous oxide shell. d) 2nm thick, dense oxide shell with 2:2.7 Al:O ratio. Blue spheres represent oxygen atoms and yellow spheres denote aluminum atoms.

Figure 2. Cross section of an 8.2nm Al core with 2nm thick crystalline oxide shell.

Yellow denotes Al atoms and oxygen atoms are blue.

Figure 3. Plot showing diffusion of aluminum cations (blue) through the 1nm thick oxide shell (red) as the temperature increases from 300K to 1000K and held for 100 ps.

Figure 4. Arrhenius plot of $\ln(D)$ versus $1/T$, where D is the diffusivity of the core aluminum atoms. The slope of this plot is the activation energy required for diffusion of aluminum cations and shows an expected decrease above the melting point of the core, at approximately 0.001/K.

Figure 5. Radial charge distribution through the oxide shell for a 1nm (a) thick shell and a 2nm (b) thick shell.

Figure 6. Schematic of assumed charge distributions affecting electric field around core surface aluminum atoms.

Figure 7. Electric field (N/C) at each of the core Al atoms in the nanoparticle core computed using Coulomb's Law. These results are for the 5.6nm core with a 2nm thick crystalline shell. Note the generally radial direction of the field.

Figure 8. Plot of mass flux versus temperature and shell configuration.

Figure 9. Cross section of oxide (green) coated aluminum core (blue) showing surrounding oxygen (red) atoms. Higher rates of diffusion for aluminum cations is

observed by aluminum atoms moving radially outward into the oxide shell atoms while adsorbed oxygen atoms remain on the outer surface or desorb from the shell. Figures a and b are at 600K and represent 10ps and 100ps of simulation time, respectively. Figures c and d are at 1000K, after 10ps and 100ps, respectively.

Characteristic features of the transient ion emission during nanocomposite thermite reactions

INTRODUCTION

Nanocomposite thermites, also known as Metastable Intermolecular Composites (MIC), have attracted great attention because of their promising features. In nanocomposite thermites, the reactive components consisting of nanostructured particles are intimately mixed. The unique nanostructure of MICs not only enhance the reactivity, but also allow a control over the reactivity by varying parameters such as particle size, morphology and local composition.[1-3] Currently this class of material is under intense research because of wide range of potential applications.

Because this class of material is relatively new they have not been studied as extensively as traditional organic based energetic materials. Research on thermite energetic materials typically focuses on developing new thermite formulations, as well as studying the thermite reaction mechanism. In general, a thermochemical point of view is emphasized in mechanism studies by means of characterizing combustion properties such as flame speed, reaction rate, ignition temperatures or reaction products.[4-9] On the other hand, literature shows that there are complex ionization phenomena observed through a variety of combustion systems.[10, 11] Ershov studied the detonation of solid explosives such as TNT and PETNA, and observed high degrees of ionization in the detonation front. The corresponding electron density is several orders of magnitude higher than the theoretical value estimated from the Saha equation, which indicates nonthermal channels of ionization.[12] Experiments also revealed transient electric/magnetic field generation from combustion of a variety of metal-gas and metal-metal reaction systems, and such

electric behaviors may attribute to the different diffusion rates of charge carriers through the oxide shell.[13-20] More recently, molecular dynamic simulations shows that strong electric field is intrinsically formed across the oxide shell of aluminum nanoparticles.[21] In fact, the electrical/magnetic fields can be considered as inherent reaction parameters which provide us one more dimension of controlling the reaction system, e.g. through using external electric field.[22, 23]

The above experimental and theoretical investigations suggest the knowledge on electrical/magnetic aspects of the nanocomposite thermite system is essential for comprehensive understanding of the reaction mechanism, and can provide us critical information on the issues of reaction control or the development of new diagnostic tools. However, there are only a few studies that report on ionization phenomena for nanocomposite thermites. Douglas and co-workers took a similar approach to Ershov's work and studied the electrical conductivity induced by nanocomposite thermite reactions. Their work showed that a conduction zone was observed in the reaction front, the conductivity profile was much longer than organic high explosives, and that the conduction mechanism is associated with the chemical reaction in nano-thermites.[24] Korogodov and co-workers observed a microwave radiation pulse from the combustion of an Al/Fe₂O₃ nanocomposite thermite system, and the radiation power is several orders of magnitude higher than thermal radiation.[25] These results indicate high degrees of ionization for nanocomposite thermite reactions, and the goal of our work is to investigate the characteristic nature of these ionizations.

In our previous work, we studied the nanocomposite thermite reactions using a recently developed T-Jump/Mass Spectrometer.[4, 26] During the course of the investigation, we

found that initiation of the exothermic reaction caused a catastrophic malfunction of the high voltage bias on the ion extraction optics, and resulted in loss of mass spectra signal. We also found the malfunction can be overcome and the operation of the mass spectrometer can be restored by operating the ion optics at negative voltage and ground. These results show that an intense flux of charged species (ions and electrons) are emitted from the thermite reactions, and the emission is much higher than that of organic high explosives and can interfere with the ion optics. This strong interference on the ion extraction provides us an opportunity to probe the characteristic nature of the transient ion pulse emission from nanocomposite thermite reactions. Compared with other experimental methods, we have some unique and incomparable advantages from using the mass spectrometer. As we will see from the experimental results, the thermite reactions emit extremely short ion pulses, which require a tool with high temporal resolution for characterization. In our experimental apparatus, the Micro-channel Plate Detector (MCP) detector is used to record the ion signals. MCPs are intrinsically fast detectors, which usually have a time resolution of picoseconds. Therefore, the overall temporal resolution is limited by our 500 MHz digital oscilloscope. In addition to the ultra fast time response, the mass spectrometer probes the ionization processes through the ion optics, so that the positive and negative species can be studied separately. Above all, the unique capability of conducting mass spectrometric measurement during the ionization events makes the ionization species identification possible for the first time, and the mass spectra can provide us critical information for better understanding of the ionization phenomena and the underlying ionization mechanisms.

EXPERIMENTAL APPRAOCH

In this work, we investigate the transient ionization behaviors of nanocomposite thermite reactions. Thermite composite samples were prepared by mixing aluminum nanoparticles with oxidizer particles to obtain a stoichiometric mixture. The aluminum used was 50 nm ALEX powder obtained from Argonide Corporation. Four types of oxidizers, copper oxide (CuO), iron oxide (Fe_2O_3), bismuth oxide (Bi_2O_3) and tungsten oxide (WO_3) nanopowders of $\sim 100\text{nm}$ obtained from Sigma-Aldrich, were used to mix with aluminum particles. Nanocomposite thermite samples were mixed in hexane and the suspensions were sonicated for about 30 minutes to break the agglomerate and ensure intrinsic mixing between the fuel and oxidizer. The prepared sample suspensions could then be coated on the T-Jump probe with a dropper. The T-Jump probe is a $\sim 10\text{ mm}$ long platinum wire with diameter of $76\mu\text{m}$, for which the center of the wire is coated with a thin layer of sample with coating length of $\sim 5\text{mm}$. From our previous work, we have estimated that the sample on the probe is no more than 0.3 mg.

The primary analytical tool used in this work was a recently developed Temperature-Jump/Time-of-flight (T-Jump/TOF) Mass Spectrometer.[4, 26] The T-Jump/TOF mass spectrometer is comprised of a linear Time-of-Flight chamber, an electron gun ionization source, and the T-Jump probe with an electrical feed-through for rapid sample heating. A detailed description of the T-Jump/TOF mass spectrometer can be found in our previous work.[4] Here in this work, different configurations on the ion optics were used to extract ions of interest. The schematic of ion optics is shown in figure 1. The ion optics consist of an ion repeller plate A1, an ion extraction plate A2 and an ion acceleration plate A3. A

liner system was used to ensure a field-free ion drifting region in the Time-of-flight tube, and a Micro-channel plate (MCP) detector was used to measure the extracted ions. Since we were probing thermite reaction induced ionization, the electron impaction ionization source was turned off, and with appropriate ion optics voltage settings and T-Jump probe locations, we are able to measure the total positive or negative ions generated from nanocomposite thermite reactions, as well as mass spectra for ion species identification using the T-Jump/TOF Mass Spectrometer. The experimental configurations of ion optics voltages and probe position are summarized in table 1.

Total ions were measured by inserting the T-Jump probe in between the repeller plate A1 and the extraction plate A2 as shown in figure 1. Total positive ions can be measured by using the following DC voltage bias settings: A1 to ground, A2 to -200V, A3 and the liner to -1500V and the total negative ions/electrons can be measured by using the DC voltage bias settings: A1 to -200V, A2 to ground, A3 and the liner to +1300V, as listed in table 1. Ions/electrons were continuously extracted by ion optics, and consequently, the ion signal detected from the MCP corresponds to the total number of ions/electrons generated during the thermite reaction, but do not contain any ion mass information. For mass spectra measurement, we operate the mass spectrometer by pulsing the ion optics. Essentially, the T-Jump/TOF Mass Spectrometer was operated in the same way as we illustrated in our previous work,[4] except no electron impaction ionization source. The T-Jump probe was placed outside, but close to the ion extraction region, and the voltages on the ion optics were set as A1 to ground, A2 pulsed from ground to -200V at 10 kHz repetition rate, A3 and the liner to DC -1500V. This configuration enables us to obtain the positive ion mass spectra. We also attempted to measure the negative ion mass

spectra by setting the ion optics as, A1 pulsed from ground to -200V, A2 to ground, A3 and the liner to +1300V. However, the thermite reaction induced electrical pulse caused an arcing in the ion extraction region. As a result, the ion signals from the MCP detector were corrupted and we were not able to obtain the negative mass spectra.

In addition to the total ion and mass spectra measurements, the T-Jump/TOF Mass Spectrometer was also equipped with a high speed camera system. (Phantom XXX) The same trigger signal was used to simultaneously initiate the T-Jump probe heating and capture images. The camera captured the ignition/combustion process of thermite samples at a rate of up to 30 us per frame, and the time resolved images can be directly compared with the ion signal obtained from the same ignition event.

RESULTS AND DISSCUSSION

Figure 2 shows the typical results of the total positive ion measurement for (a) Al/Fe₂O₃ (b) Al/CuO, (c) Al/WO₃ and (d) Al/Bi₂O₃ nanocomposite thermite mixtures. The ion signals are plotted as function of T-Jump heating time. The Zoom-in views are also plotted in Figure 2 to show the fine structure of the ion signals. An important piece of information that is available from figure 2 is the temporal evolution of the ion emission process, which corresponds to the width of the ion signal. As we can see in the zoom-in view of Figure 2 (a), the ion signal from Al/Fe₂O₃ reaction, which lasted for about ~0.4 ms (from 2.3 ms to 2.7 ms), exhibits the longest ionization period among all four nanocomposite thermites. Similarly, the ionization duration for Al/CuO reaction (figure 2 (b)) is ~0.3 ms, with the major ion peak width lasting less than ~0.1 ms. Al/Bi₂O₃ mixture shows the shortest ionization period among all four nanocomposite thermite

systems, the ion signal in figure 2 (c) is ~0.1 ms with the major ion peak width lasting less than ~0.03 ms, and Al/WO₃ has an ionization interval of ~0.3 ms but the width of the major peak is only ~0.02ms (figure 2 (d)).

Our previous work has shown that the overall burn time of nanocomposite thermite reactions in T-Jump experiments is in the order of ~1 ms.[26] Compared with the ion emission duration observed from Figure 2, it is clear that the thermite reaction induced ionization does not correlate with the whole reaction interval, but shows a transient nature. Here an obvious question is how the ion pulses are related to the nanocomposite thermites reactions. This can be answered by examining the time resolved images taken by the high speed camera for the same ignition events. Here we would like to first point out that although the camera and the heating of the probe are triggered simultaneously, the ions were detected by the MCP detector after the ions drifted in the linear TOF tube, so the ion signals are slightly delayed compare with the time resolved images. However, as the delay time is only on the order of ~10 us. As an example, for a singly charged Al ion the drifting time is about 7.8 us, and we ignore this difference in the following analysis.

Figure 3 shows the camera captured images for the same ignition event for (a) Al/Fe₂O₃, (b) Al/CuO, (c) Al/Bi₂O₃ and (d) Al/WO₃ nanocomposite thermite samples. Figure 3 shows that the ignition was initiated from the two ends of the sample coating instead of the center of the wire where the temperature is supposed to be the highest. In our previous work, we have developed a simple heat transfer model to predict the energy coupling between the sample powder and T-Jump wire.[26] The model suggests that much of the energy is transferred from the wire to the powder during the heating. As the

result, the wire temperature is significantly lowered compare to the temperature trace resulted from heating of a bare wire. In our experiments, the center of the wire was coated with sample powder where significant amount of energy was transferred to heat the sample, therefore the highest temperature points are indeed at the two ends of the coating at where the ignition was started. Now we take Al/CuO as an example for temporal analysis. If we compare figure 3 (b) with figure 2 (b), we can see the ion signal start to rise at \sim 1.85 ms, much before the first ignition event at 2.042 ms was observed from the camera. Also, the major ion peak in figure 2 (b) occur at \sim 2.05 ms, which roughly coincides with the first ignition event. As the ignition initiated, it propagated from the two ends toward the center, and the whole thermite sample was ignited at time 2.219 ms. The thermite sample was continuously reacting and the reaction was complete at \sim 2.6 ms as shown in figure 3 (b). On the other hand, the ion emission process was well over before the whole sample had been ignited. From this result, we can conclude that the positive species generation actually occurred right before the ignition, and ended around the time when the nanocomposite thermite ignites. This relation can also be observed for the cases of Al/Fe₂O₃ and Al/Bi₂O₃, and is particularly clear for the case of Al/WO₃ as the ion signal in figure 2 (d) is complete well before 2.1 ms in contrast to the figure 3 (d) where the ignition did not start until \sim 2.2 ms, and the sample powder was not fully ignited even at \sim 2.4 ms.

Similar experiments were conducted to measure the total negative species (ions or electrons). Figure 4 shows the total negative signal and figure 5 shows the corresponding time resolved images from the camera for (a) Al/Fe₂O₃, (b) Al/CuO and (c) Al/WO₃. The Al/Bi₂O₃ nanocomposite thermite reaction caused arching for this experimental

configuration and we will discuss it later. The ion emission duration can also be estimated based on negative ion/electron signals. The ion signal from the Al/Fe₂O₃ reaction (figure 4 (a)) rise from ~2.4 ms and lasted for ~0.6 ms, and the major peak is only ~0.1 ms width. The ionization duration for Al/CuO reaction (from figure 4 (b)) is ~0.2 ms, and for Al/WO₃ mixture is ~0.5 ms (figure 4 (c)). Compared with the results obtained from the positive ion measurements, the negative ion/electron signals suggest a slightly longer ionization interval. As we further examine the ion signals together with the time resolved images shown in figure 5, we can see that this discrepancy is not coming from experimental artifacts such as different coating morphology, etc. The analysis reveals that it is actually an inherent character of the thermite reaction. Here again we take Al/CuO nanocomposite thermite system as our example and compare ion signals in figure 4 (b) and images in figure 5 (b). In this heating event, the ignition was first observed at 2.04 ms and further propagated so that the whole thermite sample was ignited at time 2.187 ms. On the other hand, the temporal evolvement of negative ion signal also happened in the same interval from ~2.05 ms to ~2.2 ms. Unlike positive species which were observed before the ignition, negative species were generated during the ignition, suggesting there is a separate ionization process and that the negative species were closely associated with the ignition of thermite powders. A similar analysis was performed for Al/Fe₂O₃ and Al/WO₃ nanocomposite thermite systems (figure 4 (a), (c) and figure 5 (a), (c)), and the same behavior were also observed. These results suggest this characteristic ionization behavior is quite generic and independent of the composite formulation.

From the above temporal analysis on the positive/negative signals, we can conclude that there are two primary ionization steps around the ignition point. The first ionization step happened prior to the ignition and dominant species are positive ions. Also, the ignition of nanocomposite thermite mixtures leads to the second ionization step which primarily produces negative species. After the ignition has propagated along the T-Jump probe, the reactants were blown off from the wire but the thermite reaction still continued. However, no significant ions emission were observed, which suggest aggressive ionization has been finished. Later analysis shows that there were still some ions detected during this time.

In the experiments of measuring total ion signal, ions or electrons were continuously extracted by the ion optics since we applied constant DC voltage bias to the plates. Therefore, information on the total number of ions can also be extracted from the results shown in figure 2 and figure 4. Quantitative signal analysis requires knowledge on the ion extraction efficiency as well as ion beam transport efficiency, which is determined by the initial kinetic energies of the ions and the electric field in the ion extraction region.[27, 28] The experiments require us to put the T-Jump probe inside the ion extraction region, and the probe is actually slightly biased to a positive potential due to the heating current. Due to the presence of the probe, the electric field from the parallel plates is significantly altered, and positive and negative species would also have different extraction efficiencies. Positive species tend to be repelled by the probe so that they are easily extracted by the ion optics, while negative species tend to be trapped locally by the probe potential.(should we show the simion simulation of this?) Furthermore, as we concluded from temporal analysis of ion signals, the positive species and negative species were generated in different processes which are presumably governed by different ionization

mechanisms, which could cause the initial kinetic energy distribution to also be significantly different. As a result, only a fraction of the total ions are detected by the MCP detector, and since the detection efficiency is unknown, we can only compare the ion signals in a semi-quantitative manner.

The MCP signal is an amplification of the ion current that reaches the detector, the number of ions detected is proportional to the integral of the ion signal. Figure 6 shows the integrated ion signals for (a) Al/Fe₂O₃, (b) Al/CuO, (c) Al/Bi₂O₃ (only positive ion signal available) and (d) Al/WO₃. The integrated positive and negative signals are plotted in the same figures. Because the positive and the negative signals are not measured from the same heating events, and the ignition time may be slightly different in each heating event due to experimental artifacts, it may be inappropriate to directly compare the temporal evolution of the integrated curves. Nevertheless, the results for Al/Fe₂O₃ and Al/CuO systems and especially the Al/WO₃ system clearly shows that the traces for the negative species rise prior to the positive ones, consistent with our observation that there are multiple steps of ionization occurring throughout the ignition of nanocomposite thermites.

The integrated ion signals can be divided into three regions, pre-ignition heating, ignition and post ignition, as shown in figure 6. During the initial heating, the integrated ion signals remain flat, which suggests there are no ion emissions, thus no occurrence ionization. As time advanced, both positive and negative ion signals rise sharply indicating the birth of the ion pulses from the aggressive ionization processes which are associated with the ignition events. Following that stage, the integrated signals continuously increased, but at a much slower rate. This result indicates that there are still

ions detected after the ion pulse has ended, though with a much lower ion concentration. Notice that the Figure 2 and Figure 4 do not show a significant amount of ion detection after the strong ion pulses, which is probably due to the low ion densities generated over relatively long time periods, however, we can clearly observe the slow rise of the ion signal in the accumulated mode as shown in Figure 6. Regarding the origin of these post ignition ions, one may naturally think that the chemical reaction leads to a relatively “soft” ionization, therefore ions are produced as the thermite reaction continues. However, as we can see in figure 6, the post ignition ions were detected over quite a long period, about 2 to 3 ms after the ignition event, while the observed reaction time in the T-Jump experiments is usually in the order of \sim 1 ms.[26] In particular, the result for Al/Bi₂O₃ system (figure 6 (c)) shows that there is a plateau region in the integrated ion signal curve that separates the ignition ion signals and the post ignition ion signals. This behavior indicates that the post ignition ions are not likely to correlate with the thermite reaction, instead, they are actually detected after the thermite reaction. Here if we consider the transient and aggressive nature of the ionization, there is an excessive amount of ions generated from the thermite ignition events. In fact, we have observed that the thermite reaction induced ionization is so aggressive that it can cause arching in the ion optics for some of our experimental configurations. Therefore, it is possible that these post ignition ions are simply the residue ions resulting from the ignition ionization. In the extreme case of Al/Bi₂O₃ reaction system, the presence of an enormous amount of ions in the ion extraction region would result a space charging effect and significantly reduce the ion extraction efficiency, which lead to the plateau region shown in figure 6 (c). However, we are not able to completely rule out the possibility of the “soft” ionization during the

chemical reactions. Presumably, our experimental observation is the result of both scenarios.

In addition to the total integrated ion signals, we also calculated the peak area of the ignition associated positive/negative ion peaks, e.g. the integral of the zoom-in view signal, and the results are also listed in each of the figure 2 and figure 4. The peak areas for positive ion signals are 0.46, 0.46, 0.42 and 0.53 for Al/Fe₂O₃, Al/CuO, Al/WO₃ and Al/Bi₂O₃ thermite systems, respectively. As we can see from figure 2, the intensities of ion signals varied depending on the composite mixtures, from ~5 mV for Al/Fe₂O₃ thermite system to ~ 30 mV for Al/Bi₂O₃ thermite systems, the peak areas of the ion signals are remarkably similar. Since the signal intensity represents the ion current reaching the detector, a higher intensity indicates a higher rate of ionization and higher ion density. Therefore, the experimental results shown in figure 2 suggest the ionization rate is thermite composition dependent, and the order of the ionization rates can be roughly correlated with the reactivity of nanocomposite thermite mixtures. The Al/Bi₂O₃ thermite system produces the most intense positive ion current density, and thus the most aggressive ionization among all four tested nanocomposite thermite mixtures. Al/Fe₂O₃ produces the weakest positive ion current density and is the least intense ionization system. On the other hand, even though the signal intensities are significantly different, peak areas observed from different nanocomposite thermite mixtures are comparable. Since the peak area represents the total number of ions reaching the detector, if we assume ions from different thermite reactions are extracted with the same efficiency, this result suggests that the numbers of positive ions produced are about the same regardless of the thermite compositions. In other words, Al/Fe₂O₃ system ionizes at a slower rate

but for longer time contradictory to the Al/Bi₂O₃ system which ionizes much more aggressively during a shorter interval. The result is that the overall number of positive ions generated from the ionization process are about the same. Of course this conclusion is based on the assumption of the same ion extraction efficiency. However, the fact that all four thermite reaction systems show remarkably similar peak areas suggests this assumption should be true. Furthermore, considering that fact that the extraction efficiency is determined by the ion initial kinetic energy distribution, this also implies that the ions are produced with similar initial ion kinetic energy distributions in spite of the different thermite compositions. A similar scenario can also be found for negative species, the peak areas for negative ion signals are 0.51, 0.57, and 0.65 for Al/Fe₂O₃, Al/CuO, and Al/Bi₂O₃ thermite systems, respectively. As we can see different thermite systems result in comparable negative ion peak areas, implying that about the same amount of negative species are generated in the thermite T-Jump experiments and it is independent of the thermite composition. Now as we compare the peak areas for the positive and negative species, we can see that there are slightly more negative species detected than the positive species. Moreover, if we consider the fact that the positive and negative ions are extracted differently, the presence of the T-Jump probe tend to repel the positive species but attract negative ones, so that the positive ions may be extracted with a higher efficiency contrast to negative species. Therefore, there is a possibility that more negative species generated than the positive species, which presumably due to the fact that there are multiple steps of ionization and the positive and negative ions are created by different mechanisms.

In fact, there is a polarity effect observed through the course of our experiments, which can be related to the different ion densities between the positive and negative species. As we mentioned in the introduction, one of the motivations of this work is arcing on the high voltage extraction optics caused by the thermite reaction induced ion emissions , which resulted in a loss of mass spectrum signal. We found that the ionization induced arch has a polarity preference, it only happens if we have positively biased ion optics plates near the T-Jump probe. For example, we can conduct successful experiments to measure the total positive ions signal by using -200V on the A2 plate. However, our attempt of using +200V on A2 plate for negative ion measurements failed because of arching within the ion extraction region. The images recorded by the high speed camera confirmed that the arcing event happened immediately following the ignition, which suggest this behavior is related with the thermite ignition ionization. Further experiments show that even +50V bias still leads to arcing and all four nanocomposite thermite systems show similar behavior. As a result, we have to negatively bias the A1 plate to extract negative ion species. Through the course of our investigation we have concluded that, in general, the arcing behavior would occur if there is an open path from the T-Jump probe to a positively biased electrode. For example, in our experiments of measuring total negative ion signals, since the probe was put inside the ion extraction region, even with A3 biased to +1300V, most of the experiments can be conducted free of arcing. However, if we pull the probe out and ignite the thermite samples, the positively biased A3 plate can be exposed directly to the T-Jump probe and result in arcing behavior. Consequently, we are not able to conduct mass spectra measurement on negative species since that experimental setup requires us to put the probe outside, but

close to the ion extraction region, and to positively bias the A3 plate for negative extraction. One exception from this conclusion is the Al/Bi₂O₃ thermite system. In the case of a positively biased electrode near the T-Jump probe, the ignition of the Al/Bi₂O₃ thermite system shows much stronger arcing than other thermite systems judging by the brightness and the sound of the plasma. In fact, the plasma is remarkably strong that the ion current from less than 0.3 mg of sample can damage our T-Jump heating power supply. Because of this violent nature, we still observe arching in the experiments of measuring the negative ions of Al/Bi₂O₃ thermite system, even though there is no positive biased electrode near the T-Jump probe. We believe the polarity effect can be attributed to the density differences between the positive and negative ion formations. Since negative species have higher ion density than positive ones, the transient current pulse collected by the positively biased electrode is much more intense, and creates a higher possibility of arching. Here we would like to point out that we have conducted successful experiments to characterize the combustion of RDX and Nitrocellulose using the T-Jump/TOF mass spectrometry with standard high voltage biased ion optics with no arching behavior observed,[4] even though the ionization phenomena from traditional high explosives has been reported.[12] This result implies that the degree of ionization from nanocomposite thermite systems is orders magnitude higher than high explosives, and indicates unique underlying chemical/physical mechanisms that are responsible for the thermite reaction induced ionization processes.

So far we have limited our scope on the total positive/negative ion signals, and our analyses reveal many characteristic features of the thermite reaction induced ionization processes. However, what makes our experimental apparatus exceptional is the capability

of conducting mass spectrometric measurement so that the ion species can be identified. We have conducted mass spectrometric measurements for both positive and negative ions species, but negative mass spectra measurements failed because of the polarity effect describe above. Positive mass spectra for all four thermite systems were measured in the experiments. The mass spectra for the Al/Fe₂O₃ thermite system does not contain any ion signals, so that no ion species information can be extracted for Al/Fe₂O₃ ionization. This result is not surprising considering the small total signal intensity shown in figure 2 (a) for Al/Fe₂O₃ which indicates a weak ion current density from ionization. On the other hand, mass spectra for Al/CuO, Al/Bi₂O₃ and Al/WO₃ systems contain intense signals. Example spectra for Al/CuO thermite is shown in figure 7. In the experiments the electron impact ionization source in our mass spectrometer was turned off to ensure the thermite reaction as the sole source of ions, however, the tradeoff of not using the electron impaction beam is losing the mass spectra resolution. As we can see the mass spectra in figure 7 shows poor quality, and we can not resolve the broad peak range at m/z 5 to 10 to identify the ion species. Nevertheless, ion peaks of Na (m/z = 23), Al (m/z = 27) and K (m/z = 39) can be clearly identified from figure 7, and the mass spectra suggest Na is the dominant positive species generated from thermite reaction. There is also a small peak at m/z = 64, which corresponding to Cu and suggests Cu ions may generated as minor species from thermite reaction induced ionization. However, since the high noise to signal ratio of the Cu ion peak, it is difficult to draw a clear conclusion about the generation of Cu species. Mass spectra were also obtained for Al/Bi₂O₃ and Al/WO₃ thermite systems, and we found the results are similar to the Al/CuO case. Independent of thermite compositions, the positive mass spectra all contain strong Na

peak, suggesting the positive ion species distributions are dominated by Na with minor species of Al and K, for all the tested thermite systems. There is also a clear Bi peak ($m/z = 209$) observed for Al/Bi₂O₃ thermite system, but no W species can be found for the case of Al/WO₃. This observation is consistent with the fact that Al/Bi₂O₃ produces the most intense ionization so that Bi has better chances to be ionized.

As we can see from the mass spectrometric measurement, the major positive ion species generated from thermite reactions are actually not from thermite metal/metal oxide particles. Instead, they are Na and K ions which are obviously a result of sodium chloride and potassium chloride contaminations. Furthermore, the mass spectra patterns obtained for three different thermites show similar ion peak patterns, suggesting a common ionization mechanism that governs the generation of positive ion species. Together with the observation of Al species in the mass spectra, we believe that the underline ionization mechanism for positive ions should be closely related to the ion flux in the shell of the aluminum nanoparticles. Recently, we have studied the ignition behavior of nanocomposite thermites under T-Jump heating conditions (heating rate $\sim 10^5$ K/s), and the results suggest that the ignition of nanocomposite thermites is controlled by diffusion of molten aluminum through the oxide shell.[29] The diffusion controlled metal oxidation theories have been studied for several decades. Depending on types of the metal or thickness of the oxide layer, many theoretical models have been developed to study metal oxidation.[30-32] It is believed that the diffusion of ions and electrons through the oxide shell due to concentration and pressure gradients, or electric field within the oxide layer, is the controlling transport process for metal oxidation.[33-35] From Cabrera and Mott's thin film growth theory, a strong electric field on the order of $\sim 10^7$ V/cm is predicted

across the oxide shell caused by tunneling electrons, and the ion transport is assisted by the electric field.[36, 37] We also observed similar electric field phenomena on aluminum nanoparticles at high temperatures through molecular dynamics simulations.[21] The simulation results show that the strong electric field is intrinsically self-generated due to the presence of the oxide shell, which provides a tremendous driving force for the diffusion process. In the case of small aluminum nanoparticles of 6 nm with a thin oxide shell of 2 nm, the molecular dynamics simulations show that a strong Al ion flux of \sim 20 mole/cm²/sec is formed through the initial stage of the transport processes, and 99% of which are driven by the electric field instead of the concentration and pressure gradients. For the larger aluminum nanoparticles that we used in the T-Jump experiments, an even higher ion flux should be expected.

Based on the above discussion, we conjecture that the positive ion generation can be correlated with the diffusion of the Al ion flux. The observation of Na and K ions suggest the nanocomposite thermite mixtures are contaminated with minor sodium chloride and potassium chloride salts. It is quite reasonable considering these salts are ubiquitous and insignificant amount of salts could be introduced to the particle's surface during the sample preparation and handling process. Prior to the ignition point the aluminum particles are already at elevated temperatures and the electric field are well formed across the oxide shell. Assisted by the electric field, enormous aluminum ions start to diffuse and approach the particle surface. On the other hand, the salts exist at the particle surface in the form of Na^+ , K^+ and Cl^- ions and are weakly bonded with surface atoms. As the aluminum ions reach the particle surface, the electrostatic repulsion force between Al^+ and Na^+ or K^+ due to the coulomb potential eject the Na^+ and K^+ ions from particle

surface. As the result, transient ion emissions composed of Na^+ , K^+ and some Al^+ is formed prior to the ignition of the thermites. The ionization rate can be estimated using the Al ion flux of ~ 20 mole/cm²/sec predicted by our molecular dynamic simulations.[21] If we assume the electrostatic repulsion force from coulomb potential becomes significant only when two ions are in 1 nm range, the aluminum ions will be moving toward a single Na^+ or K^+ ion at the rate of $\sim 10^{11}$ per sec. In other words, during our observed ionization interval of ~ 0.1 ms, there are $\sim 10^7$ aluminum ions around a single Na^+ or K^+ ion. As a result of the strong electrostatic repulsion force, high degrees of ionization which primarily depend on ion ejection efficiency should be expected. This argument also explains our observation of Na^+ ions as the most abundant species in the mass spectra even though the salt contaminations in the thermite should be extremely low. In addition, our experimental results suggest that the total number of positive ions produced from different thermite reaction systems are about the same regardless of the thermite compositions, and this observation agrees with the fact that similar salt contamination levels should be expected for all the tested thermite samples because of the similar handling procedure.

The diffusion flux based ionization mechanism can qualitatively explain the positive ionization step induced by thermite reactions. The temporal evolution analysis of total positive ion signal shows that the ionization step occur prior to the thermite ignition, which can be attributed to the initial Al ion flux created by the electric field across the oxide shell. Since high the reactivity of thermite mixtures implies high ion flux through the shell, a correlation between the ionization rates and the reactivity of nanocomposite thermite mixtures should be expected and is also observed experimentally. The system

reactivity can be linked to oxidizer particles which behaved as an oxygen storage device and release oxygen upon heating,[26] the electric field and the ions transport properties are affected by degree of oxidation and oxygen concentration. As the results, different thermite compositions lead to different ionization rates. The weak total ion signal intensity obtained for Al/Fe₂O₃ system (figure 2 (a)) suggests a slow ionization rate and the Al/Bi₂O₃ system (figure 2 (d)) show the strongest ions signal intensity which indicating the most intense ionization. The weak total ion signal intensity obtained for Al/Fe₂O₃ system (figure 2 (a)) suggests a slow ionization rate compare with other thermite systems, and because of the low ion density produced from Al/Fe₂O₃ system, the mass spectra do not have any ion signals. Here to test our theory, an Al/Fe₂O₃ thermite sample was prepared by intentionally adding sodium chloride salt. The sample is made sodium chloride rich by mixing the thermite powder with NaCl at 1:2 mass ratio, and we conducted experiments to measure the positive ion mass spectra for the Al/Fe₂O₃/NaCl mixture. As we can see from figure 8, the mass spectra shows a strong Na, Al and K peaks, agreeing with our expectation. The result shown in figure 8 confirms the salt contamination as the primary positive ions source, and suggests our diffusion flux based ionization mechanism for positive ion pulse generation should be true.

With the advantage of mass spectra measurement, we are able to develop a qualitative model to explain the initial step of thermite reaction induced ionization which produces positive species. As our experimental results suggest, the ionization is a multi-step process. The first ionization step ends at around the time of ignition, and the thermite ignition induces another ionization process which primarily produces negative species, with even higher current density. However, our current mass spectrometer configuration

would not allow us to obtain negative mass spectra, and consequently, it is difficult to extract complete mechanistic information without the knowledge of species identification. The fact that the negative ionization step occurs during the ignition event, suggests the strong relation between the solid phase nanocomposite thermite reaction and the ionization process. Therefore, it is essential for us to gain comprehensive knowledge on the negative ionization process in order to understand the nanocomposite thermite reactions.

CONCLUSIONS

REFERENCE

1. K. Sullivan, G. Young, and M.R. Zachariah, *Enhanced Reactivity of Nano-B/Al/CuO MICs*. Combustion and Flame., 2009. **156**: p. 302.
2. Umbrajkar, S.M., S. Seshadri, M. Schoenitz, V.K. Hoffmann, and E.L. Dreizin, *Aluminum-rich Al-MoO₃ nanocomposite powders prepared by arrested reactive milling*. J. Propul. Power, 2008. **24**(2): p. 192-198.
3. Prakash, A., A.V. McCormick, and M.R. Zachariah, *Tuning the reactivity of energetic nanoparticles by creation of a core-shell nanostructure*. Nano Lett., 2005. **5**(7): p. 1357-1360.
4. Zhou, L., N. Piekiel, S. Chowdhury, and M.R. Zachariah, *T-Jump/Time-of-Flight Mass Spectrometry for Time Resolved Analysis of Energetic Materials*. Rapid Communications in Mass Spectrometry, 2009. **23**(1): p. 194-202.
5. Young, G., K. Sullivan, and M.R. Zachariah, *Combustion Characteristics of Boron Nanoparticles*. Combustion and Flame, 2009. **156**: p. 332.

6. Sanders, V.E., B.W. Asay, T.J. Foley, B.C. Tappan, A.N. Pacheco, and S.F. Son, *Reaction propagation of four nanoscale energetic composites (Al/MoO₃, Al/WO₃, Al/CuO, and Bi₂O₃)*. J. Propul. Power, 2007. **23**(4): p. 707-714.
7. Pantoya, M.L. and J.J. Granier, *The effect of slow heating rates on the reaction mechanisms of nano and micron composite thermite reactions*. Journal of Thermal Analysis & Calorimetry, 2006. **85**(1): p. 37-43.
8. Trunov, M.A., M. Schoenitz, and E.L. Dreizin, *Ignition of aluminum powders under different experimental conditions*. Propellants Explosives Pyrotechnics, 2005. **30**(1): p. 36-43.
9. Plantier, K.B., M.L. Pantoya, and A.E. Gash, *Combustion wave speeds of nanocomposite Al/Fe₂O₃: the effects of Fe₂O₃ particle synthesis technique*. Combustion and Flame, 2005. **140**(4): p. 299-309.
10. Fialkov, A.B., *Investigations on ions in flames*. Progress in Energy and Combustion Science, 1997. **23**(5-6): p. 399-528.
11. Filimonov, I. and N. Kidin, *High-Temperature Combustion Synthesis: Generation of Electromagnetic Radiation and the Effect of External Electromagnetic Fields (Review)*. Combustion, Explosion, & Shock Waves, 2005. **41**(6): p. 639-656.
12. Ershov, A.P., *Ionization During Detonation of Solid Explosives*. Combustion Explosion and Shock Waves, 1975. **11**(6): p. 798-803.
13. Setoodeh, M., K.S. Martirosyan, and D. Luss, *Electrical pulse formation during high temperature reaction between Ni and Al*. Journal of Applied Physics, 2006. **99**(8).
14. Martirosyan, K.S., M. Setoodeh, and D. Luss, *Electric-field generated by the combustion of titanium in nitrogen*. Journal of Applied Physics, 2005. **98**(5).
15. Kirdyashkin, A.I., V.L. Polyakov, Y.M. Maksimov, and V.S. Korogodov, *Specific features of electric phenomena in self-propagating high-temperature synthesis*. Combustion Explosion and Shock Waves, 2004. **40**(2): p. 180-185.
16. Martirosyan, K.S., J.R. Claycomb, J. H. Miller, Jr., and D. Luss, *Generation of the transient electrical and spontaneous magnetic fields by solid state combustion*. Journal of Applied Physics, 2004. **96**(8): p. 4632-4636.
17. Igor Filimonov, D.L., *Formation of electric potential during the oxidation of a metal particle*. AIChE Journal, 2004. **50**(9): p. 2287-2296.
18. Martirosyan, K.S., J.R. Claycomb, G. Gogoshin, R.A. Yarbrough, J.H. Miller, and D. Luss, *Spontaneous magnetization generated by spin, pulsating, and planar combustion synthesis*. Journal of Applied Physics, 2003. **93**(11): p. 9329-9335.
19. Martirosyan, K.S., I.A. Filimonov, and D. Luss, *Self-Heating by Joule Dissipation during Gas-Solid Combustion Reactions*. International Journal of Self-Propagating High-Temperature Synthesis, 2003. **12**(2): p. 91.
20. Martirosyan, K.S., I.A. Filimonov, M.D. Nersesyan, and D. Luss, *Electric field formation during combustion of single metal particles*. J. Electrochem. Soc., 2003. **150**(5): p. J9-J16.
21. Henz, B.J., T. Hawa, and M.R. Zachariah, *On the Role of Built-in Electric Fields on Oxidation of Oxide Coated NanoAluminum: ion mobility versus Fickian Diffusion*. submitted to Phys. Rev. B., 2009.
22. Munir, Z.A., *The effect of external electric fields on the nature and properties of materials synthesized by self-propagating combustion*. Materials Science and Engineering A, 2000. **287**(2): p. 125-137.
23. Carleton, F.B. and F.J. Weinberg, *Electric field-induced flame convection in the absence of gravity*. Nature, 1987. **330**(6149): p. 635-636.

24. Douglas, G.T., W.A. Blaine, C.K. James, V.E. Sanders, and F.S. Steven, *Dynamic measurements of electrical conductivity in metastable intermolecular composites*. Journal of Applied Physics, 2006. **99**(2): p. 023705.
25. Korogodov, V.S., A.I. Kirdyashkin, Y.M. Maksimov, A.A. Trunov, and R.M. Gabbasov, *Microwave radiation from combustion of an iron-aluminum thermite mixture*. Combustion Explosion and Shock Waves, 2005. **41**(4): p. 481-483.
26. Zhou, L., N. Piekiel, S. Chowdhury, and M.R. Zachariah, *Time-Resolved Mass Spectrometry of nanocomposite thermite reactions*. manuscript in preparation, 2009.
27. Zhou, L., K. Park, H.M. Milchberg, and M.R. Zachariah, *Understanding the Interaction of an Intense Laser Pulse with Nanoparticles: Application to the Quantification of Single Particle Mass Spectrometry*. Aerosol Science and Technology, 2007. **41**(9): p. 818-827.
28. Lee, D., K. Park, and M.R. Zachariah, *Determination of the size distribution of polydisperse nanoparticles with single-particle mass spectrometry: The role of ion kinetic energy*. Aerosol Science and Technology, 2005. **39**(2): p. 162-169.
29. Chowdhury, S., K. Sullivan, N. Piekiel, L. Zhou, and M.R. Zachariah, *Diffusive vs. Explosive Reaction at the Nanoscale*. in preparation, 2009.
30. Atkinson, A., *Transport processes during the growth of oxide films at elevated temperature*. Reviews of Modern Physics, 1985. **57**(2): p. 437.
31. A. T. Fromhold, Jr., *Theory of Metal Oxidation Volume 2*. Vol. 2. 1980: North-Holland Publishing Company.
32. A. T. Fromhold, Jr., *Theory of Metal Oxidation Volume 1*. Vol. 1. 1976: North-Holland Publishing Company.
33. Rai, A., K. Park, L. Zhou, and M.R. Zachariah, *Understanding the mechanism of aluminium nanoparticle oxidation*. Combustion Theory and Modelling, 2006. **10**(5): p. 843 - 859.
34. Fromhold, A.T. and E.L. Cook, *Kinetics of Oxide Film Growth on Metal Crystals: Electronic and Ionic Diffusion in Large Surface-Charge and Space-Charge Fields*. Physical Review, 1968. **175**(3): p. 877.
35. Wagner, C., *The theory of the warm-up process*. Z. Phys. Chem. Abt. B, 1933. **21**(25).
36. Cabrera, N. and N.F. Mott, *Theory of the Oxidation of Metals*. Reports on Progress in Physics, 1948. **12**: p. 163-184.
37. Zhdanov, V.P. and B. Kasemo, *Cabrera-Mott kinetics of oxidation of nm-sized metal particles*. Chem. Phys. Lett., 2008. **452**(4-6): p. 285-288.

	Total positive ions	Total negative ions [#]	Positive mass spectra	Negative mass spectra*
Probe position	Inside	Inside	Outside	Outside
A1	Ground	DC -200V	Ground	Pulsed ground to -200V
A2	DC -200V	Ground	Pulsed ground to -200V	Ground
A3 and	DC -1500V	DC +1300V	DC -1500V	DC +1300V

liner					
-------	--	--	--	--	--

Al/Bi₂O₃ thermite mixture caused arcing in this configuration

* All four types of thermite mixtures caused arching in this configuration

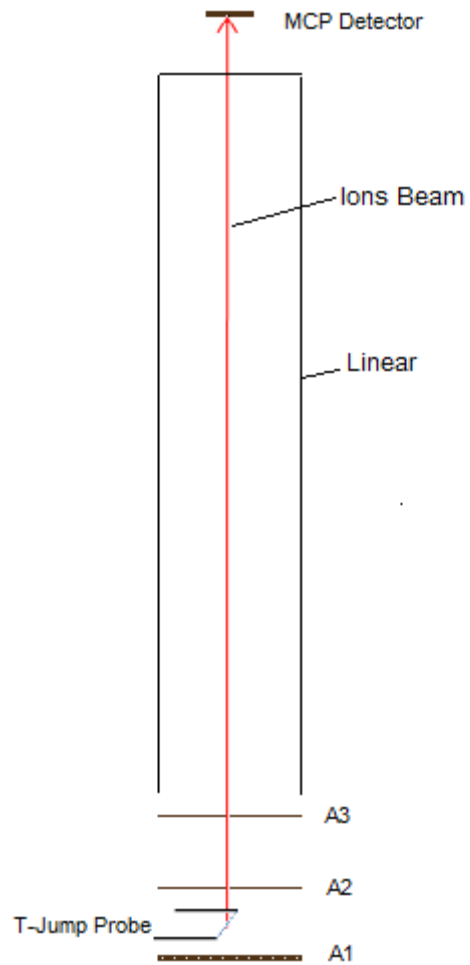
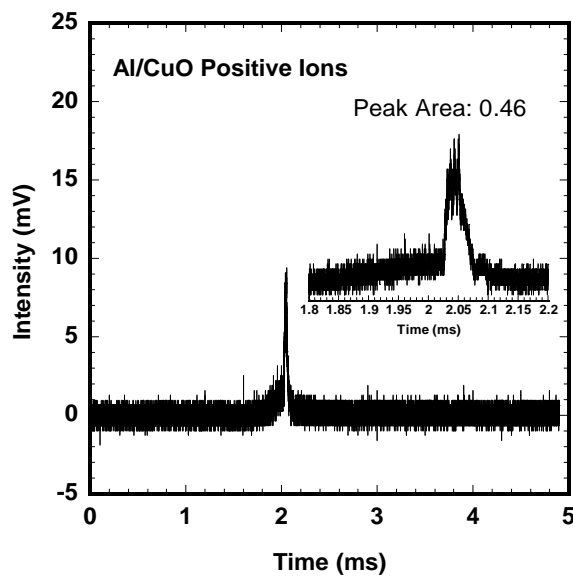
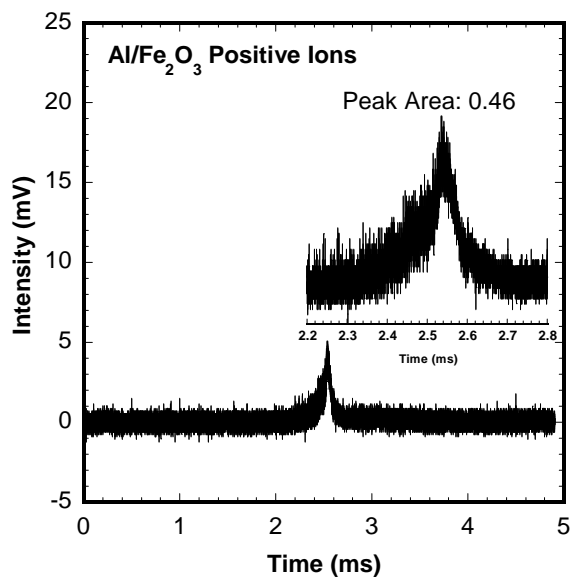
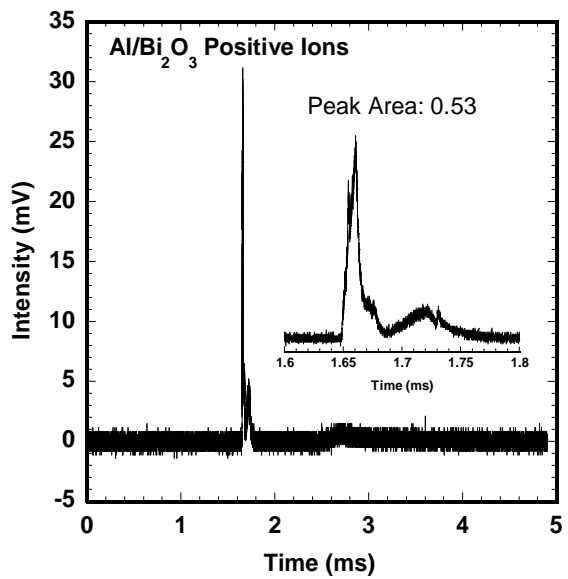
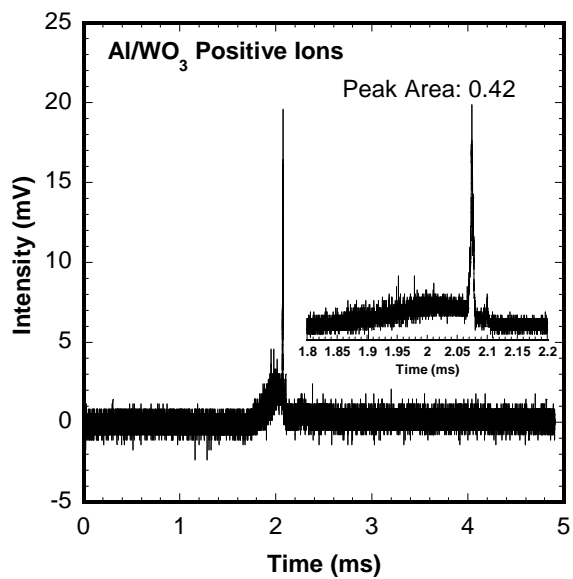


Figure 1



(a)

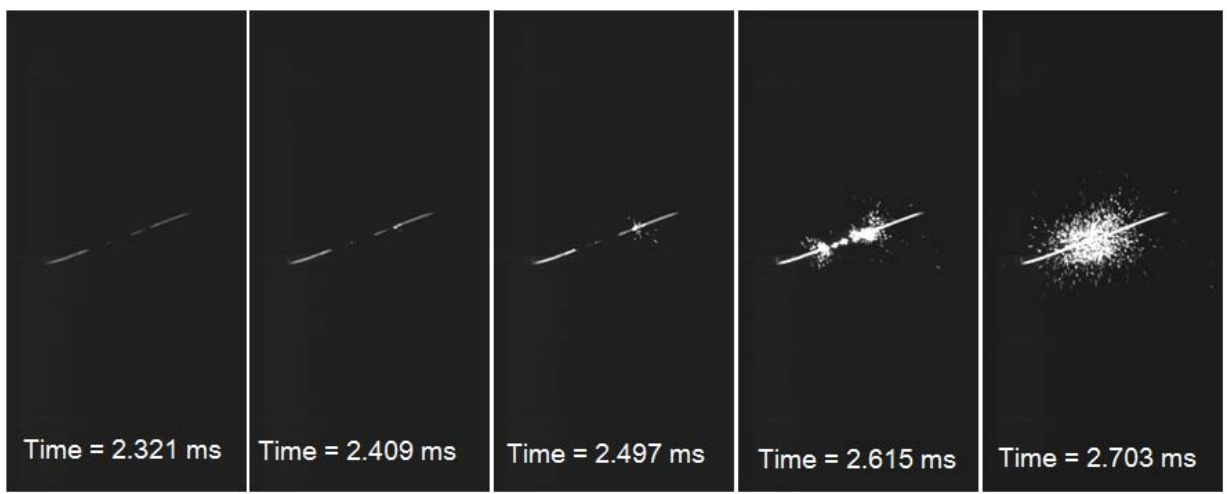
(b)



(c)

(d)

Figure 2



(a)

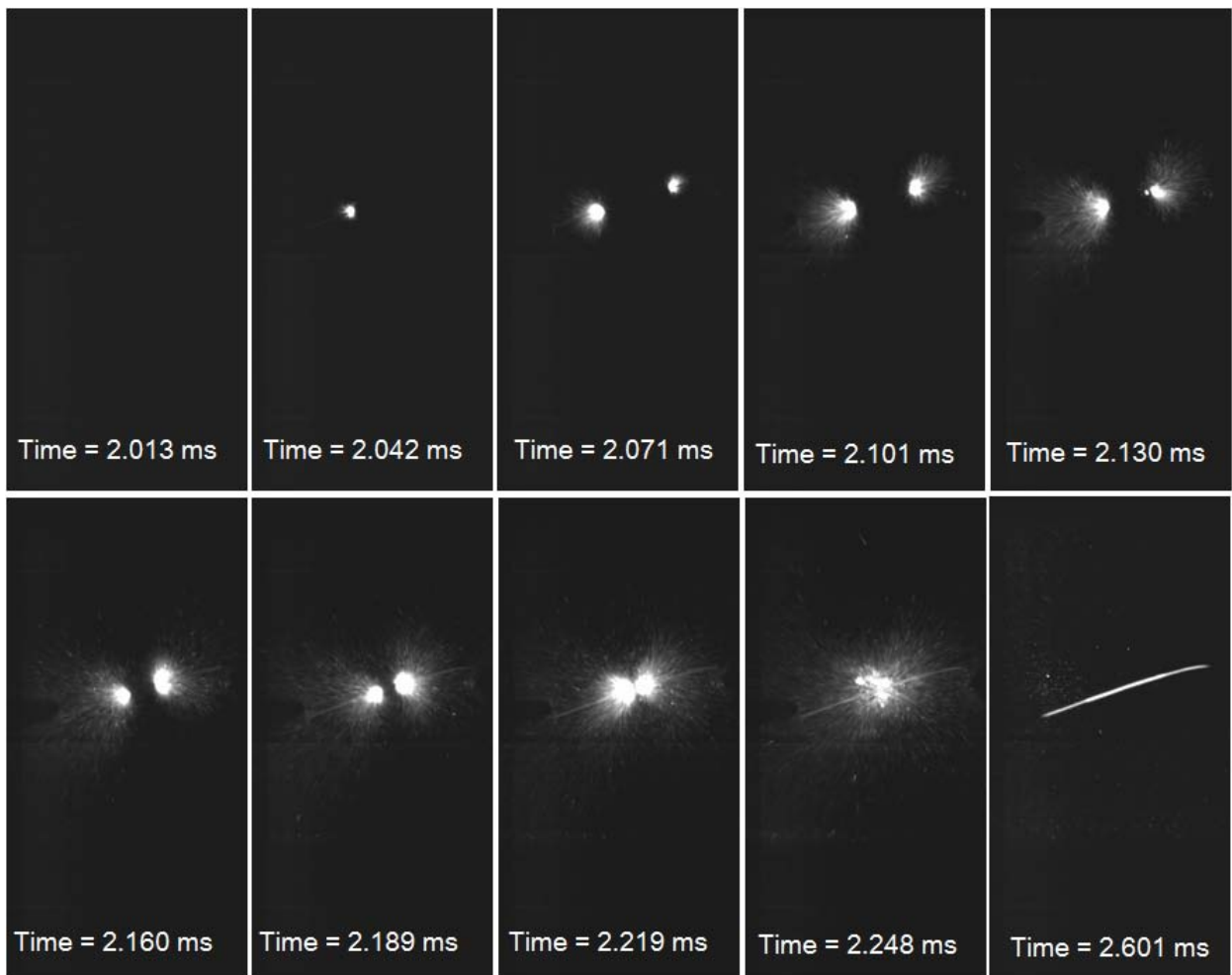


Figure 3 (b)

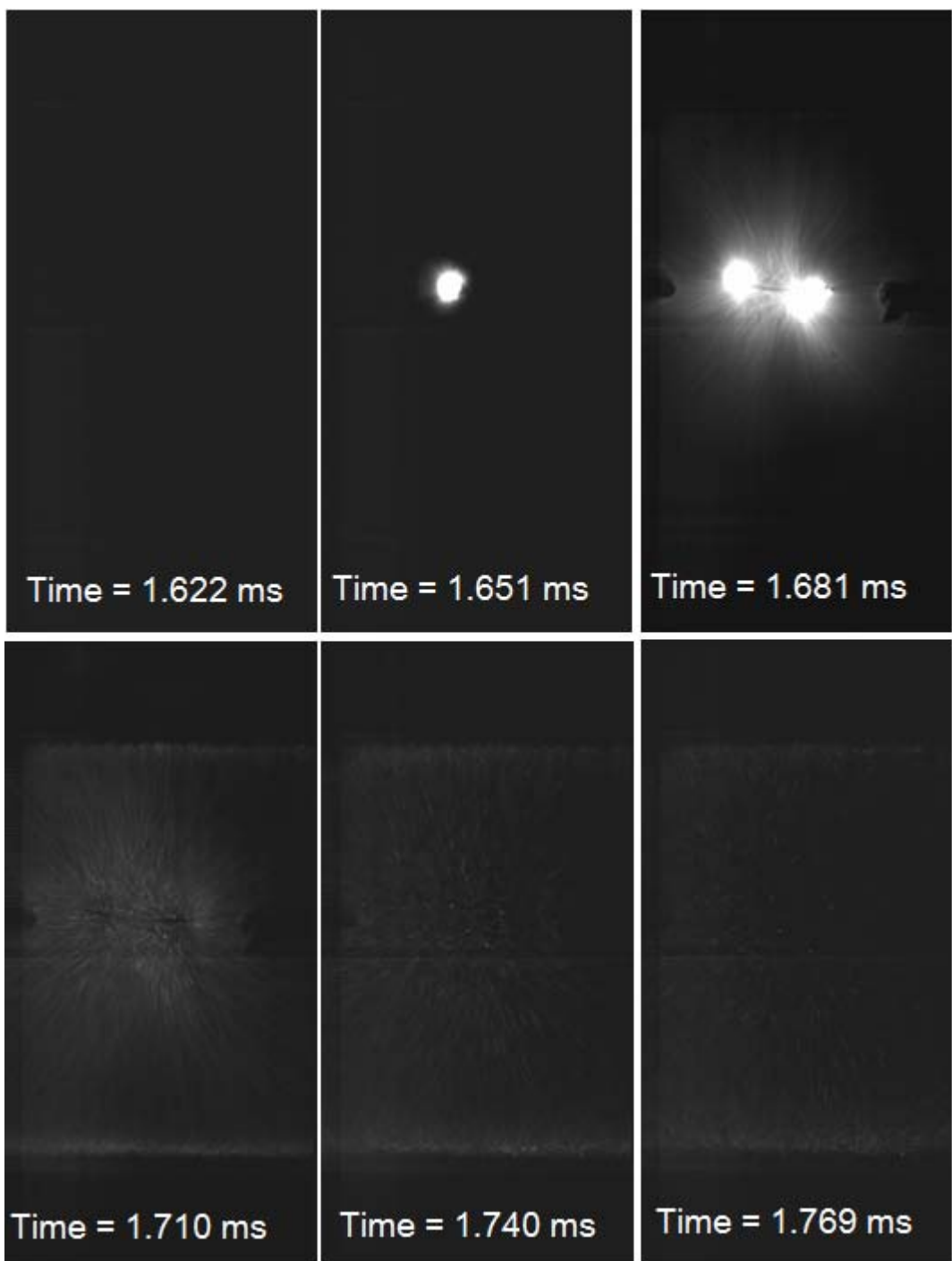


Figure 3 (c)

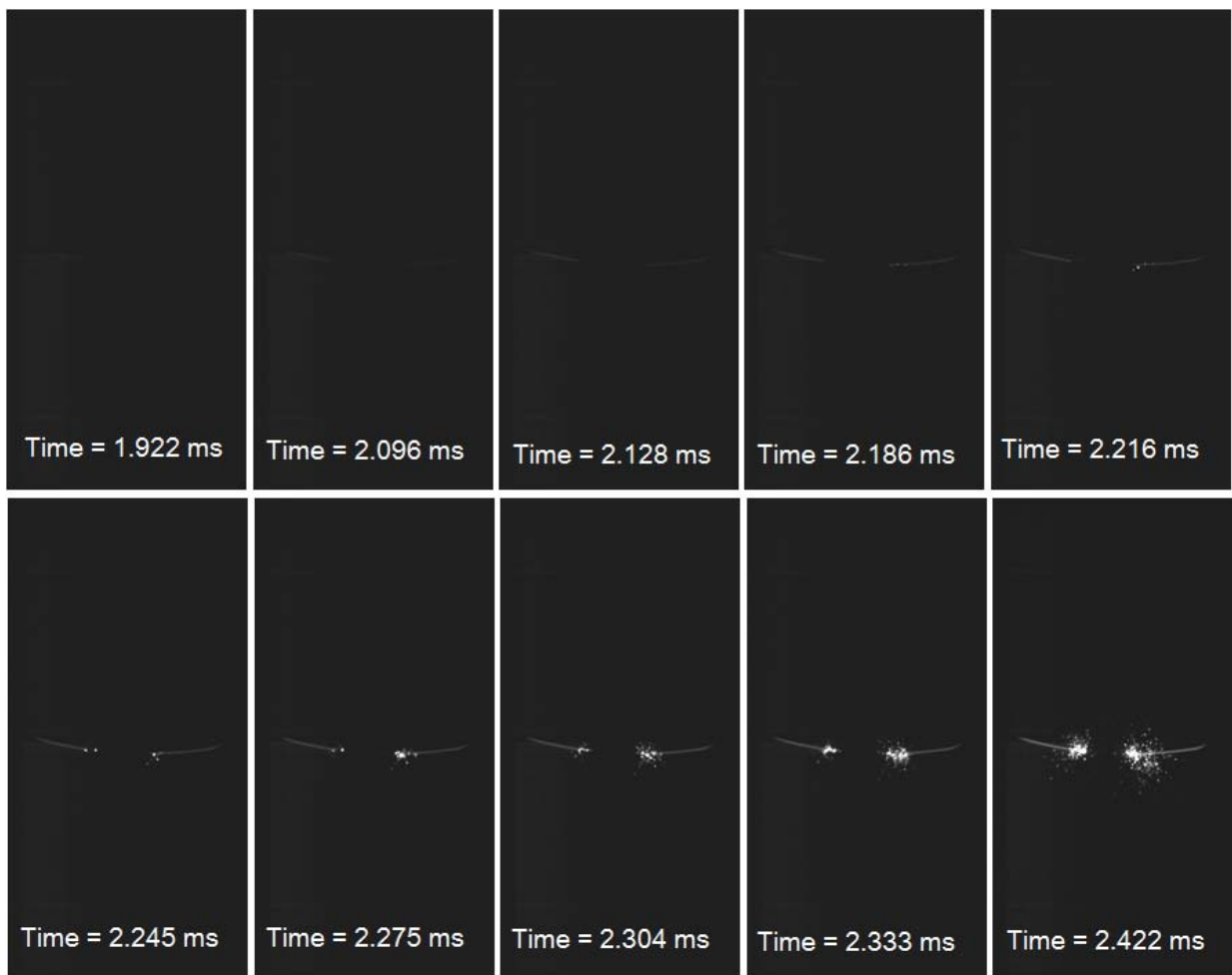
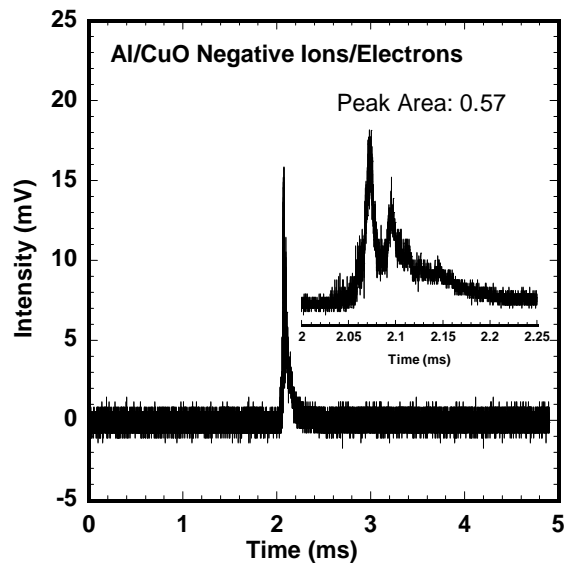
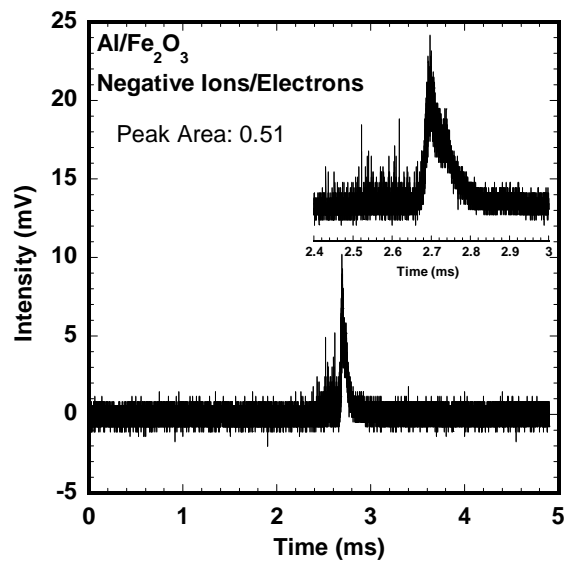
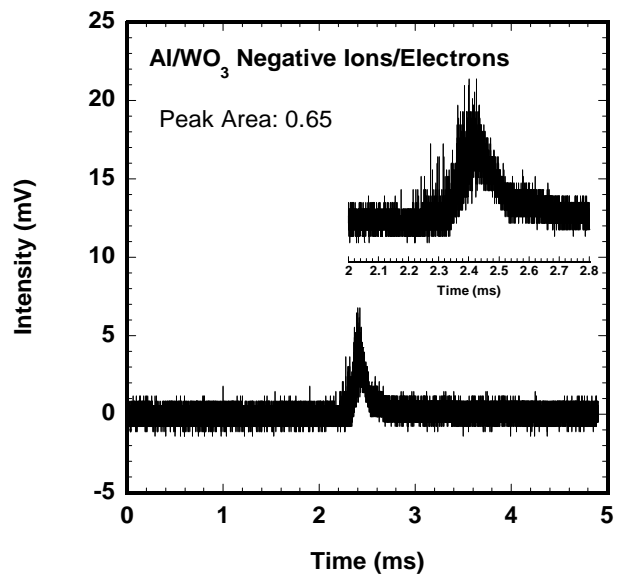


Figure 3 (d)



(a)

(b)



(c)

Figure 4

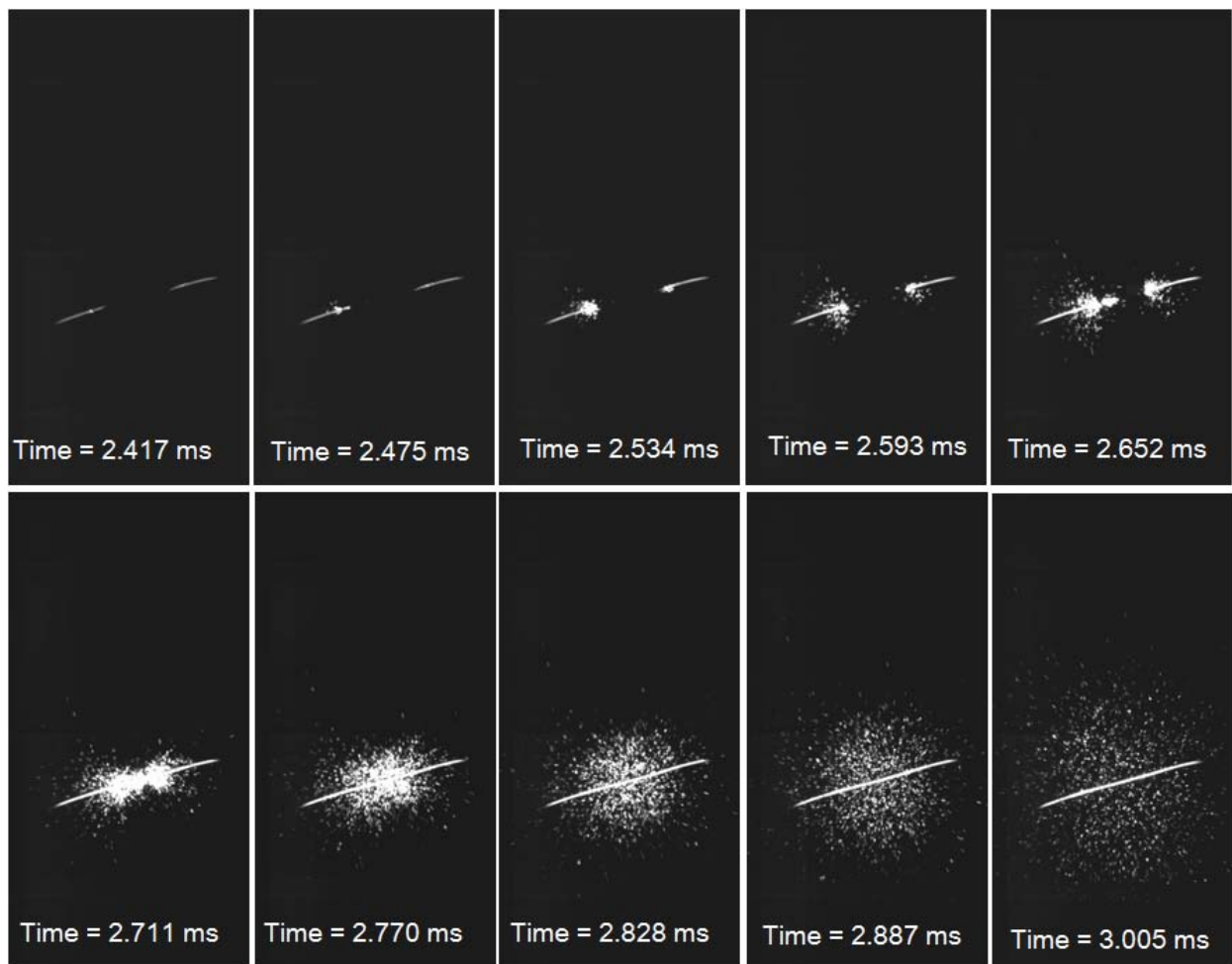


Figure 5 (a)

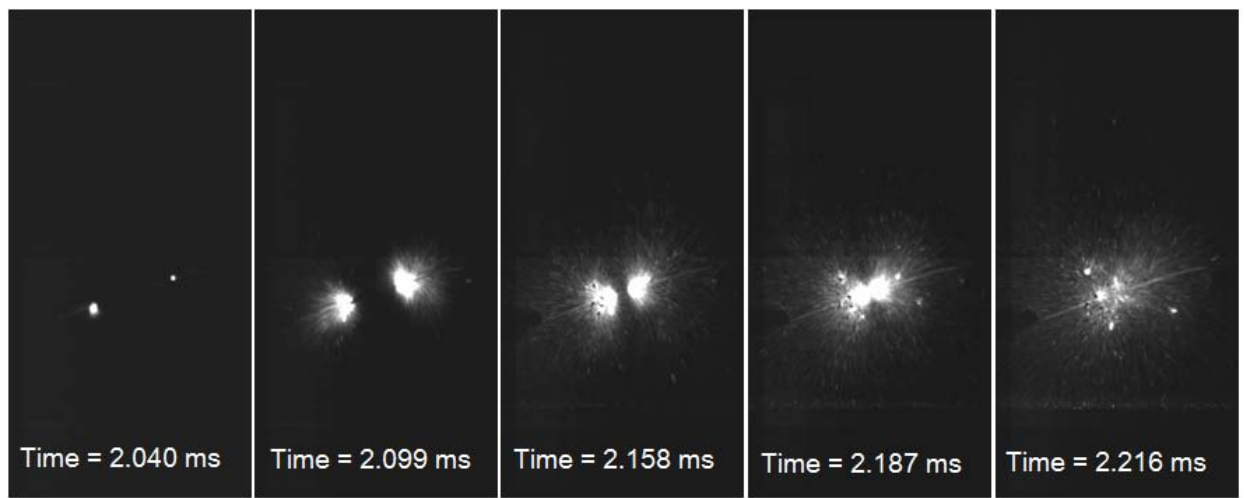


Figure 5 (b)

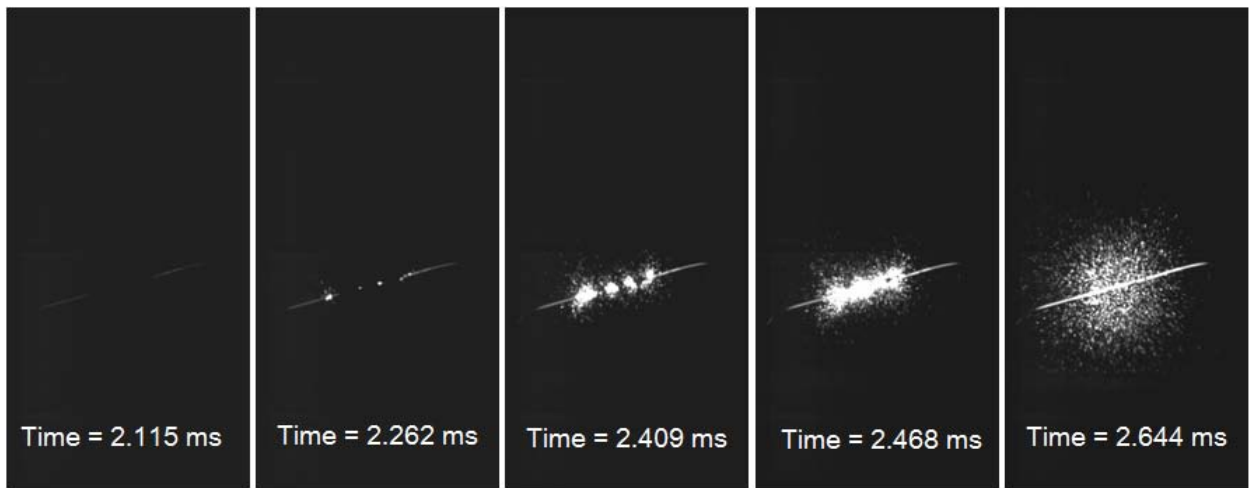
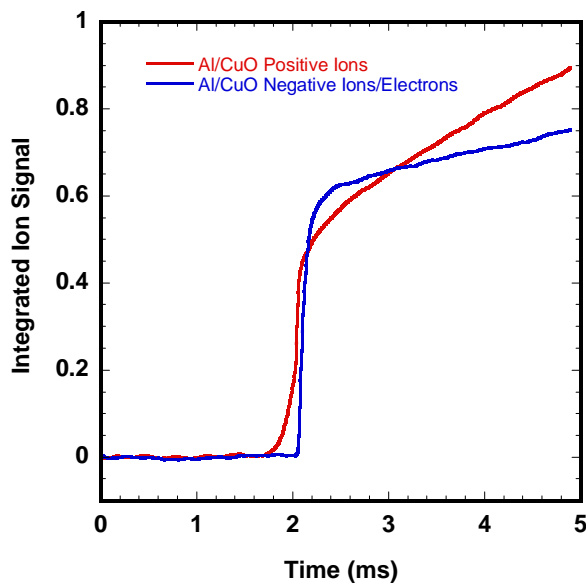
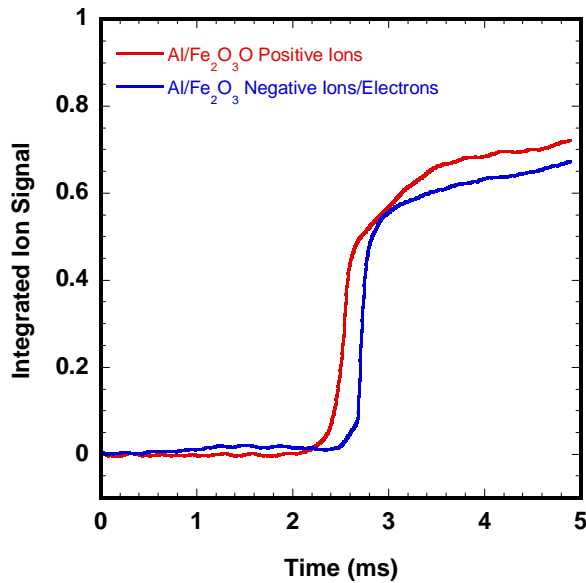
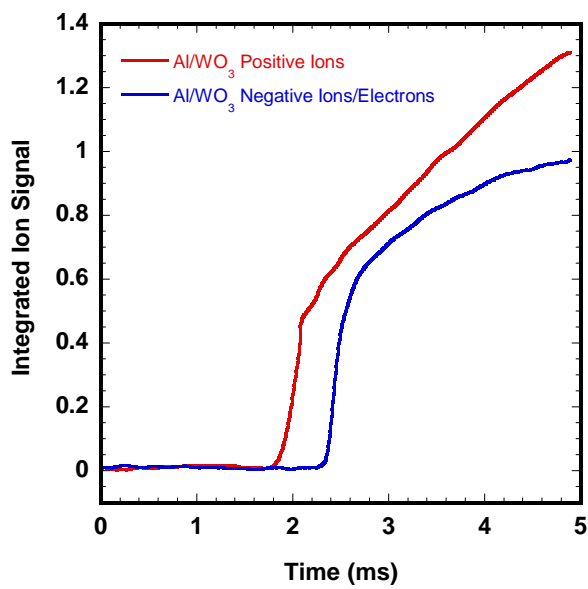
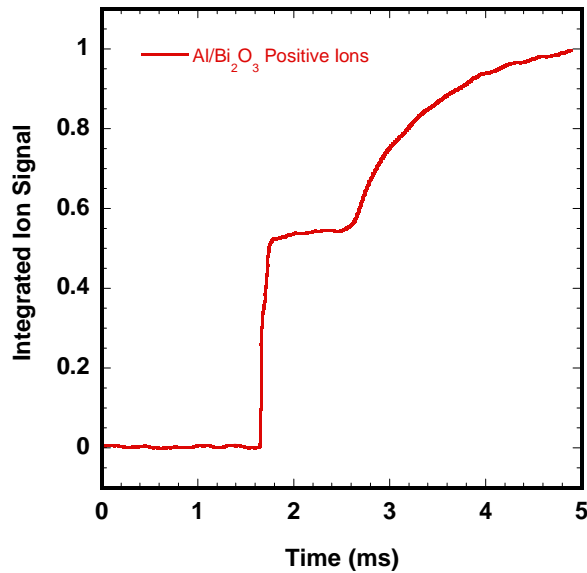


Figure 5 (c)



(a)

(b)



(c)

(d)

Figure 6

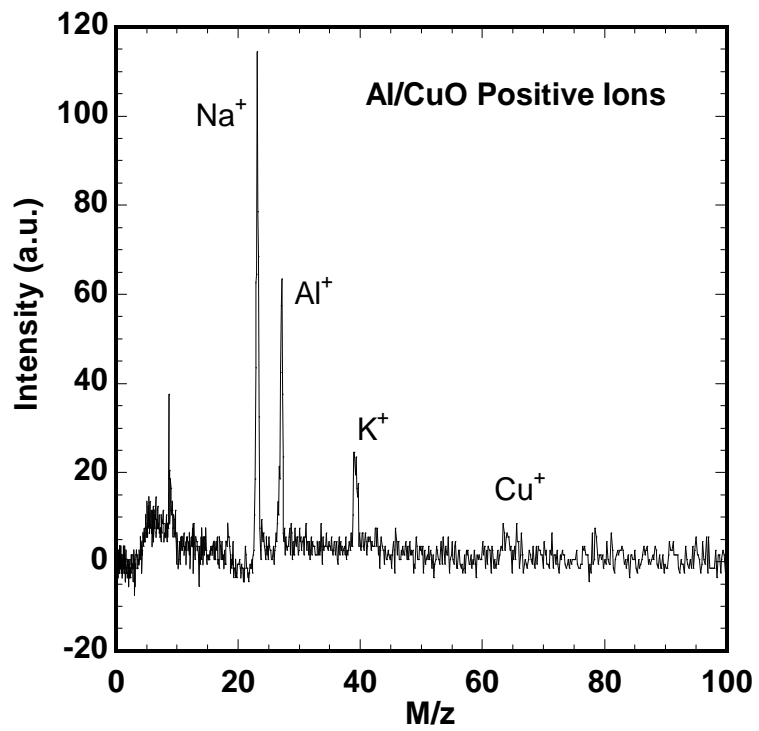


Figure 7

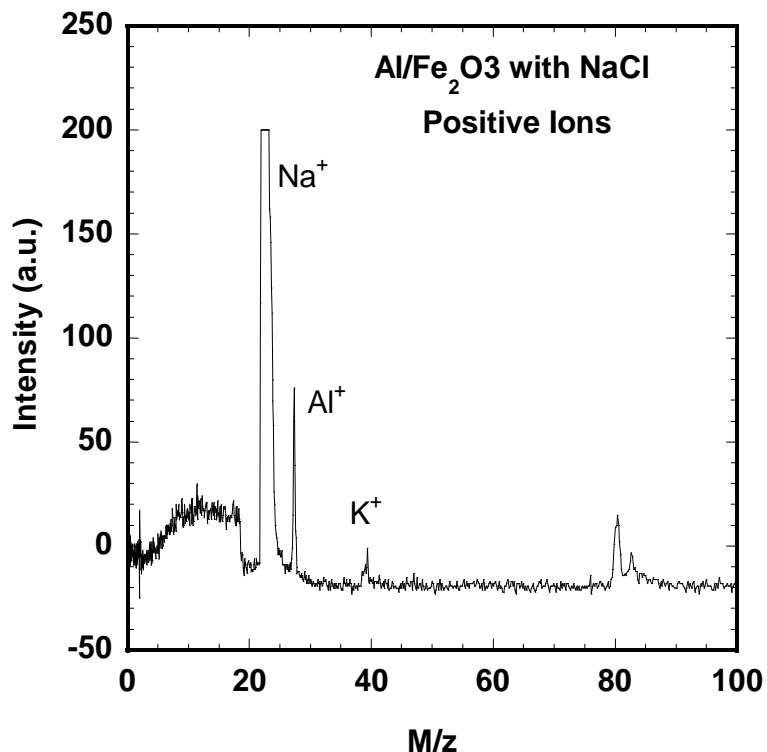


Figure 8